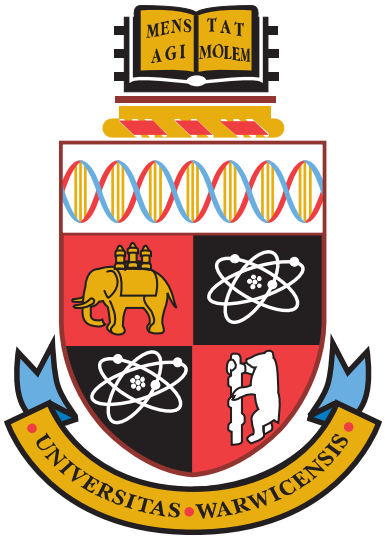

The Structure of Vitreous Binary Oxides: Silicate, Germanate and Plumbite Networks

by

Oliver Lawrence George Alderman

Thesis

Submitted to the University of Warwick

for the degree of

Doctor of Philosophy

Department of Physics

June 2013

THE UNIVERSITY OF WARWICK

For

Samaneh,
Amanda and Nigel

Contents

List of Tables

List of Figures

Acknowledgments

Thanks firstly to Diane, it is difficult to imagine a better supervisor and mentor. To Alex Hannon for his guidance, I hope I have absorbed at least a fraction of his expertise in diffraction and glass science. To Steve Feller and Mario Affatigato for hosting my fruitful and enjoyable visit to Coe College, and to the many students I met there. To Gavin Mountjoy for hosting my visit to the University of Kent, and the chance to learn about molecular dynamics. To Alan Soper, Rowan Hargreaves, Daniel Bowron and Silvia Imberti for support and teaching me about EPSR at the annual workshops of the ISIS facility, STFC. To Uwe Hoppe for showing us around HASYLAB, and in particular, beamline BW5. To Ray Dupree, Andy Howes, Tom Kemp, Kevin Pike, and Dinu Iuga for much NMR related support and expertise. To Richard Beanland for TEM and Steve York for SEM support. To the Diamond group at Warwick for use of their Raman spectrometers. To Dave Hammond and Keith Briggs for their support in the lab. To Emma Barney for many interesting discussions. To fellow officemates through the ages: Steve, Andy, Aoife, Meng, Martin, Robin, Dan, Dean and Iain for companionship and assistance. To the many students and colleagues whom I have had the pleasure of meeting at conferences, workshops and training courses. To the STFC Centre for Materials Physics and Chemistry under Grant CMPC09105 and the EPSRC for funding. To the UK 850 MHz Solid State NMR facility PhD travel fund supported by Bruker and the C. R. Barber Trust Fund of the IoP for additional travel funds. To the Niels Bohr Institute for supporting my trip to the Second Annual Niels Bohr International Academy Workshop on Neutron Science in Copenhagen. To the Society of Glass Technology for providing a platform for young researchers to speak at their annual meetings.

Declaration and published work

I declare that the work presented in this thesis is my own except where stated otherwise, and was carried out entirely at the University of Warwick, during the period of September 2009 to May 2013, under the supervision of Dr Diane Holland. The research reported here has not been submitted, either wholly or in part, in this or any other academic institution for admission to a higher degree.

Some parts of the work reported and other work not reported in this thesis have been published, as listed below. It is anticipated that further parts of this work will be submitted for publication in due course.

[1] O. L. G. Alderman, D. Iuga, A. P. Howes, D. Holland and R. Dupree, *Phys. Chem. Glasses Eur. J. Glass Sci. Technol. B* **53** (3), (2012), 132–140.

[2] O. L. G. Alderman, D. Iuga, A. P. Howes, K. J. Pike, D. Holland and R. Dupree, *Phys. Chem. Chem. Phys.* **15** (21), (2013), 8208–8221.

[3] O. L. G. Alderman, A. C. Hannon, D. Holland, S. Feller, G. Lehr, A. J. Vitale, U. Hoppe, M. Von Zimmermann and A. Watenphul, *Phys. Chem. Chem. Phys.* **15** (22), (2013), 8506–8519.

O. L. G. Alderman

June 2013

Abstract

Structural aspects of three related binary oxide glass systems have been studied in detail using a combination of neutron and x-ray diffraction, empirical modelling techniques, and information from bulk property and spectroscopic measurements.

The local Pb^{2+} environment in $PbO{-}SiO_2$ glasses changes only subtly with composition, having, on average 3.33 short (≤ 2.70 Å) and 1.3 long ($2.70 \leq r_{PbO} \leq 3.27$ Å) Pb-O bonds at 35 mol% PbO, and 3.57 short and 1.3(2) long Pb-O bonds at 80 mol% PbO. Therefore, over the entire series, lead behaves as a glass network forming cation, with highly asymmetric ligand distribution and stereochemically active electron lone-pair (LP), with gradual transition toward more axially symmetric environments (*cf.* crystalline PbO) as the PbO content increases. Structural modelling of the highest lead content oxide glass ($80\,PbO \cdot 20\,SiO_2$) to date reveals organisation of LPs to form voids, analogous to interlayer spaces in crystalline PbO polymorphs, and channels found within other crystalline lead oxide compounds such as $Pb_{11}Si_3O_{17}$. The plumbite glass network is characterised by a high degree of intermediate-range ordering, evidenced by a very narrow first sharp diffraction peak (FSDP), as well as significant edge-sharing of Pb polyhedra and high oxygen-cation coordination numbers, e.g. $[OPb_4]$, $[OPb_3Si]$.

$PbO{-}GeO_2$ glass formation was found as high as 75 mol% PbO using rapid twin-roller quenching. Such high lead glasses are analogues of the silicates, but with a ~10% enhancement in correlation length derived from the FSDP. In the low PbO region a broad maximum in Ge-O coordination number of $n_{GeO} = 4.14(3)$ at ~26.5(5) mol% PbO was observed. This is much smaller, and at higher metal oxide content than in Na, K and Cs germanate glasses and contradicts published results [N. Umesaki *et al.*, *Physica B* **213**, (1995), 490]. The weakness of the effect is attributed to Pb^{2+} playing a predominantly network forming role, although Ge-O and Pb-O coordination numbers showed positive correlation, such that the presence of $[GeO_5]$ or $[GeO_6]$ is indicative of Pb having some 'modifying' character. It was argued, based on empirical models and the known crystal chemistry, that Pb may occupy sites of intermediate character, with mixed *s-p* LP character, rather than invoking a bimodal distribution of network forming and modifying Pb sites.

Homogeneous calcium germanate glasses were obtained in the region 21 to 41 mol% CaO by rapid twin-roller quenching, with glass-in-glass phase separation occuring in the low CaO region, and crystallisation around the $CaGeO_3$ composition. A very broad maximum of $n_{GeO} = 4.30(3)$ at ~28.0(5) mol% CaO was observed, correlating approximately with maxima in atomic number densities and glass transition temperatures. Non-bridging oxygen (NBO) are present in all glasses, again in contrast to alkali germanates. The position of the maximum is attributed to stabilisation of vertex sharing $[GeO_{m>4}]$ and/or $[GeO_6]$ units by divalent Ca^{2+}. The presence of NBOs is related to the Ca-O coordination number of ~7, with higher n_{GeO} and less NBO predicted in Sr and Ba germanate glasses, where M-O coordination is expected to be larger.

In both Ca and Pb germanate systems, the equilibrium crystals have much larger n_{GeO} than the glasses, and this implies a decrease of n_{GeO} with liquid, supercooled liquid and glass fictive temperatures. This tentative conclusion is supported by measurements on two $40\,PbO \cdot 60\,GeO_2$ glasses with different thermal histories.

Glossary and abbreviations

3QMAS	Triple quantum magic angle spinning (NMR)
AXS	Anomalous x-ray scattering
BAD	Bond angle distribution
BO	Bridging oxygen
BV	Bond valence
CN	Coordination number
CND	Coordination number distribution
CSA	Chemical shift anisotropy
DFT	Density functional theory
DSC	Differential scanning calorimetry
DTA	Differential thermal analysis
EBS	Electrostatic bond strength
EDX	Energy dispersive x-ray (spectroscopy)
EELS	Electron energy loss spectroscopy
EFTEM	Energy-filtered transmission electron microscopy
EPSR	Empirical potential structure refinement
ESR	Electron spin resonance
EXAFS	Extended x-ray absorption fine structure
FCC	Face-centred cubic
FEGSEM	Field emission gun scanning electron microscope
FSDP	First sharp diffraction peak
FT	Fourier transform
FWHM	Full width at half maximum
HCP	Hexagonal close packed
IR	Infrared
IRO	Intermediate-range order
LP	Lone-pair

MAS NMR	Magic angle spinning NMR
MBO	Metal-bridging oxygen
MC	Monte Carlo
MD	Molecular dynamics
MQMAS	Multiple quantum magic angle spinning (NMR)
NBO	Non-bridging oxygen
ND	Neutron diffraction
NLO	Non-linear optical
NMR	Nuclear magnetic resonance
NN	Nearest neighbour
NNO	Next-nearest oxygen
PPDF	Partial pair distribution function
RCP	Random close packed
RDF	Radial distribution function
RF	Radio frequency
RMC	Reverse Monte Carlo (modelling)
RMS	Root-mean-square
SAXS	Small angle x-ray scattering
SEM	Scanning electron microscope
TEM	Transmission electron microscopy
TGA	Thermogravimetric analysis
TTT	Time-temperature-transformation
UV	Ultraviolet
VSEPR	Valence shell electron pair repulsion
XANES	X-ray absorption near edge structure
XPS	X-ray photoelectron spectroscopy
XRD	X-ray diffraction

Chapter 1

Introduction

1.1 Condensed matter and the vitreous state

Solid state physics was built upon the study of crystalline solids and the relationships between their physical properties and their periodic structure and dynamics. Such periodic systems often have simple mathematical descriptions, and the phenomenon of Bragg diffraction allows experimental access to the atomic scale - the basis of crystallography. However, it was soon discovered that many properties are strongly dependent on *disorder*, manifest, for example, as point defects, dislocations, chemical inhomogeneity in alloys or doping in semiconductors. The latter provide inspiration for P. W. Anderson's theory of electron localisation [1] which won him a share of the 1977 Nobel Prize for physics. Nonetheless, systems exhibiting strong topological order - that of the periodic crystal lattice - remained inherently more tractable than those systems lacking periodicity. The latter systems however encompass a diverse range of condensed materials. These include: both equilibrium and supercooled liquids; amorphous solids, including polymers, plastics, rubbers, amorphous semiconductors and, in particular, glasses - which may be formed from organic, inorganic and even metallic liquids.

The amorphous nature of these materials precludes Bragg diffraction and necessitates alternative approaches to understanding their structure and properties. A wide range of structural and dynamical probes, including computational models, are required in order to gain sufficient information to address the pertinent questions, and it is advances in experimental and computational methodologies and technologies which have allowed recent advancements in the physics and chemistry of amorphous materials [2].

Many fundamental aspects of condensed matter are captured within the burgeoning phenomenology of amorphous systems, and Greaves and Sen [2] give an excellent recent review in the context of inorganic materials. Key examples, all of which are active areas of research, include: polyamorphism and the existence of liquid-liquid

phase transitions - analogous to polymorphism in crystalline solids; rheological processes of viscous flow, structural relaxation, terahertz modes and the boson peak; the glass transition and kinetic phenomena associated with crystallisation and liquid-liquid phase separation; long-range order beyond the local structure, as well as chemical and structural inhomogeneity and the concept of 'frozen-in' density fluctuations; the role of thermal history, quench rate and fictive temperature upon the structure of glass and the hypothesised existence of 'perfect glasses' with identical entropy to their crystalline analogues.

Whilst the above provides more than sufficient motivation for the study of condensed amorphous systems, the wide ranging technological applications of such materials cannot be understated. Just considering glassy materials, these go far beyond the 'everyday' soda-lime-silicate window glasses and borosilicates such as Pyrex®, which we often take for granted. Diverse high-technology applications include: glass fibres for optical communication, the development of which [3] won C. K. Kao part of the 2009 Nobel Prize for physics; biocompatible and bioactive (phosphate) glasses; nuclear waste encapsulation; non-linear optical materials; solid state memory (chalcogenides); hosts for luminescent or scintillating inclusions.

The present thesis deals particularly with structure determination of selected oxide glasses, and structure variation with glass composition under ambient conditions. However, it is important to bear in mind the broader context, as illustrated above. Fundamental concepts particularly relevant to this thesis are the influence of thermal history on glass structure, and the links between glass structure and that of the parent liquid melt, as well as its rheological properties. Known applications of the particular systems of interest will be introduced where relevant.

1.2 Overview

Some basic principles pertinent to the vitreous state will be introduced in the opening section of Chapter 2. Subsequent sections will introduce: some of the tools and methodologies applied to the study of glasses, with an emphasis on structure elucidation; oxide glasses in general, followed by relevant subclasses including the silicates, germanates and heavy-metal oxides. Chapter 3 reviews the literature relevant to the

three specific binary glass systems that form the subject of the thesis: the calcium and lead germanates, and the lead silicates. In Chapter 4 the theoretical basis behind the experimental and computational methods employed will be outlined, as well as details given of specific experimental arrangements and practices. The primary experimental tools used are those of neutron and x-ray diffraction, which are applied within the framework of the total scattering formalism. Subsequent chapters present the results, analysis, discussion and conclusions obtained for each of the three systems, calcium germanates in Chapter 5, lead silicates in Chapter 6 and lead germanates in Chapter 7. In some sense the $PbO-GeO_2$ glasses are the most complex, and understanding their structural behaviour builds upon the knowledge gained through the study of the related $PbO-SiO_2$ and $CaO-GeO_2$ glasses. Chapter 8 sets the new knowledge gained in a wider context, and some predictions and suggestions for further study are given.

References

[1] P. W. Anderson, *Phys. Rev.* **109** (5), (1958), 1492–1505.

[2] G. N. Greaves and S. Sen, *Adv. Phys.* **56** (1), (2007), 1–166.

[3] K. C. Kao and G. A. Hockham, *Proc. IEE* **113** (7), (1966), 1151–1158.

Chapter 2

Glass Forming Oxides

2.1 The vitreous state

Glass is an amorphous solid that is obtained upon cooling from the liquid state without crystallisation. This necessitates that the supercooled region be traversed at a rate sufficient to preclude crystallisation, until the structural relaxation and observational time-scales cross over. At such a point, viscosity and the structural relaxation time become so large that, as cooling proceeds, the liquid is unable to equilibrate and its non-equilibrium structure is 'frozen-in'. The resultant glass has higher enthalpy and entropy and lower density than the equilibrium - crystalline - solid (Fig. 2-1a). However, the degree to which these parameters differ between the vitreous and crystalline states is not immutable, but rather is a function of the fictive temperature, T_f, at which equilibrium is lost, whilst T_f correlates with the applied cooling rate. For example, Fig. 2-1 illustrates schematically how some thermodynamic parameters vary with temperature during cooling. Whilst crystallisation occurs discontinuously (a first-order phase transition), implicit in Fig. 2-1 is that the glass transition occurs over a range of temperatures. This does not mean that it can be considered as a second-order phase transition, for it is fundamentally non-equilibrium in nature. Two different glass transition temperatures, T_g and T_g', are indicated in Fig. 2-1, for rapidly and slowly cooled glasses respectively, note however that these merely characterise the location of the transition region. For convenience a calorimetric T_g is often defined by extrapolation of the heat capacity curves, as in Fig. 2-1b. Note that a commonly used alternative definition for T_g is the temperature at which the viscosity equals 10^{12} Pa s.

Given that the liquid-like structure of glass precludes Bragg diffraction, as well as a simple structure description based on a finite unit cell, not only are alternative experimental methodologies required, but so too are alternative means of structure specification and description. Shelby [1] and Wright [2] list various features necessary for

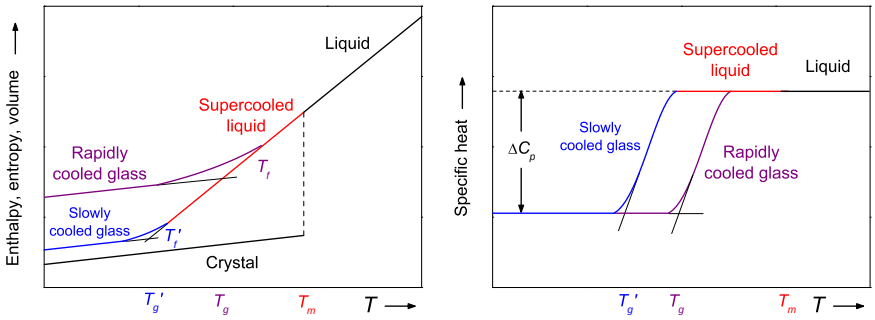

(a) **(b)**

Figure 2-1 a) Schematic illustration of enthalpy, entropy or volume variation with temperature for various equilibrium and non-equilibrium states of matter. T_f and T_g indicate fictive and glass transition temperatures respectively for a rapidly cooled glass, whilst primed symbols denote the same quantities for a slowly cooled glass. b) The temperature variation of the specific heat contains a step change of size ΔC_p at the glass transition, whilst T_g can be defined by extrapolation of linear regions.

the structure description of an amorphous solid, and in a similar vein, Table 2-1 gives a (necessarily incomplete) account of commonly discussed structural characteristics on various length scales.

The list in Table 2-1 may seem, at least in places, arbitrary, and indeed an alternative description of an amorphous solid could simply involve the specification of the coordinates of all (or a large number of) the constituent atoms. Such an approach follows that of the crystallographic unit cell, but without any of the simplifications arising from symmetry and periodicity, such that a finite and non-unique system must be considered. Nonetheless, three-dimensional models of amorphous systems can prove invaluable, and can be broken down into the contrived aspects listed (Table 2-1) at will, in order to gain greater understanding of specific properties. Of course it should be stated that no model is valid unless consistent with all available experimental information.

In practice not all of the aspects listed are experimentally accessible. Furthermore, it is often average values rather than full distributions which are available, and these facts necessitate a combination of both modelling, experimental, and theoretical approaches, some of which are described in §2.2 below.

Implicit in Table 2-1 are several key concepts, including the (random) network construct, which stems from the seminal work of Zachariasen [3]. A network description

Table 2-1 Commonly discussed features necessary for the structural description of an amorphous solid.

Scale	Feature
Local/	Coordination numbers
short-range	Average bond lengths (2-body)
	Bond length static and thermal variations
	Site specific bonding and symmetry
	Intra-polyhedral bond angles (3-body)
Intermediate	Polyhedral connectivity (number of connections)
	Polyhedral connection type (corner-, edge- or face- sharing)
	Superstructural units (rigid units larger than local polyhedra)
	Inter-polyhedral bond angles (3-body)
	Inter-polyhedral torsion angles (4-body)
Topological/	Network dimensionality
longer-range	Shortest path ring sizes
	Chemical ordering
	Void distribution
Longer-range/	Density and/or chemical fluctuations
meso-/	Morphology of the inhomogeneity
macroscopic	Clustering/phase-separation
	Dopants, impurities and defects

of an atomic arrangement, as opposed to a consideration of atomic packing, arises naturally for low density structures, and the presence of well defined local order, in the form of coordination polyhedra, typically with low ($\leq$ 4) coordination numbers. The fact that chemical composition can be tuned almost continuously in amorphous solids constitutes part of their great appeal as functional materials, providing huge flexibility, far beyond that of non-stochiometry and solid solution in crystals. Another feature of amorphous solids which is not common to crystalline solids, is that of longer-range fluctuations. These may be chemical in nature, and relate to the phenomenon of liquid-liquid immiscibility, or may be density fluctuations, which relate to the phenomenon of polyamorphism.

2.2 Experimental and analytical approaches

As noted above, the amorphous nature of glasses necessitates a multi-technique approach to structure elucidation, as well as a synthesis of experimental, computational and theoretical aspects. This thesis, and to a greater extent the literature referred to herein, contains information garnered from a profusion of different methods, and, as

in any scientific field, the scientist wishing to make sense of a particular problem must have at least a rudimentary grasp of all of them. Therefore, in the present section, techniques commonly applied to structure determination in glasses are briefly introduced, such that their specific applications can be discussed without preamble later on.

2.2.1 Experimental Techniques

Central to this thesis are diffraction techniques, and, more specifically, the use of total scattering. This technique is introduced in detail in Chapter 4, and in brief here, see also Wright [2]. Typically, neutrons from a reactor or pulsed-proton spallation source, or x-rays from an x-ray tube or in the form of synchrotron radiation are used, although high energy electrons are also applicable in the case of very thin samples. These are incident upon a material of interest and the scattered radiation detected. The elastically scattered signal can be separated from other contributions, and this contains structure information due to interference if there are certain interatomic distances which are more probable than others. Fourier transform of the entire pattern yields a time-averaged spatial correlation function which is a scattering length weighted 'probability' distribution of interatomic spacings. From this, information on mean bond lengths, coordination numbers and isotropic displacements can be extracted. The technique can be made element specific by use of isotopic substitution in neutron diffraction, use of anomalous scattering near an absorption edge or resonance, or even by isomorphic substitution. The information on interatomic distances derives from the so called wide-angle region, however, if longer-range fluctuations in scattering density exist, then there will also be small-angle scattering, and this contains information on the spatial size, morphology and chemistry of the fluctuations.

Nuclear magnetic resonance (NMR) spectroscopy exploits shifts in nuclear Larmor precession frequencies, of spin $I \neq 0$ nuclei, arising from local electromagnetic fields and interactions within a material. These interactions include the chemical shift arising from induced magnetic fields, through-space nuclear dipole-dipole, through-bond J-couplings, and nuclear electric quadrupole ($I > 1/2$) interaction with local electric field gradients. NMR is therefore an isotope specific probe of the local structure and dynamics, and can yield diverse information ranging from coordination and local symmetry, out to second coordination sphere, polymerisation and connectivity informa-

tion. In oxide glasses, commonly exploited isotopes include spin-1/2 ^{29}Si and ^{31}P, and quadrupolar nuclei such as ^{27}Al, ^{11}B and ^{17}O, although the latter is less commonly employed due the very low natural abundance of ^{17}O. Both homo- and heteronuclear correlation experiments allow for the determination of proximities of like or unlike nuclei respectively. Importantly NMR spectroscopy can detect very low abundance structural species, which nonetheless may play vital roles in property determination. See Eden [4], Massiot *et al.* [5] and Mackenzie and Smith [6] for further discussion.

Extended x-ray absorption fine structure (EXAFS) is a spectroscopic technique which relies upon the modulation of x-ray absorption, at post absorption edge energies, due to the interference of emitted and backscattered photoelectrons. Since the backscattering occurs from neighbouring atoms, EXAFS is sensitive to the local structural arrangement in the material. Furthermore, the technique is element specific, depending upon which absorption edge is studied. EXAFS spectroscopy is, in principle, capable of providing the same local structural information as total scattering, but is based upon more complex physical phenomena which in practice can result in large uncertainties, particularly in coordination number and displacement parameters. The related x-ray absorption near-edge structure (XANES) spectroscopy deals with the energy region close to an absorption edge, at energies below the EXAFS regime, where multiple scattering processes dominate. XANES, in principle, can be used to infer structural information, including oxidation and hybridisation states, since core-level phenomena are dependent on these.

X-ray photoelectron spectroscopy (XPS) is used to measure the binding energies of electrons, which, in general depend upon chemical bonding. A limitation of the technique when applied to bulk structure determination is its surface sensitivity, which increases with increasing binding energy.

Vibrational spectroscopies, typically Raman, infrared or inelastic neutron or x-ray scattering, can also be used to infer structural information based on the variation of local vibrational modes with structure and bonding arrangements. The aforementioned techniques are in general complementary owing to differences in selection rules.

Electron microscopy, and specifically transmission electron microscopy (TEM), uses relativistic electrons combined with sophisticated electron optics, and can be used for diffraction (including total scattering) from thin materials, inelastic scattering, as

well as for imaging using various contrast schemes. As such, both local structural information can be gained, alongside information on chemical fluctuations and inhomogeneity, albeit for limited sample volumes.

Many other experimental techniques, such as Mössbauer spectroscopy, nuclear resonant scattering, and physical property measurements such as inert gas diffusion, conductivity and elastic response are also often employed in the elucidation of structure in amorphous materials, but are not central to this thesis. What is clear is that a holistic approach combining numerous experimental techniques, as well as computational methods (*vide infra*) is required to understand the complexities of disordered structures.

2.2.2 Computation and modelling

Computational modelling and simulation of amorphous materials are used in several ways to help understand their electronic and/or atomic structure and dynamics. Predictive tools include Monte Carlo (MC) and molecular dynamics (MD) methods. *Ab initio* implementations treat the full many-body system of electrons and nuclei, usually under the Born-Oppenheimer approximation, and simplification by density functional theory (DFT), at various levels of approximation, has proved extremely effective. Other than pure prediction of structure and dynamics, *ab initio* modelling techniques can be used as powerful tools for understanding how material specific properties give rise to various experimental spectroscopic signatures. Classical manifestations of MC and MD typically involve simulation at the atomic scale based on analytical two-body interaction potentials, although three-body and higher terms can also be introduced at computational expense. Nonetheless, a classical treatment allows for larger systems to be simulated on longer time-scales as compared to *ab initio* treatments. It should be noted however that the paramaterisations of the potentials used often rely upon *ab initio* calculations or experimental measurements.

An empirical modelling approach is employed in this thesis, namely that of empirical potential structure refinement (EPSR), and this is akin to reverse Monte Carlo (RMC) modelling, both of which can be compared to the Rietveld method of crystal structure refinement based on powder diffraction patterns. Both EPSR and RMC seek to derive atomistic models which are consistent with measured total-scattering diffraction patterns, although spectroscopically derived information may also be included,

and ideally all known experimental constraints are satisfied by the final (ensembles of) atomic distributions. The need for empirical modelling techniques stems from the computational intensiveness, and sensitivity to the level of approximation, of predictive methods. This is particularly relevant for disordered materials, such as glasses, which require the treatment of large numbers of atoms to allow for chemical complexity, large scale density and chemical fluctuations and to prevent artefacts arising from (periodic) boundary conditions. Furthermore, in MD, integration of the equations of motion over large time periods is required to simulate the quenching of a glass from the liquid state, limiting the method to unrealistically high quench rates and glass fictive temperatures.

2.3 Oxide glasses

For the purpose of the present thesis, oxide glasses may be defined as those glasses in which oxygen is the sole anionic species. Oxide glasses are characterised by a very high degree of chemical ordering, specifically, homopolar bonds are not expected. Single oxide glasses contain a single cationic species and are often grouped according to their glassforming ability. For example, Sun's criterion [7], which builds upon the earlier work of Zachariasen [3], ranks single oxides in order of increasing single bond-strength, E_B, which is the dissociation energy per mole MO_n divided by the cation-oxygen coordination number. Such oxides as B_2O_3, SiO_2, GeO_2, P_2O_5 and V_2O_5 have large E_B, are consequently found to vitrify in pure form, and in glass science terminology are referred to as *glass (network) forming* oxides (or cations). Oxides of the alkali and alkaline earth metals have small E_B, do not vitrify, and are referred to as *glass (network) modifying* oxides (or cations). Compounds of intermediate E_B, such as Al_2O_3, Ga_2O_3, TiO_2 or PbO also do not vitrify in pure form, but may form glasses in combination with one another, with network formers, or even with network modifiers. Such oxides are referred to simply as *intermediates*. Clearly the delineation between glass formers, intermediates and modifiers is somewhat arbitrary, since glass formation depends on the method of preparation, and glass forming ability, i.e. the critical cooling rate required for vitrification, is not often determined. Furthermore, the role of certain cations can change in a complex (> 1 cationic species) glass if their coordination numbers can change under different preparation conditions, or with glass composition. Moreover, the simple

classification in terms of single bond strengths is inadequate because important effects due to polarisability and polarisation, of both O^{2-} and M^{2n+}, are not accounted for, as discussed by Fajans and Kreidl [8].

Binary oxide glasses are those which contain two distinct cationic species of given oxidation states. Such $xM_aO_b.(1-x)X_pO_q$ $(a, b, p, q \in \mathbb{N})$ systems, which have a single free compositional parameter, x, are the subject of the present thesis and will be the focus in subsequent sections. Reference to ternary and higher order systems will be made only where relevant.

2.3.1 Silicates

Silicate glasses are simply defined as those containing the most ubiquitous glass-forming oxide: SiO_2. Pure vitreous silica (also 'fused quartz') is *the* prototypical network glass and, as for crystalline quartz [9], is built from $[SiO_4]$ tetrahedral units, with each oxygen forming a Si-O-Si bridge. In the glassy state the tetrahedra are linked together with broad distributions of Si-O-Si bond and torsion angles, see for example Mozzi and Warren [10], Wright [11] and Poulsen *et al.* [12].

In binary silicates, under ambient conditions, the $[SiO_4]$ tetrahedral units are typically retained, whilst addition of alkali oxides, for example, results in depolymerisation of the silicate network and the presence of non-bridging oxygen (NBO) atoms, which are bonded to only a single silicon ion. NBOs have a formal negative charge and so charge compensate the glass modifying cations. The distribution of NBOs among the Si ions is conventionally represented by the Q^n species distribution, where Q denotes a 4-fold Si ion and $n \in [0, 4]$ is the number of coordinating bridging oxygen (BO). Binary and statistical Q^n species model distributions (see [4]) represent limiting cases, in which either a maximum of two Q species, or a random distribution of all Q species, exist respectively. Disproportionation reactions of the form $2Q^n \rightleftharpoons Q^{n-1} + Q^{n+1}$ allow for interpolation between the two limiting cases. ^{29}Si magic angle spinning (MAS) NMR allows for an experimental determination of the Q^n species based upon the chemical shift distribution of the spectrum, and is a function of a single compositional parameter, x, in binary silicates. Note that for modified silicates a limit to glass formation is predicted at $x = 2/3$ or 66.7 mol% modifier oxide, at which point all Si are present as Q^0 monomers in the absence of metal bridging oxygen (MBO), M-O-M links. A useful

parameter is the polymerisation index

$$\langle n(x)\rangle = \sum_{n=0}^{4} nQ^n(x) = n_{SiSi}(x), \tag{2-1}$$

where the Q^n are fractional abundances of the Q^n, and $\langle n\rangle$ is effectively equal to the average Si-Si coordination number n_{SiSi}. The fractions of BO, NBO and MBO can also be calculated from the Q^n species distribution using

$$f_{BO} + f_{NBO} + f_{MBO} = 1, \tag{2-2}$$

the average O-Si coordination number:

$$n_{OSi} = f_{NBO} + 2f_{BO} = n_{SiO}\frac{(1-x)}{(2-x)}, \tag{2-3}$$

and the ratio

$$\frac{f_{BO}}{f_{BO} + f_{NBO}} = \frac{\sum_{n=0}^{4} \frac{n}{2} Q^n}{\sum_{n=0}^{4} \left(4 - \frac{n}{2}\right) Q^n}, \tag{2-4}$$

as well as the fact that $n_{SiO} = 4$.

There are rare exceptions to the rule that Si is always 4-fold coordinated to oxygen under ambient conditions. For example, Stebbins [13] has shown by ^{29}Si NMR that 5-fold Si can be present at $\sim 0.1\%$ levels in potassium tetrasilicate glass, which is related to processes of viscous flow in the liquid state. In high P_2O_5 content silicophosphates, Si may be 5- or 6-fold coordinated, due to a stronger preference for P to remain as $[PO_4]$ [4].

2.3.2 Germanates

Germanate glasses are those based on the silica analogue, GeO_2. Just like vitreous silica, vitreous germania is composed of a network of tetrahedral, $[GeO_4]$, units, although with some distinct differences, see for example Micoulaut *et al.* [14] and Salmon *et al.* [15]. In particular, the mean Ge-O bonds are longer than Si-O bonds, and the mean Ge-O-Ge angle ($\sim$132° [15]) is smaller than the mean Si-O-Si angle ($\sim$147° [12]). There is a crystalline GeO_2 quartz analogue [16], but there exists in addition a rutile form [17] which contains Ge in 6-fold coordinated, octahedral environments, with all oxygen atoms bonded to three Ge atoms. Such highly coordinated sites occur in the glass at elevated pressures, and indeed, the high-pressure behaviour of GeO_2 glass is often

studied as an analogue of SiO_2, due to the lower onset pressure of local structural transformations [14, 18–20].

The presence of 6-fold Ge sites in ambient binary alkali germanate glasses was hypothesised early on by Ivanov and Evstropiev [21] and Murthy and Ip [22]. The proposal was made based on the observance of extrema in physical properties (such as mass density and refractive index) as a function of binary glass composition. This phenomenon is commonly referred to as the 'germanate anomaly' owing to the lack of such extrema in silicate glasses. There is an analogous phenomenon in binary borate glasses, known as the 'borate anomaly'. An alternative model based on Raman spectroscopic observations was proposed by Henderson and Fleet [23] to describe the density maximum in sodium germanate glasses in terms of network densification and three-membered rings of $[GeO_4]$, without invoking more highly coordinated Ge. See also Henderson and Wang [24] and Henderson [25] for a review. However, it is now clear from neutron diffraction measurements on Na [26], K [27] and Cs [28] germanate glasses that a maximum in Ge-O coordination number ($n_{GeO} > 4$) does occur. Furthermore, during the rise in n_{GeO} upon initial addition of alkali oxide, either no NBOs are present, or there is a perfect balance between the number of NBOs and $[OGe_3]$ triclusters, yielding an average $n_{OGe} \simeq 2$. Based on the former, and some other simple assumptions, a model has been derived [28, 29] to describe the variation of n_{GeO} with glass composition. Specifically, $n_{GeO} = n_{GeO}(x, x_{max}, x_C, n)$, where x is the binary glass composition parameter, x_{max} is the composition at which n_{GeO} is maximised, $x_C > 0$ is the composition at which n_{GeO} returns to 4 and n is the coordination number of the more highly coordinated Ge, typically 5 *or* 6. In general, for a binary glass of composition $xM_aO_b.(1-x)GeO_2$, [29]

$$n_{GeO}(x, x_{max}, x_C, n) = \begin{cases} 4 + \frac{2bx}{1-x}, & \text{if } x \leq x_{max} \\ 4 + \frac{(n-4)(2n-4-x[n(2+b)-4(1-b)])}{(n+4)(1-x)}, & \text{if } x_{max} \leq x \leq x_C \\ 4, & \text{otherwise.} \end{cases} \tag{2-5}$$

In the case of alkali or alkaline earth germanates ($b = 1$) and for $n = 5$, then

$$n_{GeO}(x, x_{max}, x_C, n = 5) = \begin{cases} 4 + \frac{2x}{1-x}, & \text{if } x \leq x_{max} \simeq 0.182 \\ 4 + \frac{2-5x}{3(1-x)}, & \text{if } x_{max} \leq x \leq x_C = 0.4 \\ 4, & \text{otherwise,} \end{cases} \tag{2-6}$$

or for $n = 6$, then

$$n_{GeO}(x, x_{max}, x_C, n = 6) = \begin{cases} 4 + \frac{2x}{1-x}, & \text{if } x \leq x_{max} \simeq 0.286 \\ 4 + \frac{2(4-9x)}{5(1-x)}, & \text{if } x_{max} \leq x \leq x_C \simeq 0.444 \\ 4, & \text{otherwise.} \end{cases} \quad (2\text{-}7)$$

Equations 2-6 and 2-7 are represented graphically later on in this thesis, see Figs 5-9 and 7-9. Note that the value of x_{max} is a function of n (and b [29]), and this was used by Hannon *et al.* [28] to infer the presence of [GeO_5], rather than [GeO_6], in alkali germanate glasses, based on the neutron diffraction derived n_{GeO}. Furthermore, it is important to note that the position of the maxima, at x_{max}, depends on an assumption of the models, which is that saturation occurs when [GeO_n] alternate with [GeO_4] in the glass network. This may explain why the data [28] deviate from the model prior to x_{max}, on entropic grounds.

The presence of [GeO_5], rather than [GeO_6], in alkali germanate glasses went against earlier assumptions that only [GeO_6] occur, based on their occurrence in the rutile form of GeO_2 and in many ambient crystalline binary germanates. However, Hannon *et al.* [28] provide an exhaustive list of compounds containing [GeO_5] polyhedra, providing precedence for their existence.

It is worth noting that whilst suitable isotopes of B, Al and Si exist for NMR studies capable of quantifying the abundances of various coordination species, this is not so for Ge. Only the ^{73}Ge isotope is NMR accessible, and its spectroscopy is not thought capable of such quantification in the solid state [30, 31]. Therefore, the direct measurement of (mean) coordination numbers in germanate glasses relies heavily on diffraction (and potentially EXAFS) methods. This is in contrast to borate glasses, for which n_{BO} is routinely measured by ^{11}B NMR, as well as diffraction, and accounts somewhat for the much larger literature concerning the borate anomaly.

Other methods which have been shown to be capable of detecting changes in n_{GeO} in glasses are ^{17}O 3QMAS NMR [32, 33] and O K-edge XANES [34–36]. Modelling schemes such as classical MD [37, 38] have also been used to shed light on the structure of sodium germanate glasses.

There are many discussions in the literature of NBOs at low alkali content in binary germanate glasses. These are not consistent with the interpretation of neutron

diffraction (ND) derived coordination numbers, which imply no NBOs, and are based on spectroscopic studies. Specifically, on assignments of Raman bands [39–42] and O 1s XPS spectra [43, 44].

Whilst the fact that the mean Ge-O coordination number can exceed four has been demonstrated almost irrefutably, at least in some specific alkali germanate glasses, this does not necessarily explain all of the manifestations of the germanate anomaly. For example, the importance of atomic packing [45–47] and small ring formation [25, 41] in the densification mechanism have been cited. The explanation, in terms of structural changes, of the germanate anomaly manifest in the physical properties of germanate glasses, remains an open topic of research.

Evident from the above is that focus has traditionally been on binary germanate glasses containing monovalent alkali cations. More recently thallium germanate glasses have been studied [48]. Structural studies on germanate glasses containing divalent cations such as the alkaline earths or Sn^{2+} [49] are less common. The former are reviewed in detail in Chapter 3 of this thesis, and the $CaO-GeO_2$ glasses are the subject of Chapter 5. Lead germanate glasses are an exception and have received much attention owing to their optical properties [50–55]. Structural studies on lead germanates are reviewed in Chapter 3 of this thesis, whilst $PbO-GeO_2$ glasses are the subject of Chapter 7. A notable result which can be inferred from the solid state ^{17}O 3QMAS NMR spectra from binary glass former, $B_2O_3-GeO_2$ glasses [56], is that no change in n_{GeO} occurs across the compositional series as the number of trivalent boron is varied.

2.3.3 Lone-pair cations in oxide glasses

Lone-pair (LP) cations are main group elements with oxidation number two less than their group number. For example, the stability of the 4+ valence state of the group 4 elements decreases in the order C → Si → Ge → Sn → Pb, such that Pb^{2+} is the oxidation state found in the vast majority of lead oxide glasses. Sn^{2+} is also the dominant state found, although minority amounts of Sn^{4+} can often be detected using Mössbauer spectroscopy [49, 57–59]. On the other hand, the lighter group 4 elements are invariably found without LPs, in the 4+ oxidation state. Other LP cations commonly studied in oxide glasses include Tl^{+}, Bi^{3+}, Sb^{3+}, As^{3+} and Te^{4+}. The oxides As_2O_3, Sb_2O_3, and TeO_2 have all been prepared as glasses in their pure forms, and can be considered

glass forming oxides. PbO, SnO and Bi_2O_3 are intermediate oxides, or conditional glass formers, and may form binary glasses with other intermediates, or with glass forming oxides. Tl_2O behaves predominantly as a modifying oxide.

A key attribute of LP cations is that their bonding schemes in oxides may change drastically, depending upon material composition. This can be visualised in terms of hybridisation of the lone-pair of electrons. Electron LPs with predominant *s*-character are stereochemically inactive, resulting in relatively spherically symmetric distributions of ligands about the LP cation [60]. On the other hand, if the *s*-character is diminished and the LP electrons occupy non-bonding orbitals with *p*-character, then they exert steric forces upon surrounding anionic ligands, and are said to be stereochemically active. The valence shell electron pair repulsion (VSEPR) theory [61, 62] ranks the repulsive interaction strengths LP-LP > LP-anion > anion-anion, which has direct bearing on local structural arrangements. Furthermore, in the stereochemically active configuration, cation-oxygen coordination numbers are smaller, cation-oxygen bonds are stronger, and the LP cation plays a glass network forming role. The asymmetry of the polyhedral units is also thought to increase glass forming ability [8]. Conversely, higher coordination, more symmetric configurations, are typical of glass network modifying cations. Hence LP cations may play complex roles in binary and multicomponent oxide glasses, potentially changing character with binary glass composition, or even coexisting in both types of environment in the same glass.

Another fundamental property of LP cations is their large electric susceptibilities, $\chi^{(n)}$, and hence polarisabilities. In particular, the first order $\chi^{(1)}$ relates to the refractive index of the material, $\chi^{(2)}$ is zero in centrosymmetric materials such as isotropic glasses, whilst $\chi^{(3)}$ gives rise to non-linear optical (NLO) properties, such as the Kerr effect. The LP of electrons contribute significantly to the polarisabilities of LP cations [63, 64], and hence glasses containing these in their low coordination, highly polarised configurations have found numerous applications in optics. Dumbaugh and Lapp [65] discuss heavy-metal oxide (HMO) glasses and their applications as NLO materials, as well as their other attractive properties (applications) including large infrared transmission windows (low loss fibres) and low working and glass transformation temperatures (glass solders).

In the present thesis, the role of Pb^{2+} in oxide glasses is studied in detail, in particular, within the lead silicate and germanate binary systems. Literature published to date

dealing with structural studies of these glasses, as well as their crystalline counterparts, will be reviewed in Chapter 3. §2.3.4 briefly discusses some aspects of the chemistry of Pb^{2+} in other binary oxide glass systems.

2.3.4 Lead in oxide glasses

Lead may behave quite differently in binary oxide glasses, depending upon both the nature of the second oxide, and upon the relative proportions of PbO to second oxide. For example, Hoppe *et al.* [66] have shown, by x-ray total scattering, that Pb-O coordination numbers increase in the order $PbO{-}SiO_2$, $PbO{-}V_2O_5$, $PbO{-}P_2O_5$. This result is supported by ^{207}Pb NMR studies on lead phosphate [67] and silicate [68] glasses. In the $PbO{-}B_2O_3$ glass system, the Pb-O coordination number decreases from about 6 at low PbO content, to about 3 at high PbO content [69], and again, this is supported by ^{207}Pb NMR [70]. The changes in n_{PbO} appear to be related to the borate anomaly and changes in n_{BO} due to $[BO_3] \rightleftharpoons [BO_4]^-$ interconversion [69, 70].

One of the reasons that the structural studies of lead silicate and germanate glasses, presented in Chapters 6 and 7, are important, is that they include glasses with the highest lead contents (up to 80 mol% PbO) of any oxide glasses studied to date, exploring well beyond the conventional glass-forming limit of 67 mol% PbO. However, the preceeding statement requires some qualification, as follows. High lead oxide glasses from $PbO{-}M_2O_3$ systems such as the lead borates [69], aluminates [71] and gallates [72, 73], have been studied, but contain a lower atom percentage Pb than the $PbO{-}MO_2$ glasses, such as the silicates and germanates. For example, at 80 mol% PbO, the MO_2 glasses contain 36.4 at.% Pb whilst the M_2O_3 glasses contain only 30.8 at.% Pb. An x-ray diffraction study on lead titanate ($PbO{-}TiO_2$) glasses [74] includes claims of a composition of 90 mol% PbO, however, the laboratory x-ray diffraction data are of insufficient quality to rule out Al_2O_3 contents (arising from crucible contamination) larger than those stated, and the absence of a Pb-O peak in the radial distribution function was not explained. Takaishi *et al.* [75] claimed to have studied an 89 mol% PbO lead silicate glass, however, their radial distribution function is consistent with a much lower Pb concentration, estimated at 72 mol% PbO from their reported glass density of 7.50 g cm^{-3}. Combined with the fact that the authors [75] do not take into account apodization effects, their quoted coordination numbers are subject to large uncertain-

ties. An extremely dense (9.3 g cm^{-3}) lead silicate glass, with as high as 96 mol% PbO, has been reported [76], but under the assumption that only a maximum of 4 mol% SiO_2 entered the melt from the porcelain crucible used. In attempting to replicate the results a lead aluminosilicate glass of approximate composition $73PbO \cdot 17SiO_2 \cdot 10Al_2O_3$ was obtained, see Appendix A. There is also a report of silicate glass formation at 91.2 mol% PbO [77], although the density is very similar to that measured for the 80 mol% PbO glass of the present study (Chapter 6) and the refractive index reported is close to other reports [78] for glasses in the 60 to 70 mol% PbO range.

References

[1] J. E. Shelby, *Introduction to Glass Science and Technology* (Royal Society of Chemistry, 1997).

[2] A. C. Wright, in: *Experimental Techniques of Glass Science*, edited by C. J. Simmons and O. H. El-Bayoumi (The American Ceramic Society, Westerville, Ohio, 1993), pp. 205–314.

[3] W. H. Zachariasen, *J. Am. Chem. Soc.* **54** (10), (1932), 3841–3851.

[4] M. Eden, *Ann. Rep. Prog. Chem. Sect. C* **108**, (2012), 177–221.

[5] D. Massiot, F. Fayon, V. Montouillout, N. Pellerin, J. Hiet, C. Rolland, P. Florian, J. P. Coutures, L. Cormier and D. R. Neuville, *J. Non-Cryst. Solids* **354** (2-9), (2008), 249–254.

[6] K. J. D. Mackenzie and M. E. Smith, *Multinuclear solid state NMR of inorganic materials*, vol. 6 of *Pergamon Materials Series* (Pergamon, 2002).

[7] K.-H. Sun, *J. Am. Ceram. Soc.* **30** (9), (1947), 277–281.

[8] K. Fajans and N. J. Kreidl, *J. Am. Ceram. Soc.* **31** (4), (1948), 105–114.

[9] S. M. Antao, I. Hassan, J. Wang, P. L. Lee and B. H. Toby, *Can. Mineral.* **46**, (2008), 1501–1509.

[10] R. Mozzi and B. Warren, *J. Appl. Cryst.* **2** (4), (1969), 164–172.

[11] A. C. Wright, *J. Non-Cryst. Solids* **179**, (1994), 84–115.

[12] H. F. Poulsen, J. Neuefeind, H. B. Neumann, J. R. Schneider and M. D. Zeidler, *J. Non-Cryst. Solids* **188** (1-2), (1995), 63–74.

[13] J. F. Stebbins, *Nature* **351** (6328), (1991), 638–639.

[14] M. Micoulaut, L. Cormier and G. S. Henderson, *J. Phys. Condens. Mat.* **18** (45), (2006), R753–R784.

[15] P. S. Salmon, A. C. Barnes, R. A. Martin and G. J. Cuello, *J. Phys. Condens. Mat.* **19** (41), (2007), 415110.

[16] J. Haines, O. Cambon, E. Philippot, L. Chapon and S. Hull, *J. Solid State Chem.* **166** (2), (2002), 434–441.

[17] A. A. Bolzan, C. Fong, B. J. Kennedy and C. J. Howard, *Acta Crystallogr. B* **53**, (1997), 373–380.

[18] J. W. E. Drewitt, P. S. Salmon, A. C. Barnes, S. Klotz, H. E. Fischer and W. A. Crichton, *Phys. Rev. B* **81** (1), (2010), 014202.

[19] P. S. Salmon, J. W. E. Drewitt, D. A. J. Whittaker, A. Zeidler, K. Wezka, C. L. Bull, M. G. Tucker, M. C. Wilding, M. Guthrie and D. Marrocchelli, *J. Phys. Condens. Mat.* **24** (41), (2012), 415102.

[20] K. Wezka, P. S. Salmon, A. Zeidler, D. A. J. Whittaker, J. W. E. Drewitt, S. Klotz, H. E. Fischer and D. Marrocchelli, *J. Phys. Condens. Mat.* **24** (50), (2012), 502101.

[21] A. O. Ivanov and K. S. Evstropiev, *Dokl. Akad. Nauk SSSR* **145**, (1962), 797.

[22] M. K. Murthy and J. Ip, *Nature* **201**, (1964), 285.

[23] G. S. Henderson and M. E. Fleet, *J. Non-Cryst. Solids* **134** (3), (1991), 259–269.

[24] G. S. Henderson and H. M. Wang, *Eur. J. Mineral.* **14** (4), (2002), 733–744.

[25] G. S. Henderson, *J. Non-Cryst. Solids* **353** (18-21), (2007), 1695–1704.

[26] M. Ueno, M. Misawa and K. Suzuki, *Physica B & C* **120** (1-3), (1983), 347–351.

[27] U. Hoppe, R. Kranold, H. J. Weber and A. C. Hannon, *J. Non-Cryst. Solids* **248** (1), (1999), 1–10.

[28] A. C. Hannon, D. Di Martino, L. F. Santos and R. M. Almeida, *J. Phys. Chem. B* **111** (13), (2007), 3342–3354.

[29] A. C. Hannon, D. Di Martino, L. F. Santos and R. M. Almeida, *J. Non-Cryst. Solids* **353** (18-21), (2007), 1688–1694.

[30] V. K. Michaelis, P. M. Aguiar, V. V. Terskikh and S. Kroeker, *Chem. Commun.* (31), (2009), 4660–4662.

[31] V. K. Michaelis and S. Kroeker, *J. Phys. Chem. C* **114** (49), (2010), 21736–21744.

[32] S. K. Lee and B. H. Lee, *J. Phys. Chem. B* **110** (33), (2006), 16408–16412.

[33] L. S. Du and J. F. Stebbins, *J. Phys. Chem. B* **110** (25), (2006), 12427–12437.

[34] D. Cabaret, F. Mauri and G. S. Henderson, *Phys. Rev. B* **75** (18), (2007), 184205.

[35] H. M. Wang and G. S. Henderson, *Phys. Chem. Glasses* **46** (4), (2005), 377–380.

[36] H. M. Wang and G. S. Henderson, *Chem. Geol.* **213** (1-3), (2004), 17–30.

[37] T. Nanba, J. Kieffer and Y. Miura, *J. Non-Cryst. Solids* **277** (2-3), (2000), 188–206.

[38] A. Karthikeyan and R. M. Almeida, *J. Non-Cryst. Solids* **281** (1-3), (2001), 152–161.

[39] G. S. Henderson, L. G. Soltay and H. M. Wang, *J. Non-Cryst. Solids* **356** (44-49), (2010), 2480–2485.

[40] E. I. Kamitsos, Y. D. Yiannopoulos, M. A. Karakassides, G. D. Chryssikos and H. Jain, *J. Phys. Chem-US* **100** (28), (1996), 11755–11765.

[41] Y. D. Yiannopoulos, C. P. E. Varsamis and E. I. Kamitsos, *Chem. Phys. Lett.* **359** (3-4), (2002), 246–252.

[42] Y. D. Yiannopoulos, C. P. E. Varsamis and E. I. Kamitsos, *J. Non-Cryst. Solids* **293**, (2001), 244–249.

[43] W. C. Huang, H. Jain and M. A. Marcus, *J. Non-Cryst. Solids* **180** (1), (1994), 40–50.

[44] D. Di Martino, L. F. Santos, R. M. Almeida and M. F. Montemor, *Surf. Interface Anal.* **34** (1), (2002), 324–327.

[45] U. Hoppe, *J. Non-Cryst. Solids* **248** (1), (1999), 11–18.

[46] S. Giri, C. Gaebler, J. Helmus, M. Affatigato, S. Feller and M. Kodama, *J. Non-Cryst. Solids* **347** (1-3), (2004), 87–92.

[47] H. J. Weber, *J. Non-Cryst. Solids* **243** (2-3), (1999), 220–232.

[48] E. R. Barney, A. C. Hannon, N. Laorodphan and D. Holland, *J. Phys. Chem. C* **115** (30), (2011), 14997–15007.

[49] D. Holland, M. E. Smith, I. J. F. Poplett, J. A. Johnson, M. F. Thomas and J. Bland, *J. Non-Cryst. Solids* **293**, (2001), 175–181.

[50] M. Dussauze, A. Giannoudakos, L. Velli, C. P. E. Varsamis, M. Kompitsas and E. I. Kamitsos, *J. Chem. Phys.* **127** (3), (2007), 034704.

[51] A. Cereyon, B. Champagnon, V. Martinez, L. V. Maksimov, O. V. Yanush and V. N. Bogdanov, *Opt. Mater.* **28**, (2006), 13011304.

[52] H. Nasu, Y. Ito, Y. Yamamoto, T. Hashimoto and K. Kamiya, *J. Ceram. Soc. Jpn.* **109** (4), (2001), 366–368.

[53] D. Lezal, J. Pedlikova and J. Horak, *J. Non-Cryst. Solids* **196**, (1996), 178–182.

[54] J. Wang, J. R. Lincoln, W. S. Brocklesby, R. S. Deol, C. J. Mackechnie, A. Pearson, A. C. Tropper, D. C. Hanna and D. N. Payne, *J. Appl. Phys.* **73** (12), (1993), 8066–8075.

[55] J. R. Lincoln, W. S. Brocklesby, C. J. Mackechnie, J. Wang, R. S. Deol, D. C. Hanna and D. N. Payne, *Electron. Lett.* **28** (11), (1992), 1021–1022.

[56] S. K. Lee, H. N. Kim, B. H. Lee, H. I. Kim and E. J. Kim, *J. Phys. Chem. B* **114** (1), (2010), 412–420.

[57] J. A. Johnson, J. Urquidi, D. Holland, C. E. Johnson and P. G. Appelyard, *J. Non-Cryst. Solids* **353** (44-46), (2007), 4084–4092.

[58] J. A. Johnson and C. E. Johnson, *J. Phys. Condens. Mat.* **17** (8), (2005), R381–R412.

[59] J. A. Johnson, C. E. Johnson, K. F. E. Williams, D. Holland and M. M. Karim, *Hyperfine Interact.* **95** (1-4), (1995), 41–51.

[60] L. Shimoni-Livny, J. P. Glusker and C. W. Bock, *Inorg. Chem.* **37** (8), (1998), 1853–1867.

[61] R. Gillespie and R. Nyholm, *Q. Rev. Chem. Soc.* **11** (4), (1957), 339–380.

[62] R. J. Gillespie and I. Hargittai, *The VSEPR Model of Molecular Geometry* (Prentice Hall International, London, 1991).

[63] E. Fargin, A. Berthereau, T. Cardinal, G. LeFlem, L. Ducasse, L. Canioni, P. Segonds, L. Sarger and A. Ducasse, *J. Non-Cryst. Solids* **203**, (1996), 96–101.

[64] B. Jeansannetas, S. Blanchandin, P. Thomas, P. Marchet, J. C. Champarnaud-Mesjard, T. Merle-Mejean, B. Frit, V. Nazabal, E. Fargin, G. Le Flem, M. O. Martin, B. Bousquet, L. Canioni, S. Le Boiteux, P. Segonds and L. Sarger, *J. Solid State Chem.* **146** (2), (1999), 329–335.

[65] W. H. Dumbaugh and J. C. Lapp, *J. Am. Ceram. Soc.* **75** (9), (1992), 2315–2326.

[66] U. Hoppe, R. Kranold, A. Ghosh, C. Landron, J. Neuefeind and P. Jovari, *J. Non-Cryst. Solids* **328** (1-3), (2003), 146–156.

[67] F. Fayon, C. Bessada, A. Douy and D. Massiot, *J. Magn. Reson.* **137** (1), (1999), 116–121.

[68] F. Fayon, C. Bessada, D. Massiot, I. Farnan and J. P. Coutures, *J. Non-Cryst. Solids* **232**, (1998), 403–408.

[69] T. Takaishi, J. S. Jin, T. Uchino and T. Yoko, *J. Am. Ceram. Soc.* **83** (10), (2000), 2543–2548.

[70] J. L. Shaw, U. Werner-Zwanziger and J. W. Zwanziger, *Phys. Chem. Glasses Eur. J. Glass Sci. Technol. B* **47** (4), (2006), 513–517.

[71] E. R. Barney, A. C. Hannon, D. Holland, D. Winslow, B. Rijal, M. Affatigato and S. A. Feller, *J. Non-Cryst. Solids* **353** (18-21), (2007), 1741–1747.

[72] A. C. Hannon, J. M. Parker and B. Vessal, *J. Non-Cryst. Solids* **196**, (1996), 187–192.

[73] A. C. Hannon, J. M. Parker and B. Vessal, *J. Non-Cryst. Solids* **232**, (1998), 51–58.

[74] Y. Dimitriev, V. Mihailova and E. Gattef, *Phys. Chem. Glasses* **34** (3), (1993), 114–116.

[75] T. Takaishi, M. Takahashi, J. Jin, T. Uchino, T. Yoko and M. Takahashi, *J. Am. Ceram. Soc.* **88** (6), (2005), 1591–1596.

[76] C. Dayanand, G. Bhikshamaiah and M. Salagram, *Mater. Lett.* **23** (4-6), (1995), 309–315.

[77] E. Ellis, D. W. Johnson, A. Breeze, P. M. Magee and P. G. Perkins, *Philos. Mag. B* **40** (2), (1979), 125–137.

[78] *SciGlass Professional 7.3* (ITC Inc., 2008).

Chapter 3

Review of Literature

3.1 Alkaline earth germanate glasses

Whilst much attention has been paid to the binary alkali germanate glasses (see § 2.3.2), very few studies have focussed on the structure of binary alkaline earth germanate glasses. One of the main reasons for this is the propensity for such systems to demonstrate immiscibility in the liquid, or supercooled liquid states, which can be frozen in upon cooling through the glass transition resulting in a 'phase separated' glass comprised of two or more vitreous phases of different chemical compositions. As such, the following review will focus on the reports of immiscibility, glass formation and physical properties reported for alkaline earth germanate systems, as well as on any existing structural studies.

3.1.1 Miscibility gaps

The upper consolute, or critical, temperatures (T_{crit}) for phase decomposition have been reviewed by Hudon and Baker [1] for binary germanate [2] as well as silicate [1] and borate [2] systems. In all three system types the upper consolute temperature increases with the modifier cation potential (= z/r, with r the ionic radius and z the valence), and decreases with increasing modifier cation radius. As such, whilst the $MgO-GeO_2$ [3, 4] and $CaO-GeO_2$ [4, 5] systems exhibit stable regions of immiscibility, there is only metastable immiscibility (below the liquidus) present in the strontium [4] and barium [4, 6] germanates. All of these regions lie in the GeO_2 rich portion of the binary phase diagrams. Hudon and Baker [1] point out that miscibility gap widths should be compared only at the same temperature if any correlation with z/r is sought. Nonetheless it is useful, for practical purposes, to compare the miscibility gap widths of the binary alkaline earth germanates at the liquidus, despite differences in liquidus temperatures

between systems (the silicate analogues all have very similar liquidus temperatures), and some reported widths are given in Table 3-1. It is clear that the gap widths compared in this manner tend to decrease with increasing cation radius (being effectively zero in the SrO and BaO, metastable, cases), and that the critical compositions do likewise. Shelby [7, 8] reports broader miscibility gaps in the alkaline earth germanate systems, though these are not comparable to those in Table 3-1 due to the lower cooling rates used and the annealing of the glasses close to their glass transition temperatures, which likely resulted in metastable phase separation. Morinaga and Nakashima [9] studied the kinetics of phase separation in germanate glasses, including calcium and strontium binaries, by measurement of time-temperature-transformation diagrams.

Table 3-1 Reported miscibility gaps and critical temperatures (T_{crit}) and compositions for two-liquid phase separation in binary alkaline earth germanate systems. The upper and lower limits correspond to the intersections of the liquidus and binodal curves and therefore no values are given for the BaO and SrO germanate systems where the phase separation is metastable.

	Composition in mol%			T_{crit}	
System	Lower	Upper	Critical	°C	Ref.
MgO	8	34	-	-	Robbins and Levin [3]
	6	38	19	1672	Tabata *et al.* [4]
CaO	5	15	10	1370	Shirvinskaya *et al.* [5]
	6	14	10	1282	Tabata *et al.* [4]
SrO	-	-	8	1135	Tabata *et al.* [4]
BaO	-	-	6	912	Tabata *et al.* [4]

3.1.2 Physical properties

Mass densities of alkaline earth germanate glasses have been measured by various authors [8, 10–15] and these are plotted as a function of glass composition in Fig. 5-1. The mass densities for SrO–GeO_2 and BaO–GeO_2 glasses both pass through a maximum at about 30 mol% modifier oxide, as shown by the two extensive datasets of Kasymova [13]. This is a hallmark of the germanate anomaly, most often discussed in the context of alkali germanate glasses, where the density maxima occur at lower modifier oxide (M_2O) contents. The various density datasets for CaO–GeO_2 glasses [10–12] are not all consistent, but notably the highest densities measured (those by Kamiya *et al.* [10])

occur around 30 mol% modifier oxide, as for the Ba and Sr containing systems.

Shelby [7, 8] measured various physical properties of MO−GeO_2 glasses obtained by inertial cooling and subsequent annealing. Many of the glasses formed were opalescent and two glass transition events in differential scanning calorimetry traces were often observed, which was taken as evidence for phase separation.

3.1.3 Structural investigations

Schlenz *et al.* [16] used anomalous x-ray scattering and electron diffraction to study a $BaGe_{2.55}O_{6.10}$ (28.2 mol% BaO) glass. Notably, even using a twin-roller quencher for rapid cooling, crystallisation of the supercooled liquid could not be wholly prevented, although enough glassy material was obtained for the scattering experiments. A key conclusion was that the ratio of 6-fold to 4-fold coordinated germanium was 1:3. Such a ratio corresponds to an average Ge-O coordination number of 4.5, in contrast to the value of 3.9 ± 0.1 derived from the peak areas. The discrepancy is due to the fitting of Gaussian functions to the RDF extracted by high energy (100 keV) x-ray total scattering, which neglects the broadening arising from the x-ray form factors and the truncation in reciprocal space. The result is that the area under the termination ripples is not included in the calculation of Ge-O coordination number made by the authors [16]. Were this included, it is evident that an average Ge-O coordination number > 4 would result.

Devitrification studies of binary germanate glasses in the Ca [17], Sr [18] and Ba [14] systems have been performed, in conjunction with measurement of the infrared spectra of the glasses. The decrease in Ge-O-Ge bond stretching vibration frequency with addition of MO to the composition was interpreted as due to the presence of a fraction of Ge in octahedral (6-fold) coordination to oxygen in all cases. Furthermore Pernice *et al.* [14] correlated the compositional behaviour of the glass transition temperature and of the glass mass density, although they report maxima at 20 mol% BaO, rather than at about 30 mol% modifier oxide as found by Kasymova [13].

3.2 Crystalline calcium germanates

A first step toward understanding the short range atomic order in glasses is to understand that of related crystalline phases. Indeed, in many cases the short range order of the vitreous and crystalline phases is the same, the [SiO_4] tetrahedron found in vitreous silica and several crystalline SiO_2 polymorphs being a prime example. Table 3-2 lists some site specific coordination numbers for four ambient pressure crystal structures in the $CaGeO_3$–GeO_2 system. These correspond to the three (calcium bearing) congruently melting phases in the $CaGeO_3$–GeO_2 equilibrium phase diagram of Shirvinskaya *et al.* [5], though it should be noted that $Ca_2Ge_7O_{16}$ [19] replaces the (presumably nonexistent) $CaGe_4O_9$ phase. Key points concerning the local structure in the calcium germanate crystals summarised in Table 3-2 are as follows:

- They contain $[GeO_6]^{2-}$ octahedra and [GeO_4] tetrahedra but no $[GeO_5]^{-}$ species
- The Ca-O coordination number ranges from 6 to 9 and the average n_{CaO} correlates approximately with the average n_{GeO}, such that when one is large, so is the other
- Other than in $CaGeO_3$ [23], all oxygen atoms form bridges between two Ge atoms ($n_{OGe} = 2$) and these bridging oxygen atoms bond to either one or two Ca^{2+}
- The total oxygen-cation coordination (n_{OX}) passes through a maximum (as a function of composition) of 3.6 to 3.8 in $CaGe_2O_5$ [22]
- The two $CaGe_2O_5$ polymorphs [22] contain $[GeO_6]^{2-}$ octahedra which share a common vertex (as necessary based on the composition and the lack of non-bridging oxygen)
- The non-bridging oxygen atoms in $CaGeO_3$ [23] bond to either two or three Ca^{2+}

In addition to the above, closer inspection of the structures reveals that each Ca^{2+} in $Ca_2Ge_7O_{16}$ [19] is bonded to two oxygen atoms (O1 and $O1^{i}$ [19]) which bridge [GeO_4] tetrahedra. These are particularly long Ca-O bonds of $r_{CaO} = 2.923$ Å, with bond-valence of only 0.08 [19], but nonetheless, they lead to a lengthening of the distances Ge1-O1 and Ge1-$O1^{i}$ to 1.759 and 1.783 Å respectively. In LT-$CaGe_2O_5$ [22], very short Ca-O bonds of $r_{CaO} = 2.152$ Å exist which compensate the lack of Ge-O bond valence at the oxygen bridging two $[GeO_6]^{2-}$ octahedra. Therefore a very wide range of Ca-O bond lengths are exhibited. Furthermore, all crystals containing the $[GeO_6]^{2-}$ octahedra tend to have these in edge sharing configurations with [CaO_m] polyhedra,

Table 3-2 Selected local structural parameters for atomic sites in ambient pressure calcium germanate crystals and GeO_2 polymorphs. The coordination numbers n_{ij} refer to averages only where stated (rows beginning with Av.), whereas all bond lengths r_{ij} are averaged, either over a single polyhedron, or over all polyhedra (Av.) centred on a particular metal cation (X = Ca, Ge). The average values of n_{GeO} and r_{GeO} are plotted in Fig. 5-9 and 5-10 respectively. All Ca-O bonds shorter than 3.10 Å have been considered. The mass densities for each crystal are also given.

Site	Mult.	n_{XO}	r_{XO} (Å)	Site	Mult.	n_{OGe}	n_{OCa}	n_{OX}
Quartz GeO_2 [20], 4.29 g cm^{-3}								
Ge1	3	4	1.737	O1	6	2	-	2
Rutile GeO_2 [21], 6.31 g cm^{-3}								
Ge1	2	6	1.884	O1	4	3	-	3
$Ca_2Ge_7O_{16}$ [19], 22.2 mol% CaO, 4.70 g cm^{-3}								
Ca1	4	8	2.502	O1	8	2	1	3
				O2	8	2	1	3
Ge1	8	4	1.762	O3	8	2	1	3
Ge2	4	6	1.887	O4	8	2	1	3
Ge3	2	4	1.746	Av. O		2	1	3
Av. Ge		4.571	1.807					
Low T $CaGe_2O_5$ [22], 33.3 mol% CaO, 4.85 g cm^{-3}								
Ca1	4	9	2.570	O1	4	2	1	3
				O2	8	2	2	4
Ge1	4	6	1.923	O3	8	2	2	4
Ge2	4	4	1.766	Av. O		2	1.8	3.8
Av. Ge		5	1.860					
High T $CaGe_2O_5$ [22], 33.3 mol% CaO, 4.80 g cm^{-3}								
Ca1	4	8	2.492	O1	4	2	2	4
				O2	4	2	1	3
Ge1	4	4	1.738	O3	4	2	1	3
Ge2	2	6	1.903	O4	4	2	2	4
Ge3	2	6	1.911	O5	4	2	2	4
Av. Ge		5	1.865	Av. O		2	1.6	3.6
Wollastonite $CaGeO_3$ [23], 50.0 mol% CaO, 3.73 g cm^{-3}								
Ca1	2	7	2.433	O1	2	1	3	4
Ca2	2	6	2.394	O2	2	1	3	4
Ca3	2	6	2.384	O3	2	1	3	4
Av. Ca		6.333	2.405	O4	2	2	1	3
				O5	2	1	3	4
Ge1	2	4	1.732	O6	2	2	1	3
Ge2	2	4	1.735	O7	2	1	2	3
Ge3	2	4	1.750	O8	2	1	2	3
Av. Ge		4	1.739	O9	2	2	1	3
				Av. O		1.333	2.111	3.444

and in the $CaGe_2O_5$ polymorphs [22] [CaO_m] polyhedra also share edges with [GeO_4] tetrahedra.

From the preceding discussion of relevant $CaO-GeO_2$ crystal structures, it is apparent that their topologies are not highly conducive to formation of glassy analogues. This is because they are relatively densely packed systems, containing edge sharing, as well as corner sharing, polyhedra, resulting in high oxygen-cation coordination numbers of up to four. Since the X-O-X (X = cation) bond angle is a key degree of freedom allowing the presence of disorder in an oxide network, any increase in the oxygen-cation coordination number, above the value of two, typical to single component glasses such as SiO_2, GeO_2 and B_2O_3, constrains the X-O-X bond angles and reduces the scope for disorder. Furthermore, without the presence of non-bridging oxygen atoms, it is necessary to pack a number of $[GeO_n]^{(n-4)-}$, $n > 4$, about a divalent Ca^{2+} ion in order to provide charge balance and satisfy electrostatic bond strength, and bond-valence, sums. In the crystals, this appears to result in the stabilisation of $[GeO_6]^{2-}$ octahedra as opposed to $[GeO_5]^{-}$ and in the edge sharing of the octahedra with [CaO_m] polyhedra.

3.3 Lead silicate glasses

Whilst lead oxides have not been found to vitrify under any conditions that can be obtained in the laboratory, stable glasses can be obtained upon the addition of a third elemental species. This can be anionic, for example in lead oxyhalide systems, or cationic, in which case we refer to pure oxide glass systems. With silica being the archetypal glass-forming oxide, it is not surprising that the lead silicate, $PbO-SiO_2$, binary system has become the model for studying the structural role of Pb^{2+} in oxide glasses. As such, a significant literature exists dealing with experimental studies on these glasses, and the present review attempts to summarise those which yield information pertaining to the structural arrangement of the constituent atoms.

3.3.1 Lead in glass

"Lead in Glass" is the title of a review by Rabinovitch [24] who summarises much of the work on lead silicate glasses prior to 1976. The majority of structural studies were conducted using laboratory x-ray sources to extract radial distribution functions by total

scattering, with the earliest by Bair [25] in 1936 being later contested by Krogh-Moe [26]. The most recent in the period covered by the review [24] is that of Mydlar *et al.* [27] who cite structural similarity to the crystalline forms of lead monoxide and lead silicates known at that time, namely tetragonal 'red' α-PbO [28], orthorhombic 'yellow' β-PbO [29] and alamosite, $PbSiO_3$ [30, 31] (see §3.4). Notably the local Pb environment was concluded to have about four oxygen atoms located between 2.2 and 2.8 Å within a single hemisphere, the other hemisphere containing a non-bonding lone-pair (LP) of electrons.

An important contribution from this era was made by Leventhal and Bray [32] using ^{207}Pb NMR. A detailed study was conducted on ten lead silicate glass compositions covering the range 30 to 75 mol% PbO. Furthermore, measurements on the crystalline compounds $PbO \cdot SiO_2$, $2\,PbO \cdot SiO_2$ and γ-$4\,PbO \cdot SiO_2$ were made for comparison. The chemical shifts measured from the typically extremely broad ^{207}Pb resonances reveal two important features: i) that the crystalline compounds have very similar values to the glasses of corresponding composition and ii) that between 20 to 50 mol% PbO the ^{207}Pb chemical shift is independent of the composition, whilst from 50 to 75 mol% PbO a trend of increasing chemical shift with increasing PbO content is observed. The second point is in contrast to the measurements made on lead borates [32], in which ^{207}Pb chemical shift was shown to increase monotonically with PbO content increasing from 20 to 74 mol% PbO. It was pointed out by the authors that point i) *could* imply structural similarity of the local Pb environments between the vitreous and crystalline states, but does not require it. The plateau in chemical shift at moderate PbO concentrations was explained based on the equilibrium phase diagram [33] and the expected similarity of structural groupings (larger scale than single polyhedra) in the glasses and the crystalline compounds bordering the relevant field in the phase diagram. For example, there exist no equilibrium stoichiometric compounds between SiO_2 and $PbO \cdot SiO_2$, and based on the concept of stoichiometric structural groupings in the glasses, all glasses between 0 and 50 mol% PbO would be based on the same groupings.

3.3.2 Post Rabinovitch

The present section aims to summarise the literature not covered by the review paper of Rabinovitch [24]. Due to the large number of relevant publications they are grouped

by the experimental technique applied, and only the main results are discussed.

3.3.2.1 Chemical identification of silicate polyanions

Gotz *et al.* [34] were responsible for developing direct chemical analysis methods for measuring the silicate polyanion distribution in insoluble silicates, and applied these methods to lead silicate crystals and glasses [34–37]. These revealed a breakdown of the three-dimensional silicate network as PbO content was increased, as well as revealing differences in polyanion distribution between polymorphs of $2\,PbO \cdot SiO_2$. Furthermore, an influence of cooling rate of the glass-forming melt on the measured polyanion distribution was demonstrated [37]. Similar measurements were made by Smart and Glasser [38] and Hoebbel *et al.* [39].

3.3.2.2 Silicon-29 nuclear magnetic resonance

^{29}Si MAS NMR studies by Lippmaa *et al.* [40] showed that the chemical shift dispersion in lead silicate glasses is much greater than that in the crystals, leading to overlapping, unresolved, resonances from each Q^n species. Dupree *et al.* [41] applied the technique to a series of glasses, which allowed them to contest the earlier, static, NMR results of Fujiu and Ogino [42] who assumed only two different Q^n species were present for all glasses with 30 to 60 mol% PbO. This is not a good assumption based on the very different chemical shift anisotropies of the different Q^n species which give rise to considerably different anisotropic broadenings. The authors [41] were led to the conclusion that Pb^{2+} played the role of glass modifier below 30 mol% PbO, and that of an intermediate ion above this limit, with the 70 mol% PbO glass consisting of a lead-oxygen network containing mostly Q^0 anions. This conclusion rested critically upon the description of the ^{29}Si chemical shift distribution by a binary Q^n species distribution below 30 mol% PbO, as found for alkali silicate glasses [43], and a statistical distribution above 30 mol% PbO. ^{29}Si MAS NMR measurements on crystalline lead silicates [44, 45] justified the interpretation of the spectra from glasses, and the resolution of resonances from individual crystallographic sites allowed Bessada *et al.* [45] to suggest a deeper correlation between ^{29}Si chemical shift and local environment, at least for the five Q^2 sites and one Q^1 site considered. It was found that, in addition to the deshielding caused by an increase in n, an increase in p, the number of Pb ions in the

second coordination sphere of a Si ion, led to a further deshielding. Hence the observed larger average deshielding in the glasses as compared to the isocompositional crystals represents a larger average *p*-value and therefore a tendancy for Pb ions to cluster and form a plumbite glass subnetwork. Fayon *et al.* [46] made a detailed NMR study of silicate glasses containing from 31 to 73 mol% PbO, supporting to some extent the previous work of Dupree *et al.* [41], but reporting that the Q^n species distribution lay inbetween the limiting cases defined by the binary (most ordered) and statistical (most disordered) distributions. The most recent appraisal of the situation had been made by Feller *et al.* [47] who contribute the most extensive ^{29}Si MAS NMR dataset to date, covering eleven glasses containing 33 to 83 mol% PbO. The extracted Q^n species distributions are in close accord with the statistical model up to 60 mol% PbO but deviate strongly beyond 67 mol% PbO where all models predict only Q^0 species. Feller *et al.* [47] compare their results to those of Fayon *et al.* [46]. The quantitative differences present are attributed to the cooling rates applied to the melts during glass production, with the faster (by at least two orders of magnitude) cooling rate allowing the retention of the statistical Q^n distribution presumed in the liquid, and a glass formed in the zero cooling rate limit hypothesised to have a binary distribution.

3.3.2.3 Lead-207 nuclear magnetic resonance

MAS NMR has also been applied to the ^{207}Pb nuclei in inorganic plumbous compounds including some lead silicates [48, 49]. Fayon *et al.* [49] established several empirical correlations between ^{207}Pb isotropic chemical shift, as well as the anisotropy of the shielding tensor, and the local structure about the lead cation. Firstly, the Pb nuclei in more ionic environments, with high coordination number, longer bonds and more spherically symmetric ligand distributions, were found to be shielded with respect to those nuclei with lower coordination number that bonded more covalently, and furthermore the ionic sites have smaller chemical shift anisotropies. The covalently bonded sites found in PbO and lead silicate compounds have a wide range of isotropic chemical shifts, and it was possible to correlate these to a function of the average Pb–O–X (X = Si, Pb) bond angle with an additional term accounting for the different electronegativities of Si and Pb. Thus the positive *average* chemical shifts, and large breadth, attributed to large CSA interactions and chemical shift dispersion, of the static ^{207}Pb

NMR spectra of glassy lead silicates [46] were taken as evidence for local structural similarity between the lead silicate crystals and their vitreous counterparts, in accord with Leventhal and Bray [32].

3.3.2.4 Electron spin resonance

Hosono *et al.* [50] used γ-irradiation from a ^{60}Co source to induce Pb^{3+} hole centres in a very wide range of glasses, including binary lead silicates. The authors argue that the degree of Pb 6s character present can be inferred from the observed hyperfine absorptions, and that this relates to the bonding environment of Pb. In particular, more ionic Pb sites, which are more highly coordinated to oxygen, and have spherically symmetric ligand distributions, show greater Pb 6s character in the ESR spectra than do more covalent Pb sites, with lower coordination numbers, and with asymmetric ligand distributions. Although the glasses used in the study may contain Al_2O_3 dissolved from the crucibles used, the results show a distinction between the silicate and phosphate systems, the latter glasses showing higher Pb 6s character, implying a higher coordination number to oxygen than in the silicates. Furthermore, the ESR spectra from the γ-irradiated lead silicate glasses containing from 30 to 75 mol% PbO show a small decrease in inferred Pb 6s character with increasing PbO content.

3.3.2.5 Total scattering of x-rays and neutrons

Following Mydlar *et al.* [27] both Imaoka and Hasegawa [51] and Morikawa *et al.* [52] contributed analyses of x-ray diffraction measurements on lead orthosilicate (66.7 mol% PbO) glass. Some controversy arose [53, 54] over the differing interpretations of the experimental data, which were based either upon [PbO_3] trigonal pyramids and $[SiO_4]^{4-}$ anions, with heavy reliance upon known crystal structures [51], or on [PbO_4] square pyramids, [PbO_6] octahedra and larger silicate anions [52]. Investigations covering a range of glass compositions followed: both silicate liquids and glasses containing 30 to 66 mol% PbO were subject to x-ray diffraction analyses [55, 56] and Imaoka *et al.* [57] made a reappraisal of their analysis of lead orthosilicate glass, and included a similar analysis of lead metasilicate glass. These studies did not resolve the issue regarding the short range structural models proposed earlier, particularly with regard to the lead-oxygen polyhedra present.

A step forward was taken in 1986 when Yamada *et al.* [58] published the neutron scattering curves taken from five lead silicate glasses, from 33 to 66 mol% PbO. The neutron scattering data are complementary to the equivalent x-ray scattering functions, being dominated by atomic pairs containing oxygen, rather than those containing lead. This allowed much more accurate measurement of the Si-O peak in the real-space correlation functions, confirming that the Si-O coordination was four to within the experimental uncertainty of ± 5%, and the first demonstration of the lengthening of the average Si-O bond with increasing PbO content of the glass. Pb-O coordination was reported to be about three for all of the glasses considered, although it was also concluded that different types (lengths) of Pb-O bonds existed.

A further leap forward came with the first *combined* analysis of neutron and x-ray scattering curves from a lead metasilicate glass by Suzuya *et al.* [59]. This was also the first time that synchrotron radiation had been applied to the problem. Two measurements close to the Pb L_{III} edge (13.055 keV) were taken in order to take advantage of the form factor anomalies, in a technique known as anomalous x-ray scattering (AXS). After suitable corrections, including subtraction of fluorescence backgrounds, a difference function containing scattering only from atom pairs including Pb was obtained. The focus of the study was the intermediate-range, and not short-range, order present in the $PbSiO_3$ glass, which is implied by a small contribution to the scattering curves of both radiation, and to the AXS difference function, at about 1.2 $Å^{-1}$. This was attributed to Pb-O correlations between layers or chains of lead-oxygen, in which Pb acts as an intermediate or glass-forming cation, rather than as a glass modifying cation.

The experimental data collected by Suzuya *et al.* [59] were later subjected to analysis by reverse Monte Carlo modelling [60]. This represented a shift from partial models constructed from combinations of idealised motifs, toward models that were three-dimensional, space-filling, and that therefore naturally included all pair correlations, at least out to the length scale defined by the size of the periodically bounded cubic box. In this case 2500 atoms were considered, in a box with a constant density of $\rho_0 = 0.0626$ $Å^{-3}$, leading to a box size $L = 34.2$ Å. An initial configuration was obtained via hard-sphere Monte Carlo simulation with the additional constraint that all silicon atoms were coordinated to four oxygen atoms.* Some interesting conclu-

*It is also stated that all oxygen were constrained to $n_{OSi} = 2$, but this must be in error given $n_{SiO} = 4$, $n_{OSi} = (c_{Si}/c_O)\, n_{SiO}$ and therefore, for the metasilicate composition, $n_{OSi} = 4/3$.

sions regarding the structure of the $PbSiO_3$ glass were reached. Firstly the pre-peak at 1.2 $Å^{-1}$ was confirmed to arise from the Pb-O partial structure factor, in agreement with the earlier assignment [59]. Secondly, an asymmetric distribution of Pb-O bonds was observed, with a tail to high r which is not separated from next-nearest neighbour Pb-O distances. The coordination numbers extracted were $n_{PbO} = 2.0$ up to 2.4 Å and $n_{PbO} = 3.9$ up to 2.8 Å. Note that $n_{SiO} = 3.8$ was found, indicating the presence of under-coordinated Si. The Pb-O bond length distribution suggests an, on average, distorted polyhedron, and goes some way towards explaining the disagreements in the earlier literature as to the Pb-O coordination. The Pb-O polyhedra were concluded to be distorted square-based pyramids, based on the bond angle distributions (BADs) calculated from the RMC model. Angles of 60° in the Si-Si-Si BAD were interpreted as arising from three membered rings of tetrahedra, in the form of the $[Si_3O_9]^{6-}$ ring anion. This is likely the case but the following discussion states that this result is in accord with the ^{29}Si MAS NMR measurements of Fayon *et al.* [46]. Whilst the Q^2 species were shown to be dominant in $PbSiO_3$ glass, this is not evidence for rings of any particular size. Indeed the $[Si_3O_{10}]^{8-}$ anion stated to be representative of Q^2 species by Fayon *et al.* [46], and to be present in the high lead content glasses, is incorrectly equated to the $[Si_3O_9]^{6-}$ ring by Suzuya *et al.* [60], when it is in fact a $Q^1 - Q^2 - Q^1$ chain. Furthermore, the earlier work of Gotz *et al.* [36] had shown evidence only for $[Si_3O_{10}]^{8-}$ and not for $[Si_3O_9]^{6-}$. Finally, the statement that the similarity between X-X-X and X-O-X BADs with X = Pb or Si implies that the intermediate range order is similar for the two parts of the glass network is ambiguous and does not consider the different valencies of Pb and Si and therefore the topological differences that must arise based on both cations being coordinated to four oxygen atoms.

Small angle x-ray scattering (SAXS) was employed by Golubkov *et al.* [61] to investigate the presence of larger scale structures within the lead silicate glasses. Their experiments revealed an important feature: that whilst SAXS intensity was low for glasses with > 40 mol% PbO, indicating homogeneous mixtures of the components, at smaller lead concentrations there is significant small angle x-ray scattering, with the peak total SAXS intensity occurring at 25 mol% PbO. The length scale derived for the microinhomogeneity was 5 to 7 Å and it was proposed that this represented the frozen-in equilibrium thermal fluctuations of the glass-forming liquid. The authors [61] fall

upon the same explanation as that used by Leventhal and Bray [32] to explain the measured ^{207}Pb NMR chemical shifts as a function of PbO concentration, i.e. that the only equilibrium structural groupings available between zero and 50 mol% PbO are those associated with pure silica and lead metasilicate, and that furthermore these stoichiometric groupings must have a repulsive interaction giving rise to small scale inhomogeneities in the melt.

An important contribution was made by Hoppe *et al.* [62] using high energy x-ray diffraction on 31, 50 and 66 mol% PbO silicate glasses. The x-ray energy of 140 keV greatly reduces absorption and increases the real-space resolution that can be obtained, whilst the fluorescence contribution from the Pb K-edge (~88 keV) was discriminated electronically. Peak fitting to the high quality real-space correlation functions, led to an interesting conclusion: that the Pb-O environment was approximately independent of the concentration of PbO, each lead being coordinated by approximately 3 oxygen atoms centred about 2.30 Å with a further one or two oxygen atoms at distances of about 2.7 Å. This finding is in relatively good agreement with that of Suzuya *et al.* [59, 60] for the 50 mol% PbO silicate glass. In addition it was shown that larger Pb-O coordination numbers occurred in lead vanadate and phosphate glass networks.

Takaishi *et al.* [63] presented a combined x-ray and neutron diffraction study on five PbO−SiO_2 glasses covering 25 to 89 mol% PbO. It should however be noted that the measured density of 7.50 g cm^{-3} is not consistent with such a high lead content as 89 mol% PbO. Indeed comparison to the trend exhibited by the large body of existing density measurements on lead silicate glasses, that can be accessed, for example, using the SciGlass database [64, 65], indicate that a composition of about 72 mol% PbO is more likely. This is qualitatively in accord with the size of the various nearest-neighbour peaks in the reported radial distribution functions (RDFs) [63], and is clearly evident in the curvature of the baseline of the neutron RDF. Densities measured for the other four glasses are consistent with previously reported values, and therefore the 66 mol% PbO glass is that with the highest lead content from which reliable information can be drawn. The Pb-O coordination numbers and approximate bond lengths extracted by peak fitting mostly agree quantitatively with the results of Hoppe *et al.* [62], although a higher coordination number at the longer distance of 2.78 Å is reported which decreases from three at 25 mol% PbO to about one at 50 mol% PbO and was not present at higher

PbO concentrations. The authors [63] further propose the $[Pb_2O_4]$ unit as the basic building block of the plumbite network, where the two edge-sharing $[PbO_3]$ pyramids comprising the unit have opposed orientations due to repulsion between the electron lone-pairs, giving rise to the observed nearest neighbour Pb-Pb distance.

Recently Kohara *et al.* [66] have followed up the earlier work of Suzuya *et al.* [59, 60] and analysed a range of lead silicate glass compositions using neutron and x-ray diffraction and RMC modelling. Synchrotron x-rays at 113.3 keV and pulsed neutrons were used to obtain diffraction patterns out to $Q_{max} = 20.0$ Å^{-1} (see Ch. 4) for three glasses from 34 to 65 mol% PbO, whilst the low angle region was measured for five glasses from 30 to 65 mol% PbO at an incident x-ray energy of 61.6 keV. An asymmetric distribution of nearest neighbour Pb-O bonds was ascertained, with total average coordination number of four, up to about 3 Å. Peaks in the x-ray structure factors at low scattering vector magnitude ($Q \simeq 0.4$ Å^{-1}), and at the lower PbO concentrations, were observed, in agreement with the work of Golubkov *et al.* [61]. A new result was the observation of similar peaks, but in the neutron structure factors for the higher PbO concentrations, at about $Q \simeq 1.2$ Å^{-1}. The 5000 atom RMC models indicated that these 'prepeaks' arose from scattering from isolated silicate anions such as $[Si_2O_7]^{6-}$ dimers and $[SiO_4]^{4-}$ monomers in the high-lead glasses, and from large cages of Pb atoms surrounding areas of low lead concentration in the 34 mol% PbO glass, on a scale ~ 15 Å. That is to say that the 34 mol% PbO silicate glass model derived from RMC modelling demonstrated an inhomogeneous distribution of the cationic species. Regarding the short range structure about Pb atoms, the models showed a majority were coordinated to four oxygen atoms, but with some $[PbO_3]$ and $[PbO_5]$ species. The local structural arrangement was independent of PbO concentration over the compositional range explored, as supported by the O-Pb-O bond angle distributions (BADs), and was found to be predominantly asymmetric with respect to the arrangement of oxygen atoms around the lead atom. The low coordination number and asymmetry of the Pb^{2+} bonding environment are strongly indicative of the presence of stereochemical interactions between a non-bonding lone-pair and surrounding electrons, as found in numerous Pb^{2+} containing oxide compounds (§3.4), and whilst the authors [66] report a large fraction of free volume in the RMC derived glass structure models, they do not explicitly state that this may be evidence for stereochemically active lone-pairs, which seems most probable.

3.3.2.6 Extended x-ray absorption fine structure

Pb L_{III} edge EXAFS spectroscopy has been applied to 31, 50.5 and 66 mol% PbO silicate glasses by Fayon *et al.* [67] who found that the results based on a two shell model were in accord with earlier diffraction studies. This was confirmed later by Hoppe *et al.* [62] who compared their x-ray total correlation functions with the predictions based on the EXAFS derived [67] peak parameters. Fayon *et al.* [67] found Pb-O coordination numbers of just below four for all three glasses and report a lengthening of the second shell Pb-O bond lengths with increasing PbO concentration, although the latter point may arise from the fitting model applied ($n_{PbO} = 2$ fixed for first shell). Mastelaro *et al.* [68] compared the Pb L_{III} edge EXAFS signals of vitreous and crystalline $PbSiO_3$. They find similar Pb-O bond lengths in the two materials but a higher Pb-O coordination number of 4.2 in the glass as compared to 3.0 in the crystal. This result is used to explain the fact that alamosite $PbSiO_3$ nucleates heterogeneously, on the glass surface, the reason proposed being the differing local structures about the Pb cation. This result can be questioned based on the fact that the authors [68] have to assume that the EXAFS signal is not influenced by bonds beyond 2.5 Å in length, in order to obtain agreement with the known crystal structure [30]. Rybicki *et al.* [69] again used Pb L_{III} edge EXAFS spectroscopy on 30, 50 and 70 mol% PbO silicate glasses and found results very similar to those of Fayon *et al.* [67], in particular coordination numbers, n_{PbO}, very close to four for all three glasses.

3.3.2.7 X-ray photoelectron spectroscopy

Smets and Lommen [70] reported x-ray photoelectron spectra for crystalline lead metasilicate and orthosilicate and glasses containing 30 to 70 mol% PbO. Their analysis of the O 1s peaks allowed them to reveal an excess of BO at $\gtrsim 40$ mol% PbO, indicating retention of a silicate network beyond that present in alkali silicate glasses. Wang and Zhang [71] collected XPS spectra from $x\mathrm{PbO} \cdot (1-x)\mathrm{SiO_2}$ glasses with $15 \leqslant x \leqslant 70$ mol% PbO. The Pb $4f_{7/2}$, Si 2p and O 1s binding energies all decreased with PbO concentration increasing, with a discontinuity at around 40 mol% PbO. Such behaviour was interpreted as showing a breakdown of the silicate network at the discontinuity, and a continuous increase in polarisation of the Pb ions, associated with the apparent increase in covalency of the Pb-O bonds with PbO concentration and a reduction in Pb-O coordination

number. However, such a discontinuity in binding energies was not observed in a later, higher resolution study, where Gee *et al.* [72] showed approximately linear decreases in Pb $4f_{7/2}$, Si 2p and O 1s binding energies over the region $25 \leqslant x \leqslant 67$ mol% PbO. The high resolution O 1s spectra clearly show two contributions, attributed to bridging oxygen, and other species, but no difference in binding energy between oxygen bonded to one silicon and oxygen bonded to no silicon could be resolved. Dalby *et al.* [73] conducted an XPS study on silicate glasses containing 50 to 67 mol% PbO, with results in accord with those of Gee *et al.* [72].

3.3.2.8 Vibrational spectroscopy

Raman and infrared spectroscopies were used as probes of lead silicate glasses and crystals by Furukawa *et al.* [74, 75]. The high frequency ($\nu \gtrsim 600\,\mathrm{cm}^{-1}$) bands are attibuted to modes of silicate species. In particular a small, fully polarised, band at $840\,\mathrm{cm}^{-1}$ was assigned to the $[SiO_4]^{4-}$ monomer, the larger, also fully polarised, band at $950\,\mathrm{cm}^{-1}$ to $[Si_2O_7]^{6-}$ dimers, and the higher frequency bands to more highly polymerised species. Due to the unknown Raman scattering cross-sections of the various modes, the degree of polymerisation, or Q^n species distribution could not be quantified, but the vibrational spectra clearly show a higher degree of polymerisation (above 50 mol% PbO), as well as a broader distribution of silicate species, than in alkali silicate glasses. This led the authors [74] to conclude that some oxygen must exist bonded only to Pb, which is supported by the appearance of a low frequency, $140\,\mathrm{cm}^{-1}$, band which increases rapidly in intensity beyond the metasilicate composition, and is assigned to vibrations involving Pb atoms. Worrell and Henshall [76] report results in excellent agreement with those of Furukawa *et al.* [74], although they additionally point out that the infrared band at $460\,\mathrm{cm}^{-1}$ can be attributed to librations of bridging oxygen atoms. Piriou and Arashi [77] pointed out the great similarity between spectra of the vitreous and liquid lead silicates. Liu [78] measured the infrared reflectance of lead silicate glasses, with their findings in accord with earlier works. Meneses *et al.* [79] also present IR reflectivity spectra, though their analysis and interpretation is somewhat different to preceeding studies. Firstly, several bands show discontinuous changes in position, amplitude and width as a function of PbO content, at about 45 mol% PbO. These include the two low frequency ($\nu \lesssim 300\,\mathrm{cm}^{-1}$) bands assigned to Pb-O stretching vibrations. The au-

thors [79] identify the existence of two bands with two distinct Pb environments. This is questionable based on the lack of support from calculations, and the fact that multiple bands are observed in the Raman spectrum of lead monoxide [76] which contains only a single Pb environment. Meneses *et al.* [79] compared the compositional dependence of the high-frequency band amplitudes to the ^{29}Si MAS NMR results of Fayon *et al.* [46], which allowed assignment to specific Q^n species. A renormalisation of the intensities was applied in order to quantify the Q^n species distributions, however, this relies on the assumption that only three Q^n species ever coexist. The observed discontinuities in some parameters of the dielectric function model [79] at 45 mol% PbO were reconciled with UV absorption measurements of the Urbach edge [80, 81]. Feller *et al.* [47] report the most recent Raman and IR spectra for lead silicate glasses, including, for the first time, compositions containing $\gtrsim$ 67 mol% PbO. Assignments of spectral bands were in accord with the earlier studies, with the following additions. The low frequency plateau observed in Raman spectra terminating between 460 and 550 cm^{-1} was assigned to delocalised vibrations with mixed bond stretching and bond bending character. A band at 160 cm^{-1} in the IR spectra was assigned to rattling of Pb ions in cages formed by oxygen bonded to SiO_4 tetrahedra, whilst the 240 cm^{-1} IR band was attributed to asymmetric stretching within Pb-O polyhedra surrounded predominantly by Pb rather than Si, and corresponding to the symmetric, Raman-active, mode at 140 cm^{-1}.

3.3.2.9 Molecular dynamics

Damodaran *et al.* [82] were the first to attempt to model a lead silicate ($PbSiO_3$) glass using classical molecular dynamics. The RDF of the model obtained does not compare favourably with the x-ray RDF of Mydlar *et al.* [27]. This is not surprising based on the fact that the interatomic potentials used were *isotropic*, whilst the atomic arrangement of oxygen atoms around a lead atom is known in many cases to be *anisotropic* due to the existence of a lone-pair of non-bonding electrons. This point regarding the use of isotropic potentials is stated in the closing sentence of the paper [82]. What is surprising then, is that many subsequent publications exist [69, 83–85] based on use of the same interatomic potentials used by Damodaran *et al.* [82], or on alternative isotropic potentials [86].

Without allowing for the polarisability of the Pb^{2+} cations (as well as O^{2-} anions),

molecular dynamics cannot be expected to reproduce accurately the structural arrangements in real materials. As such, the contributions made in the literature to date are useful primarily for the methodology and analysis routines developed, and not for yielding insight into the structure of lead silicate glasses.

3.3.2.10 Other relevant studies

Mizuno *et al.* [87] studied the leaching behaviour of Pb from lead silicate glass powders containing from 25 to 70 mol% PbO in aqueous solution, and measured the Pb diffusion coefficients. A remarkable feature is the dramatic rise in diffusion coefficient between 35 and 50 mol% PbO, of over three orders of magnitude. The behaviour is consistent with a percolation transition from an infinite silicate cluster containing isolated plumbite clusters, for glasses $\lesssim$ 40 mol% PbO, into an infinite plumbite network containing isolated silicate anions above this threshold. Support for this explanation is evident in the diffusion behaviour of Pb from glasses with > 40 mol% PbO which at longer times deviates from the expected $t^{1/2}$ dependence as a result of the formation of a silicious gel layer. Formation of the gel layer was evinced by ^{29}Si MAS NMR, oxygen XPS and ^{1}H-^{29}Si CP-MAS NMR which revealed the presence of a large proportion of silanol [Si-OH] groups in the originally 70 mol% PbO glass, post leaching.

3.3.3 Summary

3.3.3.1 Local lead environment

A large body of evidence exists supporting the notion that at least a majority of Pb^{2+} cations in lead silicate glasses exist in environments similar to those found in the known crystalline silicates and monoxides of lead; that is, with an occupied non-bonding or lone-pair orbital, and a low coordination number of three to four oxygens distributed anisotropically about the lead cation. In particular this conclusion is supported by studies employing ^{207}Pb NMR [32, 46], ESR on Pb^{3+} hole centres [50], x-ray and neutron diffraction [58–60, 62, 63, 66], Pb L_{III} edge EXAFS [67, 69] and vibrational spectroscopy [47, 74–79]. Both diffraction and EXAFS measurements indicate an asymmetric distribution of Pb-O bond lengths, skewed toward the longer bond length side, with around three Pb-O bonds at an average of 2.30 Å and a further one or two oxygen

atoms at distances of about 2.7 Å [62].

Regarding the dependence of local lead environment on glass composition, two schools of thought can be identified in the literature. One involves the idea that Pb^{2+} changes from glass modifier to glass former, or intermediate, at higher PbO concentrations [41]. First of all there is great ambiguity with any such statements, since the concepts of glass former and glass modifier are not rigorously defined. However, at the most basic level, a change, from glass modifier to glass former or intermediate, must involve a change in coordination number, n_{PbO}, from a higher to a lower value respectively. This has not been measured directly by diffraction or EXAFS measurements, giving rise to a second school of thought, which states that the role of lead is approximately independent of the concentration of PbO in the binary silicate glass system [62]. Clearly any such change in n_{PbO} with mole fraction PbO, if it exists, is subtle. Formation of a clear picture is hindered by the paucity of information at very low and very high PbO contents, which is a consequence of the difficulty of forming glasses in these regions. At low PbO content, very high melting temperatures, in excess of 1700 °C, are required [88], which are beyond the capabilities of most conventional furnaces, and in addition a metastable immiscibility gap has been reported [88]. At high PbO contents, volatilisation of PbO from the melt becomes an increasing problem [89], as does the reduction process of lead oxide into metallic lead and crystallisation.

Beyond the local coordination polyhedra about Pb^{2+}, the predominance of $[Pb_2O_4]$ structural units formed from edge sharing pairs of trigonal $[PbO_3]$ pyramids has been suggested as consistent with the Pb-Pb separation of 3.7 to 3.8 Å observed in x-ray RDFs [63, 87], which is independent of PbO concentration. Such a motif has not been confirmed or otherwise in three-dimensional models obtained by RMC modelling [66]. What does appear clear, from ^{207}Pb NMR in particular, as well as diffraction and EXAFS results, is that a wide range of Pb^{2+} environments exist, and that qualitative models based on regular $[PbO_3]$ and/or $[PbO_4]$ pyramids are oversimplistic and may not be sufficient to understand the network properties of the glass.

3.3.3.2 Local silicon and oxygen environments

Diffraction, ^{29}Si NMR measurements and vibrational spectra indicate the presence of the $[SiO_4]$ tetrahedron as the sole polyhedral environment for silicon in the lead silicate

glasses. A dependence of the polyanion distribution and the related Q^n species distribution on the cooling rate applied to the glass forming melt has been evidenced by both destructive chemical analyses [37], and by ^{29}Si MAS NMR [47]. The latter spectroscopic technique [41, 44, 45, 47], as well as XPS [70–73] and Raman and IR spectroscopies [47, 74–79] reveal that polymerisation of the silicate network persists beyond the composition (2/3 by mole of PbO) at which only $[SiO_4]^{4-}$ anions would exist based upon the formation of a NBO for each unit of formal (non-Si) cation charge present in the glass. This implies that metal-bridging oxygen (MBO) atoms exist, bonded only to Pb, at compositions in excess of approximately 50 mol% PbO. There exist therefore at least three different oxygen environments in the lead silicate glasses, the BO, NBO and MBO. Unfortunately O 1s XPS spectra resolve only the BO from the other contributions, which remain unresolved from one another, and hence cannot be quantified. On the other hand ^{29}Si MAS NMR is effectively sensitive only to the oxygen bonded to silicon, and extraction of the Q^n species distribution therefore allows a quantitative estimate of the relative amounts of BO, NBO and MBO (equations 2-2, 2-3, 2-4). It is also clear, from the approximate independence of cation-oxygen coordination numbers on PbO concentration, that the average oxygen-cation coordination in the lead silicate glasses is greater than two, and should increase with PbO content. A quantitative speciation of $[OPb_nSi_m]$ environments is something that has not been made or even discussed to any extent in the literature. It is touched upon in the analysis of some classical MD derived models [86], but, such models are not thought to provide good models of lead containing glasses without inclusion of polarisability (§ 3.3.2.9).

3.3.3.3 Beyond local structure

Small, low Q peaks, at high PbO content in the neutron structure factors, and at low PbO content in the x-ray structure factors, indicate the presence of structural ordering on length scales greater than the shortest scales defined by the nearest neighbour interatomic distances, or bond-lengths. RMC models [60, 66] which reproduce these 'pre-peaks' have shown that they arise from scattering from the silicate part of the network at high PbO concentrations, and from the plumbite part at low PbO concentrations. The SAXS intensity has been shown to pass through a maximum at 25 mol% PbO [61], with the length scale for inhomogeneities arising from concentration fluctuations in the silica

rich region estimated as between 5 and 7 Å.

3.4 Crystalline lead silicates

3.4.1 Introduction

The present section aims to summarise the local structural arrangements found within known forms of crystalline lead silicate compounds. Four crystal structures for binary compounds within the $PbO{-}SiO_2$ system have been determined. These correspond to the $PbO{:}SiO_2$ stoichiometries 1:1 ($PbSiO_3$ [30, 31]), 3:2 ($Pb_3Si_2O_7$ [90]), 2:1 (Pb_2SiO_4 [91, 92]) and 11:3 ($Pb_{11}Si_3O_{17}$ [93]). Note that most equilibrium phase diagrams reported for the lead silicate system [33, 94–96] include the incongruently melting 4:1 phase, whereas Hirota and Hasegawa [97] report the congruently melting 11:3 phase, for which there is stronger evidence in the form of the structure determination by Kato [93]. The 2:1 phase melts congruently and four polymorphs have been identified [33]. The structure determinations by Kato [91] and Glasser *et al.* [92] correspond to the stable (high-T) phase and one of the metastable phases respectively. They both contain the $[Si_4O_{12}]^{8-}$ ring anion, which is remarkable in that it represents a large degree of over-polymerisation of the silicate anions with respect to the $[SiO_4]^{4-}$ monomers which would be expected in the absence of oxygen bonding only to Pb. The 3:2 phase [90] is one of several subsolidus compounds [95] reported to decompose into solid compounds rather than melting. Other such compounds, for which no structural solutions exist, include the 5:1 [97], 3:1 [33, 95] and 5:8 [33]. The 1:1 phase melts congruently, and is the most silica rich of the known crystal structures. The two reported structure determinations are essentially the same, having been performed on natural alamosite [30] and synthetic $PbSiO_3$ [31].

3.4.2 Silicon-oxygen bond lengths

The average Si-O bond length tends to increase with PbO content (see Fig. 6-7). This is an interesting result given that the Si-O coordination number does not change. Inspection of the lead silicate crystal structures (Table 3-3) indicates that Si-(NBO) bonds (length $r_{SiO_{nb}}$) are typically shorter than Si-(BO) bonds (length r_{SiO_b}), and indeed the

Table 3-3 Average bond lengths between silicon and oxygen and Si-O-Si angles in crystalline lead silicates. O_{nb} - Non-Bridging Oxygen, O_b - Bridging Oxygen.

Crystal	mol% PbO	r_{SiO} (Å)	$r_{SiO_{nb}}$ (Å)	r_{SiO_b} (Å)	$\overline{\theta}$ (°)
Quartz [100]	0.00	1.6080	-	1.6080	143.8
$PbSiO_3$ [31]	50.00	1.6250	1.6045	1.6454	143.5
$Pb_3Si_2O_7$ [90]	60.00	1.6367	1.6273	1.6647	125.1
Pb_2SiO_4 [92]	66.67	1.6601	1.6452	1.6751	160.7
$Pb_{11}Si_3O_{17}$ [93]	78.57	1.6269	1.6303	1.6098	168.1

former can often be shorter than the average Si-O bond in quartz or vitreous silica. However, there is an overall increase in *both* the average $r_{SiO_{nb}}$ *and* r_{SiO_b} with PbO content. One factor contributing to changes in the Si-O_b bond lengths is the Si-O_b-Si bond angle, θ, and the two have been shown to correlate inversely, see Boisen *et al.* [98], Gibbs *et al.* [99] and references therein. Table 3-3 shows the average Si-O_b-Si bond angles, $\overline{\theta}$, calculated from the crystal structures, and comparison of these to the average r_{SiO_b}* reveals no simple correlation, which indicates the existence of additional mechanisms of Si-O_b bond length elongation/contraction. An obvious contribution to Si-O bond elongations, especially for Si-O_b bonds, is the increase in O-Pb coordination number, see §3.4.3. As far as bond angle effects are concerned, the changes in r_{SiO_b} and $\overline{\theta}$ are at least qualitatively consistent with those expected when increasing PbO content from $PbSiO_3$ to $Pb_3Si_2O_7$ and from Pb_2SiO_4 to $Pb_{11}Si_3O_{17}$, but *not* from quartz to $PbSiO_3$ or from $Pb_3Si_2O_7$ to Pb_2SiO_4.

Presumably reduction of the Si-O_{nb}-Pb bond angle, or indeed, increasing the number of Pb coordinating to an NBO, would have a similar effect on the Si-O bond length to reducing the Si-O_b-Si angle, i.e. they would lead to elongation. See §6.3.2.3 for further discussion.

3.4.3 Local oxygen environments

The increase in O-Pb coordination number with PbO content is shown in Fig. 6-8 and, for the crystals, has been broken down into [OPb_pSi_q] species in Fig. 3-1. Note that two different cut-off radii for Pb-O bonds have been considered, which is instructive

*Although individual values of θ and r_{SiO_b} should be compared, the functional form of their relationship taken into account, along with the effects of other independent parameters [98], this does not alter the present argument.

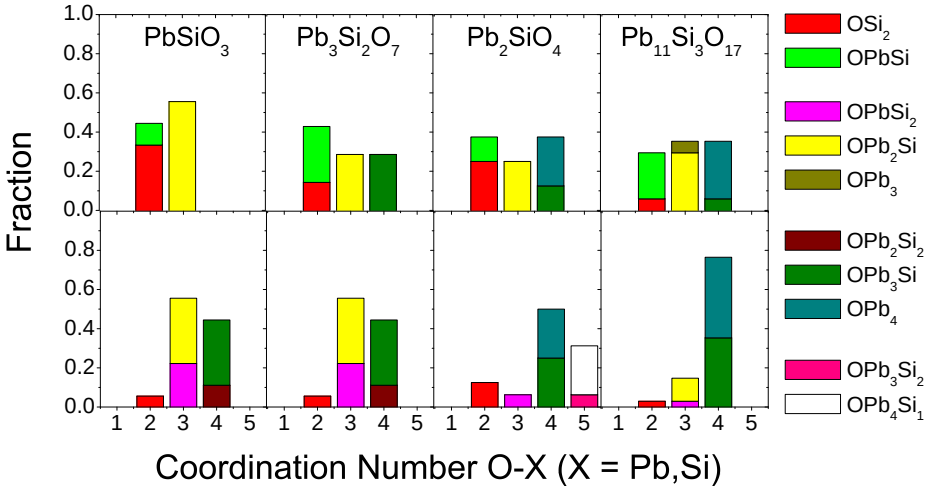

Figure 3-1 Oxygen-cation coordination species distributions in lead silicate crystals [31, 90, 92, 93]. Pb-O bond length cut-offs of 2.7 Å and 3.27 Å have been used for the upper and lower rows respectively. The Si-O bond length cut-off is 2.0 Å in all cases.

based on the lack of a clear radial divide between first and second Pb coordination shells. The choice of 2.70 Å and 3.27 Å is somewhat arbitrary but serves as a qualitative divide between short Pb-O bonds with $\gtrsim 0.20$ valence units ($\gtrsim$10.2% of the formal Pb^{2+} valence) and longer bonds with $\gtrsim 0.04$ valence units.

It is apparent from Fig. 3-1 that longer ($2.7 \leq r_{PbO} \leq 3.27$ Å) Pb-O bonds often form with bridging oxygen, giving rise to $[OPb_pSi_2]$ species with $p = 1, 2$ and even 3 in the Pb_2SiO_4 [92] crystal. From simple bond valence considerations, an increase in p, with $q = 1$ or 2 a constant, should naturally increase the Si-O bond length, assuming no counteractive changes in the r_{O_bPb}. Such an increase in average r_{SiO} with the number of coordinating Pb atoms, p, is at the heart of the correlation between isotropic ^{29}Si NMR chemical shift and the number of Pb atoms coordinating a silicate tetrahedron, identified by Bessada *et al.* [45].

Calculation of O-Pb BV sums reveals some strange results, see Table 3-4. The 'plumbite' oxygen, which are those bonded only to Pb, and not to Si, in the high lead silicate crystals, have large BV sums, far in excess of the formal oxygen valence of (-)2. Meanwhile the O_{nb}-Pb BV sums, particularly for the high lead silicate crystals, are less than one, which should lead to a contraction of the Si-O_{nb} bonds, typically of ~0.05 Å, down to $r_{SiO_{nb}} \simeq 1.55$ Å, but which is not the case, as can be seen from

Table 3-4 Average bond valence sums for oxygen in crystalline lead silicates, excluding Si-O bonds, and in PbO polymorphs. Sums were calculated for Pb-O bond lengths between zero and the values indicated in parentheses. Oxygen species are subdivided by their numbers of coordinating silicon: q = 2 (BO), 1 (NBO) or zero (Plumbite).

Crystal	BV sum (2.70 Å)			BV sum (3.27 Å)		
	BO	NBO	Plumbite	BO	NBO	Plumbite
$PbSiO_3$ [31]	0.00	0.93	0.00	0.06	1.00	0.00
$Pb_3Si_2O_7$ [90]	0.00	0.90	0.00	0.00	1.01	0.00
Pb_2SiO_4 [92]	0.00	0.69	2.68	0.08	0.83	2.68
$Pb_{11}Si_3O_{17}$ [93]	0.00	0.79	2.49	0.05	0.92	2.50
α-PbO [102]	-	-	2.22	-	-	2.22
β-PbO [29]	-	-	2.17	-	-	2.17

Table 3-3. These unexpectedly large discrepancies in BV sums are likely due to Pb^{2+} polarisation effects associated with stereochemically active electron lone pairs. In other words, the BV parameter for Pb^{2+} of 2.112 ± 0.020 Å [101] is not suitable for highly polarised Pb^{2+}, having been obtained from a large number of materials containing Pb^{2+}-O bonds, many of which with unpolarised Pb and stereochemically *in*active lone pairs of electrons. Indeed, Wang and Liebau [103] have shown that the polarisation associated with stereochemically active lone electron pairs leads to larger effective valences and discrepancies in traditional BV sums for many lone pair cations (see also [104, 105]), including Pb^{2+} [106].

In the lead silicates, an increase in effective Pb valence tends to draw NBOs away from Si and increases the Si-O_{nb} bond lengths. The increase in average Si-O bond length (Fig. 6-7) can therefore be considered as indicative of polarised Pb sites with low coordination number and asymmetric oxygen ligand distributions. Other factors, such as bonding of Pb to BOs, changes in Si-O-Si, and presumably Si-O-Pb, bond angles also influence r_{SiO}, making it a rather multivariate function of glass composition.

3.4.4 Local lead environments

It was alluded to above that the local Pb environments in crystalline lead silicates have highly asymmetric oxygen ligand distributions, characteristic of the presence of a sterically active LP of electrons. Fig. 3-2 shows the Pb-O coordination number distributions (CNDs) for the four compounds, and for two different cut-off radii, and in

fact reveals a startling diversity in local Pb environments. Nonetheless, several characteristics are common to all four compounds, for instance, they all contain at least some sites with 3 and/or 4 short (≤ 2.7 Å) Pb-O bonds, which have additional longer ($2.7 \leq r_{PbO} \leq 3.27$ Å) Pb-O bonds, bringing the coordination numbers up to 5, 6 or 7. In fact, this is the full story in $PbSiO_3$, whilst Pb_2SiO_4 and $Pb_{11}Si_3O_{17}$ contain some sites with 5 short bonds. It should be explicitly stated that the short bonds are indeed directed into a single hemisphere of the Pb atom owing to valence shell electron pair repulsion (VSEPR) [107]. The $Pb_3Si_2O_7$ crystal contains some sites with 6 Pb-O bonds ≤ 2.7 Å in length. However, even these are not symmetric octahedral sites, the Pb2 site being highly distorted, with an additional 3 long bonds to one side, and the Pb3 site being somewhat distorted, with no longer Pb-O bonds, and being the closest to a typical glass network modifier environment. It should be borne in mind that the peculiarities of the $Pb_3Si_2O_7$ crystal, as compared to the other lead silicate compounds, may be related to the fact that it is a low temperature structure, being stable only below 585 °C [95], and therefore is probably less like glasses obtained from melt quenching. The $Pb_{11}Si_3O_{17}$ structure notably contains some sites with only 4 (or even 3) bonds with $0 < r_{PbO} \leq 3.27$ Å, these being akin to the four coordinated sites in the PbO polymorphs. Fig. 3-3 shows some projections of the α-PbO and $Pb_{11}Si_3O_{17}$ crystal lattices to illustrate the asymmetry of the Pb sites, as well as to show the LP organisation within layers in α-PbO and in linear channels in $Pb_{11}Si_3O_{17}$.

3.5 Lead germanate glasses

3.5.1 Total scattering of x-rays and neutrons

Nanba *et al.* [109] present the x-ray RDF, measured using a conventional Mo K_α source, of a 47 mol% PbO germanate glass, as part of a broader investigation into the structure of lead fluorogermanate glasses. Unfortunately their analysis of the RDFs is limited to a statement of the observed average bond-lengths which were approximately 1.8, 2.5 and 4 Å for Ge-(O,F), Pb-(O,F) and Pb-(Pb,Ge) respectively. Umesaki *et al.* [110] measured the neutron scattering cross-sections of three annealed lead germanate glass rods containing 20, 33 and 40 mol% PbO and present the corresponding total correlation functions. The high value of $Q_{max} = 42$ Å^{-1}, made possible by use of the time-of-

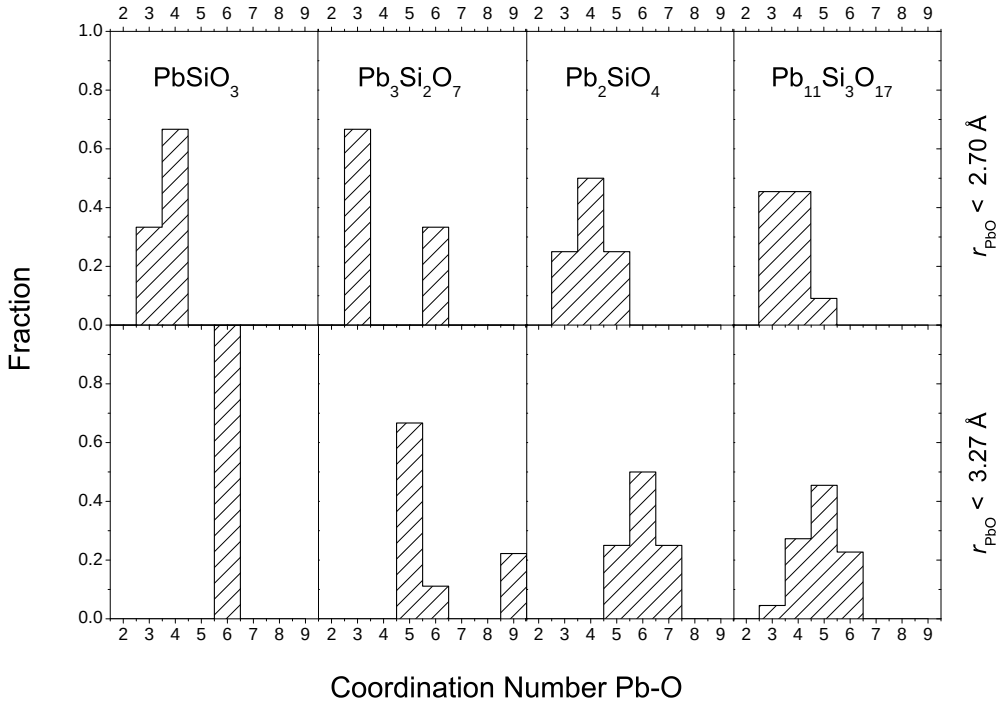

Figure 3-2 Pb-O coordination number distributions in lead silicate crystals [31, 90, 92, 93]. Pb-O bond length cut-offs of 2.7 Å and 3.27 Å have been used for the upper and lower rows respectively. The Si-O bond length cut-off is 2.0 Å in all cases.

flight technique, led to high real-space resolution. Difference functions between the lead germanate correlation functions, and that measured for vitreous germania reveal a shoulder to the high-r side of the Ge-O correlation, indicative of the presence of some GeO_n polyhedra with $n > 4$. Parameters are derived from fitting the total correlation functions with three separate peaks attributed to short and long Ge-O bond length distributions, and to the Pb-O bonds. The Ge-O average bond length increases from 1.742 Å, in GeO_2 glass, to 1.772 Å* in $40\,PbO \cdot 60\,GeO_2$ glass. The corresponding average Ge-O coordination numbers rise from 3.78 to 4.77, see Fig. 3-4. This rise is continuous with increasing PbO content, and does not show the maximum observed for alkali germanate glasses [111, 112]. The parameters for the Pb-O peak fits show a drop in Pb-O average bond length from 2.343 Å in lead tetragermanate glass, to 2.336 Å in the 40 mol% PbO germanate glass. The coordination numbers for Pb-O are given as 6.72 ± 0.21, 6.72 ± 0.32 and 6.23 ± 0.13 for the 20, 33 and 40 mol% PbO germanates

*Calculated from the coordination number weighted average of the reported [110] positions for the two Ge-O peaks.

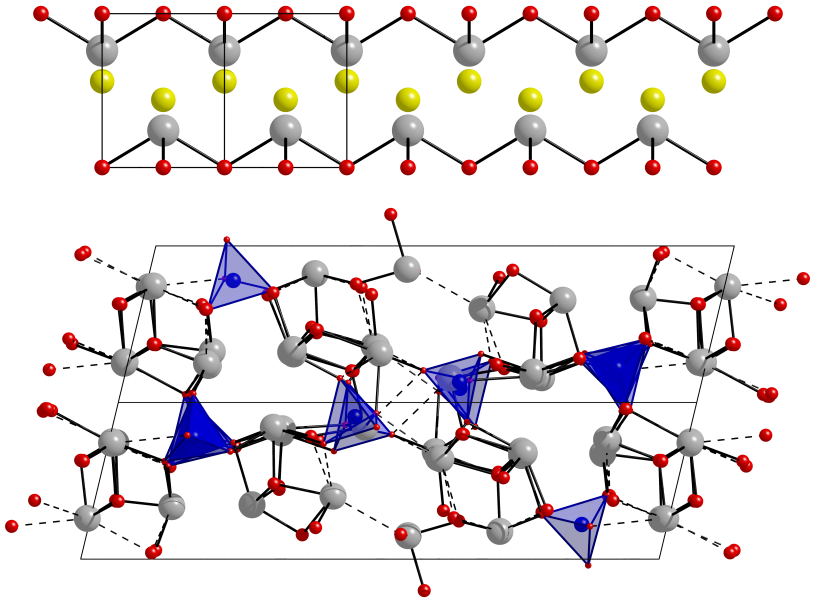

Figure 3-3 Parallel projections along the [010] direction of the α-PbO [102] (upper) and along the [01$\bar{1}$] direction of the $Pb_{11}Si_3O_{17}$ [93] (lower) crystal lattices. Si atoms are shown within shaded (blue) tetrahedra, Pb atoms as large (grey) spheres, bonded to O atoms (smaller spheres, red). Pb-O bonds shorter than 2.7 Å are shown as solid lines, whilst those between 2.7 and 3.27 Å are dashed. The positions of electron lone-pairs determined by Lebellac *et al.* [108] for α-PbO are indicated with yellow spheres.

respectively. Unfortunately, details of the peak fitting procedure are not given, and nor are any graphical representations of the resultant fits compared to the measured correlation functions. These are important because there is overlap between the Ge-O and Pb-O peaks, as well as between the Pb-O and O-O correlations. Hence it is hard to judge the validity of the parameters quoted, particularly since certain discrepancies are apparent. For one, a Pb-O coordination number of greater than six is not consistent with the short Pb-O distances of around 2.3 Å based on bond-valence [113] considerations. Indeed, such a short distance implies a coordination number of around three to four, whilst a n_{PbO} between six and seven would be consistent with an average bond length of 2.52 to 2.58 Å. Another inconsistency lies with the reported Ge-O coordination numbers. These are derived from fitting two peaks, at around 1.75 and 1.89 Å. The reported difference functions [110], in the region of the first Ge-O correlation, clearly show a negative contribution on the low-r side, followed by the aforementioned positive contribution to the high-r side. Therefore, the coordination number calculated from the first peak, which is ascribed to Ge-O bonds in [GeO_4] tetrahedra, should be less than four, especially considering the measured number of 3.78 in vitreous GeO_2,

which may arise as a result of the instumental resolution in reciprocal space. This is not the case in the reported parameters, and at the very least means that the two peaks cannot be ascribed to tetrahedral and octahedral contributions, which is clear from the fact that they are not resolved in the measured correlation functions. The use of the second peak position as evidence of six coordinated germanium is therefore suspect, and the conclusion that [GeO_4] tetrahedra and [GeO_6] octahedra, rather than any other combination of coordination species, exist in the glass can be treated as an assumption only. Further inconsistencies lie in the statement that the 'expected' Pb-O coordination in orthorhombic PbO is six, which is incorrect (in context) and contradicts the earlier (approximately correct [29]) statement that Pb in orthorhombic PbO is coordinated to two oxygen atoms at 2.21 Å and two at 2.42 Å.

Cervinka *et al.* [114] used monochromated x-rays generated using a Mo K_α source to measure the radial distribution functions for two lead germanate glasses, containing 20 and 36 mol% PbO. They were not able to discriminate between models of the 1.75 Å correlation based on [GeO_4] tetrahedra and those based on a mixture of [GeO_4] tetrahedra and [GeO_6] octahedra. This is due to the real-space resolution resulting from a Q_{max} = 16.51 $Å^{-1}$ and the additional real-space broadening that results from the form factor dependence of x-ray scattering. The authors imply that a Pb-O coordination number of four is evident, centred about 2.40 Å, based on the use of orthorhombic PbO as a basis for their models of the RDFs.

Bogdanov *et al.* [115] report SAXS measurements on fourteen germanate glasses containing between zero and approximately 65 mol% PbO. A maximum in SAXS is reported at 10 mol% PbO, with a similar trend observed in the Landau-Placzek ratio, measured by optical (632.8 nm wavelength) scattering as the ratio of Rayleigh to Mandelshtam-Brillouin intensities. Such a maximum is qualitatively similar to that observed for lead silicate glasses [61], although the maximum in the latter glass series is at the higher concentration of 25 mol% PbO.

3.5.2 Lead-207 nuclear magnetic resonance

Ghigna *et al.* [120] measured static ^{207}Pb NMR spectra at an operating frequency of 83.7 MHz for crystalline $PbGeO_3$ and $PbGe_3O_7$ as well as for six vitreous lead germanates containing between 5 and 50 mol% PbO. Unfortunately the spectra have very

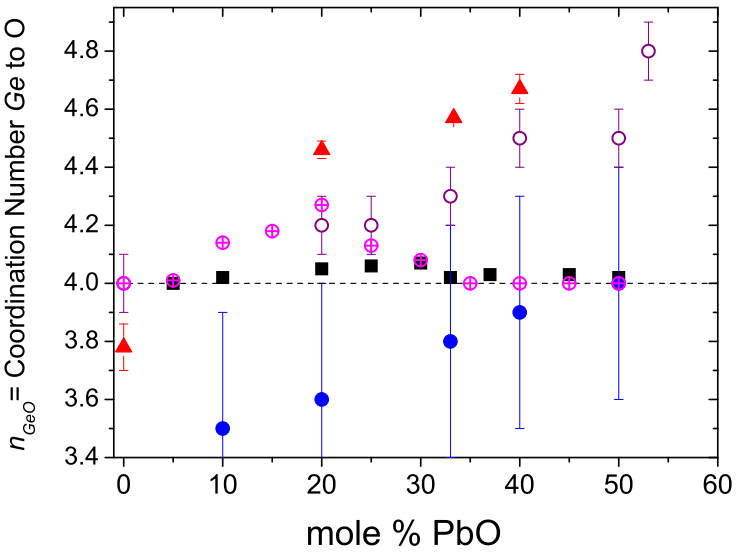

Figure 3-4 Ge-O coordination numbers as a function of PbO concentration in lead germanate glasses as reported by various authors. ▲ ND Umesaki *et al.* [110], ■ MD Ghobadi [116], ● EXAFS Ribeiro *et al.* [117], ○ EXAFS Witkowska *et al.* [118], ⊕ EXAFS Yamamoto *et al.* [119].

poor signal-to-noise ratios, and are not quantitative based on the non-uniform irradiation of the (very broad) spectra by a single RF pulse. However, they provide tentative evidence of the existence of two different distributions of Pb-O environments, one with lower coordination number and a higher degree of covalency, and one more ionic, with higher coordination number, with this interpretation being based on the work of Fayon *et al.* [49].

3.5.3 Extended x-ray absorption fine structure

A number of authors have conducted EXAFS studies of lead germanate glasses, both at the Ge K-edge [117–120] and at the Pb L_{III}-edge [117, 120, 121]. Fig. 3-4 shows the reported Ge-O coordination numbers as a function of glass composition. There is no consensus between the measurements: Witkowska *et al.* [118] conclude that a coordination number of four in all glasses with between 10 and 50 mol% PbO is consistent with their measurements, despite large uncertainties and a systematic increase in n_{GeO} with increasing PbO content (from 3.5(4) up to 4.0(4)). Ribeiro *et al.* [117] report monotonically increasing n_{GeO} and average bond lengths, r_{GeO}, with increasing lead content, with a maximum n_{GeO} = 4.8(1) at 53 mol% PbO. However, based on their

vibrational spectroscopic measurements [117], they suggest a continuous depolymerisation of the germanate network with addition of PbO, which is inconsistent with the reported increase in Ge-O coordination number. Yamamoto *et al.* [119] found quite different behaviour of n_{GeO} with lead germanate glass composition, with it passing through a maximum of 4.27 at 20 mol% PbO. Meanwhile r_{GeO} was found initially to increase with PbO addition, and then plateau, whilst the Debye-Waller factor (rms bond length deviation) similarly passes through a maximum between 20 and 30 mol% PbO. Ghigna *et al.* [120] also report Ge K-edge EXAFS, as well as XANES, spectra, but do not quote coordination numbers. They do report an excess of longer Ge-O bonds in the spectra for lead germanate glasses, as compared to that for glassy GeO_2, but cannot definitively state that the average Ge-O coordination number exceeds four. All authors observe a contribution from Ge-Ge correlations to the Ge K-edge EXAFS, in addition to the Ge-O contribution.

Pb L_{III}-edge EXAFS spectra have been collected by Ribeiro *et al.* [117] who report approximate values of $n_{PbO} = 3.0(5)$ and $r_{PbO} = 2.35(5)$ Å for all samples with between 20 and 53 mol% PbO. Ghigna *et al.* [120] also report little change in the local Pb environment with glass composition (5 to 50 mol% PbO) and measure Pb-O bond lengths of between 2.27 and 2.30 Å. They point out that this is consistent with low Pb-O coordination numbers of three to four but state that EXAFS is incapable of yielding quantitatively accurate values. Importantly Witkowska *et al.* [121] conclude that the distribution of Pb-O bonds has a tail to the high r side, and report mean values of 2.37(1) Å and most probable values of around 2.29(1) Å. The Pb-O coordination was found to drop from 4.1(4) at 10 mol% PbO to 3.7(4) at 50 mol% PbO. The authors [121] also claim a small contribution from Pb-Pb pairs to the EXAFS signal. Therefore the Pb L_{III}-edge EXAFS studies [117, 120, 121] are at least all in qualitative agreement, all reporting low Pb-O coordination numbers and short Pb-O bond lengths in glasses containing from 5 to 53 mol% PbO.

3.5.4 Vibrational spectroscopy

Canale *et al.* [122] made a detailed vibrational spectroscopic study of 6 lead germanate glasses from 10 to 60 mol% PbO using both Raman (488 nm and 514.5 nm laser excitations) and infra-red spectroscopies. Notably the glasses were prepared by Shelby [7]

using slow cooling rates, and thought to be phase separated below about 30 mol% PbO based upon thermal expansion coefficient and glass transition temperature measurements. A key conclusion [122] was that a Raman band at 820 cm^{-1}, attributed to Ge-O stretching involving NBOs, was present for all glasses, and that this behaviour is not the same as observed for alkali germanate glasses, where NBOs are not present in detectable quantities below about 20 mol% alkali oxide. Unfortunately however, the appearance of the 820 cm^{-1} band at low PbO contents is also qualitatively consistent with the presence of phase separation. In addition, no conclusive statements regarding a change in average Ge-O coordination number could be made. Ribeiro *et al.* [117] and Sigaev *et al.* [123] both observed the presence of a Raman band at ~820 cm^{-1} in glasses between 20 and 62.5 mol% PbO, but unfortunately do not report results for any glasses with < 20 mol% PbO.

3.5.5 Molecular dynamics

A number of classical molecular dynamics simulations of lead germanate glasses have been conducted [109, 116, 118, 121, 124], although the same criticism, made against analogous studies on lead silicates (§3.3.2.9) applies. Specifically, without allowing for the polarisability of the Pb^{2+} cations, which is associated with stereochemical activity of the lone-pair of electrons, the simulations are unlikely to produce atomic configurations representative of the real glasses. For example, Rybicki *et al.* [124] found [PbO_4] groups mainly in tetrahedral configurations (Pb at centre), with only a minority in square pyramidal geometries (Pb at apex). Notably some models were found to contain germanium coordinated to greater than four oxygen atoms. In particular, Nanba *et al.* [109] found that a 47 $PbO \cdot 53\ GeO_2$ glass simulated using Born-Mayer type pair potentials had average Ge-O coordination of 4.1, whilst Ghobadi [116], using the two-body Mitra potential, found that n_{GeO} passed through a maximum of 4.07 at 30 mol% PbO, see Fig. 3-4. However, Ghobadi [116] also showed that Ge with higher than four-fold coordination occurred in MD models of GeO_2 glass, there being 4% in five-fold coordination when the ionic radius was the same as that used for the lead germanate MD simulations. Much greater concentrations of higher coordinated species occurred upon increasing the Ge ionic radius.

3.5.6 Physical properties

Minima in molar volumes [125] and maxima in resistivity [125], and the Young's and shear moduli [126] of lead germanate glasses have been observed at ~30 mol% PbO. No extrema in refractive index or mass density are apparent [125] due to the dominance of the polarisability and mass respectively of the Pb^{2+} cation. Shelby [7] interpreted a plateau in glass transition temperature between 5 and 25 mol% PbO as evidence for glass-in-glass phase separation, also reporting two T_g events over this region, measured by DSC. Canale *et al.* [122] report similar results, but only observe the lower T_g. Both groups [7, 122] performed DSC experiments on slowly (inertially) cooled glasses. The immiscible region in the $PbO-GeO_2$ system has been measured [4, 9] to be metastable, and to have a low consolute temperature of 580 °C.

3.5.7 Summary

There is no consensus in the literature regarding the variation of average Ge-O coordination number with lead germanate glass composition. Therefore, it is far from clear whether or not a maximum in n_{GeO}, as found in alkali germanate glass systems, even occurs, let alone whether this can be correlated with the observed extrema in the compositional dependence of physical properties, such as molar volume, refractive index, elastic moduli or conductivity. There is some evidence from Raman spectroscopy [122] that non-bridging oxygen atoms occur in glasses with as little as 10 mol% PbO, which implies a lower n_{GeO} as compared to alkali germanate glasses.

The majority of Pb L_{III}-edge EXAFS and total scattering (diffraction) studies consistently measure short Pb-O bonds of ~2.3 Å and report Pb-O coordination numbers of between 3 and 4. Umesaki *et al.* [110] report the most accurate Pb-O bond lengths, based on high resolution neutron diffraction, but report inconsistently high coordination numbers of > 6.

3.6 Crystalline lead germanates

There are three known lead germanate crystal structures containing tetrahedral Ge in coexistence with Ge in higher coordination states. α-$PbGe_4O_9$ [127] is isomorphous with $BaGe_4O_9$ [128, 129], $SrGe_4O_9$ [130] and the mineral benitoite ($BaTiSi_3O_9$), within

which the M^{2+} cations are 10-fold coordinated. The Pb-O bonds in α-$PbGe_4O_9$ [127] range from 2.630 Å to 3.179 Å, with mean value 2.865 Å. γ-$PbGe_4O_9$ [131] contains [PbO_7] polyhedra and Pb-O bonds from 2.440 Å to 2.805 Å, with mean value 2.615 Å. $PbGe_3O_7$ [132] also contains [PbO_7] polyhedra (though with a less well defined cut-off between first and second oxygen shells) and Pb-O bonds from 2.356 Å to 2.989 Å, with mean value 2.626 Å.

For comparison, note that $PbGeO_3$ [133] is isomorphous with $PbSiO_3$ [30, 31], and therefore has Pb sites with 3 or 4 short ($\leq$ 2.7 Å) bonds to oxygen and 3 or 2 longer ($\leq$ 3.27 Å) ones (see Fig. 3-2). Hydrothermally synthesised $PbGeO_3$ [134] has Pb sites with 5 short and 1 long Pb-O bond. There are too many known lead germanate crystal structures with $>$ 50 mol% PbO [135–143] for them all to be discussed here. Note however that all Ge are 4-fold coordinated in these structures (average r_{GeO} shown in Fig. 7-10), and the Pb sites are typically highly asymmetric, with low coordination numbers similar to the lead silicate crystals with similar stoichiometries (§3.4.4).

References

[1] P. Hudon and D. R. Baker, *J. Non-Cryst. Solids* **303** (3), (2002), 299–345.

[2] P. Hudon and D. R. Baker, *J. Non-Cryst. Solids* **303** (3), (2002), 354–371.

[3] C. R. Robbins and E. M. Levin, *Am. J. Sci.* **257** (1), (1959), 63–70.

[4] Y. Tabata, Y. Ohta, K. Morinaga and T. Yanagase, *Journal of the Ceramic Association, Japan* **91** (11), (1983), 509–516.

[5] A. K. Shirvinskaya, R. G. Grebenshchikov and N. A. Toropov, *Izv. Akad. Nauk SSSR, Neorg. Mater.* **2** (2), (1966), 332.

[6] J. P. Guha, *J. Mater. Sci.* **14** (7), (1979), 1744–1748.

[7] J. E. Shelby, *J. Am. Ceram. Soc.* **66** (6), (1983), 414–416.

[8] J. E. Shelby, *J. Am. Ceram. Soc.* **67** (8), (1984), 557–560.

[9] K. Morinaga and K. Nakashima, *J. Non-Cryst. Solids* **103** (1), (1988), 108–116.

[10] K. Kamiya, S. Sakka and T. Yoko, *Res. Rep. Fac. Eng., Mie Univ.* **7**, (1982), 107–119.

[11] A. Margaryan and M. L. Wai, *J. Mater. Sci. Lett.* **11** (22), (1992), 1511–1513.

[12] A. A. Margaryan and A. M. Narekatsyan, *Fiz. Khim. Stekla* **12** (4), (1986), 477.

[13] S. S. Kasymova, *Dokl. Akad. Nauk UzSSR* **1**, (1982), 36.

[14] P. Pernice, A. Aronne, M. Catauro and A. Marotta, *J. Non-Cryst. Solids* **210** (1), (1997), 23–31.

[15] S. Inaba, S. Oda and K. Morinaga, *J. Jpn. I. Met.* **65** (8), (2001), 680–687.

[16] H. Schlenz, S. Rings, M. Schmucker, K. Schulmeister, W. Mader, A. Kirfel and J. Neuefeind, *J. Non-Cryst. Solids* **320** (1-3), (2003), 133–142.

[17] M. Catauro and G. Laudisio, *J. Eur. Ceram. Soc.* **18** (11), (1998), 1587–1591.

[18] G. Laudisio, M. Catauro and G. Luciani, *Mater. Chem. Phys.* **58** (2), (1999), 109–113.

[19] G. J. Redhammer, G. Roth and G. Amthauer, *Acta Crystallogr. C* **63**, (2007), I47–I50.

[20] J. Haines, O. Cambon, E. Philippot, L. Chapon and S. Hull, *J. Solid State Chem.* **166** (2), (2002), 434–441.

[21] A. A. Bolzan, C. Fong, B. J. Kennedy and C. J. Howard, *Acta Crystallogr. B* **53**, (1997), 373–380.

[22] H. Aust, H. Vollenkle and A. Wittmann, *Z. Kristallogr.* **144** (1-2), (1976), 82–90.

[23] J. Barbier and D. Levy, *Z. Kristallogr.* **212** (7), (1997), 519–528.

[24] E. M. Rabinovitch, *J. Mater. Sci.* **11**, (1976), 925–948.

[25] G. J. Bair, *J. Am. Ceram. Soc.* **19**, (1936), 339–347.

[26] J. Krogh-Moe, *Z. Phys. Chem. Neue Fol.* **18**, (1958), 223–229.

[27] M. F. Mydlar, N. J. Kreidl, J. K. Hendren and G. T. Clayton, *Phys. Chem. Glasses* **11** (6), (1970), 196.

[28] J. Leciejewicz, *Acta Cryst.* **14**, (1961), 1304.

[29] R. J. Hill, *Acta Crystallogr. C* **41** (Sep), (1985), 1281–1284.

[30] M. L. Boucher and D. R. Peacor, *Z. Kristallogr. Kristallgeom. Kristallphys. Kristallchem.* **126**, (1968), 98–111.

[31] S. Krivovichev and P. Burns, *Zapiski RMO* **133** (5), (2004), 70–76.

[32] L. Leventhal and A. J. Bray, *Phys. Chem. Glasses* **6** (4), (1965), 113–125.

[33] R. M. Smart and F. P. Glasser, *J. Am. Ceram. Soc.* **57** (9), (1974), 378–382.

[34] J. Gotz, D. Hoebbel and W. Wieker, *Z. Anorg. Allg. Chem.* **418** (1), (1975), 29–34.

[35] J. Gotz, D. Hoebbel and W. Wieker, *J. Non-Cryst. Solids* **20** (3), (1976), 413–425.

[36] J. Gotz, D. Hoebbel and W. Wieker, *J. Non-Cryst. Solids* **22** (2), (1976), 391–398.

[37] J. Gotz, D. Hoebbel and W. Wieker, *J. Non-Cryst. Solids* **37** (3), (1980), 367–380.

[38] R. M. Smart and F. P. Glasser, *Phys. Chem. Glasses* **19** (5), (1978), 95–102.

[39] D. Hoebbel, J. Gotz, A. Vargha and W. Wieker, *J. Non-Cryst. Solids* **69** (1), (1984), 149–159.

[40] E. Lippmaa, A. Samoson, M. Magi, R. Teeaar, J. Schraml and J. Gotz, *J. Non-Cryst. Solids* **50** (2), (1982), 215–218.

[41] R. Dupree, N. Ford and D. Holland, *Phys. Chem. Glasses* **28** (2), (1987), 78–84.

[42] T. Fujiu and M. Ogino, *J. Non-Cryst. Solids* **64** (1-2), (1984), 287–290.

[43] A. R. Grimmer, M. Magi, M. Hahnert, H. Stade, A. Samoson, W. Wieker and E. Lippmaa, *Phys. Chem. Glasses* **25** (4), (1984), 105–109.

[44] A. R. Grimmer, D. Hoebbel, J. Gotz and M. Magi, *Z. Anorg. Allg. Chem.* **547** (4), (1987), 45–56.

[45] C. Bessada, D. Massiot, J. Coutures, A. Douy, J. P. Coutures and F. Taulelle, *J. Non-Cryst. Solids* **168** (1-2), (1994), 76–85.

[46] F. Fayon, C. Bessada, D. Massiot, I. Farnan and J. P. Coutures, *J. Non-Cryst. Solids* **232**, (1998), 403–408.

[47] S. Feller, G. Lodden, A. Riley, T. Edwards, J. Croskrey, A. Schue, D. Liss, D. Stentz, S. Blair, M. Kelley, G. Smith, S. Singleton, M. Affatigato, D. Holland, M. E. Smith, E. I. Kamitsos, C. P. E. Varsamis and E. Ioannou, *J. Non-Cryst. Solids* **356** (6-8), (2010), 304–313.

[48] T. Yoko, K. Tadanaga, F. Miyaji and S. Sakka, *J. Non-Cryst. Solids* **150** (1-3), (1992), 192–196.

[49] F. Fayon, I. Farnan, C. Bessada, J. Coutures, D. Massiot and J. P. Coutures, *J. Am. Chem. Soc.* **119** (29), (1997), 6837–6843.

[50] H. Hosono, H. Kawazoe and T. Kanazawa, *Journal of the Ceramic Association, Japan* **90** (9), (1982), 544–551.

[51] M. Imaoka and A. Hasegawa, *Journal of the Ceramic Association, Japan* **88** (3), (1980), 141–150.

[52] H. Morikawa, Y. Takagi and H. Ohno, *J. Non-Cryst. Solids* **53** (1-2), (1982), 173–182.

[53] H. Hasegawa and M. Imaoka, *J. Non-Cryst. Solids* **68** (1), (1984), 157–158.

[54] H. Morikawa, Y. Takagi and H. Ohno, *J. Non-Cryst. Solids* **68** (1), (1984), 159–162.

[55] H. Ohno, K. Igarashi, Y. Takagi, H. Toratani, K. Furukawa, J. Mochinaga, T. Nakamura and T. Izumitani, *J. Jpn. I. Met.* **47** (2), (1983), 132–141.

[56] Y. Takagi, H. Ohno, K. Igarashi, H. Toratani, T. Nakamura, K. Furukawa, J. Mochinaga and T. Izumitani, *T. Jpn. I. Met.* **26** (7), (1985), 451–461.

[57] M. Imaoka, H. Hasegawa and I. Yasui, *J. Non-Cryst. Solids* **85** (3), (1986), 393–412.

[58] K. Yamada, A. Matsumoto, N. Niimura, T. Fukunaga, N. Hayashi and N. Watanabe, *J. Phys. Soc. Jpn.* **55** (3), (1986), 831–837.

[59] K. Suzuya, D. L. Price, M. L. Saboungi and H. Ohno, *Nucl. Instrum. Meth. B* **133** (1-4), (1997), 57–61.

[60] K. Suzuya, S. Kohara and H. Ohno, *Jpn. J. Appl. Phys. 1* **38**, (1999), 144–147.

[61] V. V. Golubkov, V. N. Bogdanov, A. Y. Pakhnin, V. A. Solovyev, E. V. Zhivaeva, V. O. Kabanov, O. V. Yanush, S. V. Nemilov, A. Kisliuk, M. Soltwisch and D. Quitmann, *J. Chem. Phys.* **110** (10), (1999), 4897–4906.

[62] U. Hoppe, R. Kranold, A. Ghosh, C. Landron, J. Neuefeind and P. Jovari, *J. Non-Cryst. Solids* **328** (1-3), (2003), 146–156.

[63] T. Takaishi, M. Takahashi, J. Jin, T. Uchino, T. Yoko and M. Takahashi, *J. Am. Ceram. Soc.* **88** (6), (2005), 1591–1596.

[64] *SciGlass Professional 7.3* (ITC Inc., 2008).

[65] O. V. Mazurin, M. V. Strel'tsina, T. P. Shvaiko-Shvaikovskaya and A. O. Mazurina, *Glass Phys. Chem.* **29** (6), (2003), 555–570.

[66] S. Kohara, H. Ohno, M. Takata, T. Usuki, H. Morita, K. Suzuya, J. Akola and L. Pusztai, *Phys. Rev. B* **82**, (2010), 134209 1–7.

[67] F. Fayon, C. Landron, K. Sakurai, C. Bessada and D. Massiot, *J. Non-Cryst. Solids* **243** (1), (1999), 39–44.

[68] V. R. Mastelaro, E. D. Zanotto, N. C. Lequeux and R. Cortes, *J. Non-Cryst. Solids* **262** (1-3), (2000), 191–199.

[69] J. Rybicki, A. Rybicka, A. Witkowska, G. Bergmanski, A. Di Cicco, M. Minicucci and G. Mancini, *J. Phys. Condens. Mat.* **13** (43), (2001), 9781–9797.

[70] B. M. J. Smets and T. P. A. Lommen, *J. Non-Cryst. Solids* **48** (2-3), (1982), 423–430.

[71] P. W. Wang and L. P. Zhang, *J. Non-Cryst. Solids* **194** (1-2), (1996), 129–134.

[72] I. A. Gee, D. Holland and C. F. McConville, *Phys. Chem. Glasses* **42** (6), (2001), 339–348.

[73] K. N. Dalby, H. W. Nesbitt, V. P. Zakaznova-Herzog and P. L. King, *Geochim. Cosmochim. Ac.* **71** (17), (2007), 4297–4313.

[74] T. Furukawa, S. A. Brawer and W. B. White, *J. Mater. Sci.* **13** (2), (1978), 268–282.

[75] T. Furukawa, S. A. Brawer and W. B. White, *J. Am. Ceram. Soc.* **62** (7-8), (1979), 351–356.

[76] C. A. Worrell and T. Henshall, *J. Non-Cryst. Solids* **29** (3), (1978), 283–299.

[77] B. Piriou and H. Arashi, *High Temp. Sci.* **13** (1-4), (1980), 299–313.

[78] L. P. Liu, *Z. Phys. B Con. Mat.* **90** (4), (1993), 393–399.

[79] D. D. Meneses, M. Malki and P. Echegut, *J. Non-Cryst. Solids* **352** (8), (2006), 769–776.

[80] I. A. Vainshtein, A. F. Zatsepin, V. S. Kortov and Y. V. Shchapova, *Phys. Solid State+* **42** (2), (2000), 230–235.

[81] I. A. Weinstein, A. F. Zatsepin and V. S. Kortov, *J. Non-Cryst. Solids* **279** (1), (2001), 77–87.

[82] K. V. Damodaran, B. G. Rao and K. J. Rao, *Phys. Chem. Glasses* **31** (6), (1990), 212–216.

[83] J. Rybicki, W. Alda, A. Rybicka and S. Feliziani, *Comput. Phys. Commun.* **97** (1-2), (1996), 191–194.

[84] A. Rybicka, J. Rybicki, A. Witkowska, S. Feliziani and G. Mancini, *Computational Methods in Science and Technology* **5**, (1999), 67–74.

[85] G. Bergmanski, M. Bialoskorski, M. Rychcik-Leyk, A. Witkowska, J. Rybicki, G. Mancini, S. Frigio and S. Feliziani, *Task Quarterly* **8** (3), (2004), 393–412.

[86] G. Cormier, T. Peres and J. A. Capobianco, *J. Non-Cryst. Solids* **195** (1-2), (1996), 125–137.

[87] M. Mizuno, M. Takahashi, T. Takaishi and T. Yoko, *J. Am. Ceram. Soc.* **88** (10), (2005), 2908–2912.

[88] P. D. Calvert and R. R. Shaw, *J. Am. Ceram. Soc.* **53** (6), (1970), 350–&.

[89] O. Andersen, *J. Am. Ceram. Soc.* **2** (10), (1919), 784–789.

[90] W. Petter, A. B. Harnik and U. Keppler, *Z. Kristallogr. Kristallgeom. Kristallphys. Kristallchem.* **133**, (1971), 445–458.

[91] K. Kato, *Acta Crystallogr. B* **36**, (1980), 2539–2545.

[92] L. S. D. Glasser, R. A. Howie and R. M. Smart, *Acta Crystallogr. B* **37** (Feb), (1981), 303–306.

[93] K. Kato, *Acta Crystallogr. B* **38**, (1982), 57–62.

[94] R. F. Geller, A. S. Creamer and E. N. Bunting, *J. Res. Nat. Bur. Stand.* **13** (2), (1934), 237–244.

[95] W. R. Ott and M. G. Mclaren, *J. Am. Ceram. Soc.* **53** (7), (1970), 374–375.

[96] E. Jak, S. Degterov, P. Wu, P. C. Hayes and A. D. Pelton, *Metall. Mater. Trans. B* **28** (6), (1997), 1011–1018.

[97] K. Hirota and Y. T. Hasegawa, *B. Chem. Soc. Jpn.* **54** (3), (1981), 754–756.

[98] M. B. Boisen, G. V. Gibbs, R. T. Downs and P. Darco, *Am. Mineral.* **75** (7-8), (1990), 748–754.

[99] G. V. Gibbs, F. C. Hill and M. B. Boisen, *Phys. Chem. Miner.* **24** (3), (1997), 167–178.

[100] S. M. Antao, I. Hassan, J. Wang, P. L. Lee and B. H. Toby, *Can. Mineral.* **46**, (2008), 1501–1509.

[101] N. E. Brese and M. Okeeffe, *Acta Crystallogr. B* **47**, (1991), 192–197.

[102] R. G. Dickinson and J. B. Friauf, *J. Am. Chem. Soc.* **46**, (1924), 2457–2463.

[103] X. Wang and F. Liebau, *Z. Kristallogr.* **211** (7), (1996), 437–439.

[104] X. Q. Wang and F. Liebau, *Acta Crystallogr. B* **65**, (2009), 99–101.

[105] X. Wang and F. Liebau, *Acta Crystallogr. B* **63**, (2007), 216–228.

[106] M. M. Murshed, R. X. Fischer and T. M. Gesing, *Z. Kristallogr.* **227** (8), (2012), 580–584.

[107] R. Gillespie and R. Nyholm, *Q. Rev. Chem. Soc.* **11** (4), (1957), 339–380.

[108] D. Lebellac, J. M. Kiat and P. Garnier, *J. Solid State Chem.* **114** (2), (1995), 459–468.

[109] T. Nanba, T. Miyaji, J. Takada, A. Osaka, Y. Miura and I. Yasui, *J. Non-Cryst. Solids* **177**, (1994), 131–136.

[110] N. Umesaki, T. M. Brunier, A. C. Wright, A. C. Hannon and R. N. Sinclair, *Physica B* **213**, (1995), 490–492.

[111] M. Ueno, M. Misawa and K. Suzuki, *Physica B & C* **120** (1-3), (1983), 347–351.

[112] A. C. Hannon, D. Di Martino, L. F. Santos and R. M. Almeida, *J. Phys. Chem. B* **111** (13), (2007), 3342–3354.

[113] A. Hannon and J. Parker, *Phys. Chem. Glasses* **43** (C; SPI), (2004), 6–12.

[114] L. Cervinka, J. Bergerova, V. N. Sigaev and F. Rocca, *J. Non-Cryst. Solids* **293**, (2001), 502–509.

[115] V. N. Bogdanov, A. V. Anan'ev, V. V. Golubkov, A. V. Golovnev, L. V. Maksimov, A. Y. Pakhnin, V. A. Solovyev, S. N. Smerdin, O. V. Yanush and B. Champagnon, *J. Phys. Conf. Ser.* **93**, (2007), 012033.

[116] E. Ghobadi, *Molecular Dynamics Simulation of Lead Germanate Glasses*, Ph.D. thesis (2008).

[117] S. J. L. Ribeiro, J. Dexpertghys, B. Piriou and V. R. Mastelaro, *J. Non-Cryst. Solids* **159** (3), (1993), 213–221.

[118] A. Witkowska, B. Sikora, K. Trzebiatowski and J. Rybicki, *J. Non-Cryst. Solids* **352** (40-41), (2006), 4356–4361.

[119] H. Yamamoto, K. Kamiya, J. Matsuoka and H. Nasu, *J. Ceram. Soc. Jpn.* **101** (9), (1993), 974–979.

[120] P. Ghigna, P. Mustarelli, C. Tomasi, E. Quartarone, M. Scavini, A. Speghini and M. Bettinelli, *J. Phys. Chem. B* **106** (38), (2002), 9802–9809.

[121] A. Witkowska, A. Madecka, K. Trzebiatowski, J. Dziedzic and J. Rybicki, *Rev. Adv. Mater. Sci.* **12** (2), (2006), 112–119.

[122] J. E. Canale, R. A. Condrate, K. Nassau and B. C. Cornilsen, *J. Can. Ceram. Soc.* **55**, (1986), 50–56.

[123] V. N. Sigaev, I. Gregora, P. Pernice, B. Champagnon, E. N. Smelyanskaya, A. Aronne and P. D. Sarkisov, *J. Non-Cryst. Solids* **279** (2-3), (2001), 136–144.

[124] J. Rybicki, A. Witkowska, G. Bergmanski, J. Bosko, G. Mancini and S. Feliziani, *Computational Methods in Science and Technology* **7** (1), (2001), 91–112.

[125] J. A. Topping, I. T. Harrower and M. K. Murthy, *J. Am. Ceram. Soc.* **57** (5), (1974), 209–212.

[126] J. A. Topping, *J. Am. Ceram. Soc.* **57** (10), (1974), 455–455.

[127] A. Y. Shashkov, V. A. Efremov, I. Matsichek, N. V. Rannev, Y. N. Venevtsev and V. K. Trunov, *Zh. Neorg. Khim+* **26** (3), (1981), 583–587.

[128] Y. I. Smolin, *Dokl. Akad. Nauk SSSR* **181**, (1968), 595–598.

[129] A. Y. Shashkov, N. V. Rannev and Y. N. Venevtsev, *Koordinats. Khim+* **10** (10), (1984), 1420–1426.

[130] F. Nishi, *Acta Crystallogr. C* **52**, (1996), 2393–2395.

[131] A. Y. Shashkov, N. V. Rannev and Y. N. Venevtsev, *Zh. Neorg. Khim+* **26** (11), (1981), 2926–2928.

[132] H. H. Otto, *Z. Kristallogr.* **149** (3-4), (1979), 197–205.

[133] Y. Z. Nozik, B. A. Maksimov, L. E. Fykin, V. Y. Dudarev, L. S. Garashina and V. T. Gabrielyan, *J. Struct Chem+* **19** (4), (1978), 628–630.

[134] Y. Xu, L. Y. Cheng, G. P. Zhou and Y. L. Wang, *Acta Crystallogr. E* **62**, (2006), I135–I137.

[135] Y. Iwata, *J. Phys. Soc. Jpn.* **43** (3), (1977), 961–967.

[136] Y. Iwata, N. Koyano and I. Shibuya, *J. Phys. Soc. Jpn.* **35** (4), (1973), 1269–1269.

[137] M. I. Kay, R. E. Newnham and R. W. Wolfe, *Ferroelectrics* **9** (1-2), (1975), 1–6.

[138] R. E. Newnham, R. W. Wolfe and C. N. W. Darlington, *J. Solid State Chem.* **6** (3), (1973), 378–383.

[139] T. Baikie, S. S. Pramana, C. Ferraris, Y. Z. Huang, E. Kendrick, K. S. Knight, Z. Ahmad and T. J. White, *Acta Crystallogr. B* **66**, (2010), 1–16.

[140] S. A. Ivanov, N. V. Rannev, A. A. Bush, A. I. Leichenko and Y. N. Venevtsev, *Kristallografiya+* **24** (2), (1979), 252–256.

[141] H. H. Otto, *Z. Kristallogr.* **149** (3-4), (1979), 227–240.

[142] K. Kato, K. Hirota, Y. Kanke, A. Sato, K. Ohsumi, T. Takase, M. Uchida, O. Jarchow, K. Friese and G. Adiwidjaja, *Z. Kristallogr.* **210** (3), (1995), 188–194.

[143] K. Kato, *Acta Crystallogr. B* **35** (Apr), (1979), 795–797.

Chapter 4

Experimental and Analytical Approach

4.1 Total scattering

The present section summarises the various functions and parameters used and referred to extensively in the results Chapters 5, 6 and 7. For detailed treatments of the theory of scattering of x-rays and neutrons by amorphous materials, and specifically application to diffraction experiments, see Fischer *et al.* [1] and references therein.

4.1.1 Correlation functions and scattering cross-sections

The number of atoms of type j in radial distance interval r to $r + \mathrm{d}r$, from an atom of type i, is defined by

$$n_{ij}(r) = 4\pi r^2 c_j \rho_0 g_{ij}(r)\mathrm{d}r = g_{ij}^{RDF}(r)\mathrm{d}r, \tag{4-1}$$

where ρ_0 is the average atomic number density, c_j is the fraction of atoms of type j present, and the $g_{ij}(r)$ are variously known as partial pair correlation functions or partial pair distribution functions (PPDFs). The partial radial distribution functions, $g_{ij}^{RDF}(r)$, are also defined. Note that the $g_{ij}(r) = \langle g_{ij}(\mathbf{r})\rangle_\Omega$ are averaged over all directions Ω of the interatomic vectors $\mathbf{r} = \mathbf{r}_{ij} = \mathbf{r}_j - \mathbf{r}_i$. The $g_{ij}(r)$ provide a convenient means of describing the structure of polyatomic amorphous materials, where, for a system of M atom types, there are $M(M+1)/2$ unique PPDFs, see for example Fig. 6-21. The $g_{ij}(r)$ are special cases of the generalised Van Hove [2] correlation functions, $G_{ij}(\mathbf{r}, t)$, for time differences $t = 0$.

In a total scattering diffraction experiment, energies of the scattered radiation are

not discriminated, and it is the differential cross-section of the material,

$$I(Q) = \frac{\mathrm{d}\sigma}{\mathrm{d}\Omega}(Q) = \int_{-\infty}^{\infty} \frac{\mathrm{d}\sigma}{\mathrm{d}\Omega \mathrm{d}\omega} \mathrm{d}\omega = I^S(Q) + i(Q), \tag{4-2}$$

which is measured. In equation 4-2, σ is the total cross-section, $\hbar\omega$ is the energy transfer during scattering, $\hbar\mathbf{Q} = \hbar(\mathbf{k}_i - \mathbf{k}_f)$ is the momentum transfer, with $\mathbf{k}_i$ and $\mathbf{k}_f$ the initial and final wave-vectors respectively. For an isotropic sample, only $|\mathbf{Q}| = Q$ need be considered and, for elastic scattering where $|\mathbf{k}_f| = |\mathbf{k}_i| = k = 2\pi/\lambda$, the scattering vector magnitude

$$Q = \frac{4\pi}{\lambda} \sin\theta, \tag{4-3}$$

where λ is the wavelength of the radiation, and 2θ is the scattering angle between vectors $\mathbf{k}_i$ and $\mathbf{k}_f$. Equation 4-2 has been split into *self*, $I^S(Q)$, and *distinct*, $i(Q)$, terms after Van Hove [2], where

$$I^S(Q) = \sum_i^M c_i \overline{f_i^2(Q)} \left(1 + P_l(Q, \theta, T, \ldots)\right) \tag{4-4}$$

and

$$i(Q) = \sum_i^M \sum_j^M c_i c_j f_i(Q) f_j(Q) \left(S_{ij}(Q) - 1\right) \equiv i^N(Q). \tag{4-5}$$

In equations 4-4 and 4-5, summations are over the M elemental species in the sample, the $f_i(Q)$ denote either atomic form factors for x-ray scattering or coherent neutron scattering lengths, conventionally denoted $\overline{b_i}$, where the overbar represents isotopic averaging over the sample for the ith element. The factor $P_l(Q, \theta, T, \ldots)$ is zero in the static approximation, which holds in the limit of large incident energy $\hbar\omega_i \gg \hbar\omega$. However, Placzek [3] corrections, $P_l(Q, \theta, T, \ldots)$, become necessary as energy transfers, $\hbar\omega$, become appreciable compared to the incident energies. In equation 4-5 the $S_{ij}(Q)$ are Faber-Ziman [4] partial structure factors, and note that $i(Q)$ has been equated to $i^N(Q)$, where N denotes neutron radiation. This latter distinction is made such that the distinct x-ray scattering can be formulated as

$$i^X(Q) = \frac{i(Q)}{\left(\sum_i^M c_i f_i(Q)\right)^2}, \tag{4-6}$$

where the denominator acts to 'sharpen' [5] the distinct scattering diffraction pattern by approximately dividing out the form factor dependence. No such procedure is necessary

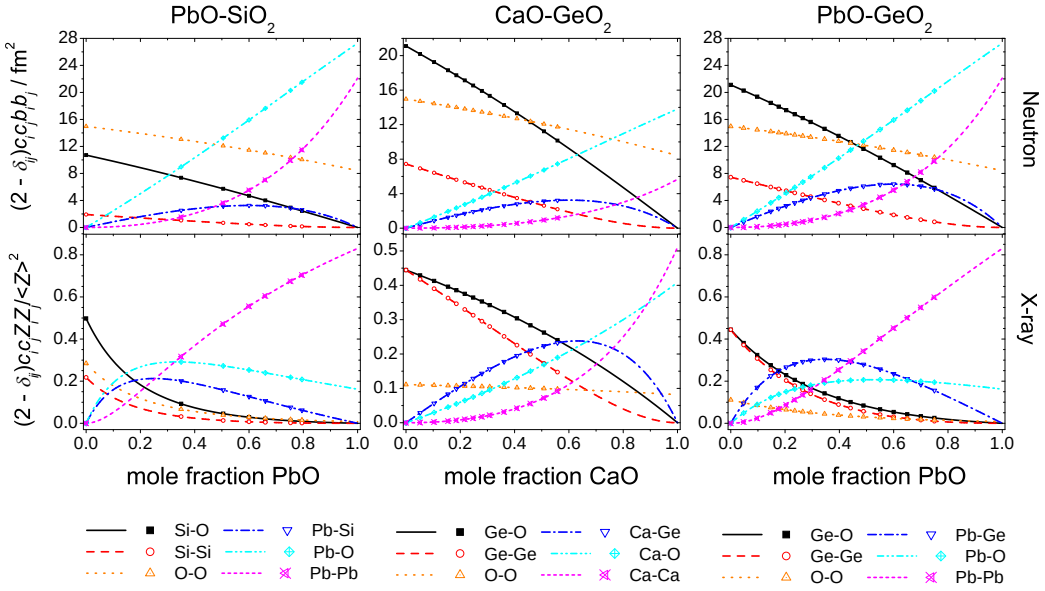

Figure 4-1 Neutron (upper) and x-ray (lower) pair weighting factors for the systems lead silicate, calcium germanate and lead germanate, as a function of molar composition. In the x-ray case the Q dependence has been removed by replacing the form factors, $f_i(Q)$, with atomic numbers, $Z_i \simeq f_i(Q = 0)$. The points indicate the glass compositions studied in this thesis, Tables 5-1, 6-2 and 7-1.

for neutron scattering, where, far from nuclear resonances, the $\overline{b_i}$ are independent of Q. For convenience the neutron (N) and x-ray (X) weighting factors are defined by

$$w_{ij}^N = c_i c_j \overline{b_i} \overline{b_j} \tag{4-7}$$

and

$$w_{ij}^X(Q) = \frac{c_i c_j f_i(Q) f_j(Q)}{\left(\sum_i^M c_i f_i(Q)\right)^2}. \tag{4-8}$$

The w_{ij}^N are plotted, for the materials of the present study, in Fig. 4-1, where the $\overline{b_i}$ are taken from Sears [6]. The free atom x-ray $f_i(Q)$ from Waasmaier and Kirfel [7] are used to calculate the $w_{ij}^X(Q)$, but to allow for comparison to w_{ij}^N, Fig. 4-1 shows the functions $w_{ij}^X(Q = 0)$. The factor $(2 - \delta_{ij})$, with δ_{ij} the Kronecker delta, has been included in Fig. 4-1 such that the values plotted are appropriate to the $M(M + 1)/2 = 6$ unique partial structure factors, rather than the total $M^2 = 9$ terms. The functions

$$S_{ij}(Q) = S_{ji}(Q) = 1 + \frac{1}{c_i c_j} \sum_{\alpha}^{N_i} \sum_{\beta \neq \alpha}^{N_j} e^{i\mathbf{Q}\cdot\mathbf{r}_{\alpha\beta}} = 1 + \frac{1}{c_i c_j} \sum_{\alpha}^{N_i} \sum_{\beta \neq \alpha}^{N_j} \frac{\sin\left(r_{\alpha\beta} Q\right)}{r_{\alpha\beta} Q} \tag{4-9}$$

are sums over scattered wave intensities, with Greek letters denoting atomic sites in the material and N_i are the number of atoms of element i. The latter equality in equation 4-9

holds for isotropic samples where averaging over all relative orientations of interatomic vectors, $\mathbf{r}_{\alpha\beta}$, and scattering vectors, $\mathbf{Q}$, can be made [1]. The distributions of interatomic vectors between elements of type i and j are given by the $n_{ij}(r)$ of equation 4-1*, and therefore the summations over α and β in equation 4-9 can be replaced by an integral

$$S_{ij}(Q) - 1 = 4\pi\rho_0 \int_0^\infty r^2 \left(g_{ij}(r) - 1\right) \frac{\sin(rQ)}{rQ} \mathrm{d}r \tag{4-10}$$

which explicitly relates the reciprocal-space and real-space functions of interest by sine Fourier transform (FT). The inverse FT is written

$$g_{ij}(r) - 1 = \frac{1}{2\pi^2\rho_0} \int_0^\infty Q^2 \left(S_{ij}(Q) - 1\right) \frac{\sin(rQ)}{rQ} \mathrm{d}Q, \tag{4-11}$$

and, by analogy to equation 4-5, the summed correlation function for neutron diffraction can be written

$$G^N(r) = \sum_i^M \sum_j^M c_i c_j \overline{b_i b_j} \left(g_{ij}(r) - 1\right) \tag{4-12}$$

which must be generalised for x-rays to

$$G^R(r) = \sum_i^M \sum_j^M k_{ij}^R(r) \otimes \left(g_{ij}(r) - 1\right) \tag{4-13}$$

where $\otimes$ is the convolution operator and the

$$k_{ij}^R(r) = \frac{1}{\pi} \int_0^\infty w_{ij}^R(Q) \cos(rQ)\, \mathrm{d}Q \tag{4-14}$$

are the FTs of the pair weighting functions in equations 4-7 or 4-8, with $R = N$ or X. The real space function used most often in this thesis is

$$T^R(r) = 4\pi r\rho_0 G^R(r) + T^{R,0}(r) = 4\pi r\rho_0 \sum_i^M \sum_j^M \frac{1}{c_j} k_{ij}^R(r) \otimes g_{ij}(r) \tag{4-15}$$

with

$$T^{N,0}(r) = 4\pi r\rho_0 \left(\sum_i^M c_i \overline{b_i}\right)^2 \tag{4-16}$$

and

$$T^{X,0}(r) = 4\pi r\rho_0. \tag{4-17}$$

$T^R(r)$ is used as a convenient compromise between other commonly used functions such as $G^R(r)$ which, by comparison, suppresses high r structure, and the RDF, which

*For convenience, $r_{\alpha\beta} = r$.

includes an additional factor of r, and thereby suppresses low r structure. Furthermore, symmetric distributions of interatomic distances remain symmetric in $T^R(r)$. Unfortunately there are no universally accepted conventions in total scattering, see Keen [8] for a disambiguation of various formalisms. Finally, $T^R(r)$ can be directly defined in terms of the interference functions $Qi^R(Q)$ by

$$T^R(r) = T^{R,0}(r) + \frac{2}{\pi}\int_0^\infty Qi^R(Q)\sin(rQ)\,\mathrm{d}Q \equiv T^{R,0}(r) + D^R(r), \tag{4-18}$$

and $T^R(r)$ and $D^R(r)$ are referred to respectively as the *total* and *differential* correlation functions. A final caveat to be made is that all of the functions used in the present thesis are defined either *per atom*, in the case of neutron scattering, or *per electron* in the case of x-ray scattering.

4.1.2 Coordination numbers

Partial coordination numbers, $n_{ij}(r_1, r_2)$, are the number of atoms of type j within a radial distance window, $\Delta r = r_2 - r_1$, of an atom of type i and can be calculated directly from the $g_{ij}(r)$ using

$$n_{ij}(r_1, r_2) = 4\pi c_j \rho_0 \int_{r_1}^{r_2} r^2 g_{ij}(r)\mathrm{d}r = \frac{c_j}{c_i} n_{ji}(r_1, r_2) \tag{4-19}$$

where the second equality states the general relationship between n_{ij} and n_{ji}. For a given interatomic bond of mean length $\bar{r}_{ij}$ between atoms of type i and j in a material, at any given instance in time there will be a distribution of instantaneous interatomic distances, which, in the harmonic approximation, will be Gaussian. Such a distribution has a reciprocal-space manifestation in the measured distinct scattering of the form

$$i_{ij}^R(Q) = n'_{ij} w_{ij}^R \frac{\sin\left(\bar{r}_{ij}Q\right)}{c_i \bar{r}_{ij} Q} \exp\left(\frac{-\langle u_{ij}^2\rangle Q^2}{2}\right) \tag{4-20}$$

with $\langle u_{ij}^2\rangle^{1/2}$ the root-mean-square (RMS) deviation from the mean value, $\bar{r}_{ij}$. The number n'_{ij} is subtly different from $n_{ij}(r_1, r_2)$ above because it relates specifically to a Gaussian distribution which may simply be a component of the $g_{ij}(r)$. In particular

$$n'_{ij} = \frac{\bar{r}_{ij} A_{ij}^R c_j \int_0^\infty \mathrm{d}Q}{\left(2 - \delta_{ij}\right)\int_0^\infty w_{ij}^R(Q)\mathrm{d}Q} = \frac{c_j}{c_i} n'_{ji}, \tag{4-21}$$

which, for neutrons reduces to

$$n'_{ij} = \frac{\bar{r}_{ij} A_{ij}^N}{\left(2 - \delta_{ij}\right) c_i \overline{b_i b_j}}. \tag{4-22}$$

In equations 4-21 and 4-22, A_{ij}^{R} is the integrated area of a symmetric Gaussian peak, obtained, for example, by fitting to a region of $T^{R}(r)$ assigned to a particular *unique* partial pair term $4\pi r\left(2-\delta_{ij}\right)\rho_0 k_{ij}^{R}(r)\otimes g_{ij}(r)$ or $4\pi r\rho_0\left(2-\delta_{ij}\right)c_i c_j\overline{b_i b_j}g_{ij}(r)$ for neutrons.

4.1.3 Practical considerations

In reality, the integrals in equations 4-11, 4-14, 4-18 and 4-21 cannot be evaluated to infinite values of Q, rather there is a maximum attainable $Q \equiv Q_{max}$. This limit introduces truncation oscillations into the real-space functions obtained by FT of the experimental distinct scattering. Specifically, the differential correlation function obtained from experiment is

$$\tilde{D}^{R}(r) = \frac{2}{\pi}\int_{Q_{min}}^{Q_{max}} Qi^{R}(Q)M(Q)\sin(rQ)\,\mathrm{d}Q \tag{4-23}$$

where $M(Q)$ is a modification function. The consequence of truncation is that

$$M(Q) = \begin{cases} 1, & \text{if } |Q| \leq Q_{max} \\ 0, & \text{otherwise.} \end{cases} \tag{4-24}$$

Therefore $\tilde{D}^{R}(r)$ is convolved with the FT of equation 4-24, a sinc function. The truncation effects due to this convolution can be suppressed if a suitable form for $M(Q)$ is chosen, and the form used throughout this thesis is that due to Lorch [9]:

$$M(Q) = \begin{cases} \frac{\sin(\pi Q/Q_{max})}{\pi Q/Q_{max}}, & \text{if } |Q| \leq Q_{max} \\ 0, & \text{otherwise.} \end{cases} \tag{4-25}$$

Such modification greatly reduces the truncation oscillations, at the expense of some real-space resolution. The real-space resolution, or peak function is defined, for neutrons, by

$$L(r) = \frac{1}{\pi}\int_{0}^{\infty} M(Q)\cos(rQ)\,\mathrm{d}Q \tag{4-26}$$

or for x-rays, by

$$P_{ij}^{X}(r) = \frac{1}{c_i c_j}k_{ij}^{X}(r)\otimes L(r), \tag{4-27}$$

and these must be convolved, for example, with any (Gaussian) distributions (§4.1.2) fitted to the experimental $\tilde{T}^{R}(r) = \tilde{D}^{R}(r) + T^{R,0}(r)$, see for example Fig. 5-11.

4.1.4 Data collection and reduction

The present section summarises the methods used for diffraction data collection and reduction to obtain the distinct scattering functions $i^R(Q)$, equations 4-5 and 4-6. Typical experimental conditions are described, with details specific to certain samples given in the relevant Chapters 5, 6 and 7.

4.1.4.1 Neutron diffraction

Time-of flight neutron diffraction measurements were made using the GEM [10] diffractometer at the ISIS Facility, Rutherford Appleton Laboratory, UK. This instrument has a large number of detectors which cover a large solid angle, and therefore offers high count rates over a large portion of reciprocal space. Glass samples were typically held in thin-walled vanadium cans inside the evacuated sample tank through which the incident neutron beam passed. The beam cross section was 40×15 mm^2, larger than the diameter, but shorter than the height of the cylindrical sample. Data were acquired typically for $\sim$1000 µA h of proton beam current, corresponding to approximately 6 to 7 hours of counting time per sample. This yielded sufficient statistics to justify use of a maximum scattering vector of $Q_{max} = 40.0$ Å^{-1} for Fourier transform. Measurements were also performed on empty vanadium cans, the empty instrument, and an 8.34 mm vanadium rod for normalisation purposes and to allow for subtraction of background signals. Corrections for absorption, multiple scattering, inelasticity effects, backgrounds, normalisation and reduction of the measured data to obtain $i^N(Q)$ were performed using the GudrunN [11] software and the Atlas [12] suite of programs. A quadratic fitted to $i^N(Q)$ for $0.45 = Q_{min} \leq Q \leq 0.7$ Å^{-1} was used to extrapolate back to $Q = 0$. Results of measurements of an 8 mm diameter silica glass rod (no V can required) and vitreous GeO_2 are presented in Appendix B. The SiO_2 and GeO_2 glasses act as measurement standards, illustrating the highly accurate coordination numbers that can be extracted, whilst also providing useful comparisons, as the end members of the binary glass systems studied herein.

4.1.4.2 X-ray diffraction

Wiggler beamline BW5 [13, 14] on the DORIS III synchrotron, HASYLAB at DESY, was used for x-ray diffraction measurements of glasses, which were held inside 1.5 mm

diameter silica glass capillaries (10 μm wall thickness). Measurements of an empty capillary and the empty instrument were made to allow removal of background scattering. The white beam, which has a polarisation factor of 0.92, was monochromated with a SiGe-gradient crystal to an energy of ~85 keV (wavelength ~0.146 Å), calibrated by measurement of a lanthanum hexaboride standard. The beam profile was 2×2 mm^2, chosen to be larger than the sample diameter. The x-ray energy was optimised so as to minimise the photoelectric absorption cross-section whilst avoiding fluorescence associated with the Pb K-edge at 88.0045 keV [15]. Use of such high energy x-rays also makes accessible a large $Q_{max} \simeq 23.6\,\text{Å}^{-1}$ at the maximum scattering angle of the detector arm which is 32.0°. The corresponding minimum scattering angle was 0.5° ($Q_{min} \simeq 0.4\,\text{Å}^{-1}$). The data were collected in three angular ranges using either different in-beam attenuators, or different pre-detector slit widths. These ranges were $0.5 \leq 2\theta \leq 8.0°$, $7.0 \leq 2\theta \leq 17.0°$ and $16.0 \leq 2\theta \leq 32.0°$ (no in-beam attenuation), with a step size of $\Delta 2\theta = 0.05°$. This was to ensure that the count rate in the Ge detector did not greatly exceed 5×10^4 counts per second. All sets of data were combined after omission of bad points, dead-time correction ($\tau = 2.3\,\mu$s), normalisation to the incident beam monitor counts, correction for the geometrical arrangement of the detector and sample and scaling as required for datasets for which different levels of in-beam attenuation, or pre-detector slit widths, were used. At this point the program GudrunX [11, 16] was used to correct the data for the effects of polarisation, absorption and multiple scattering, removal of backgrounds, normalisation using the Krogh-Moe [17] and Norman [18] method, and extraction of $i^X(Q)$ by removal of the self-scattering (including the Compton fraction) and sharpening. A small residual background, slowly varying with Q, was removed using the top-hat convolution method [16, 19]. Fig. 4-2 illustrates some of the stages of data reduction for the extreme case of $80\,\text{PbO} \cdot 20\,\text{SiO}_2$ glass which is highly absorbing owing to the very high Pb content. Fig. 4-2a compares $I^X(2\theta) = I^{S,X}(2\theta) + i^X(2\theta)$ to the self scattering term, $I^{S,X}(2\theta)$, which includes the Compton (inelastically) scattered fraction, showing small deviations at high Q. The differences between functions with and without top-hat convolution background subtraction are illustrated after self-scattering subtraction and sharpening (Fig. 4-2b), Q multiplication (Fig. 4-2c) and FT (Fig. 4-2d). It is clear that the effects of background removal are essentially aesthetic only, ensuring that $i^X(Q)$ has the correct high Q limit,

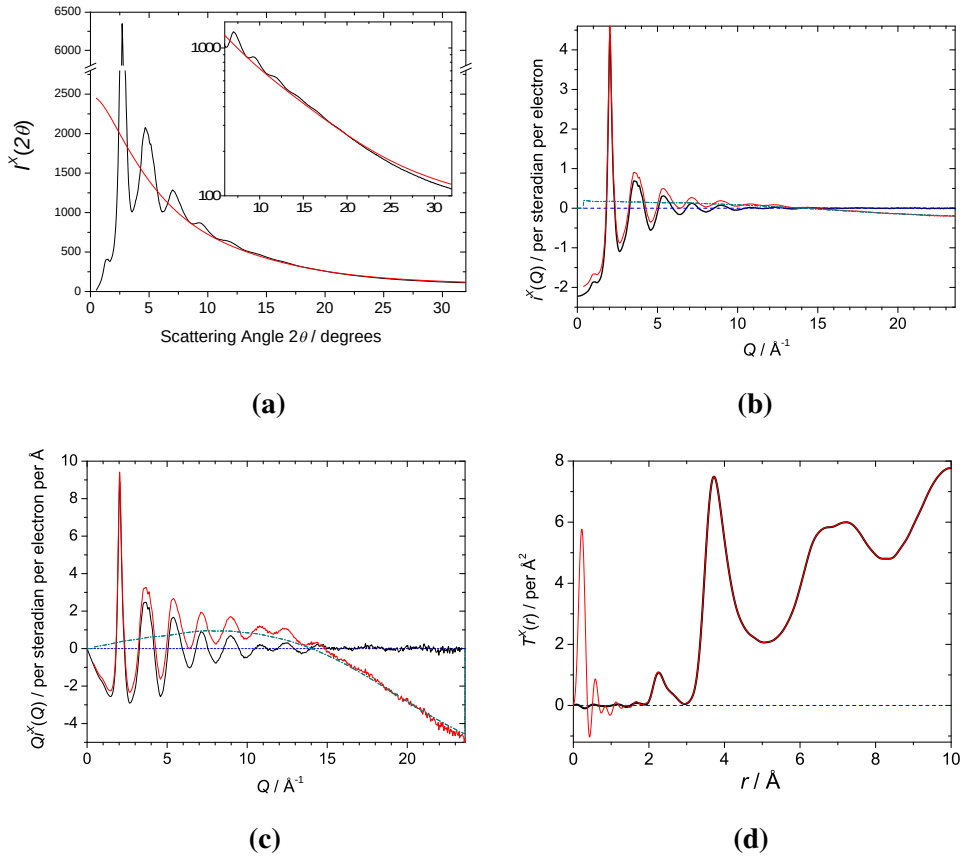

Figure 4-2 Differences between x-ray scattering functions from an $80\,PbO \cdot 20\,SiO_2$ glass, obtained with and without the top-hat convolution method [16, 19]. Part (a) shows the total scattering cross-section (black line) and the self-scattering, including Compton fraction (red line). Note the break in scale. Inset are the same functions on a $\log_{10}$ scale. Part (b) shows the distinct scattering functions (total cross-section minus the self-scattering followed by sharpening) with (black line) and without(red line) the top-hat convolution method applied (top-hat width of $6\,\text{Å}^{-1}$). The result of convolving the latter with the top-hat function is also shown (green dash dot line). Part (c) shows the functions of part (b) multiplied by Q. Part (d) shows the total correlation functions obtained by Fourier transformation of the interference functions shown in part (c), using a Lorch [9] modification function and $Q_{max} = 23.6\,\text{Å}^{-1}$ (the thick black line is the result of the top-hat convolution method).

and oscillates about zero, and the low r oscillations, below the first (Si-O) correlation are smoothed, without affecting the important structural information at higher r. Samples of commercial amorphous silica and GeO_2 glass were measured as standards and the results are presented in Appendix B.

4.2 Empirical potential structure refinement

EPSR [20] is a method for generating physically reasonable atomistic models of condensed amorphous systems which are consistent with total scattering measurements. It is related to the RMC [21] method, but distinct in that it is based on a Monte Carlo simulation using interatomic pair-potentials, with the constraints from the diffraction data imposed as a perturbation on the starting reference potentials. The various constraints that must be imposed during RMC modelling in order to ensure physically plausible models are therefore naturally included in EPSR by way of the reference potential. For simplicity and the small number of free parameters, the reference pair potentials used here are based on Lennard-Jones (LJ) plus Coulomb terms:

$$U_{ij}^{LJ+C}(r) = 4\epsilon_{ij}\left[\left(\frac{\sigma_{ij}}{r}\right)^{12} - \left(\frac{\sigma_{ij}}{r}\right)^{6}\right]\Lambda_{LJ}(r) + \frac{q_i q_j}{4\pi\epsilon_0 r}\Lambda_C(r), \tag{4-28}$$

with Lorentz-Berthelot mixing rules: $\epsilon_{ij} = \sqrt{\epsilon_i \epsilon_j}$ and $\sigma_{ij} = (\sigma_i + \sigma_j)/2$, and ϵ_0 the permittivity of free space. The terms of equation 4-28 are smoothly truncated to reduce calculation times, using

$$\Lambda_{LJ}(r) = \begin{cases} 1, & \text{if } r \leq r_l \\ \frac{1}{2}\left[1 + \cos\pi\left(\frac{r-r_l}{r_u-r_l}\right)\right], & \text{if } r_l < r < r_u \\ 0, & \text{otherwise,} \end{cases} \tag{4-29}$$

for LJ terms, and

$$\Lambda_C(r) = \left(1 - \frac{r}{r_u}\right)^4 \left(1 + \frac{8r}{5r_u} + \frac{2r^2}{5r_u^2}\right)\Theta(r_u - r) \tag{4-30}$$

for the Coulomb terms, where $\Theta(r_u - r)$ is the Heaviside step function. The cut-offs r_l and r_u are typically chosen to be 9 and 12 Å respectively, although larger values (12 and 16 Å) have been used in the present work, where stated. Intramolecular potential energies are defined by [22]

$$U_{ij}^{IM}(r) = C\frac{\left(r - \overline{d}_{ij}\right)^2}{2\overline{d}_{ij}}\sqrt{\mu_{ij}}, \tag{4-31}$$

where C is a constant, $\overline{d}_{ij}$ is the mean intramolecular separation for the given i, j pair and $\mu_{ij} = M_i M_j/(M_i + M_j)$ is their reduced mass. In addition to the terms thus far defined, contributions to the potential energy of the form [22, 23]

$$U_{ij}^{min}(r) = K_{ij}\exp\left(\frac{1}{\gamma}\left(r_{ij}^{min} - r\right)\right) \tag{4-32}$$

can also be included, where the constants K_{ij} are derived from the degree of atomic overlap (varies between MC iterations), and act to introduce minimum distances of approach for i, j pairs, r_{ij}^{min}. In the present work $\gamma = 0.3$ was chosen, and determines the hardness of the repulsive interaction. The total energy of the model system is then the sum over all atomic pair (α,β) potential energies,

$$U(r) = \sum_{\alpha}\sum_{\beta\neq\alpha}\sum_{i}\sum_{j} U_{ij}^{LJ+C}(r) + U_{ij}^{IM}(r) + U_{ij}^{min}(r) + U_{ij}^{EP}(r), \tag{4-33}$$

where $U_{ij}^{EP}(r)$ are the empirical potential terms derived from the differences between model and measured distinct scattering patterns, as described by Soper [20]. The goodness-of-fit can be characterised by the EPSR R-factor,

$$R = \frac{1}{N_d}\sum_{k=1}^{N_d}\frac{1}{N_{Q_k}}\sum_{Q_{min_k}}^{Q_{max_k}}\left(i_k(Q) - i_k^{mod}(Q)\right)^2, \tag{4-34}$$

where N_d is the number of datasets, N_{Q_k} is the number of Q values for the kth dataset and $i_k^{mod}(Q)$ is the model for the kth dataset, $i_k(Q)$.

4.3 General characterisation techniques

The following sections describe typical conditions under which various sample properties were measured, whilst any atypical conditions are stated in the results Chapters 5, 6, 7, as necessary.

4.3.1 Thermal analysis

Differential thermal analysis (DTA) is based on the measurement of temperature differences between a material of interest and a reference material whilst they are simultaneously heated (or cooled) within the same furnace. Therefore any changes in heat capacity, exo- or endothermic phase transitions can be measured either isothermally or during a controlled temperature-time profile. DTA measurements presented herein were performed using a pair of Stanton Redcroft (DTA 673-4) differential thermal analysis instruments, capable of reaching maximum temperatures of 1200 °C or 1500 °C respectively. 100 mg of powdered glass sample and 100 mg of Al_2O_3 reference powder were placed inside the furnace chambers in Pt/Rh crucibles and subjected to heating

from room temperature at a rate of 10 °C min^{-1}. Although all exothermic crystallisation events and endothermic melting events were recorded, here only the glass transition temperatures are quoted, as a means of sample characterisation, for comparison to values in the literature, and for tracking changes in T_g as a function of glass composition, which can be related to structural changes in the glasses/supercooled melts. T_g was determined as in Fig. 2-1b, by the intersection of linear extrapolations of the data below the specific heat step, and of its slope.

4.3.2 Energy dispersive x-ray spectroscopy

Glass composition was measured using energy dispersive x-ray spectroscopy (EDX) in a Zeiss SUPRA 55-VP field emission gun scanning electron microscope (FEGSEM) operating at an accelerating voltage of 20 kV. Samples were mounted on aluminium stubs using an organic silver paste and carbon coated using a vacuum evaporator to provide conduction pathways and avoid surface charging of the glass. EDX spectra were collected over 100 s exposure times at various points on the surface of a number of different glass pieces. Quantification of the glass composition was based on the integrated intensities of either the Ca K and Ge K, Si K and Pb L or Ge K and Pb L lines of the spectra after background subtraction and correction for Z dependent electron backscatter and stopping power, absorption and fluorescence, collectively known as ZAF correction, using the EDAX Genesis software which employs internal standards.

4.3.3 Density measurement

Sample volumes were measured by helium pycnometry in a Micromeritics Accupyc 1330 pycnometer and combined with mass measurements on the same sample volume in order to calculate the mass densities, ρ_m. Calibration was performed prior to each set of measurements using steel spheres of certified volume. Furthermore, measurements of a silica glass rod standard were made periodically to check for drift. The ρ_m obtained were used to derive molar volumes, V_M, and atomic number densities, ρ_0, knowledge of which is important for estimating the number of atoms illuminated by the beam in scattering experiments, and provide limiting values for the scattering equations, §4.1, as well as providing vital constraints on empirical (EPSR) structural models.

References

[1] H. E. Fischer, A. C. Barnes and P. S. Salmon, *Rep. Prog. Phys.* **69** (1), (2006), 233–299.

[2] L. Van Hove, *Phys. Rev.* **95** (1), (1954), 249–262.

[3] G. Placzek, *Phys. Rev.* **86** (3), (1952), 377–388.

[4] T. Faber and J. Ziman, *Philos. Mag.* **11** (109), (1965), 153–173.

[5] C. Finbak, *Acta Chem. Scand.* **3** (10), (1949), 1279–1292.

[6] V. F. Sears, *Neutron News* **3** (3), (1992), 26–37.

[7] D. Waasmaier and A. Kirfel, *Acta Crystallogr. A* **51**, (1995), 416–431.

[8] D. A. Keen, *J. Appl. Cryst.* **34**, (2001), 172–177.

[9] E. Lorch, *J. Phys. C Solid State* **2**, (1969), 229.

[10] A. C. Hannon, *Nucl. Instrum. Meth. A* **551** (1), (2005), 88–107.

[11] A. K. Soper, *Rutherford Appleton Laboratory Technical Report, RAL-TR-2011-013*, Tech. rep. (2011).

[12] A. C. Hannon, W. S. Howells and A. K. Soper, *Inst. Phys. Conf. Ser.* (107), (1990), 193–211.

[13] R. Bouchard, D. Hupfeld, T. Lippmann, J. Neuefeind, H. B. Neumann, H. F. Poulsen, U. Rutt, T. Schmidt, J. R. Schneider, J. Sussenbach and M. von Zimmermann, *J. Synchrotron Radiat.* **5**, (1998), 90–101.

[14] H. F. Poulsen, J. Neuefeind, H. B. Neumann, J. R. Schneider and M. D. Zeidler, *J. Non-Cryst. Solids* **188** (1-2), (1995), 63–74.

[15] J. A. Bearden and A. F. Burr, *Rev. Mod. Phys.* **39** (1), (1967), 125–142.

[16] A. K. Soper and E. R. Barney, *J. Appl. Cryst.* **44**, (2011), 714–726.

[17] J. Krogh-Moe, *Acta Cryst.* **9** (10), (1956), 951–953.

[18] N. Norman, *Acta Cryst.* **10** (5), (1957), 370–373.

[19] A. K. Soper, *Mol. Phys.* **107** (16), (2009), 1667–1684.

[20] A. K. Soper, *Phys. Rev. B* **72** (10), (2005), 104204.

[21] R. L. McGreevy, *J. Phys. Condens. Mat.* **13** (46), (2001), R877–R913.

[22] A. K. Soper, *J. Phys. Condens. Mat.* **23** (36), (2011), 365402.

[23] A. K. Soper, *J. Phys. Condens. Mat.* **22** (40), (2010), 404210.

Chapter 5

Calcium Germanate Glasses

5.1 Sample preparation and characterisation

5.1.1 Glass preparation

Glasses in the $x\mathrm{CaO} \cdot (1-x)\mathrm{GeO_2}$ system were prepared by rapid twin-roller quenching of the liquid melts at Coe College, Cedar Rapids, IA 52402, USA. $\mathrm{CaCO_3}$ (Sigma-Aldrich, $\geq$ 99.0%) and $\mathrm{GeO_2}$ (Alfa Aesar, 99.98%) powders were mixed in 20 $\mathrm{cm^3}$ platinum crucibles in sufficient quantities to yield 5 g of glass with molar compositions shown in Table 5-1. The crucibles were placed into an electric furnace and held, in most cases, at a temperature of 1450 °C. This temperature was judged to be sufficiently above the liquidus line of the equilibrium phase diagram [1] for all compositions, except those for which $x = 0.50$ and 0.55, which were melted at 1500 °C and the $x = 0.05$ melt which was remelted at the same temperature, being too highly viscous to pour from the crucible at 1450 °C. No compositions beyond $x = 0.55$ were attempted on account of the rapidly rising liquidus. After 20 minutes, crucibles were removed from the furnace and weighed in order to confirm sufficient mass loss to account for the evolution of all carbon, in the form of $\mathrm{CO_2}$ gas. CaO is highly refractory and so any additional mass loss was assumed to be due to volatilisation of $\mathrm{GeO_2}$. The resultant glass compositions calculated under this assumption are given in Table 5-1. After weighing, crucibles were returned to the furnace for a further 10 minutes. The melts were poured into a 30 µm gap between two steel cylinders counter-rotating at 590 rpm, resulting in a cooling rate of order 10^5 °C $\mathrm{s^{-1}}$ [2]. Table 5-2 records observations made during vitrification of the melts, including of the inertially cooled material remaining in the crucible, and of crystalline phases formed in the roller quenched products, identified later by diffraction. From these initial observations, the 27 and 30 mol% CaO glasses appear to be the most stable, based on their vitrification under inertial cooling, with

Table 5-1 Measured mass and number densities, molar volumes, glass transition temperatures and compositions for calcium germanate glasses. Uncertainties in parentheses.

Glass Composition in mol% CaO			ρ_m	ρ_0	V_M	T_g
Nominal	Mass Loss[†]	EDX	g cm^{-3}	nm^{-3}	cm^3 mol^{-1}	°C
0	-	-	3.650(37)	63.05(63)	28.65(29)	-
5	5.19(2)	4.91(68)	3.775(38)	65.67(66)	27.03(27)	-
10	10.35(3)	12.14(3.87)	3.842(38)	67.31(67)	25.91(26)	673(5)
15	15.48(4)	14.96(3.14)	3.987(40)	70.38(70)	24.34(24)	665(7)
18	18.55(4)	19.27(88)	4.020(40)	71.28(71)	23.78(24)	665(6)
21	21.66(6)	21.57(16)	4.116(41)	73.34(73)	22.86(23)	672(3)
24	24.75(7)	24.09(37)	4.206(42)	75.30(75)	22.01(22)	677(3)
27	27.95(12)	27.74(43)	4.270(43)	76.86(77)	21.32(22)	684(3)
30	30.84(10)	30.54(36)	4.256(43)	76.97(77)	21.06(21)	685(3)
35	36.12(14)	35.40(24)	4.178(42)	76.27(77)	20.84(21)	684(3)
40	40.87(14)	40.34(42)	3.992(40)	73.49(74)	21.23(22)	676(3)
45	45.85(17)	45.60(20)	3.951(40)	73.43(74)	20.84(21)	-
50	50.83(18)	49.88(22)	3.800(38)	71.34(72)	21.03(22)	-
55	55.80(19)	55.94(69)	3.765(38)	71.42(72)	20.59(21)	-

[†] Assuming volatilisation of the GeO_2 component.

compositions either side displaying recalescence associated with the exothermic crystallisation of the supercooled melt. For compositions below 21 mol% CaO, opalescence was observed, indicative of glass-in-glass phase separation on a length scale of order 0.1 to 1 µm, capable of scattering visible light. Phase separation has previously been observed in CaO–GeO_2 [5–7] as well as other alkaline earth and M^{2+} containing germanate glasses [5–8], with a stable region of immiscibility reported [1, 6] above the liquidus, between about 5 and 15 mol% CaO, see also § 3.1.1.

5.1.2 Density measurement

Mass densities of the roller quenched CaO–GeO_2 glasses are recorded in Table 5-1 and plotted for comparison with literature data in Fig. 5-1. The mass density passes through a maximum, a hallmark of the germanate anomaly, between 27 and 30 mol% CaO. The three glass densities, close to the maximum, measured by Kamiya *et al.* [9] are in good agreement with those of the present study. The density data of Margaryan and Wai [10] also display a maximum at approximately the same glass composition, but the densities are systematically lower than those measured for the roller quenched series. The earlier measurements made by Margaryan and Narekatsyan [11] are mostly in accord with

Table 5-2 Observations of phase-separation, recalescence and crystalline inclusions in the production of calcium germanate glasses. Crystalline phases were identified by diffraction.

Nominal mol% CaO	Roller quenched glass	Inertially cooled	Crystal phase
5	Some close to clear glass. Last part of highly viscous melt through quencher appeared white, separated out	Opalescent, vitrified	-
10	As for 5 mol% CaO	Opalescent, vitrified	Quartz GeO_2 [3]
15	Mostly clear glass, cloudy regions separated out	Opalescent, recalescence	None
18	Mostly clear glass, cloudy regions separated out	Opalescent, recalescence	None
21	Almost entirely clear glass, small amount of cloudiness	Recalescence	None
24	Clear glass	Recalescence	None
27	Clear glass	Vitrified	None
30	Clear glass	Vitrified	None
35	Clear glass	Recalescence	None
40	Clear glass	Recalescence	None
45	Some clear glass, white pieces separated	-	$CaGeO_3$ Wollastonite [4]
50	Clear glass with many white inclusions	-	$CaGeO_3$ Wollastonite [4]
55	Mostly clear glass, small amount of cloudiness	-	$CaGeO_3$ Wollastonite [4]

those of the present study, other than for their two lowest CaO content compositions. A possible reason for the discrepancies may be the compositional changes arising due to volatilisation of GeO_2 from the melt. These depend strongly on the melting conditions, such as melt surface area and partial vapour pressures within the furnace, and may have been exacerbated by the use of an argon atmosphere [10, 11]. Of further note are the measurements made by Kasymova [12] on strontium and barium germanate glasses, both of which show broad maxima at the same position (30 mol% AeO) as found for the calcium germanate series.

5.1.3 Energy dispersive x-ray spectroscopy

EDX measurements of the glass composition based on the Ca K and Ge K lines of the spectra are presented in Table 5-1 and Fig. 5-2. These are in quantitative agreement with

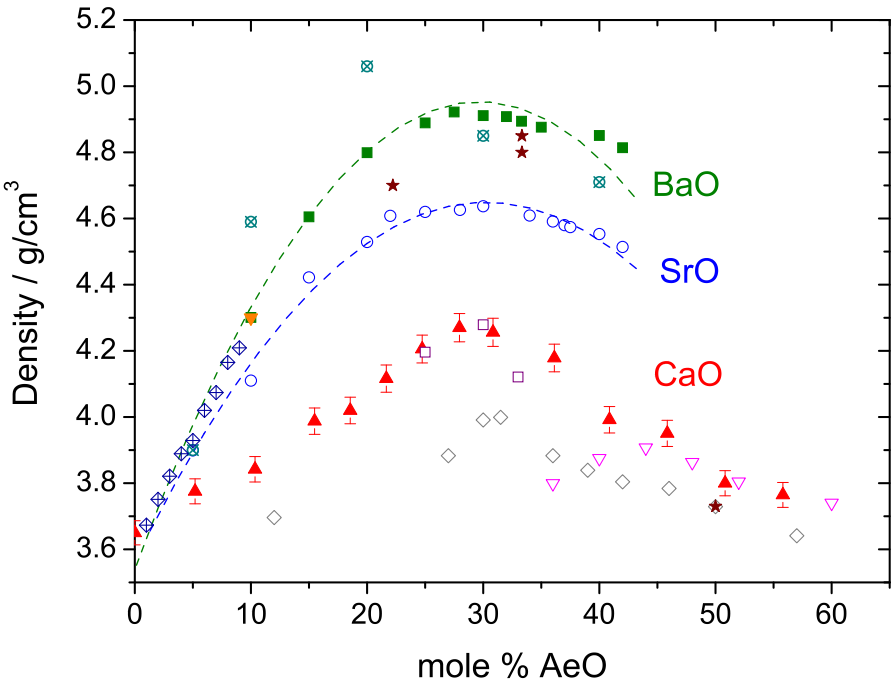

Figure 5-1 Alkaline earth germanate mass densities as a function of glass composition. $CaO-GeO_2$ system: Filled red triangles - this study, open squares - Kamiya *et al.* [9], open diamonds - Margaryan and Wai [10], open triangles - Margaryan and Narekatsyan [11]. $SrO-GeO_2$ system: Open blue circles - Kasymova [12]. $BaO-GeO_2$ system: Closed green squares - Kasymova [12], open diamonds with crosses - Shelby [8], open circles with crosses - Pernice *et al.* [13], filled orange triangle - Inaba *et al.* [14]. Lines are guides to the eye. See also Fig. 5-14 for the corresponding number densities and molar volumes. Densities of $CaO-GeO_2$ crystals (Table 3-2) are shown as filled stars.

estimations based on the mass loss from the melts, supporting the notion that the glasses are calcium rich with respect to their nominal compositions, and therefore the assumption of preferential volatilisation of the GeO_2 component during melting. Also shown in Fig. 5-2 are the results from the individual EDX measurements. These highlight the fact that, for the 10 and 15 mol% CaO glasses in particular, there is inconsistency between some measurements. This suggests that there may be compositional inhomogeneities present of comparable size to the interaction volume from which the characterisitic x-rays are generated. For 20 keV electrons this volume is large, and estimated to be of the order 1 μm in diameter using the Monte Carlo software CASINO [15], for the K edge x-rays of Ca and Ge, and approximately independent of $CaO-GeO_2$ glass composition.

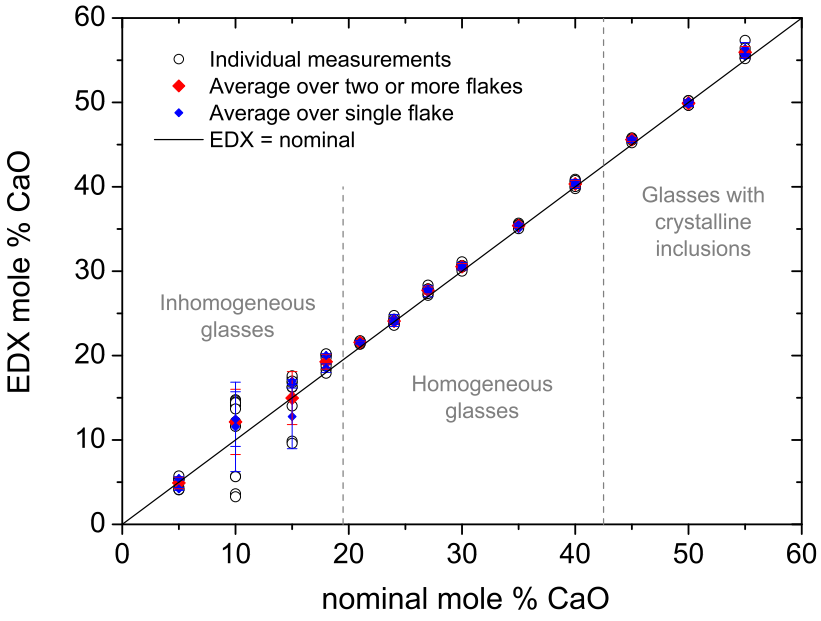

Figure 5-2 Calcium germanate glass compositions, as measured by EDX, as a function of nominal glass composition. Results from individual measurements are shown (open circles) along with averages from single flakes of glass (small blue diamonds) and averages over several flakes of the same nominal composition (large red diamonds). The straight line denotes the ideal, with EDX measured composition equal to nominal composition.

5.1.4 Thermal analysis

Glass transition temperatures measured by DTA are displayed in Table 5-1 and Fig. 5-3. These clearly show a maximum at around 30 mol% CaO, another manifestation of the germanate anomaly. The T_g for the 10 mol% CaO glass deviates from the observed trend, and this is attributable to phase separation. Shelby [5] observed two T_g events for calcium germanate glasses, the higher of which, at 675 °C, is in close agreement with that measured here for the 10 mol% CaO glass, of 673 ± 5 °C. The composition of such a phase is ~22 mol% CaO, by interpolation of the trend exhibited by the T_gs of the glasses with > 10 mol% CaO in Fig. 5-3. Shelby [5] observed a strong low temperature T_g (between 540 and 560 °C) of the 10 mol% CaO glass, but the higher temperature T_g was barely detectable for this composition. In the present case, for the roller-quenched glass, the situation is *vice versa*. The difference is almost certainly due to the different cooling rates applied during glass formation. Shelby [5] allowed the melts to cool inertially, whereas the large $\mathrm{d}T/\mathrm{d}t$ achieved by roller quenching results in a higher fictive temperature of the glass, and so a less distinct calorimetric glass transition. For this

to explain the present discrepancy in observations, the cooling rate effects on the glass transition would have to be greater for the lower T_g, GeO_2 rich, phase. In contrast to the observations made by Shelby [5], the fact that only a single T_g was observed for all glass compositions above 10 mol% CaO, and that these follow a single trend, initially increasing, before turning over at 30 mol% CaO, indicates that the glasses are single phase, the cooling rate having exceeded the critical $\mathrm{d}T/\mathrm{d}t$ for circumventing phase separation by rapidly traversing the immiscibility region [1, 6]. Morinaga and Nakashima [6] report that a single phase $12\,CaO \cdot 82\,GeO_2$ glass could not be obtained for cooling rates up to $\mathrm{d}T/\mathrm{d}t = 200\,°C\,s^{-1}$, which is much smaller than that achieved by roller-quenching. The authors [6] report, for the same glass composition, that a $\mathrm{d}T/\mathrm{d}t \geqslant 40\,°C\,s^{-1}$ is required to avoid crystallisation, which is in accord with the observance of crystallisation in the DTA trace upon cooling at $10\,°C\,min^{-1}$. Indeed, a strong exotherm attributed to crystallisation was observed upon controlled cooling of all glass compositions studied.

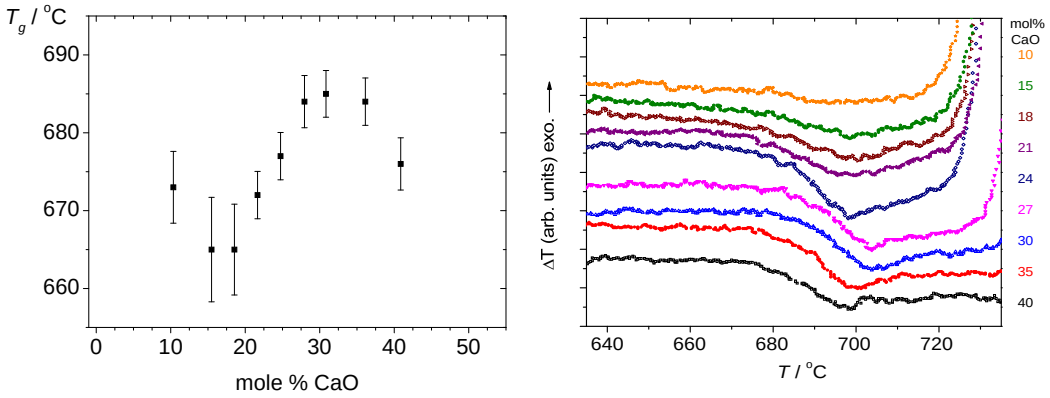

Figure 5-3 Calcium germanate glass transition temperatures as a function of glass composition (left panel), as measured by DTA at $\mathrm{d}T/\mathrm{d}t = 10\,°C\,min^{-1}$. The right panel shows the DTA traces for each glass, offset vertically for clarity, in the locale of the glass transition temperatures, which are visible at centre. The sharply rising features to the right are exothermic crystallisation events.

5.1.5 Energy-filtered transmission electron microscopy

Energy-filtered transmission electron microscopy (EFTEM) [16] is a technique capable of producing high spatial resolution images which map the elemental make-up of a material. This is made possible by exploitation of the change in intensity of the electron

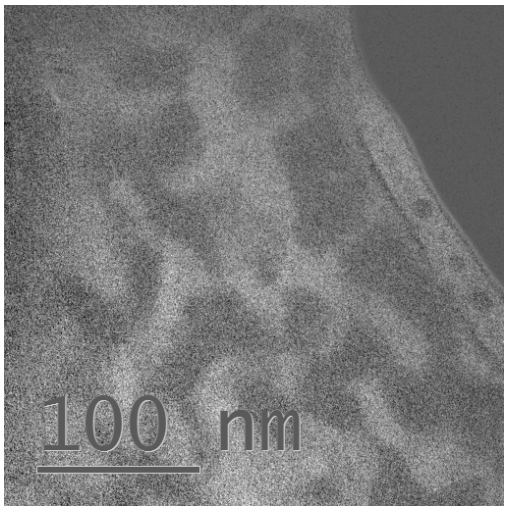

Figure 5-4 EFTEM image of a two phase 10 mol% CaO germanate glass obtained using the three-window method at the Ca L edge. Courtesy of Dr. Richard Beanland.

energy loss (EELS) spectrum at an absorption edge. EFTEM is therefore an ideal technique for providing direct evidence of glass-in-glass phase separation. Fig. 5-4 shows an EFTEM image obtained at the Ca L edge from a sample of nominally 10 mol% CaO germanate glass, and clearly reveals heterogeneity on a length scale of ~50 nm, with bright regions corresponding to the Ca rich phase. The bi-percolating morphology is consistent with a spinodal type phase decomposition, which is to be expected from the proximity of the average glass composition to the centre of the immiscibility dome [1]. The length scale ~50 nm corresponds to UV wavelengths, well below the wavelength limit for visible light scattering, and is consistent with the predominantly transparent appearance of the material (Table 5-1). Images were collected by Dr. R. Beanland of the University of Warwick using a JEOL 2100 TEM combined with a Gatan Quantum SE post-column imaging energy filter. The three-window method [16] was used to extrapolate the background contribution to the EELS spectrum into the post-edge energy window, and this was subtracted to produce the EFTEM map in Fig. 5-4.

5.1.6 Summary

The key observations of maxima in the measured mass densities and glass transition temperatures, as a function of glass composition, are typical of phenomena associated with the so-called ‘germanate anomaly’. Such features have not before been revealed in

the calcium germanate binary owing to the difficulty of preparing single phase glasses. The rapid cooling achieved by twin-roller quenching of the melts in the present study appears, in many cases, to allow single phase glasses to be obtained. The observations described above therefore motivate further study into the structural origin of the germanate anomaly in the calcium germanate glass series. A key difference, as compared to the alkali germanates [17], is in the position of the density maximum for the alkaline earth germanate glasses (Fig. 5-1), which occurs at a significantly higher, 30 mol%, modifier oxide content. This qualitative difference in the form of the phenomenon has not previously been discussed and forms the body of the present chapter.

Measurements of mass lost during melting and of EDX spectra both indicate an increase in the relative proportion of CaO in the glasses relative to the nominal compositions, which is attributed to volatilisation of germania. The compositions estimated by mass loss measurements have been used to derive atomic number densities and molar volumes, Table 5-1, and will be used in all subsequent analyses. For convenience, the nominal compositions will be used to refer to individual glasses.

An extremely important question is whether or not the glasses are single phase. None of the measurements, or observations made in Table 5-2, are indicative of glass-in-glass phase separation for glasses containing $\geqslant 21$ mol% CaO. This is roughly consistent with the reported region of stable immiscibility [1, 6], which lies below approximately 15 mol% CaO. Measured glass transition temperatures suggest that only the 10 mol% CaO germanate glass is phase separated, and this was observed directly by EFTEM, Fig. 5-4. Meanwhile inconsistency in EDX measurements indicate large scale (of order 1 μm or larger) compositional inhomogeneity for glasses containing $\leqslant 18$ mol% CaO, despite the apparent optical clarity of the majority of these glasses. A possible explanation of this apparent discrepancy could be much larger scale inhomogeneities arising from the quenching process. These may arise as a result of the finite time taken to pour the melts, which leads to a faster average cooling rate for the first part of the melt to pass through the roller quencher, and a slower average $\mathrm{d}T/\mathrm{d}t$ for the latter part, which initially cools much more slowly, before meeting the rollers. This problem is exacerbated the greater the viscosity of the liquid, which rises, isothermally, in line with the GeO_2 content, and was a clear problem for the highly viscous 5 and 10 mol% CaO melts. Whilst an attempt was made to manually separate out obviously

cloudy regions from the low CaO content glasses, this process relied on visual inspection and cannot be considered perfect. As such, the glasses containing $\geqslant 21$ mol% CaO are considered to be single phase, whilst results from glasses with < 21 mol% CaO are to be treated with caution.

It should be noted that the 5 mol% CaO batch did not yield sufficient quantity of roller quenched material for study by neutron diffraction. The majority of the batch was retained within the crucible owing to the large viscosity, which increases in line with the GeO_2 content, and formed an opalescent (phase separated) glass upon inertial cooling.

5.2 Total scattering measurements

5.2.1 Neutron diffraction

The distinct scattering functions, $i^N(Q)$, measured by neutron diffraction from calcium germanate glasses are shown in Fig. 5-5. These were measured on the GEM [18] diffractometer at the ISIS spallation source, using the as prepared glass flakes held within thin-walled, 5 mm diameter, vanadium cans. As recorded in Table 5-2, the glasses with nominal calcium contents of 45, 50 and 55 mol% CaO were all found to contain significant amounts of $CaGeO_3$ Wollastonite [4], see Fig. 5-6. As such these materials were measured only briefly, and the data collected have not been analysed beyond the identification of the crystalline phase present. The $i^N(Q)$, Fig. 5-5, demonstrate systematic changes across the compositional series, and these are most notable in the low Q region.

The Fourier transforms of $Qi^N(Q)$, namely $T^N(r)$, are displayed in Fig. 5-7, where a Lorch [19] modification function and $Q_{max} = 40\,\text{Å}^{-1}$ have been used. The most obvious systematic change is that at close to 2.4 Å, which is attributed to bonded Ca-O separations, and is indicative of Ca-O coordination numbers of 6 to 7, based on bond-valence [20, 21] considerations. There are also systematic changes in the shape of the Ge-O correlation, and these are more clearly shown in Fig. 5-8. The peak asymmetry and excess of longer Ge-O bonds are directly related to an increase in average Ge-O coordination number, and these have been extracted by means of integration of $rT^N(r)\mathrm{d}r$ from 1.52 Å up to the first minimum (beyond the peak maximum) which occurs at about 2.10 Å, approximately independent of glass composition. These coordination numbers are recorded in Table 5-3 and plotted in Fig. 5-9 and are strong evidence for the exis-

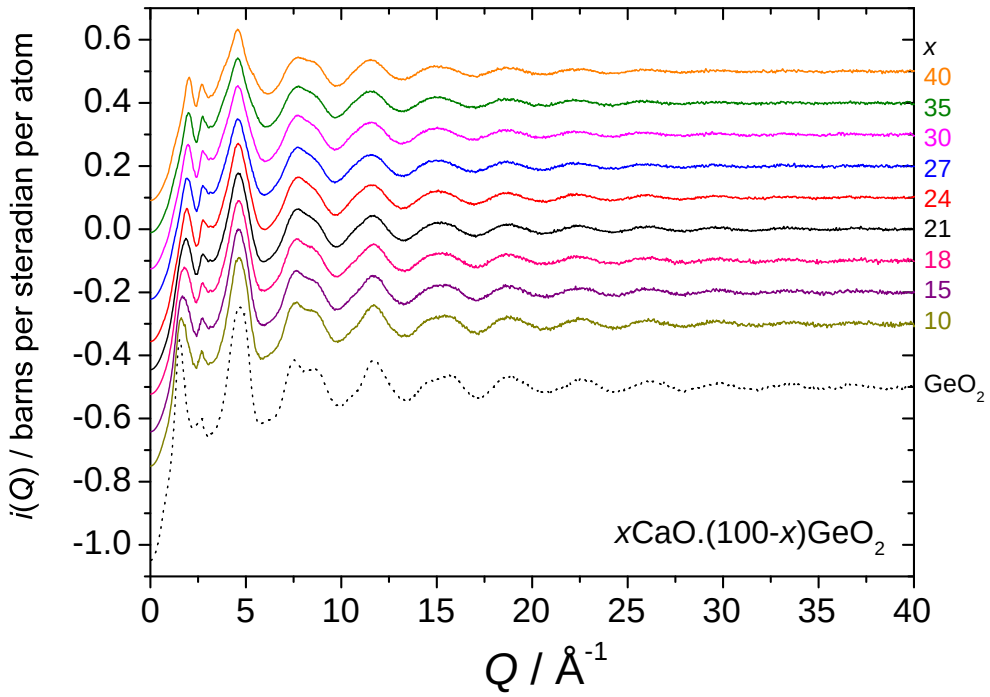

Figure 5-5 The distinct neutron scattering functions from calcium germanate glasses, as compared to that measured for vitreous germania. The molar compositions are indicated on the plot and vertical offsets have been used for clarity.

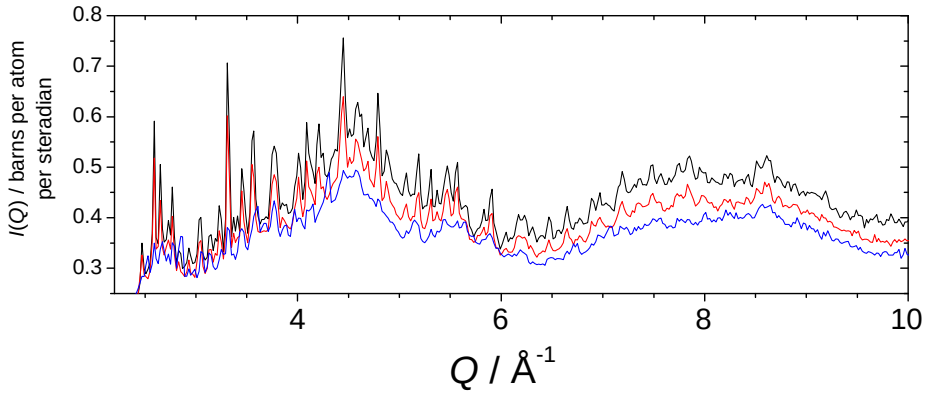

Figure 5-6 Differential neutron scattering cross-sections of high calcium germanate glasses containing $CaGeO_3$ Wollastonite [4] inclusions, as measured using the bank 5 detectors of the GEM [18] diffractometer. The nominal compositions, from top to bottom, are 45 (black), 50 (red) and 55 mol% CaO (blue).

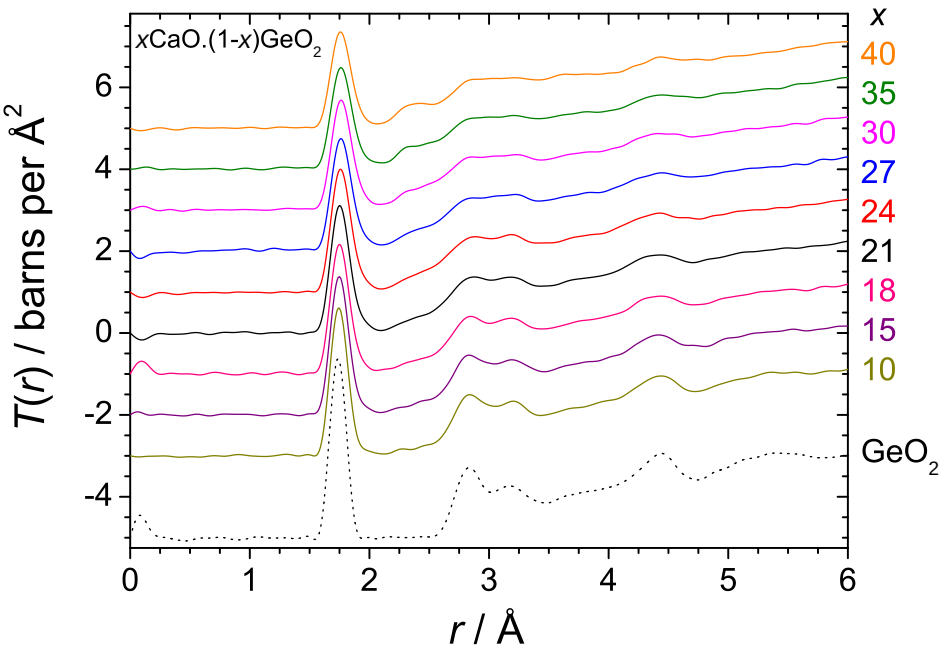

Figure 5-7 Neutron total correlation functions from calcium germanate glasses, as compared to that measured for vitreous germania. A Lorch [19] modification function and $Q_{max} = 40\,\text{Å}^{-1}$ were used. Vertical offsets have been used for clarity.

tence of germanium in oxygen coordination states higher than four. Also evident from Fig. 5-9 is that the [GeO_n], $n > 4$, coexist in the glasses with significant numbers of NBOs, in contrast to the situation in Cs_2O–GeO_2 glasses [22]. This means that the structures of the CaO–GeO_2 glasses are more complex, in that they do not follow the models, for either [GeO_5] or [GeO_6], of Hannon *et al.* [23], equations 2-6 and 2-7, although the latter is approached at high CaO contents. Furthermore, the glasses have lower average Ge-O coordination numbers as compared to the ambient pressure crystals [4, 24, 25], all of which contain [GeO_4] tetrahedra and [GeO_6] octahedra, but no [GeO_5] polyhedra (see §3.2). The points for the four germanate glasses, nominally containing 27, 30, 35 and 40 mol% CaO, all have n_{GeO} in excess of the [GeO_5] model [23], which implies that they contain [GeO_6] species, or else violate assumptions of the model and contain corner sharing [GeO_n], $n > 4$, units, or [OGe_3] triclusters, for example.

Average Ge-O bond lengths (Table 5-3) are plotted in Fig. 5-10, and these, as well as their standard deviations, mirror the trend of the average coordination numbers. Notably the average bond length (and its standard deviation) passes through a maximum, as a function of CaO content, something which has not been observed for the caesium

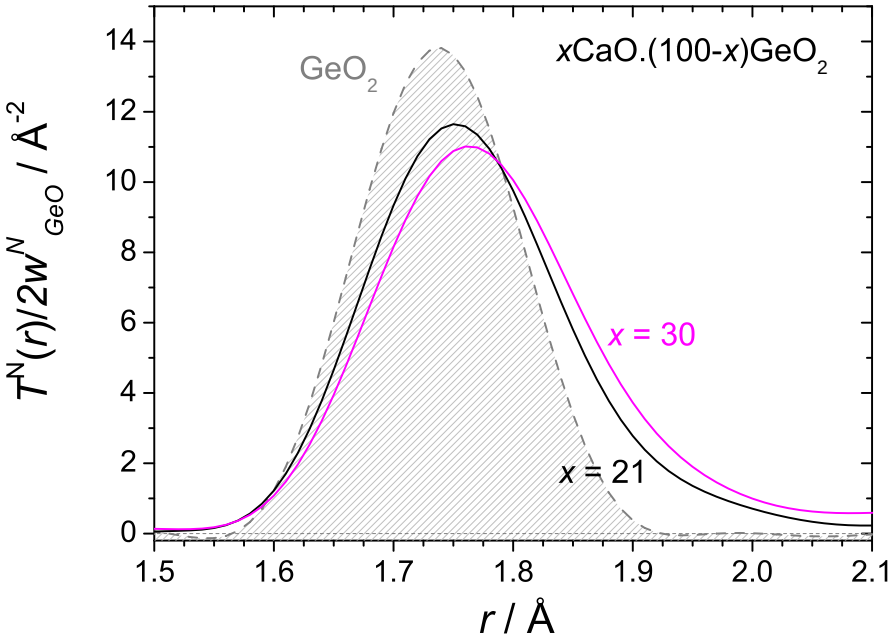

Figure 5-8 Neutron total correlation functions from calcium germanate glasses divided by the Ge-O pair weighting factor, highlighting changes in the peak shape and position. A Lorch [19] modification function and $Q_{max} = 40$ Å^{-1} were used.

Table 5-3 Parameters derived from the Ge-O bond length distribution for calcium germanate glasses (Fig. 5-8). The fraction of [GeO_5] ([GeO_6]) units, assuming no [GeO_6] ([GeO_5]) is $N_5 = n_{GeO} - 4$ ($N_6 = (n_{GeO} - 4)/2$). The fraction of NBOs is $f_{NBO} = 2 - n_{OGe}$, and the final column lists the number of NBOs per calcium ion. Uncertainties in parentheses.

mol% CaO	r_{GeO} (Å)	n_{GeO}	N_5	N_6	n_{OGe}	f_{NBO}	NBO/Ca^{2+}
0	1.7389(6)	3.98(1)	-0.02(1)	-0.01(1)	1.99(1)	0.012(2)	-
10.4(5)	1.7567(19)	4.01(2)	0.01(2)	0.00(1)	1.89(1)	0.106(2)	1.94(10)
15.5(5)	1.7617(24)	4.12(2)	0.12(2)	0.06(1)	1.89(1)	0.114(3)	1.36(7)
18.6(5)	1.7647(37)	4.09(2)	0.09(2)	0.04(1)	1.83(1)	0.166(3)	1.63(6)
21.7(5)	1.7693(26)	4.24(2)	0.24(2)	0.12(1)	1.86(1)	0.140(3)	1.15(5)
24.7(5)	1.7773(33)	4.32(2)	0.32(2)	0.16(1)	1.86(1)	0.144(3)	1.02(5)
28.0(5)	1.7846(70)	4.30(3)	0.30(3)	0.15(1)	1.80(1)	0.200(6)	1.23(6)
30.8(5)	1.7826(66)	4.32(3)	0.32(3)	0.16(1)	1.76(1)	0.235(5)	1.29(5)
36.1(5)	1.7844(78)	4.32(3)	0.32(3)	0.16(1)	1.68(1)	0.315(6)	1.43(4)
40.9(5)	1.7743(59)	4.14(3)	0.14(3)	0.07(1)	1.54(1)	0.460(4)	1.79(2)

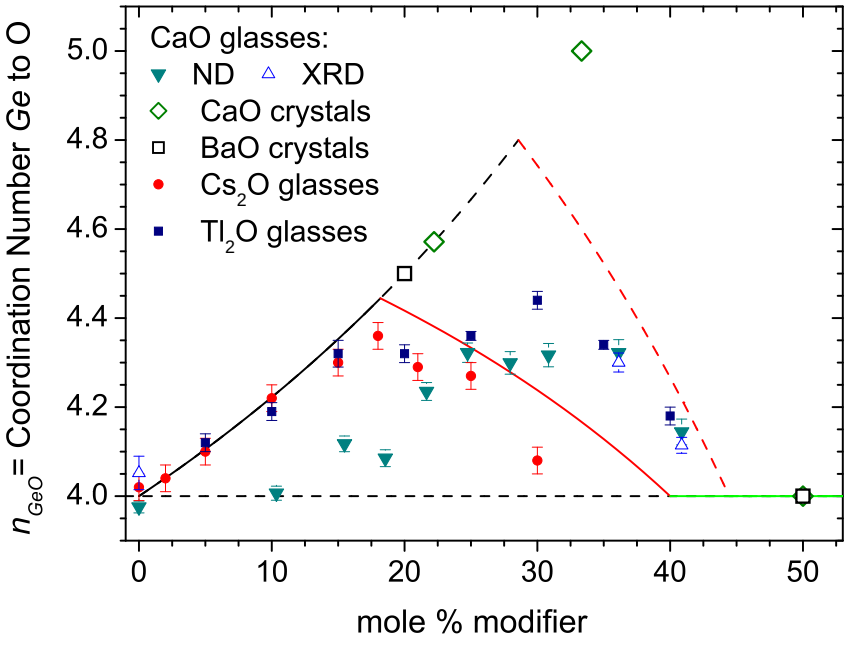

Figure 5-9 Ge-O coordination numbers in calcium germanate glasses, extracted by means of integration of $rT^N(r)\mathrm{d}r$ (filled triangles), and by peak fitting to $T^X(r)$ (open triangles), as a function of glass composition. In the case of x-ray diffraction, only the points for which reasonable fits to the Ca-O peak could be obtained are shown. Values for ambient pressure crystalline calcium [4, 24, 25] and barium [26–29] germanates, as well as vitreous caesium [22] and thallium [30] germanates are shown for comparison. The lines represent the models of Hannon *et al.* [23] for five (solid) and six (dashed) coordinated germanium, see equations 2-6 and 2-7.

germanate glasses [22], or indeed for any other binary alkali germanate glass series [17], though a similar phenomenon has been measured for thallium germanate glasses [30]. As was the case for the average Ge-O coordination numbers, the average Ge-O bond lengths of the ambient pressure calcium germanate crystals [4, 24, 25] are in excess of those measured for the glasses.

Fitting of Gaussian distributions (appropriately convolved with $L(r)$, equation 4-26) to peaks in the experimental total correlation functions can be used as a means of extracting quantitative information, alternative to the integration, or moment analysis, method used above. In the present datasets (Fig. 5-7) however, the distributions of Ge-O bonds are not symmetric, owing to the coexistence of different coordination states, the contributions from which are not resolved*. Furthermore, unlike tetrahedra, which typically contain four equivalent bonds, and hence a symmetric bond length distribution

*It has been stated [31] that the Ge-O correlations from different coordination polyhedra cannot practically be resolved by total scattering measurements.

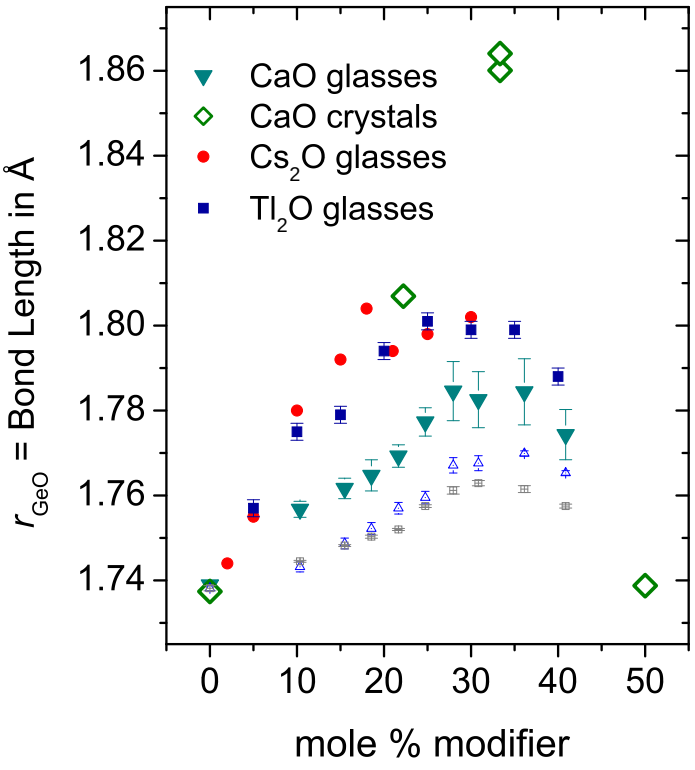

Figure 5-10 Average Ge-O bond lengths in calcium germanate glasses, extracted by means of integration of $rT^N(r)\mathrm{d}r$ (filled triangles), as a function of glass composition. Values for ambient pressure crystalline calcium germanates [4, 24, 25], as well as vitreous caesium [22] and thallium [30] germanates are shown for comparison. The smaller symbols, at shorter r, are the positions of the peak maxima in $T^N(r)$ (grey open squares) and $T^X(r)$ (blue open triangles).

in the harmonic approximation, [GeO_5] or [GeO_6] likely do not contain 5 or 6 equivalent bonds. Therefore the fitting of Gaussian distributions is somewhat arbitrary, but the summed areas remain proportional to the average coordination number. An example of peak fitting, to the $40\,CaO \cdot 60\,GeO_2$ glass neutron and x-ray (see § 5.2.2) total correlation functions, is shown in Fig. 5-11. The neutron data were first fitted with a Ge-O peak between 1 and 1.8 Å (leading edge), and then residuals were fitted sequentially for Ge-O (up to 1.95 Å), Ca-O (up to 2.462 Å), and once again Ge-O (up to 2.2 Å). The total n_{GeO} was found to be 4.15(3), in excellent agreement with the 4.14(3) obtained by integration. The average Ca-O bond length and coordination number of r_{CaO} = 2.398(4) Å and n_{CaO} = 6.91(18) are consistent with each other based on bond-valence [20] predictions, and are similar to the values found in crystalline calcium germanates (see §3.2). The standard deviation of the distribution $\langle u^2_{CaO}\rangle^{1/2}$ = 0.155(4) Å is remarkably large (*cf.* Ca

aluminates [32], for example).

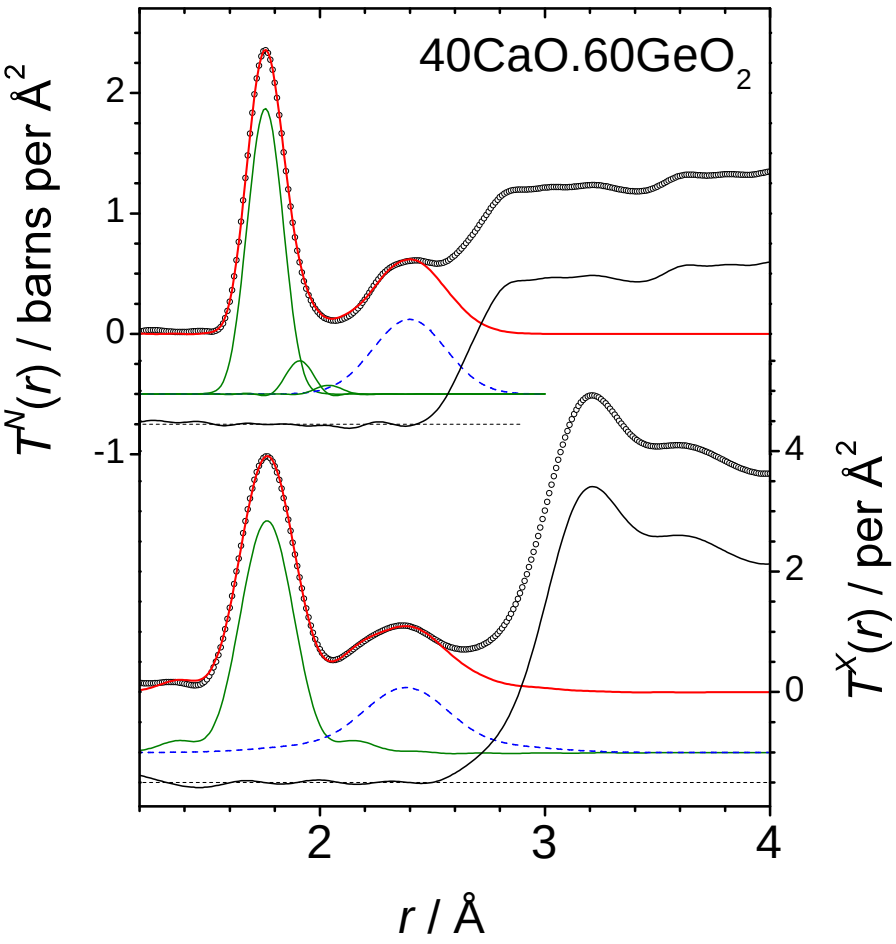

Figure 5-11 Example peak fits to the $40\,CaO \cdot 60\,GeO_2$ glass neutron (upper) and x-ray (lower) total correlation functions (see Fig. 5-7 and 5-13). The data (open circles) are overlayed with the summed peak fits (red lines), with the individual peaks (Ge-O: dark green, Ca-O: blue dashed) and residual (grey lines) offset below for clarity. The neutron and x-ray data were fitted independently, and with only a single Ge-O peak in the x-ray case, owing to the lower resolution.

The $40\,CaO \cdot 60\,GeO_2$ glass $T^N(r)$ represents a unique case in which the Ca-O correlation, close to 2.4 Å, is resolved. As such, fits to the correlation functions for the other glass compositions were limited to the Ge-O leading edge, in order to extract the positions of the peak maxima shown in Fig. 5-10. Further information about the Ca-O correlation could potentially be gained by modelling of the intra-$[GeO_n]$ O-O correlations, and these can be reasonably approximated for $n = 4$ based on the assumption of ideal tetrahedral geometry. However, for the calcium germanate glasses the abundance of $[GeO_4]$ is not known, unless a further assumption is made for the value of $n > 4$,

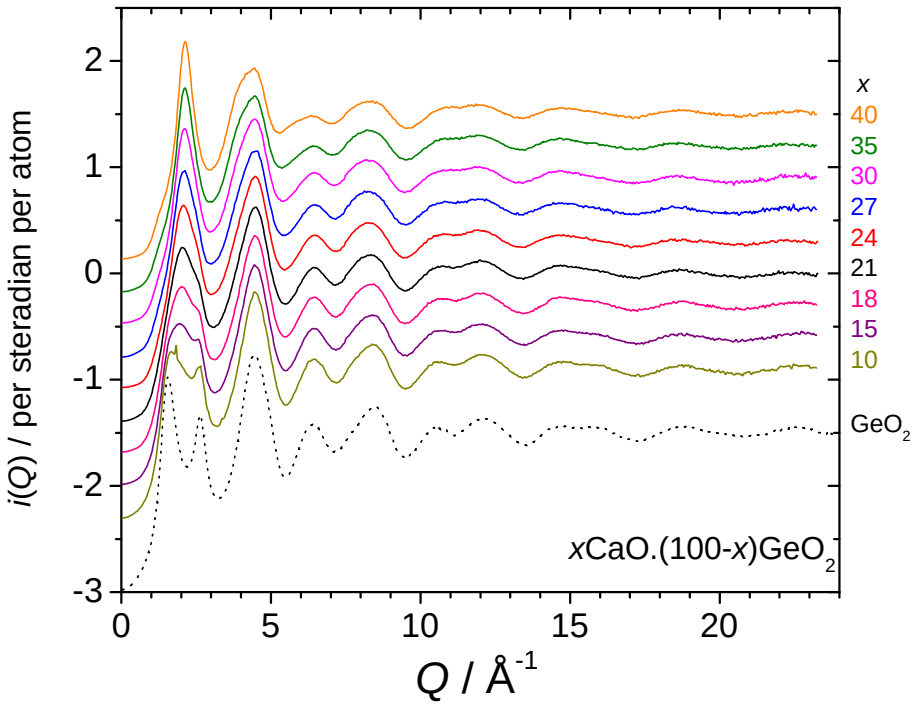

Figure 5-12 The distinct x-ray scattering functions from calcium germanate glasses, as compared to that measured for vitreous germania. Vertical offsets have been used for clarity.

but even then the intra-[GeO_n], $n > 4$, O-O contribution is difficult to model, since the geometries of the non-tetrahedral polyhedra are unknown. Is was therefore not considered worthwhile to undertake such a procedure. X-ray diffraction was expected to reveal more information regarding the Ca-O local structural parameters, given the lower relative weighting of O-O terms in the x-ray case.

5.2.2 X-ray diffraction

Sharpened x-ray diffraction patterns, $i^X(Q)$, for CaO–GeO_2 glasses are displayed in Fig. 5-12. These were measured at the wiggler beamline BW5 [33, 34] on the synchrotron radiation source DORIS III using 84.486 keV x-rays, allowing for a Q_{max} = 23.27 Å^{-1}. The $i^X(Q)$ for the 10 mol% CaO germanate glass shows some small Bragg peaks, about five of which can be discerned, all of which can be indexed according to the Quartz GeO_2 [3] crystal structure. Since some nucleation sites are required to allow Quartz GeO_2 to crystallise during rapid quenching (the pure material does not crystallise under such conditions), it is possible that these crystallites were nucleated at the interfacial regions between the two immiscible supercooled liquids.

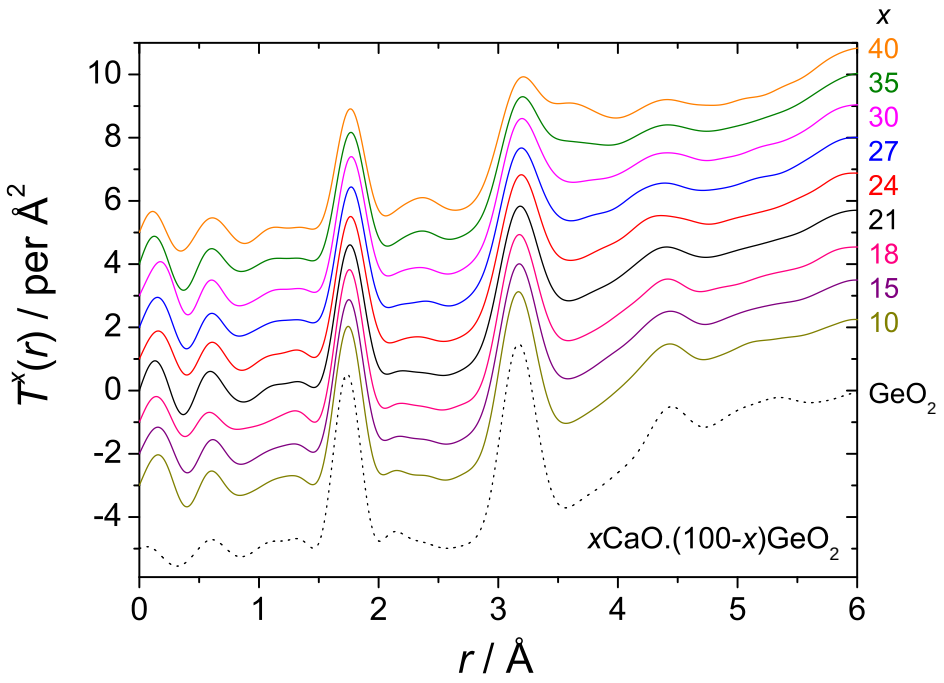

Figure 5-13 X-ray total correlation functions from calcium germanate glasses, as compared to that measured for vitreous germania. A Lorch [19] modification function and $Q_{max} = 23.27$ Å^{-1} were used. Vertical offsets have been used for clarity.

Fourier transforms of $Qi^X(Q)$, made using a Lorch [19] modification function and $Q_{max} = 23.27$ Å^{-1}, are shown in Fig. 5-13. Despite the lower spatial resolution compared to the neutron diffraction measurements, the Ca-O peak is more well defined based on the low weighting of the O-O term in the x-ray diffraction case. Another notable feature is the increase in intensity in the 3.6 Å region as the CaO content is increased. For the 40 mol% CaO germanate glass this forms a distinct peak, and is assigned to Ca-Ge correlations.

Peak fitting to $T^X(r)$ was attempted, initially using just one Ge-O peak, and one Ca-O peak, as illustrated in Fig. 5-11 for the $40\,CaO \cdot 60\,GeO_2$ glass. The use of a single Ge-O peak was based on the lower spatial resolution in the x-ray case, and led to Ge-O coordination numbers in agreement with those measured by neutron diffraction for 35 and 40 mol% CaO germanate glasses, see Fig. 5-9. In the 40 mol% CaO glass, the Ca-O peak parameters $r_{CaO} = 2.382(6)$ Å, $n_{CaO} = 6.68(17)$ and $\langle u^2_{CaO}\rangle^{1/2} = 0.168(6)$ Å are also in fair agreement. However, as the CaO content decreased, the fits to the Ca-O correlation became increasingly broad, due to overlap with the O-O and Ge-Ge correlations to the high r side, and reasonable n_{CaO} and $\langle u^2_{CaO}\rangle^{1/2}$ parameters could not

be extracted. On the other hand the r_{CaO} values for 30 and 35 mol% CaO germanate glasses were 2.392(8) and 2.40(2) Å respectively, not measurably different from the 40 mol% CaO germanate glass. Fitting to the leading edge of the Ge-O peak revealed peaks in the residual attributable to longer Ge-O bonds, but fitting sequential residuals, as performed with the neutron diffraction data, was not reliable due to the complex and broad peak shape function for x-ray diffraction. The positions of the peak maxima obtained from these fits are shown in Fig. 5-10.

5.3 Discussion

5.3.1 Short range order

Fig. 5-9 shows that all of the calcium germanate glasses contain higher coordinated [GeO_n] ($n > 4$) species, and implies that these coexist with non-bridging oxygen atoms, because the average coordination numbers fall below the $4 + 2x/(1 - x)$ prediction [23] which assumes that no NBOs are present. Table 5-3 lists n_{OGe}, as well as the fraction of NBOs, $f_{NBO} = 2 - n_{OGe}$. These results are in contrast to alkali germanate glasses containing Na [35], K [31] or Cs [22] which do not contain NBOs for alkali contents less than that at which the average Ge-O coordination number is at its maximum. It is also in contrast to the equilibrium crystal structures discussed in §3.2 which do not contain NBOs for stoichiometries with < 50 mol% CaO. The propensity for the existence of NBOs in the $CaO-GeO_2$ glasses must therefore be a property of the non-equilibrium supercooled liquid which is retained, to greater or lesser extent, by rapid quenching through the glass transition. This raises the question as to the influence of thermal history on structural properties such as the average Ge-O coordination number, see discussion in §5.3.2.

Here the behaviour of the average Ge-O coordination number, n_{GeO}, in $CaO-GeO_2$ glasses is discussed in the context of what is known about its behaviour in alkali germanate glasses and the known calcium germanate crystal structures. The most extensive set of n_{GeO} available in the literature have been measured for Cs germanate glasses [22], and Fig. 5-9 shows that these are consistent with a model based on the absence of NBOs up to the saturation of the germanate network which occurs when higher coordinated species ([GeO_5] or [GeO_6]) alternate with [GeO_4]. The position and height of the max-

imum, and subsequent decline in n_{GeO} in $Cs_2O{-}GeO_2$ glasses agrees much better with that predicted for $[GeO_5]$ species, than for $[GeO_6]$. Values for n_{GeO} in $Na_2O{-}GeO_2$ [35] and $K_2O{-}GeO_2$ [31] glasses, measured by neutron diffraction are also in accord with the same model, and the presence of $[GeO_5]$ species. The values of n_{GeO} in $CaO{-}GeO_2$ glasses differ in two respects. Firstly, as mentioned above, there are NBOs present in all of the glasses, secondly, n_{GeO} for the four glasses containing $\gtrsim 27$ mol% CaO are all in excess of the model [23] for $[GeO_5]$, indicating the existence of one or more of the following possibilities:

- $[GeO_6]$ polyhedra
- $[GeO_{n>4}]$ polyhedra which share common oxygen at their vertices
- oxygen coordinated to more than two Ge, such as triclusters, $[OGe_3]$

The latter possibility is thought unlikely, since it would necessitate that the coordinating Ge in the $[OGe_3]$ cluster be highly coordinated to avoid severe overbonding of the oxygen (i.e. all 6-fold coordinated as in rutile GeO_2 [36]). For example, triclusters $[OAl_3]$, have been discovered in Ba aluminate glasses [37], but there the O is only marginally over bonded by the trivalent Al contained in $[AlO_4]^-$ tetrahedra.

It may be possible to explain the different behaviour of n_{GeO} in $CaO{-}GeO_2$ glasses, as compared to alkali germanate glasses based on simple considerations of the differences in cation valence and size. Firstly the modifier cation charge is more spatially localised for alkaline earth cations, than for alkali metal cations. For every Ca^{2+} ion in a calcium germanate glass, for example, there are *two* A^+ ions in an equivalent alkali germanate glass, and these must be appreciably separated such that they can occupy separate oxygen coordination polyhedra. In any case the majority of metal-oxygen bonds will be either to NBOs or to BOs which are bonded to at least one $[GeO_n]$, $n > 4$, since these are then underbonded. Given that Ae−O coordination numbers are typically larger, but not double, those of A^+ cations in oxides, and instead form shorter, stronger bonds, it is not a great leap to realise that either $[GeO_6]$ (as opposed to $[GeO_5]$) polyhedra, corner sharing pairs of $[GeO_n]$, $n > 4$, or NBOs must be stabilised in alkaline earth germanates in order to satisfy the bonding requirements of the Ae cations. In the $AeO{-}GeO_2$ crystals, it is apparent that this is achieved by the stabilisation of $[GeO_6]$ octahedra, and in $CaGe_2O_5$ [25] even by the presence of $[GeO_6]$ octahedra which share a common vertex. To clarify the preceding argument, Table 5-4 summarises the electro-

Table 5-4 Electrostatic bond strength sums for various oxygen environments, to Ge and B, in germanates and borates. The final column gives the available EBS for bonding of other (modifier) cations to the oxygen, and is equal to the modulus of the formal charge on the site in question. Roman numerals denote Ge-O or B-O coordination numbers.

O site	Σ(EBS)	2 − Σ(EBS)	O site	Σ(EBS)	2 − Σ(EBS)
Ge^{IV}–O–Ge^{IV}	2	0	B^{III}–O–B^{III}	2	0
Ge^{IV}–O–Ge^{V}	9/5	1/5	B^{III}–O–B^{IV}	7/4	1/4
Ge^{IV}–O–Ge^{VI}	5/3	1/3	B^{IV}–O–B^{IV}	3/2	1/2
Ge^{V}–O–Ge^{V}	8/5	2/5	B^{III}–O^{-}	1	1
Ge^{V}–O–Ge^{VI}	22/15	8/15			
Ge^{VI}–O–Ge^{VI}	4/3	2/3			
Ge^{IV}–O^{-}	1	1			

static bond strengths (EBSs) available for modifier cations to various oxygen species. The EBS sums for the modifier cations must sum approximately to their valence (of 1 or 2), which means that, in the absence of NBOs, many $[GeO_n]$, $n > 4$, must pack around the modifier cations. Considering the simplified case where each BO bonds only to a single modifier cation, then five Ge^{IV}–O–Ge^{V} about an alkali would be sufficient, whilst ten such oxygens would be required about an Ae^{2+} cation. In §5.2 neutron and x-ray diffraction measurements on the high calcium (35 and 40 mol% CaO) germanate glasses indicated an n_{CaO} of about 7. As such, at least some $[GeO_6]$, corner sharing pairs of $[GeO_n]$, $n > 4$, or NBOs *must* be present. The requirement for oxygen sites with $2 - \Sigma(EBS) > 1/5$ (Table 5-4) is yet more dire when one considers the sharing of oxygens by more than one Ae^{2+} cation. For the particular case of $n_{CaO} = 7$, Table 5-5 ranks the most likely O environments based simply on EBS sums, where it can be seen that $[GeO_6]$–$[GeO_5]$ and $[GeO_6]$–$[GeO_4]$ are favoured. In reality, the broad distribution of Ca-O bond lengths measured permits a broad range of sites, and the bond length dependent bond valences should be considered.

A remarkable feature of Fig. 5-9 is the similarity between values of n_{GeO} in calcium and thallium [30] germanate glasses containing 35 and 40 mol% modifier oxide. The reason for this can again be rationalised in terms of EBS sums, and knowledge of the cation-oxygen coordination numbers. At such high modifier contents, most Tl+ have lone-pairs of electrons which are stereochemically active and occupy asymmetric $[TlO_3]$ sites, each bond having EBS = 1/3. Meanwhile a divalent cation, such as calcium, on a 6-fold, $[CaO_6]$, site has bonds of the same EBS = 2/6 = 1/3. Table 5-

Table 5-5 Electrostatic bond strength sums for various oxygen environments in calcium germanates, assuming $n_{CaO} = 7$. Only the top ten environments, closest to Σ(EBS) = 2 are shown, ranked in order of |2 − Σ(EBS)|. Roman numerals denote Ge-O or Ca-O coordination numbers and subscripts b = BO or nb = NBO. [OGe_3] triclusters have not been included.

O site	Σ(EBS)	O site	Σ(EBS)
$[O_bGe^{V}Ge^{VI}Ca_2^{VII}]$	2.038	$[O_{nb}Ge^{IV}Ca_3^{VII}]$	1.857
$[O_bGe^{IV}Ge^{VI}Ca^{VII}]$	1.952	$[O_{nb}Ge^{IV}Ca_4^{VII}]$	2.143
$[O_bGe^{IV}Ge^{V}Ca^{VII}]$	2.086	$[O_bGe_2^{V}Ca_2^{VII}]$	2.171
$[O_bGe_2^{VI}Ca_2^{VII}]$	1.905	$[O_bGe_2^{VI}Ca_3^{VII}]$	2.190
$[O_bGe_2^{V}Ca^{VII}]$	1.886	$[O_bGe^{IV}Ge^{VI}Ca_2^{VII}]$	2.238

Table 5-6 Electrostatic bond strength sums for various oxygen environments in germanates, with EBS = 1/3 (i.e. $[X^{+}O_3]$ or $[X^{2+}O_6]$). Only the top ten environments, closest to Σ(EBS) = 2 are shown, ranked in order of |2 − Σ(EBS)|. Roman numerals denote Ge-O or Ca-O coordination numbers and subscripts b = BO or nb = NBO. [OGe_3] triclusters have not been included.

O site	Σ(EBS)	O site	Σ(EBS)
$[O_bGe^{IV}Ge^{VI}X]$	2.000	$[O_bGe^{IV}Ge^{V}X]$	2.133
$[O_bGe_2^{VI}X_2]$	2.000	$[O_bGe^{V}Ge^{VI}X]$	1.800
$[O_{nb}Ge^{IV}X_3]$	2.000	$[O_bGe_2^{V}X_2]$	2.267
$[O_bGe_2^{V}X]$	1.933	$[O_{nb}Ge^{IV}X_4]$	2.333
$[O_bGe^{V}Ge^{VI}X_2]$	2.133	$[O_bGe_2^{VI}X_3]$	2.333

6, in analogy to Table 5-5, lists the most likely oxygen environments based on EBS sums involving various [GeO_n] and modifier cations for which EBS = 1/3. Notably, whilst Barney *et al.* [30] discuss two of the top four cases listed in Table 5-6, there are two other cases, both involving 6-fold germanium, which exactly satisfy the valence requirements of the oxygen anion. Furthermore, it can be seen from Fig. 5-9 that the n_{GeO} points for Ca and Tl germanate glasses both approach the model [23] for 6-fold Ge at high modifier compositions.

At this point a comparison to the vitreous alkaline earth borates is appropriate. Like the germanates (and silicates) these liquids all have a miscibility gap at low AeO contents [38], which itself is a consequence of the high Ae^{2+} cation field strength [39], and therefore the need for NBOs (or oxygen sites with 2 − Σ(EBS) > 1/5) to provide sufficient bonding and Coulombic shielding between cations. Various studies have been conducted which measure $N_4 = n_{BO} - 3$ in alkaline earth borate glasses using

^{11}B NMR [40–44], ND [45], MD [46] and IR spectroscopy [47]. A striking result is that N_4 is suppressed below the $x/(1-x)$ prediction ([BO_4] in preference to NBOs), somewhat for CaO−B_2O_3 glasses, and dramatically so for MgO−B_2O_3 glasses. This is a qualitatively similar effect to that observed for n_{GeO} in the calcium germanate glasses. Notably the fractions $N_5 = n_{GeO} - 4$ (or $N_6 = (n_{GeO} - 4)/2$, Table 5-3) are significantly lower than those of $N_4 = n_{BO} - 3$ in the Ca bearing glasses, having maximum values of $N_5 = 2N_6 = 0.32$ (35 mol% CaO) compared to N_4 ~0.41 [47] (45 mol% CaO*). The higher values in the borate system are likely due to the higher EBS available to the Ae cations from B^{III}−O−B^{IV} bridges (Table 5-4). Interestingly, the high N_4 in the borate systems at high AeO contents may well be a consequence of the stabilisation of corner sharing [BO_4] units, something which is common in crystalline borates [48] (within superstructural units) at lower modifier oxide contents.

5.3.2 The role of glass fictive temperature

The question is, does the fictive temperature, T_f, play a role in determining the average Ge-O coordination in germanate glasses, and if so, how so? The author is not aware of any studies which probe this question directly, although studies have been performed on other oxide glass-forming systems, focussing on cations such as B, Al and Si. Relevant work on borate, borosilicate, boroaluminate and aluminoborosilicate glasses [49–62] has shown that the average boron-oxygen coordination number, n_{BO}, is often a function of the glass fictive temperature, and hence the cooling rate of the liquid through the glass transition. For example, decreases of up to 7% in $N_4 = n_{BO} - 3$ have been reported [62] for a cooling rate increase of 4 orders of magnitude (0.033 to 798 °C s^{-1}) for an alkali borosilicate glass. This is related to a decrease in N_4 with temperature above the glass transition, owing to processes whereby $BO_4 \rightleftharpoons BO_3$ + NBO in the liquid state. In binary sodium borates however, no change in n_{BO} was detected with cooling rates of 0.017 to ~1000 °C s^{-1} [50]. Decreases in aluminium speciations in some aluminoborates [52, 53], related to mechanisms $AlO_{6,5} \rightleftharpoons AlO_{5,4}$ + NBO, occur with increased fictive temperature. However, dependent upon the glass composition, the Al-O coordination may instead *increase* with glass fictive temperature, as found in

*Direct comparison is better made to yMO · $(100 - y)BO_{3/2}$, for which the maximum in N_4 occurs at y = 29 mol% CaO.

Ca aluminosilicates [63]. In a binary potassium silicate glass, Stebbins [64] has shown that an increase in glass fictive temperature leads to an *increase* in the amount of [SiO_5], although the abundance of such species is very small (increasing from 0.06 ± 0.02 to 0.10 ± 0.02%).

The above discussion leads one to strongly suspect an effect of thermal history on n_{GeO} in glasses *in general*, but it is less than clear what sense (or indeed magnitude) of change in n_{GeO} with fictive temperature, or liquid temperature, should be expected. Considering binary alkali germanate glasses, there is a strong analogy with the binary borate systems and there is evidence [50] that the latter show no dependence of n_{BO} on T_f, despite a measurably lower n_{BO} (and increase in NBOs) in the liquid state [57, 58].

What is required are neutron diffraction [22, 31, 35] measurements, which are capable of quantifying the average Ge-O coordination numbers and NBO fractions, on germanate liquids and glasses with different fictive temperatures, but of the same chemical composition. ^{17}O MQMAS NMR measurements, which have been made on binary sodium germanate glasses [65, 66], could also be extended to glasses with varying thermal histories, in the same regard.

5.3.3 The germanate anomaly

5.3.3.1 Density maxima

The germanate anomaly, simply stated, is the appearance of extrema in physical properties of germanate glasses as a function of their composition, being completely analogous to the borate anomaly, both of which are anomalous only with respect to silicate glass systems. Commonly measured properties, which all show maxima as a function of alkali germanate binary glass composition are mass density, refractive index and glass transition temperature. Fig. 5-1 clearly illustrates that the mass densities of alkaline earth germanate glasses bearing Ca, Sr and Ba all pass through maxima at ~27 mol% AeO, as do the CaO–GeO_2 glass transition temperatures, Fig. 5-3, thus demonstrating their anomalous behaviour, in the traditional sense. AeO–B_2O_3 glasses also show such anomalous behaviour [67]. In order to relate mass density, ρ_m, variation with structural variation, clearly the masses and sizes of the constituent atoms, need to be accounted for, which is why consideration of ρ_m alone can often be misleading when

making structural interpretations. A prime example are the binary borate glass systems, many of which show only inflections in $\rho_m(x)$ [67], despite showing maxima in structural parameters, such as N_4. Fig. 5-14 shows the atomic number densities, ρ_0, and volumes per mole $x\mathrm{AeO}\cdot(100-x)\mathrm{GeO}_2$, V_M, calculated from the glass compositions and ρ_m plotted in Fig. 5-1. Remarkably, at AeO contents $\lesssim 15$ mol% AeO the data sets

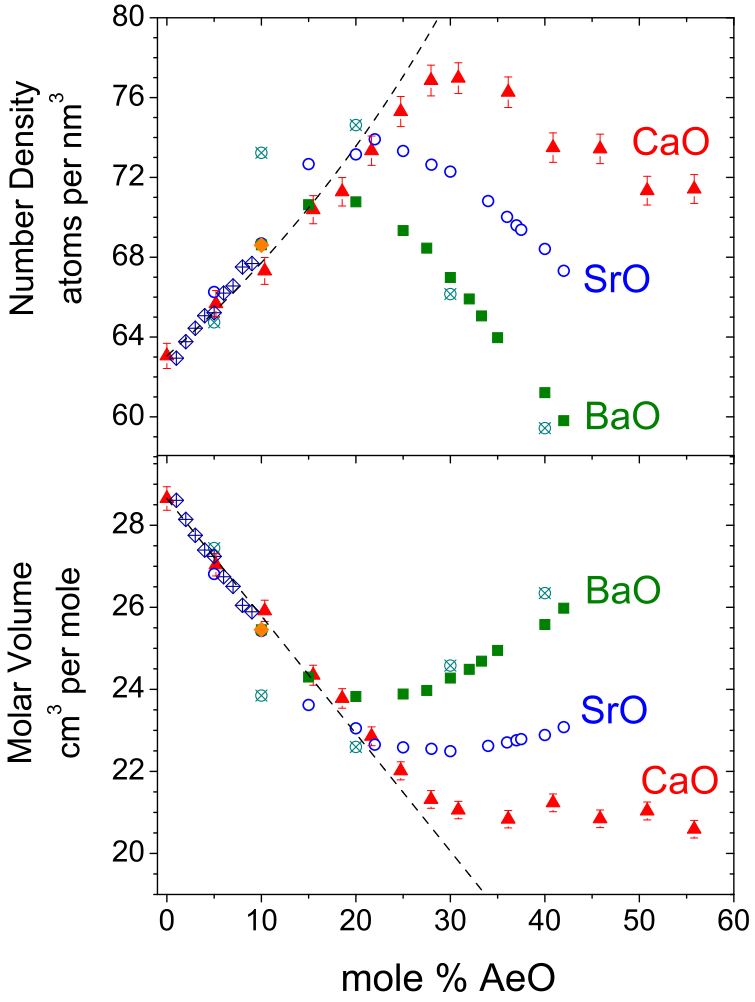

Figure 5-14 Alkaline earth germanate number densities and molar volumes as a function of glass composition. The dashed lines represent those of constant volume per mole $J\mathrm{AeO}\cdot\mathrm{GeO}_2$. CaO–$\mathrm{GeO}_2$ system: Filled red triangles - this study. SrO–GeO_2 system: Open blue circles - Kasymova [12]. BaO–GeO_2 system: Closed green squares - Kasymova [12], open diamonds with crosses - Shelby [8], open circles with crosses - Pernice *et al.* [13], filled orange triangle - Inaba *et al.* [14]. See also Fig. 5-1 for the corresponding mass densities.

for number density and for molar volume collapse onto common trends, with those for the SrO and CaO systems continuing to follow those trends up to 22 and 27 mol% AeO

respectively. All three systems show maxima in their number densities, at progressively lower ρ_0 and mol% AeO as the Ae cation size increases. The universality of the packing behaviour in the low AeO content region can be understood in terms of the filling of the voids available within the germanate network by Ae^{2+} cations. Indeed, the dashed lines in Fig. 5-14 represent those of constant volume per mole $J\mathrm{AeO}\cdot\mathrm{GeO_2}$, where $J = x/(1-x)$, such that

$$\rho_0(x) = \rho_0(0)\left(1 + \frac{2x}{3-3x}\right), \tag{5-1}$$

and

$$V_M(x) = N_A\left(\frac{3-x}{\rho_0(x)}\right) = \frac{3N_A(1-x)}{\rho_0(0)}, \tag{5-2}$$

with N_A Avagadro's number. What such relationships show is that as AeO is added to GeO_2, the free volume present in pure GeO_2 glass is taken up by the added Ae and O ions. Clearly the available free volume will be filled by a smaller number of (larger) Ba ions as compared to (smaller) Ca or Sr ions, which explains the order of the points at which each set of $AeO{-}GeO_2$ glass number densities deviate from the trends expressed in equations 5-1 and 5-2, see Fig. 5-14.

Note that glass-in-glass phase separation is not thought to have much bearing on the present discussion if it is assumed that the two glass compositions are both within the region of linear variation of molar volume, equation 5-2, Fig. 5-14.

5.3.3.2 Atomic packing fractions

It is instructive to consider the packing fraction

$$P_f = \rho_0 \frac{4}{3}\pi \sum_j c_j r_j^3 = 1 - \tilde{V}_f, \tag{5-3}$$

where c_j are atomic fractions and r_j ionic radii. P_f is equal to the 'occupied' volume fraction within a material, and $1 - P_f = \tilde{V}_f$ is the free volume fraction. Ionic radii are not well defined quantities, but using the empirical values derived by Shannon [68], one obtains for pure vitreous germania $P_f(x=0) \simeq 0.438$ and $\tilde{V}_f(x=0) \simeq 0.562$. In other words, GeO_2 glass is an open network, with a considerable amount of free volume. Note that the preceding statement can only be made in comparison to the $P_f = 0.637$ [69] of a random close packing (RCP) of similar spheres, or the $\pi/(3\sqrt{2}) \simeq 0.740$ of the HCP and FCC lattices. If one then considers the space within the germanate network being

progressively filled with Ae cations, the values of the maxima in $\rho_0(x)$ should occur at

$$\rho_0^{max} = K\rho_0(0) + \frac{3C_f\left(1 - P_f(0)\right)}{4\pi r_{Ae}^3}. \tag{5-4}$$

Note that the added oxygen (from the AeO) are not considered to fill the free space, but rather they bond to germanium to become part of the germanate network, typically to form [GeO_n], $n > 4$, or as NBOs. The factor K therefore accounts for any change in number density of the germanate network itself, from the value of $\rho_0(0)$ for pure GeO_2. C_f in equation 5-4 is then the effective filling factor for the free volume fraction, $\tilde{V}_f(0) = 1 - P_f(0)$, estimated from that of GeO_2 glass. Fig. 5-15 shows the maxima in

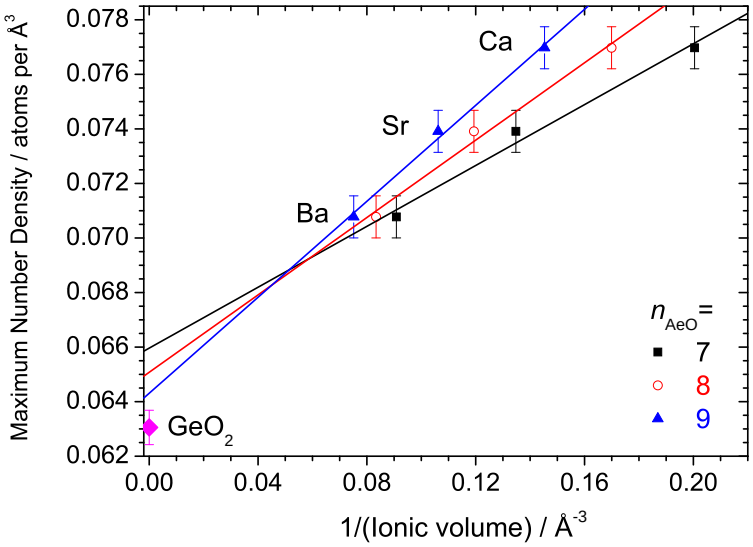

Figure 5-15 Maximum alkaline earth germanate glass number densities as a function of the reciprocal alkaline earth cationic volume. The points have been calculated using Shannon [68] ionic radii appropriate to Ae-O coordination numbers of 7, 8 and 9, as indicated on the plot. The lines are least squares fits to the points, and the number density of GeO_2 has been plotted for comparison to the infinite cationic volume limit extrapolations.

alkaline earth germanate glass ρ_0 as a function of $3/4\pi r_{Ae}^3$, and demonstrates that the two parameters are linearly correlated, as would be expected for constant values of K and C_f (Table 5-7). The ionic radii, r_{Ae}, are coordination number dependent, and since the n_{AeO} at the number density maxima are not known, Fig. 5-15 shows points calculated for $n_{AeO} = 7$, 8 and 9. These numbers were chosen based on the $n_{CaO} \simeq 7$ measured by diffraction (§5.2), and the expectation for n_{SrO} and n_{BaO} to be similar or greater. Note that there is no particular basis for the assumption that the alkaline earth germanate

Table 5-7 Parameters extracted from the variation in alkaline earth germanate glass number density maximum with reciprocal alkaline earth cation volume. See Fig. 5-15 and equation 5-4. x_d is the mole fraction AeO at which the number density maximum occurs.

n_{AeO}	K	C_f	$P_f(x_d) \simeq KP_f(0) + C_f$
7	1.05(3)	0.099(18)	0.558(21)
8	1.03(3)	0.126(22)	0.579(26)
9	1.02(3)	0.157(28)	0.604(31)

glasses are isomorphous, at least with respect to the n_{AeO}, as is implied by the least squares fitting to points of constant n_{AeO} in Fig. 5-15. The present discussion is therefore rather qualitative, but nonetheless sheds some light on the mechanisms governing the glass structures and their variation with chemical constitution.

From Fig. 5-15 and Table 5-7 it is evident that $K > 1$ which can be considered a consequence of the incorporation of the added oxygen (from the AeO) into the germanate glass network, with a concomitant densification arising from the formation of [GeO_5], [GeO_6] and/or changes in ring statistics. The infinite cation volume extrapolations of the linear least squares fits in Fig. 5-15 give estimates of K from 1.05(3) to 1.02(3) (Table 5-7). Lowering the n_{AeO} gives rise to apparently larger K and smaller C_f. Note also that allowing an increase in n_{AeO} with cation size would also give rise to larger K and smaller C_f, although this increase would need to be small to retain linearity. An estimate of the glass packing fraction $P_f(x_d)$ at the glass composition, x_d, of the number density maxima can be obtained from equation 5-4 using $P_f(x_d) \simeq KP_f(0) + C_f$ (see Table 5-7). Fig. 5-16 shows the packing fractions, $P_f(x)$, calculated from the number densities and compositions of the alkaline earth germanate glasses. These are approximate values based on radii [68] for 2-fold coordinated oxygen (1.35 Å), 4-fold Ge (0.39 Å) and 8-fold Ae cations. The dashed lines (Fig. 5-16) for 7 and 9-fold Ca give an indication of the uncertainty associated with the choice of Ae-O coordination number, which increases with AeO content (x). Note that although the effect of the presence of [GeO_5] or [GeO_6] has been neglected, the Ge cations are the smallest*, and so contribute the least to the packing fraction.

The fact that $P_f(x_d) \simeq KP_f(0) + C_f$ overestimates the packing fractions at the com-

*6-fold Ge has an ionic radius of 0.53 Å, and whilst no value for 5-fold Ge is given [68], it must lie in the range 0.39 to 0.53 Å.

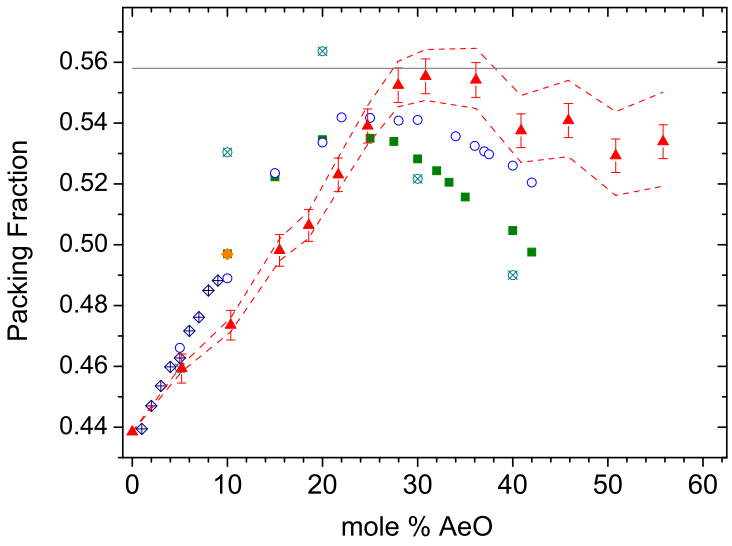

Figure 5-16 Alkaline earth germanate packing fractions as a function of glass composition. The points have been calculated using Shannon [68] ionic radii appropriate to Ae-O coordination numbers of 8. The dashed lines were calculated using ionic radii appropriate to Ca-O coordination numbers of 7 and 9. The horizontal grey line corresponds to $P_f(x_d) \simeq KP_f(0) + C_f$ for 7-fold Ae cations, see Fig. 5-15, Table 5-7, equation 5-4 and main text. $CaO-GeO_2$ system: Filled red triangles - this study. $SrO-GeO_2$ system: Open blue circles - Kasymova [12]. $BaO-GeO_2$ system: Closed green squares - Kasymova [12], open diamonds with crosses - Shelby [8], open circles with crosses - Pernice *et al.* [13], filled orange triangle - Inaba *et al.* [14].

positions, x_d, of the number density maxima (see Fig. 5-16), and more so for the Ba and Sr systems, indicates that n_{AeO} may be a function of glass composition or of Ae cation type, K and C_f may be different for different Ae cations, or a combination of the aforementioned.

A key feature of Fig. 5-16 is that the strontium and barium germanate glass $P_f(x)$ are very similar up to their broad maxima at ~25 mol% AeO, whilst those of the calcium germanate glasses are smaller prior to this point, at which they cross over and become apparently larger. The latter feature is not necessarily significant owing to the uncertainties in the alkaline earth cation-oxygen coordination numbers. However, the smaller $CaO-GeO_2$ packing fractions, in the low modifier oxide content region, where the uncertainty in n_{AeO} contributes less to the uncertainty in $P_f(x)$, is certainly significant. It suggests that the smaller Ca ions do not fill the voids in the germanate network as the Sr and Ba ions do. In other words, the cages of the germanate network tend to be

larger than a Ca ion (5.0 $Å^3$, 7-fold) but similar in size or smaller than a Sr ion (7.4 $Å^3$, 7-fold, to 9.4 $Å^3$, 9-fold), in agreement with the average value of 7.7 $Å^3$ obtained by Weber [70] for vitreous GeO_2. This may explain the very large $\langle u^2_{CaO} \rangle^{1/2}$ = 0.155(4) Å as measured by peak fitting to the neutron Ca-O correlation for the $40\,CaO \cdot 60\,GeO_2$ glass (§5.2.1).

The above discussion proposes the filling of the free (interstitial) volume within the germanate network by alkaline earth cations in $AeO{-}GeO_2$ glasses with concurrent densification of the germanate network itself. This is qualitatively the same as the discussion of bond volumes in alkali germanate glasses given by Weber [70]. Furthermore, the packing fractions of $A_2O{-}GeO_2$ glasses have been calculated previously [71, 72] and Giri *et al.* [71] have shown that these are lower for A = Li, Na than for the heavier alkalis, which can be attributed, as for Ca, to their ionic volumes being smaller than the average germanate network cage. Burgess *et al.* [73] calculated the packing fractions for $AeO{-}GeO_2$ glasses, but did not reach the same conclusions as those described herein, due to a paucity of available $CaO{-}GeO_2$ glass density data.

5.3.3.3 Glass transition temperatures

The behaviour of $T_g(x)$ as a function of calcium germanate glass composition, Fig. 5-3, can be considered at least qualitatively consistent with the measured variation in n_{GeO} (§5.2.1) and the ideas of temperature-dependent constraint theory [74, 75]. The ideas of zero-temperature constraint theory [76, 77], originally developed for covalent chalcogenide glasses were extended first to oxide systems [78, 79] and recently by Gupta and Mauro [74] to finite temperatures. Notably the glass transition temperatures, $T_g(x)$, for lithium and sodium borates were successfully modelled [75] using the latter approach. Essentially, since the number of linearly independent bond and bond-angle constraints increases with n_{GeO}, so $T_g(x)$ tends to track the behaviour of $n_{GeO}(x)$, as is apparent from Fig. 5-3 and 5-9. A complication arises if the onset of rigidity, T_α, of a constraint occurs at a temperature similar to that of $T_g(x)$, as is apparently the case for the alkali borates and the O-B-O bond-angle constraint with $T_\alpha \simeq 477$ °C [75]. This leads to a plateau over an intermediate range of binary alkali borate glass compositions, which does not appear to occur for the calcium germanate $T_g(x)$ (Fig. 5-3), or for those of the alkali germanate glasses [80]. One would expect a T_α for O-Ge-O constraints

less than that of O-B-O, and, from the absence of plateaus in the data, one that is less than the measured $T_g(x)$.

5.4 Conclusions

Homogeneous calcium germanate glasses can be obtained in the range 21 to 41 mol% CaO, with the lower limit being determined by amorphous-amorphous phase separation, and the higher by formation of $CaGeO_3$ Wollastonite crystallites, although the fraction of these at 55 mol% CaO, using high quench rates ($\sim 10^5$ °C s^{-1}), was small. The rapidly rising liquidus line for compositions containing > 55 mol% CaO prevented investigation in this region.

The average Ge-O coordination number, n_{GeO}, is smaller in vitreous calcium germanates than in the equilibrium crystals with < 50 mol% CaO. This implies that n_{GeO} is similarly smaller in the supercooled liquid state than in the equilibrium solids, and likely correlates inversely with liquid temperature, T, in analogy to borate systems [57, 58, 62]. Furthermore, the result suggests that n_{GeO} is a function of the glass fictive temperature, T_f. Such relationships have implications for structural relaxation phenomena and viscous flow, implying dynamic equilibria between $[GeO_n] \rightleftharpoons [GeO_{n-m}] + m$NBO.

In contrast to the $[GeO_5]$ units thought to be present, in addition to the $[GeO_4]$ tetrahedra, in alkali germanate glasses, the stabilisation of $[GeO_6]$ octahedra in calcium germanate glasses is proposed on the basis of the measured n_{GeO}. In the region 28 to 41 mol% CaO, n_{GeO} is in excess of the value predicted by a model based on saturation at an alternating network of $[GeO_5]$ and $[GeO_4]$, and therefore either $[GeO_6]$ are present and/or $[GeO_n]$, $n > 4$, share common oxygen atoms at some of their vertices. $[GeO_6]$ provide a more efficient means of charge balancing the Ca^{2+} ions, as in crystalline calcium germanates.

The presence of NBOs, in addition to $[GeO_6]$, in all glasses studied provides an alternative means of charge balancing the Ca^{2+} ions, and importantly, one which reduces the number of topological constraints, allowing glass network formation at sufficiently high cooling rates. In other words, it is important to maintain a high fictive temperature of the supercooled melt and resultant glass, in order to suppress the increase in n_{GeO}

with decreasing temperature, which will eventually result in crystallisation.

Calcium ions are coordinated, on average, by at least 7 oxygen, at least for high (41 mol%) CaO content. This is a similar value to known crystalline ($CaO-GeO_2$) structures, although the presence or absence of longer Ca-O bonds, such as those of 3.034 Å in low T $CaGe_2O_5$ [25] could not be determined. n_{CaO} is therefore higher in the calcium germanate glasses, as compared to $CaO-SiO_2$ glasses of similar composition [81–84]. This can be seen as a consequence of the availability of bridging oxygen which is significantly underbonded by Ge (owing to the presence of $[GeO_5]$ or $[GeO_6]$). Such oxygen species, which are not present in calcium silicates, contribute to the very broad distribution of Ca-O bond lengths observed ($\langle u^2_{CaO}\rangle^{1/2}$ = 0.155(4) Å at 41 mol% CaO), there being a broad distribution of different oxygen species to which Ca may form bonds. The large breadth of the measured Ca-O correlation may alternatively be considered a consequence of the small size of the Ca^{2+} ion in comparison to the average cage size of the germanate network.

The germanate anomaly is manifest in the calcium germanate glass system as maxima in the mass and number densities and in the glass transition temperatures. As discussed in §5.3.3, the density maxima cannot be explained purely on the basis of changes in the average Ge-O coordination numbers, and the filling of network cages by modifier ions is an important factor, as may be changes in germanate ring statistics.

References

[1] A. K. Shirvinskaya, R. G. Grebenshchikov and N. A. Toropov, *Izv. Akad. Nauk SSSR, Neorg. Mater.* **2** (2), (1966), 332.

[2] A. J. Havel, S. A. Feller, M. Affatigato, M. Karns and M. Karns, *Glass Technol. Eur. J. Glass Sci. Technol. A* **50** (4), (2009), 227–229.

[3] J. Haines, O. Cambon, E. Philippot, L. Chapon and S. Hull, *J. Solid State Chem.* **166** (2), (2002), 434–441.

[4] J. Barbier and D. Levy, *Z. Kristallogr.* **212** (7), (1997), 519–528.

[5] J. E. Shelby, *J. Am. Ceram. Soc.* **66** (6), (1983), 414–416.

[6] K. Morinaga and K. Nakashima, *J. Non-Cryst. Solids* **103** (1), (1988), 108–116.

[7] Y. Tabata, Y. Ohta, K. Morinaga and T. Yanagase, *Journal of the Ceramic Association, Japan* **91** (11), (1983), 509–516.

[8] J. E. Shelby, *J. Am. Ceram. Soc.* **67** (8), (1984), 557–560.

[9] K. Kamiya, S. Sakka and T. Yoko, *Res. Rep. Fac. Eng., Mie Univ.* **7**, (1982), 107–119.

[10] A. Margaryan and M. L. Wai, *J. Mater. Sci. Lett.* **11** (22), (1992), 1511–1513.

[11] A. A. Margaryan and A. M. Narekatsyan, *Fiz. Khim. Stekla* **12** (4), (1986), 477.

[12] S. S. Kasymova, *Dokl. Akad. Nauk UzSSR* **1**, (1982), 36.

[13] P. Pernice, A. Aronne, M. Catauro and A. Marotta, *J. Non-Cryst. Solids* **210** (1), (1997), 23–31.

[14] S. Inaba, S. Oda and K. Morinaga, *J. Jpn. I. Met.* **65** (8), (2001), 680–687.

[15] D. Drouin, A. R. Couture, D. Joly, X. Tastet, V. Aimez and R. Gauvin, *Scanning* **29** (3), (2007), 92–101.

[16] R. Brydson, *Electron Energy Loss Spectroscopy* (Bios, 2001).

[17] G. S. Henderson, *J. Non-Cryst. Solids* **353** (18-21), (2007), 1695–1704.

[18] A. C. Hannon, *Nucl. Instrum. Meth. A* **551** (1), (2005), 88–107.

[19] E. Lorch, *J. Phys. C Solid State* **2**, (1969), 229.

[20] N. E. Brese and M. Okeeffe, *Acta Crystallogr. B* **47**, (1991), 192–197.

[21] A. C. Hannon and J. M. Parker, *Physics and Chemistry of Glasses Proceedings of the XIX International Congress on Glass* **43C**, (2002), 6–12.

[22] A. C. Hannon, D. Di Martino, L. F. Santos and R. M. Almeida, *J. Phys. Chem. B* **111** (13), (2007), 3342–3354.

[23] A. C. Hannon, D. Di Martino, L. F. Santos and R. M. Almeida, *J. Non-Cryst. Solids* **353** (18-21), (2007), 1688–1694.

[24] G. J. Redhammer, G. Roth and G. Amthauer, *Acta Crystallogr. C* **63**, (2007), I47–I50.

[25] H. Aust, H. Vollenkle and A. Wittmann, *Z. Kristallogr.* **144** (1-2), (1976), 82–90.

[26] W. Hilmer, *Acta Cryst.* **15**, (1962), 1101–1105.

[27] Y. I. Smolin, *Dokl. Akad. Nauk SSSR* **181**, (1968), 595–598.

[28] A. Y. Shashkov, N. V. Rannev and Y. N. Venevtsev, *Koordinats. Khim+* **10** (10), (1984), 1420–1426.

[29] D. M. Tobbens, V. Kahlenberg, C. Gspan and G. Kothleitner, *Acta Crystallogr. B* **62**, (2006), 1002–1009.

[30] E. R. Barney, A. C. Hannon, N. Laorodphan and D. Holland, *J. Phys. Chem. C* **115** (30), (2011), 14997–15007.

[31] U. Hoppe, R. Kranold, H. J. Weber and A. C. Hannon, *J. Non-Cryst. Solids* **248** (1), (1999), 1–10.

[32] A. C. Hannon and J. M. Parker, *J. Non-Cryst. Solids* **274** (1-3), (2000), 102–109.

[33] R. Bouchard, D. Hupfeld, T. Lippmann, J. Neuefeind, H. B. Neumann, H. F. Poulsen, U. Rutt, T. Schmidt, J. R. Schneider, J. Sussenbach and M. von Zimmermann, *J. Synchrotron Radiat.* **5**, (1998), 90–101.

[34] H. F. Poulsen, J. Neuefeind, H. B. Neumann, J. R. Schneider and M. D. Zeidler, *J. Non-Cryst. Solids* **188** (1-2), (1995), 63–74.

[35] M. Ueno, M. Misawa and K. Suzuki, *Physica B & C* **120** (1-3), (1983), 347–351.

[36] A. A. Bolzan, C. Fong, B. J. Kennedy and C. J. Howard, *Acta Crystallogr. B* **53**, (1997), 373–380.

[37] L. B. Skinner, A. C. Barnes, P. S. Salmon, H. E. Fischer, J. W. E. Drewitt and V. Honkimaki, *Phys. Rev. B* **85** (6), (2012), 064201.

[38] P. Hudon and D. R. Baker, *J. Non-Cryst. Solids* **303** (3), (2002), 354–371.

[39] P. Hudon and D. R. Baker, *J. Non-Cryst. Solids* **303** (3), (2002), 299–345.

[40] S. G. Bishop and P. J. Bray, *Phys. Chem. Glasses* **7** (3), (1966), 73–81.

[41] S. Greenblatt and P. J. Bray, *Phys. Chem. Glasses* **8** (5), (1967), 190–193.

[42] M. J. Park and P. J. Bray, *Phys. Chem. Glasses* **13** (2), (1972), 50–62.

[43] W. J. Dell and P. J. Bray, *Phys. Chem. Glasses* **23** (4), (1982), 98–100.

[44] Y. X. Tang, Z. H. Jiang and X. Y. Song, *J. Non-Cryst. Solids* **112** (1-3), (1989), 131–135.

[45] N. Ohtori, K. Takase, I. Akiyama, Y. Suzuki, K. Handa, I. Sakai, Y. Iwadate, T. Fukunaga and N. Umesaki, *J. Non-Cryst. Solids* **293**, (2001), 136–145.

[46] N. Ohtori, K. Takase, I. Akiyama, K. Handa, Y. Iwadate and N. Umesaki, *Phys. Chem. Glasses* **41** (6), (2000), 369–372.

[47] Y. D. Yiannopoulos, G. D. Chryssikos and E. I. Kamitsos, *Phys. Chem. Glasses* **42** (3), (2001), 164–172.

[48] A. C. Wright, *Phys. Chem. Glasses Eur. J. Glass Sci. Technol. B* **51** (1), (2010), 1–39.

[49] P. K. Gupta, M. L. Lui and P. J. Bray, *J. Am. Ceram. Soc.* **68** (3), (1985), C82–C82.

[50] J. F. Stebbins and S. E. Ellsworth, *J. Am. Ceram. Soc.* **79** (9), (1996), 2247–2256.

[51] T. J. Kiczenski, L. S. Du and J. Stebbins, *J. Non-Cryst. Solids* **351** (46-48), (2005), 3571–3578.

[52] S. Sen, Z. Xu and J. F. Stebbins, *J. Non-Cryst. Solids* **226** (1-2), (1998), 29–40.

[53] S. Sen, *J. Non-Cryst. Solids* **253**, (1999), 84–94.

[54] S. Sen, T. Topping, P. Yu and R. E. Youngman, *Phys. Rev. B* **75** (9), (2007), 094203.

[55] S. S. Uzun and S. Sen, *J. Phys. Chem. B* **111** (33), (2007), 9758–9761.

[56] J. S. Wu and J. F. Stebbins, *J. Non-Cryst. Solids* **356** (41-42), (2010), 2097–2108.

[57] O. Majerus, L. Cormier, G. Calas and B. Beuneu, *Phys. Rev. B* **67** (2), (2003), 024210.

[58] L. Cormier, O. Majerus, D. R. Neuville and G. Calas, *J. Am. Ceram. Soc.* **89** (1), (2006), 13–19.

[59] R. Akagi, N. Ohtori and N. Umesaki, *J. Non-Cryst. Solids* **293**, (2001), 471–476.

[60] T. Yano, N. Kunimine, S. Shibata and M. Yamane, *J. Non-Cryst. Solids* **321** (3), (2003), 137–146.

[61] T. Yano, N. Kunimine, S. Shibata and M. Yamane, *J. Non-Cryst. Solids* **321** (3), (2003), 147–156.

[62] F. Angeli, O. Villain, S. Schuller, T. Charpentier, D. de Ligny, L. Bressel and L. Wondraczek, *Phys. Rev. B* **85** (5), (2012), 054110.

[63] J. F. Stebbins, E. V. Dubinsky, K. Kanehashi and K. E. Kelsey, *Geochim. Cosmochim. Ac.* **72** (3), (2008), 910–925.

[64] J. F. Stebbins, *Nature* **351** (6328), (1991), 638–639.

[65] S. K. Lee and B. H. Lee, *J. Phys. Chem. B* **110** (33), (2006), 16408–16412.

[66] L. S. Du and J. F. Stebbins, *J. Phys. Chem. B* **110** (25), (2006), 12427–12437.

[67] N. P. Lower, J. L. McRae, H. A. Feller, A. R. Betzen, S. Kapoor, M. Affatigato and S. A. Feller, *J. Non-Cryst. Solids* **293**, (2001), 669–675.

[68] R. D. Shannon, *Acta Crystallogr. A* **32** (Sep1), (1976), 751–767.

[69] R. Zallen, *The Physics of Amorphous Solids* (John Wiley & Sons, 1983).

[70] H. J. Weber, *J. Non-Cryst. Solids* **243** (2-3), (1999), 220–232.

[71] S. Giri, C. Gaebler, J. Helmus, M. Affatigato, S. Feller and M. Kodama, *J. Non-Cryst. Solids* **347** (1-3), (2004), 87–92.

[72] U. Hoppe, *J. Non-Cryst. Solids* **248** (1), (1999), 11–18.

[73] M. Burgess, D. McClarnon, M. Affatigato and S. Feller, *J. Non-Cryst. Solids* **354** (29), (2008), 3491–3502.

[74] P. K. Gupta and J. C. Mauro, *J. Chem. Phys.* **130** (9), (2009), 094503.

[75] J. C. Mauro, P. K. Gupta and R. J. Loucks, *J. Chem. Phys.* **130** (23), (2009), 234503.

[76] J. C. Phillips, *J. Non-Cryst. Solids* **34** (2), (1979), 153–181.

[77] M. F. Thorpe, *J. Non-Cryst. Solids* **57** (3), (1983), 355–370.

[78] R. Kerner and J. C. Phillips, *Solid State Commun.* **117** (1), (2000), 47–51.

[79] J. C. Phillips and R. Kerner, *J. Chem. Phys.* **128** (17), (2008), 174506.

[80] T. J. Kiczenski, C. Ma, E. Hammarsten, D. Wilkerson, M. Affatigato and S. Feller, *J. Non-Cryst. Solids* **272** (1), (2000), 57–66.

[81] R. N. Mead and G. Mountjoy, *J. Phys. Chem. B* **110** (29), (2006), 14273–14278.

[82] T. Taniguchi, M. Okuno and T. Matsumoto, *J. Non-Cryst. Solids* **211** (1-2), (1997), 56–63.

[83] M. C. Eckersley, P. H. Gaskell, A. C. Barnes and P. Chieux, *Nature* **335** (6190), (1988), 525–527.

[84] M. C. Eckersley, P. H. Gaskell, A. C. Barnes and P. Chieux, *J. Non-Cryst. Solids* **106** (1-3), (1988), 132–136.

Chapter 6

Lead Silicate Glasses

6.1 Sample preparation and characterisation

6.1.1 Glass preparation

Lead silicate glasses were prepared by Gloria Lehr and Adam Vitale of Coe College, Cedar Rapids, IA 52402, USA. Powders of PbO (Aldrich, 99.9+ %) and SiO_2 (Aldrich, 99.6 %) were mixed in quantities to yield 10 g batches of glass with nominal compositions given in Table 6-1. The mixtures, in pure platinum crucibles, were placed into an electric furnace for 20 minutes. The hold temperature of the furnace was 1000 °C for the three highest lead compositions, 1300 °C for the lowest lead composition and 1200 °C for the two intermediate compositions of 50 and 60 mol% PbO. After this 20 minute period the crucibles were removed, the mass loss recorded, and then replaced into the furnace for an additional 10 minutes. The glass compositions calculated assuming mass loss due solely to volatilisation of PbO, are given in Table 6-2. The liquids, after the second period in the furnace, were vitrified using rapid twin-roller quenching. This involved their pouring from the crucibles into a 40 μm gap between two counter-rotating steel cylinders, with an estimated cooling rate of approximately 10^5 °C s^{-1} [1]. The resultant flakes of glass have a yellow-gold colour, which is faint at low lead concentrations, but becomes very strong at 80 mol% PbO. A number of such batches were produced in order to obtain sufficient volume (4 cm^3) for neutron diffraction experiments. This has the disadvantage of potentially introducing small variations in glass composition and thermal history between batches, but does have the advantage of reducing the spread in glass fictive temperature which occurs as a result of the difference in thermal histories between the liquid which first contacts the roller-quencher, and that which contacts last.

6.1.2 Density measurement

Volume measurements were made using a helium working fluid in a Quantachrome Micropycnometer calibrated using a metallic sphere of known volume. The mass densities of the glasses, calculated using the measured masses and volumes, are given in table 6-1, along with the atomic number densities and molar volumes derived from the same measurements. These are plotted for comparison with the large amount of literature data compiled in the SciGlass database [2], references therein, in Fig. 6-1. Since the mass density is dominated by the contribution from the PbO component, it demonstrates an almost linear increase with molar glass composition. This is not the case for the atomic number density which remains at a value close to that for vitreous silica up to about 40 mol% PbO, before beginning to decrease. The dashed line in Fig. 6-1 represents a linear fit to the mass densities from SciGlass [2] and has been used as a means to estimate the glass composition, see table 6-2.

6.1.3 Energy dispersive x-ray spectroscopy

Glass composition was measured using EDX in a Zeiss SUPRA 55-VP FEGSEM operating at an accelerating voltage of 20 kV. The compositions obtained in this manner are presented in Table 6-2.

6.1.4 Thermal analysis

Glass transition temperatures, T_g, were measured by Gloria Lehr and Adam Vitale of Coe College for each batch using a Perkin-Elmer DSC-7, and a heating rate of 40 °C min^{-1}. Table 6-1 lists the average values extracted and most of these agree, within experimental uncertainties, with those reported by Feller *et al.* [3], which were measured using the same heating rate. An exception is the 50 mol% PbO glass, for which the value in Table 6-1 is 41 °C higher than that measured previously [3].

6.1.5 Summary

Evidently the measured glass densities are in agreement with the vast majority of data available in the literature, indicating that there are no major differences between nominal and actual glass composition. This is supported by EDX measurements of the glass

Table 6-1 Mass and number densities, molar volumes and glass transition temperatures measured for six lead silicate glasses. The density measured for a silica reference is included. Uncertainties in parentheses.

Nominal mol% PbO	ρ_m g cm^{-3}	ρ_0 nm^{-3}	V_M cm^3 mol^{-1}	T_g ± 3 °C
0.00	2.208(22)	66.38(67)	27.22(38)	-
33.33	4.882(49)	66.49(84)	24.00(34)	471
50.00	5.954(60)	62.80(73)	23.93(31)	424
60.00	6.660(67)	60.94(68)	23.72(29)	384
66.67	7.137(71)	59.96(66)	23.50(29)	359
75.00	7.623(76)	56.40(60)	23.99(28)	337
80.00	7.951(80)	55.64(59)	23.87(28)	319

Table 6-2 Measured molar compositions for six lead silicate glasses. Uncertainties in parentheses.

Glass Composition in mol% PbO				
Nominal	Mass Loss	Density	EDX	ND
33.33	32.92(03)	35.9(0.8)	35.3(6)	35.0(5)
50.00	49.65(03)	51.2(1.1)	47.7(4)	50.5(5)
60.00	59.77(03)	60.8(1.3)	57.5(4)	60.0(5)
66.67	66.57(03)	67.5(1.4)	64.1(2)	66.0(5)
75.00	74.92(03)	74.3(1.6)	72.2(4)	75.3(5)
80.00	79.97(03)	78.1(1.6)	77.0(6)	79.5(5)

compositions, although it should be noted that the uncertainties reported in Table 6-2, are standard deviations, and that the systematic uncertainties are likely to be larger, typically 1 to 2 mol% PbO. Both the EDX measurements, and the compositions crudely estimated from the densities, indicate that volatilisation of PbO from the melt has led to reduced lead concentrations in the high lead glasses. This is not supported by the compositions estimated from mass loss measurements, but since these do not account for volatilisation during the final 10 minutes of melting, they are not necessarily inconsistent. An unexpected observation is that the nominally 33.3 mol% PbO glass appears to be lead-rich based on its density and the EDX measurement. This can only be attributed to uncertainties in the pre-melt batch composition. A single value for each glass composition is required for subsequent data analyses, and the values in the final column of Table 6-2 have been chosen. These values were derived using the neutron diffraction data, as described in §6.2.1, with the constraint that the silicon-oxygen coordination

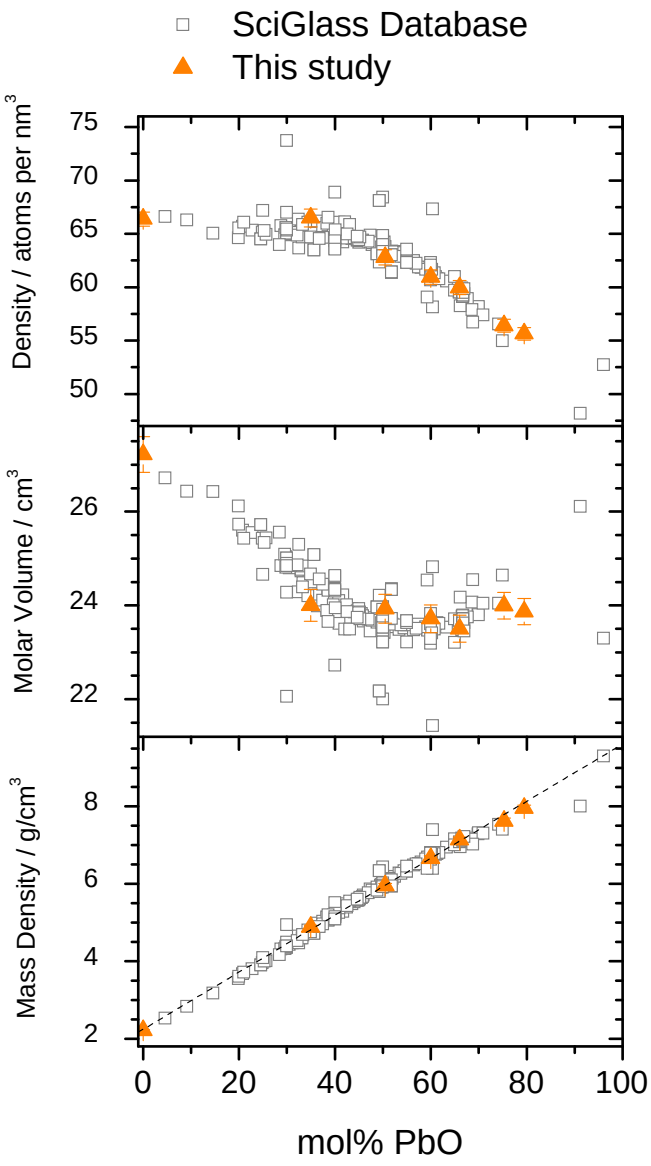

Figure 6-1 Measured mass and number densities and molar volumes for six lead silicate glasses, compared to data from the SciGlass database [2], references therein. Major outliers have been omitted. The dashed line represents a linear fit to the SciGlass mass density data.

number be 3.96 ± 0.05 (as measured for SiO_2, §B.3). This method is the most sensitive to changes in glass composition and it can be seen in Table 6-2 that it results in good qualitative agreement with other methods: a small reduction in PbO content for high lead glasses, and an increase in PbO content, with respect to nominal, in the low lead glass.

6.2 Total scattering measurements

6.2.1 Neutron diffraction

6.2.1.1 Distinct scattering and correlation functions

The neutron interference functions, $Qi^N(Q)$, measured on the GEM diffractometer [4], at the ISIS spallation neutron source are shown in Fig. 6-2 from 0 to 40 $Å^{-1}$. The functions $Qi^N(Q)$ (as opposed to $i^N(Q)$) emphasise the oscillations at large values of Q, and it is clear that the amplitude of these decrease with increasing lead content. The distinct scattering functions, $i^N(Q)$, on the other hand, show more clearly the scattering at low Q values, and these are shown in Fig. 6-3. It is apparent that the FSDP in vitreous silica at ~1.51 $Å^{-1}$ is replaced, in the lead silicate glasses, by a peak at ~2.0 $Å^{-1}$ which becomes increasingly sharp as Pb is added, and by a smaller pre-peak at ~1.1 $Å^{-1}$. Details of the low Q diffraction peaks, extracted by fitting of Lorentzian lineshapes to their leading edges, are summarised in Table 6-3, and example fits are illustrated in Fig. 6-4 for the $80\,PbO \cdot 20\,SiO_2$ glass. There are some clear trends with glass composition displayed by the peak parameters, in particular the derived periodicities, correlation lengths and their ratios $Q/\Delta Q$ all increase with PbO content, for both peaks, bar the periodicity associated with the ~2.0 $Å^{-1}$ diffraction peak which decreases as the lead content increases.

The counting statistics of the distinct scattering measurements were judged sufficient to permit Fourier transformation with a large $Q_{max} = 40\,Å^{-1}$, resulting in a real space resolution of 0.095 Å, or with modification by the Lorch [5] function, 0.136 Å. The total correlation functions are displayed in Fig. 6-5. Note that, in order to ensure the correct low r behaviour of $T^N(r)$ (oscillation about zero, with no slope), an effective renormalisation was applied to $i^N(Q)$ prior to transformation. Renormalisation factors were obtained by dividing $T^{N,0}(r)/r$ by the modulus of the low r slope of the differential correlation function, $D^N(r)$, obtained prior to renormalisation, which itself was obtained by fitting between $0 \leq r \leq 2$ Å, including the Si-O peak at ~1.6 Å. These factors account for uncertainties in the measured glass densities and compositions, as well as discrepancies in the normalisation of the diffraction data, but were typically 1.00 ± 0.01, with slightly larger deviations from unity for the 60 and 66 mol% glasses, being equal to 0.95. Fig. 6-5 shows that, as the glass composition is changed, there

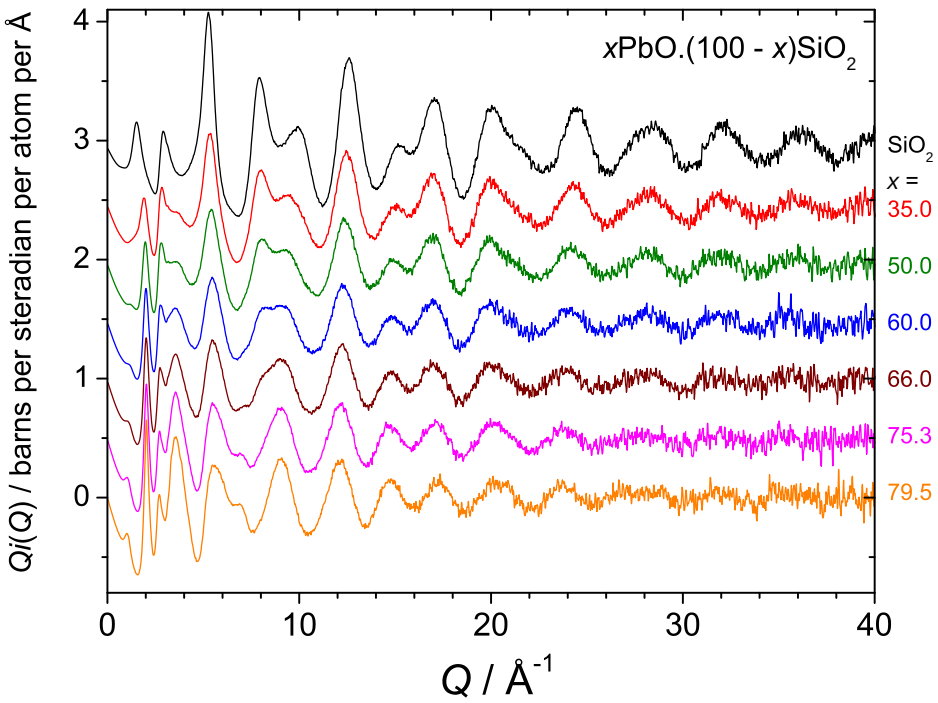

Figure 6-2 Neutron scattering interference functions for lead silicate glasses, as compared to that measured for vitreous silica, shown to emphasise the high Q region. The molar compositions are indicated on the plot and vertical offsets have been used for clarity.

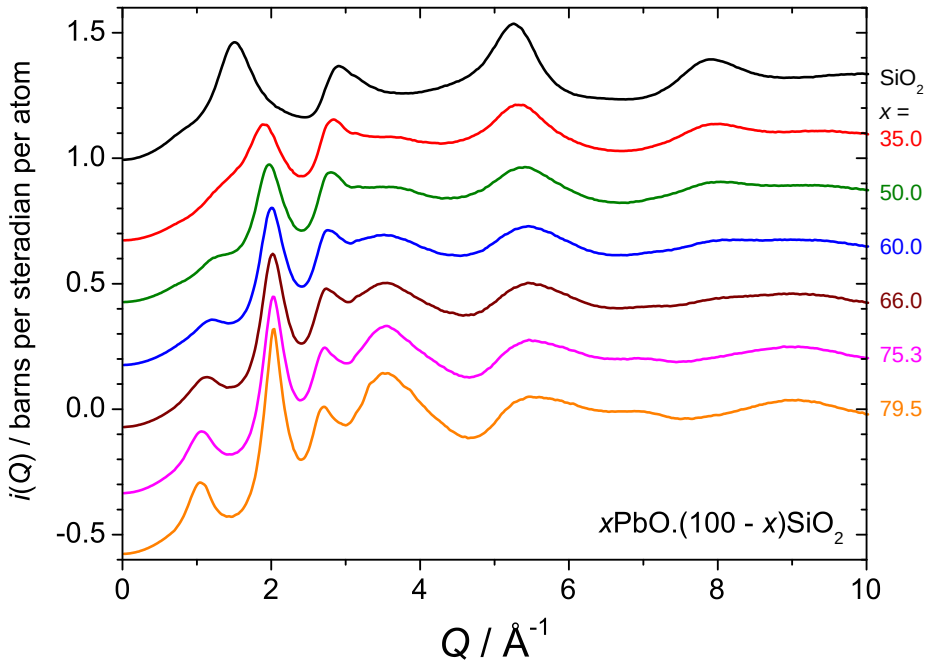

Figure 6-3 Distinct neutron scattering functions for lead silicate glasses, as compared to that measured for vitreous silica, shown to emphasise the low Q region. The molar compositions are indicated on the plot and vertical offsets have been used for clarity.

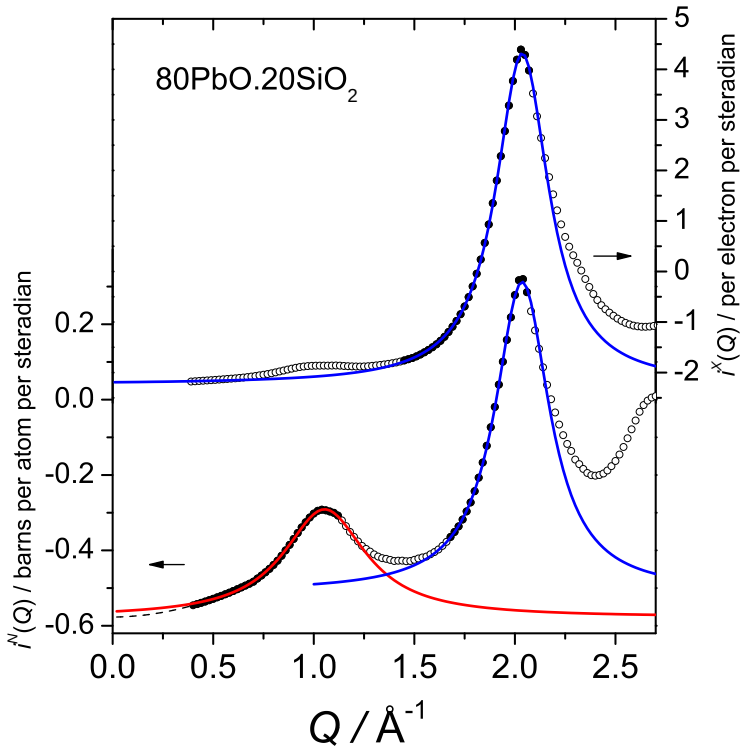

Figure 6-4 Lorentzian fits to the FSDP (~2.0 Å^{-1}) and pre-peak (~1.0 Å^{-1}) features of the low scattering vector magnitude regions of the distinct x-ray (upper) and neutron (lower) scattering functions from an 80 mol% PbO silicate glass. The experimental data are shown as open circles, which are filled in the fitting regions. The dashed line below 0.4 Å^{-1} is extrapolated from the neutron data using a quadratic function, and was not used during fitting.

are systematic changes in the heights of the three well resolved peaks at low r, and these peaks can be assigned to bonded Si-O at ~1.6 Å, bonded Pb-O at ~2.3 Å and O-O distances within [SiO_4] tetrahedra at ~2.7 Å, in accord with previous studies [6–9]. In order to extract quantitative information, in the form of average bond lengths, their RMS deviations, and coordination numbers, from the correlation functions, peak fitting with Gaussian distributions convolved with the appropriate peak function was attempted. Initially Si-O coordination numbers thus derived deviated from the value measured for vitreous silica of 3.96 ± 0.05 (§B.3), lying between 3.90 and 4.14. The latter value, for the nominally 80 mol% glass, was the largest discrepancy and this is consistent with uncertainties in the glass composition being the cause, since coordination numbers n_{ij}, as calculated, scale with $1/c_i$. Therefore n_{SiO} is much more sensitive to a given change in c_{Si} when c_{Si} is small. As such, the glass compositions were adjusted in order to yield

Table 6-3 Details of peaks at low neutron scattering vector magnitude in diffraction patterns from lead silicate glasses.

mol% PbO	Peak position Q (Å^{-1})	Peak width ΔQ (Å^{-1})	Associated periodicity $2\pi/Q$ (Å)	Correlation length $2\pi/\Delta Q$ (Å)	Number of periods $Q/\Delta Q$
			Pre-peak		
0	1.51(1)	0.61(1)	4.17(3)	10.3(2)	2.47(7)
60.0	1.24(1)	1.03(3)	5.08(4)	6.1(2)	1.20(4)
66.0	1.14(1)	0.80(1)	5.51(5)	7.8(1)	1.42(4)
75.3	1.07(1)	0.59(1)	5.86(5)	10.6(3)	1.80(6)
79.5	1.05(1)	0.50(1)	5.96(6)	12.6(4)	2.11(8)
			FSDP		
35.0	1.91(1)	0.57(2)	3.30(2)	11.0(4)	3.3(1)
50.5	1.97(1)	0.49(1)	3.19(2)	12.8(3)	4.0(1)
60.0	2.00(1)	0.42(1)	3.13(2)	15.0(4)	4.8(1)
66.0	2.02(1)	0.39(1)	3.11(2)	16.0(4)	5.1(2)
75.3	2.03(1)	0.35(1)	3.10(2)	17.7(5)	5.7(2)
79.5	2.04(1)	0.33(1)	3.09(2)	19.1(6)	6.2(2)

$n_{SiO} \simeq 3.96 \pm 0.05$, and the values obtained are listed in Table 6-2 under the heading ND. The magnitude of the changes are small and agree with those estimated both from the measured densities and by EDX. The compositions thus derived are considered the most accurate, and are used throughout the following.

6.2.1.2 Correlation function peak fits

Peak fitting of the corrected $T(r)$ (Fig. 6-5) was conducted in several steps as illustrated in Fig. 6-6. Initially the Si-O peak and the leading edge of the Pb-O feature were fitted. The area of the Si-O peak yields the O-Si coordination, $n_{OSi} = (c_{Si}/c_O)n_{SiO}$, which, based on the assumption of a corner sharing tetrahedral silicate subnetwork, can be used to predict the intratetrahedral ([SiO_4]) $n_{OO} = 3n_{OSi}$, and hence the area of the corresponding O-O peak in $T(r)$. Furthermore $r_{OO} = (8/3)^{1/2} r_{SiO}$, based on ideal tetrahedral geometry. The contribution of the intratetrahedral O-O separations to the total correlation functions can then be predicted, providing a final assumption regarding $\langle u^2_{OO} \rangle^{1/2}$ is made, and, to good approximation, the value is considered the same as measured for pure vitreous silica (see §B.3). This prediction of the O-O peak revealed a peak in the residual ($T(r)$ minus the Si-O, Pb-O and O-O peaks) at ~2.5 Å, assigned to longer Pb-O

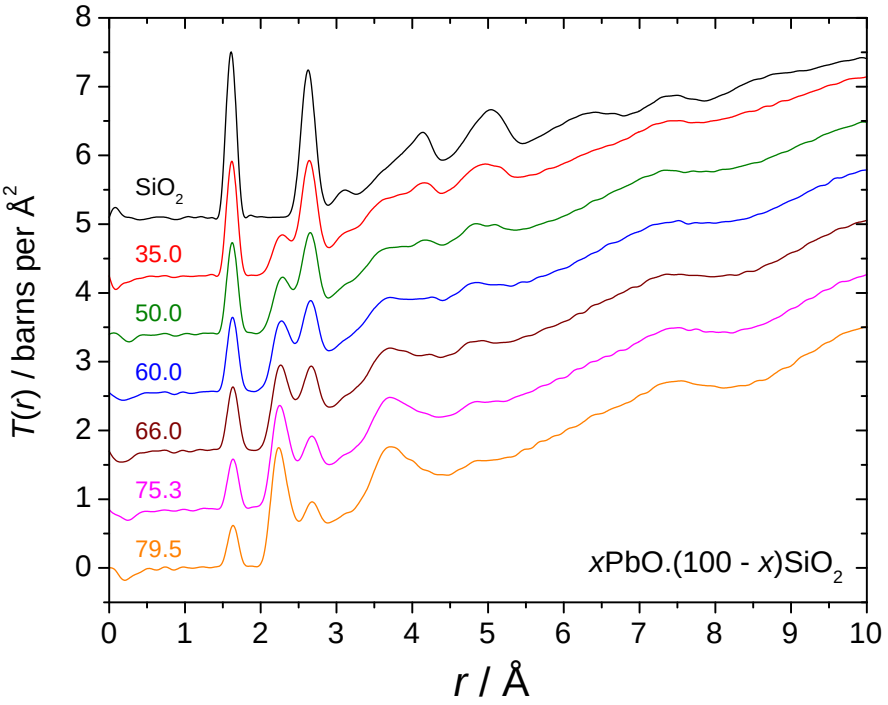

Figure 6-5 Neutron total correlation functions from lead silicate glasses, as compared to that measured for vitreous silica. A Lorch [5] modification function and $Q_{max} = 40\,\text{Å}^{-1}$ were used. Vertical offsets have been used for clarity.

bonds, see Fig. 6-6. Although fitting of multiple symmetric distributions to a clearly asymmetric Pb-O bond length distribution is somewhat arbitrary, it provides a convenient means for its characterisation, and the average coordination numbers calculated from the fits can be summed to give a total n_{PbO} and n_{OPb}.

The parameters derived from peak fitting are listed in Table 6-4 and show some clear trends with glass composition, key examples of which are illustrated in Fig. 6-7 and 6-8. From Fig. 6-7 it is apparent that the mean bond lengths and distribution widths are correlated in the cases of the Si-O and short (strong) Pb-O bond length distributions. Furthermore, the two distributions show analogous behaviour: r_{SiO} (r_{PbO}) and $\langle u^2_{SiO}\rangle^{1/2}$ ($\langle u^2_{PbO}\rangle^{1/2}$) tend to increase with decreasing SiO_2 (PbO) content. There is also a plateauing of r_{SiO} at about 75 mol% PbO, and a maximum in the width, $\langle u^2_{SiO}\rangle^{1/2}$, at about 66 mol% PbO. These two features are more reliable than the apparent decrease in r_{PbO} and $\langle u^2_{PbO}\rangle^{1/2}$ upon reducing the lead content from 50 to 35 mol% PbO, since the latter is evidenced by measurements on only a single glass (35 mol% PbO), whilst the aforementioned features of the Si-O bond length distributions are evidenced by measurements on two high lead glasses (75 and 80 mol% PbO).

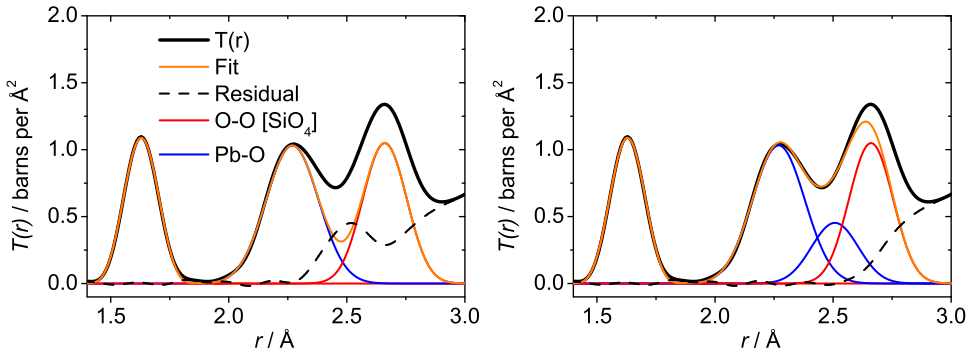

Figure 6-6 Example peak fits to the neutron total correlation function for $60\,PbO \cdot 40\,SiO_2$ glass. The left panel shows the result after fitting the Si-O peak (~1.6 Å) and the leading edge of the Pb-O feature (~2.25 Å), and includes the predicted O-O correlation arising from [SiO_4] tetrahedra (~2.65 Å). There is a clear peak in the residual at ~2.5 Å. The right panel shows the final result after fitting to the peak in the residual (attributed to longer Pb-O bonds) and allowing the two Pb-O peaks to adjust whilst keeping other peaks fixed.

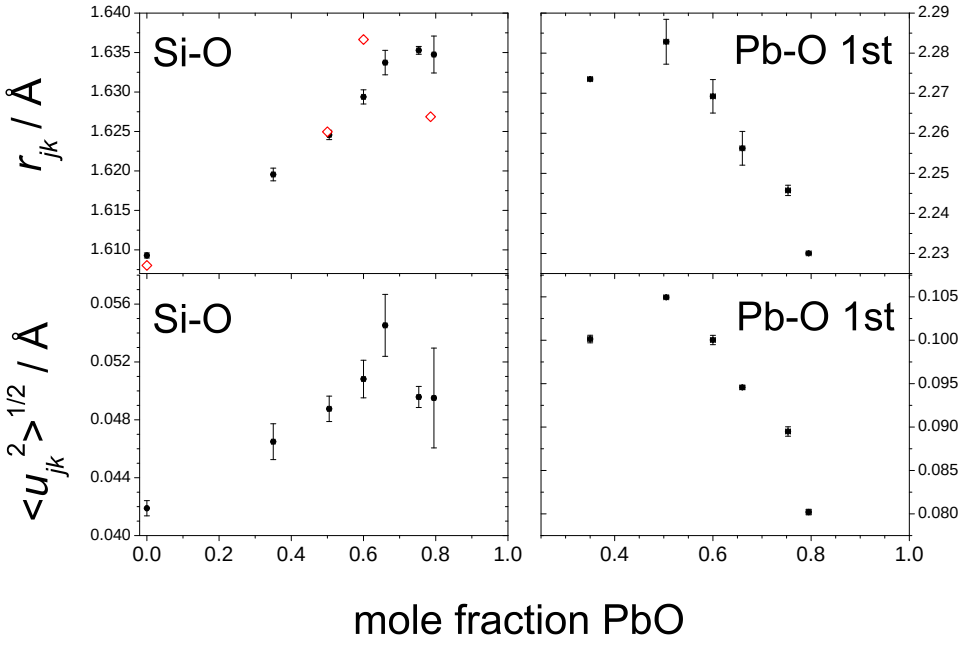

Figure 6-7 Mean lengths, r_{jk}, and widths, $\langle u_{jk}^2 \rangle^{1/2}$, for Si-O and short Pb-O bond length distributions, from fits to neutron total correlation functions from lead silicate glasses. Absolute values are listed in Table 6-4. The open diamonds represent the average Si-O bond lengths in quartz [10] and lead silicate crystals [11–14], see also Table 3-3. Note that in Pb_2SiO_4 [13], r_{SiO} = 1.6601 Å is unusually large, and is not within the range of the plot.

Table 6-4 Peak fit parameters from neutron total correlation functions from lead silicate glasses. Statistical uncertainties in parentheses.

Pair $j-k$	mol% PbO	r_{jk} (Å)	$\langle u_{jk}^2 \rangle^{1/2}$ (Å)	n_{jk}	n_{kj}
Si-O	35.0(5)	1.6196(8)	0.0465(12)	3.91(5)	1.54(2)
	50.5(5)	1.6246(6)	0.0488(9)	3.94(4)	1.31(1)
	60.0(5)	1.6294(9)	0.0508(13)	3.93(6)	1.12(1)
	66.0(5)	1.6337(16)	0.0545(21)	3.98(9)	1.01(2)
	75.3(5)	1.6353(5)	0.0496(7)	3.97(8)	0.79(1)
	79.5(5)	1.6348(23)	0.0495(35)	3.92(14)	0.67(2)
Pb-O	35.0(5)	2.2735(3)	0.1001(4)	2.57(3)	0.545(2)
	50.5(5)	2.2829(56)	0.1050(2)	2.46(2)	0.831(2)
	60.0(5)	2.2692(42)	0.1000(5)	2.38(2)	1.018(5)
	66.0(5)	2.2563(42)	0.0946(2)	2.37(1)	1.169(4)
	75.3(5)	2.2458(13)	0.0895(5)	2.32(2)	1.400(7)
	79.5(5)	2.2300(3)	0.0802(3)	2.29(1)	1.510(5)
Pb-O	35.0(5)	2.5015(15)	0.0794(13)	1.18(2)	0.250(3)
	50.5(5)	2.5127(8)	0.0692(9)	0.86(1)	0.289(2)
	60.0(5)	2.5077(24)	0.0856(19)	1.02(2)	0.437(7)
	66.0(5)	2.5025(14)	0.0937(9)	1.14(1)	0.563(4)
	75.3(5)	2.4598(30)	0.0799(25)	0.84(2)	0.510(10)
	79.5(5)	2.4227(10)	0.0705(15)	0.85(1)	0.562(7)
O-O $[SiO_4]^{\dagger}$	35.0(5)	2.6447(13)	0.07864(95)	4.47(11)	4.47(11)
	50.5(5)	2.6529(10)	0.07864(95)	3.82(8)	3.82(8)
	60.0(5)	2.6608(15)	0.07864(95)	3.27(8)	3.27(8)
	66.0(5)	2.6679(25)	0.07864(95)	2.95(10)	2.95(10)
	75.3(5)	2.6704(8)	0.07864(95)	2.30(5)	2.30(5)
	79.5(5)	2.6695(38)	0.07864(95)	1.95(9)	1.95(9)
Pb-O Total	35.0(5)			3.75(4)	0.795(3)
	50.5(5)			3.32(2)	1.120(3)
	60.0(5)			3.40(3)	1.456(9)
	66.0(5)			3.52(2)	1.733(6)
	75.3(5)			3.16(2)	1.910(13)
	79.5(5)			3.14(2)	2.071(9)
O-X Sum	35.0(5)			2.33(2)	
(X = Pb, Si)	50.5(5)			2.43(1)	
	60.0(5)			2.58(2)	
	66.0(5)			2.74(2)	
	75.3(5)			2.70(1)	
	79.5(5)			2.74(2)	

† Parameters fixed at those predicted from Si-O peak area and position and assumption of tetrahedral geometry. Width fixed at that measured for vitreous silica.

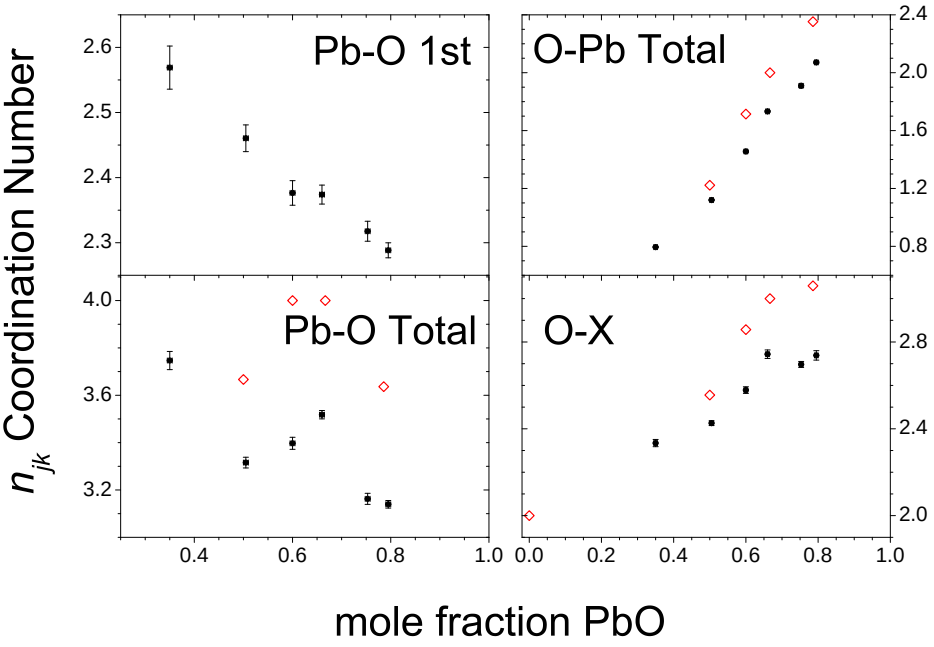

Figure 6-8 Coordination numbers from fits to neutron total correlation functions from lead silicate glasses. The numbers $n_{OX} = n_{OPb} + n_{OSi}$. Absolute values are listed in Table 6-4. The open diamonds represent the average coordination numbers in quartz [10] and lead silicate crystals [11–14] where cut-offs of 2.7 Å and 2.0 Å have been chosen for Pb-O and Si-O bonds respectively.

The Si-O coordination number was measured to be close to four in all six lead silicate glasses (both before and after renormalisation), and, on the basis of the known crystalline lead silicate crystal structures [11–16], and known silicate crystal chemistry in general, n_{SiO} is assumed to be exactly four (neglecting other species at point defect concentrations). From this follow the O-Si coordination numbers $n_{OSi} = n_{SiO}.(1 - x)/(2 - x)$ (x the mole fraction PbO) and the [SiO_4] intratetrahedral $n_{OO} = 3n_{OSi}$. Of greater interest are the local environments of the other atomic species, namely lead and oxygen. Fig. 6-8 shows some pertinent coordination numbers obtained from the areas of fitted peaks in $T^N(r)$, and it is apparent that there is a reduction in the number of short Pb-O bonds as the PbO content of the glass increases, although these bonds also become shorter (Fig. 6-7) and therefore stronger. Fig. 6-9 illustrates the evolution of the short Pb-O bond length distribution with glass composition since the functions $T^N(r)/2w_{PbO}$ plotted are equal to $t^N_{PbO}(r)$ in the regions of r where only Pb-O bonds contribute to the total correlation function.

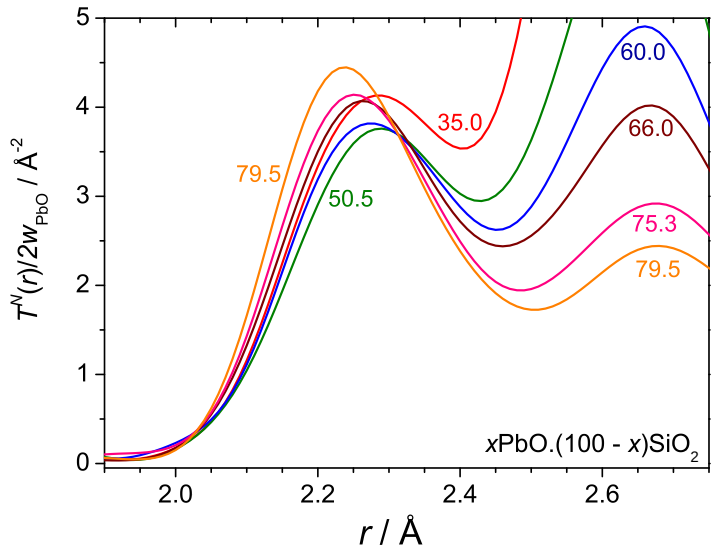

Figure 6-9 Neutron total correlation functions, $T^N(r)$, from lead silicate glasses, divided by the Pb-O weighting factors, w_{PbO}, in order to reveal $t^N_{PbO}(r)$ and directly compare the short Pb-O bond length distributions at ~2.25 Å. A Lorch [5] modification function and $Q_{max} = 40\,\text{Å}^{-1}$ were used. Colours are as in Fig. 6-5 and glass compositions are indicated within the plot.

6.2.2 X-ray diffraction

6.2.2.1 Distinct scattering and correlation functions

Wiggler beamline BW5 [17, 18] on the synchrotron radiation source DORIS III, HASYLAB at DESY, was used for x-ray diffraction measurements of the powdered lead silicate glasses, which were held inside 1.5 mm diameter silica glass capillaries (10 µm wall thickness). The x-ray energy of 84.768 keV (wavelength 0.14626 Å) makes accessible a large maximum scattering vector magnitude, $Q_{max} = 23.62\,\text{Å}^{-1}$. Interference

Table 6-5 Details of peaks at low x-ray scattering vector magnitude in diffraction patterns from lead silicate glasses.

mol% PbO	Peak position Q (Å^{-1})	Peak width ΔQ (Å^{-1})	Associated periodicity $2\pi/Q$ (Å)	Correlation length $2\pi/\Delta Q$ (Å)	Number of periods $Q/\Delta Q$
35.0	1.94(1)	0.52(1)	3.24(2)	12.1(2)	3.7(1)
50.5	1.98(1)	0.43(1)	3.18(2)	14.6(3)	4.6(1)
60.0	2.00(1)	0.39(1)	3.14(2)	16.1(4)	5.1(2)
66.0	2.01(1)	0.37(1)	3.13(2)	17.1(5)	5.5(2)
75.3	2.03(1)	0.34(1)	3.10(2)	18.4(5)	5.9(2)
79.5	2.04(1)	0.32(1)	3.09(2)	19.7(6)	6.4(2)

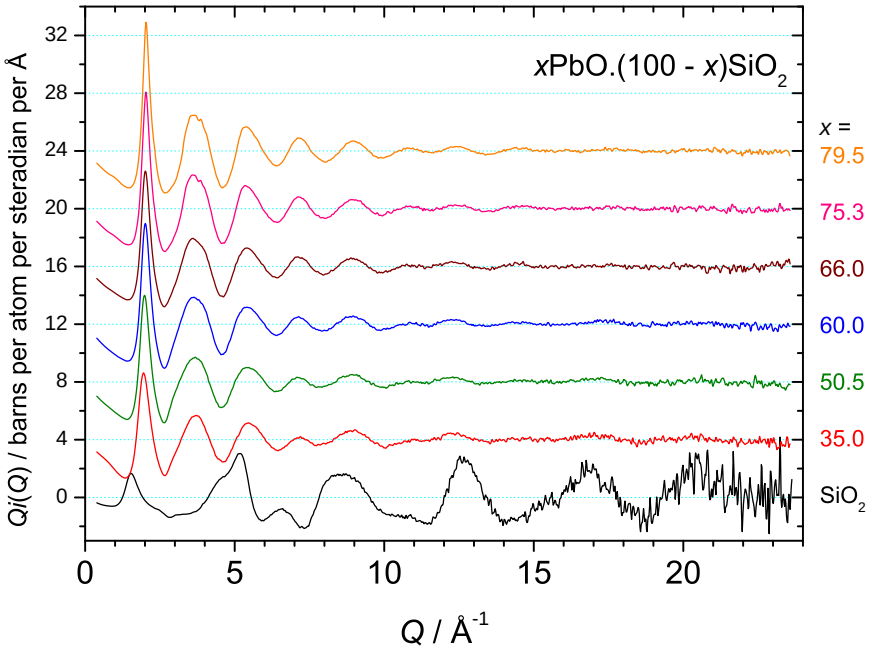

Figure 6-10 X-ray scattering interference functions for lead silicate glasses, as compared to that measured for vitreous silica, shown to emphasise the high Q region. The molar compositions are indicated on the plot and vertical offsets have been used for clarity.

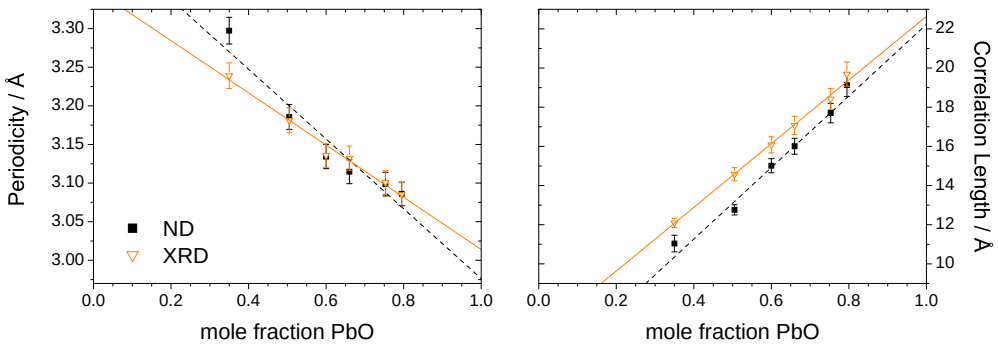

Figure 6-11 Periodicities, $2\pi/Q$, and correlation lengths, $2\pi/\Delta Q$, associated with the first sharp diffraction peak in x-ray and neutron scattering from lead silicate glasses. The lines are least squares fits to the points.

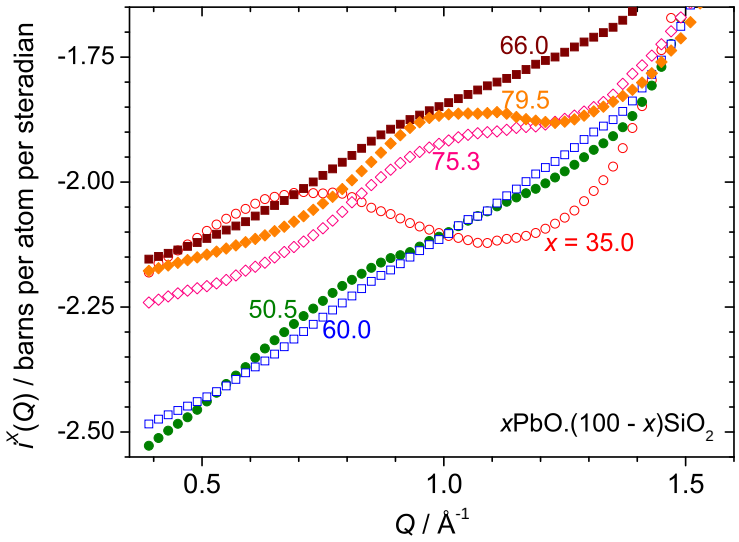

Figure 6-12 X-ray distinct scattering functions at low Q for lead silicate glasses. The molar compositions are indicated on the plot.

functions for the six roller-quenched lead silicate glasses, and for vitreous silica are shown in Fig. 6-10. The scattering for all of the lead containing glasses is dominated by the Pb-Pb term, and this presumably contributes to the largest diffraction peak at $\sim$2.0 Å^{-1}, which was also observed in the neutron diffraction patterns (Fig. 6-2, 6-3 and 6-4) and becomes increasingly sharp as the Pb content increases. Table 6-5 lists the positions and widths of the $\sim$2.0 Å^{-1} FSDP obtained by fitting of Lorentzian lineshapes to its leading edge, and an example fit is shown in Fig. 6-4. The associated periodicities and correlation lengths are plotted in Fig. 6-11 along with those obtained from neutron diffraction, Table 6-3. Both parameters show linear trends with molar glass composition, with the periodicity decreasing and the correlation length increasing with PbO content, both of which contribute to an increase in the approximate number of periods, $Q/\Delta Q$ (Tables 6-3 and 6-5), and hence the degree of intermediate range order present in the glass structure as PbO is substituted for SiO_2. Although the peak at $\sim$2.0 Å^{-1} dominates the x-ray scattering cross-sections, there are subtle features at lower Q values which can be seen upon close inspection of the distinct scattering functions, $i^X(Q)$, as shown in Fig. 6-12. The small peaks at $\sim$1.0 Å^{-1}, evident for the 75 and 80 mol% glasses, can be identified with their larger counterparts in the neutron diffraction patterns, Fig. 6-3, and their relative weightings for the two radiation types indicate that they arise from either Si-O or O-O terms since these do not contain Pb atoms which scatter x-rays strongly, and the Si-Si term is negligible. However, there exists another

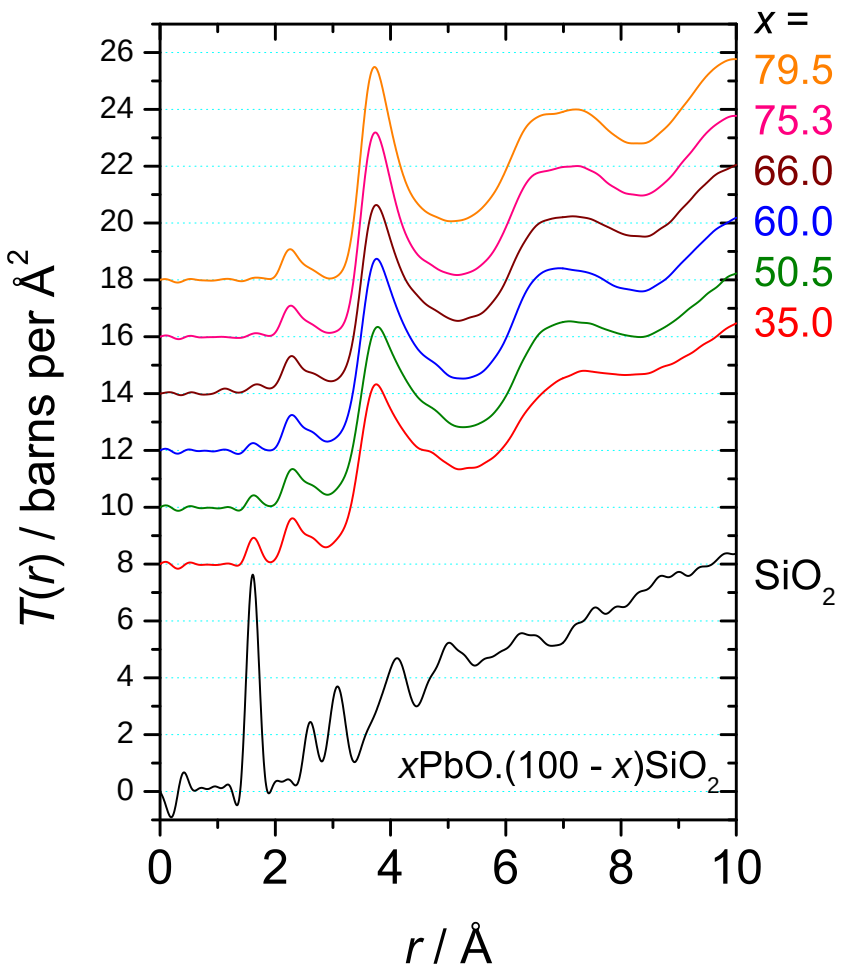

Figure 6-13 X-ray total correlation functions from lead silicate glasses, as compared to that measured for vitreous silica. A Lorch [5] modification function and Q_{max} = 23.57 Å^{-1} were used. Vertical offsets have been used for clarity.

remarkable feature, in the case of the 35 mol% glass at ~0.7 Å^{-1}. This does not have an obvious counterpart in the neutron diffraction pattern, and is similar to the feature previously observed by Kohara *et al.* [9].

The total correlation functions, obtained by Fourier transform of the interference functions in Fig. 6-10 are displayed in Fig. 6-13. They are all dominated by the Pb-Pb term, and increasingly so as the Pb content is raised, see the pair weighting factors, Fig. 4-1. Therefore the peak at ~3.7 Å, and subsequent oscillations at higher *r*, are due mainly to the distribution of Pb-Pb interatomic separations. Prior to these features the Pb-O bond length distribution is apparent at ~2.3 Å, and has a shoulder to the high *r* side, as expected from the fitting of the neutron total correlation functions. Fig. 4-1

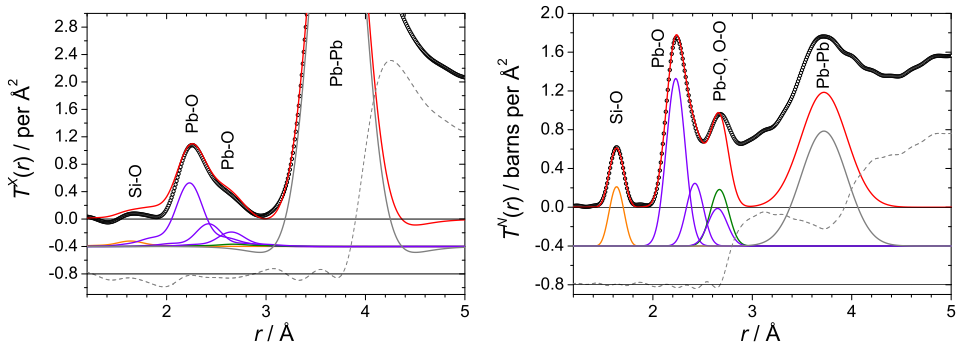

Figure 6-14 The x-ray and neutron total correlation functions for $80\,PbO \cdot 20\,SiO_2$ glass are shown over reduced regions of r (open circles, black) and with the sum of fitted peaks overlaid (solid line, red), with individual peaks offset below this, and residual further offset below.

shows that the x-ray weighting factors for pair terms not containing a Pb atom become negligibly small as the $80\,PbO \cdot 20\,SiO_2$ composition is approached, and this is reflected in the relative size of the Si-O peak at ~1.6 Å, which is barely visible for the highest lead glass $T^X(r)$.

6.2.2.2 Correlation function peak fits

Given the negligible contributions from Si-Si, Si-O and O-O terms to the x-ray scattering from the 80 mol% PbO silicate glass, peak fitting to $T^X(r)$ for this sample can be significantly simplified. Simulation of the four bond length distributions derived from $T^N(r)$, with weightings and broadenings appropriate to $T^X(r)$, allowed a third contribution to the Pb-O distribution to be fitted (to $T^X(r)$), centred at ~2.65 Å, along with the leading edge of the nearest neighbour (NN) Pb-Pb peak at ~3.72 Å, in the latter case neglecting *all* other terms including Pb-Si and Pb-O. A final adjustment to the ~2.65 Å Pb-O peak was made by simulating its contribution to $T^N(r)$ and allowing its parameters to adjust to fit the data, whilst keeping all other peaks fixed. Such a fitting procedure effectively favours the ND data over that from XRD, which is desirable based on the higher real-space resolution, and Q independence of the scattering lengths, in ND. Even so, Fig. 6-14 shows good agreement between the measured $T^X(r)$ and the peaks simulated on the basis of the fits to $T^N(r)$. The peak parameters are recorded in Table 6-6, where some values are repeated from Table 6-4 for completeness. What is clear is that fitting the neutron total correlation function alone, where the relative weighting of the O-O term is much higher, could not reveal the existence of the longest Pb-O bonds

Table 6-6 Parameters from peak fitting to $T^N(r)$ and $T^X(r)$ measured for the 80 mol% PbO silicate glass, see main text for details of the peak fitting procedure. Statistical errors from the fitting are given in parentheses. The final column indicates whether the values are obtained from fitting $T^N(r)$ or $T^X(r)$, see text for details.

Pair $j-k$	r_{jk} (Å)	$\langle u_{jk}^2 \rangle^{1/2}$ (Å)	n_{jk}	Origin
Si-O	1.6348(23)	0.050(3)	3.92(14)	N
O-Si			0.67(2)	N
Pb-O	2.2300(3)	0.0802(3)	2.29(1)	N
	2.4227(10)	0.071(2)	0.85(1)	N
	2.6507(34)	0.083(3)	0.63(2)	X + N
Total Pb-O			3.77(2)	X + N
Total O-Pb			2.48(2)	X + N
O-O $[SiO_4]^{\dagger}$	2.6695(38)	0.079(1)	1.95(9)	N
Pb-Pb‡	3.7204(17)	0.227(1)	8.02(4)	X

† Parameters fixed at those predicted from Si-O peak area and position and assumption of tetrahedral geometry. Width fixed at that measured for vitreous silica. ‡ Neglecting contributions from other terms, including Pb-Si and Pb-O.

present, and that the majority of the residual from $T^N(r)$ (Fig. 6-14), at around ~3 Å is most likely due to O-O distances within $[PbO_m]$ polyhedra. The latter point is based upon the lack of residual at ~3 Å after fitting $T^X(r)$, ruling out Pb-X terms, the negligible contribution of Si-Si scattering to $T^N(r)$ (Fig. 4-1), and the higher weighting of O-O compared to Si-O, which may have a minor contribution in the ~3 Å region. Taking the most probable Pb-O distance of ~2.23 Å, an intrapolyhedral O-O distance of ~3 Å gives an O-Pb-O angle of 84.5°, similar to that in crystalline $Pb_{11}Si_3O_{17}$ [14]. A detailed comparison of the glass and the 78.57 mol% PbO silicate crystal structure [14] is given in §6.3.3 (see also §3.4).

The approximations made during the fitting of $T^X(r)$ for the 80 mol% PbO silicate glass hold progressively less well as the PbO content decreases, and the terms other than the three Pb-X have higher relative weightings (Fig. 4-1). Fitting of $T^X(r)$ for the other glass compositions was therefore not attempted. Rather the peaks simulated from the parameters in Table 6-4 (from fitting $T^N(r)$) were simply compared to $T^X(r)$, and the extraction of further information was attempted by fitting the whole diffraction patterns simultaneously using EPSR modelling, see §6.3.

6.3 Empirical potential structure refinement

6.3.1 Preliminary refinements

EPSR models were derived by refinement against both the x-ray and neutron distinct scattering patterns simultaneously, for all six lead silicate glass compositions. Table 6-7 lists the reference potential parameters used, as well as the cubic box edge lengths, L, derived from the measured atomic number densities (Table 6-1) and the requested number of atoms of ≥ 4000. For all of the models $L \gtrsim 40\,\text{Å} > 2r_u = 24\,\text{Å}$, where r_u is the radius at which the potentials are fully truncated to zero. It is important to maintain $L/2 > r_u$ to avoid direct atomic self-interactions between the same atom in neighbouring cells of the periodic array. The only reference potential parameters varied as a function of glass composition were σ_{Si} and σ_{Pb}, to reflect the observed changes in average Si-O and Pb-O bond lengths (Fig. 6-7).

To obtain reasonable starting configurations for empirical potential structure refinement, Monte Carlo simulations were performed under the reference potentials. These began with a random distribution of atomic coordinates within the simulation box and a high temperature of 1027 °C (close to the temperature of the glass-forming melt) to

Table 6-7 Details of EPSR models for lead silicate glasses, including Lennard-Jones, ϵ and σ, parameters, partial ionic charges, q, in units of the electron charge, e, and minimum distances of approach, r_{jk}^{min}. The parameters σ_{Si} and σ_{Pb} were varied as a function of glass composition, to reflect the observed changes in average bond lengths (Fig. 6-7). The box sizes correspond to the cubic box edge lengths, which were derived from the measured atomic number densities (Table 6-1) and the requested number of atoms of ≥ 4000. U_{MC} and U_{EP} are total system energies after equilibration under the reference potentials, without and with empirical potentials, respectively, both at $T = 300$ K.

Model mol% PbO	Number of atoms	Box size Å	σ_{Pb} Å	σ_{Si} Å	U_{MC} kJ mol^{-1}	U_{EP} kJ mol^{-1}	R-factor $\times 10^{-3}$
35.00	4240	39.95	2.19	0.70	-744	-721	2.54
50.00	4000	39.94	2.19	0.70	-666	-664	2.90
60.00	4240	41.13	2.14	0.71	-607	-606	2.41
66.00	4212	41.26	2.09	0.73	-571	-566	0.79
75.00	4275	42.32	2.10	0.74	-508	-513	1.99
80.00	4400	42.92	2.10	0.72	-475	-490	1.93
Constant Parameters							
$\epsilon_O = 0.92$ kJ mol^{-1}, $\epsilon_{Pb} = 0.60$ kJ mol^{-1}, $\epsilon_{Si} = 2.49$ kJ mol^{-1}							
$\sigma_O = 3.16$ Å, $r_{PbPb}^{min} = 3.10$ Å, $r_{PbSi}^{min} = 3.00$ Å, $q_O = -1.0\,e$, $q_{Pb} = 1.0\,e$, $q_{Si} = 2.0\,e$							

increase the number of moves accepted. The total energy of the system was monitored until a minimum was reached, at which point the system temperature was lowered to 427 °C (close to the glass transition temperature range) and again equilibrated. Finally the temperature was reduced to 27 °C (close to ambient temperature during diffraction experiments) which tended to result in very similar widths for the simulated and measured Si-O bond length distributions evident in $T^R(r)$. After equilibration at this temperature, σ_{Si} and σ_{Pb} were refined manually to give the best agreement between the Si-O and Pb-O nearest neighbour peak positions in $T^R(r)$, resulting in the values recorded in Table 6-7.

EPSR of the models to the measured diffraction patterns was begun by requesting a non-zero energy amplitude for the empirical potentials. This was chosen to be ~10% of the total energy of the reference potential Monte Carlo simulation at $T = 300$ K. These total energies ranged from $-744\,\mathrm{kJ\,mol^{-1}}$ at 35 mol% PbO to $-475\,\mathrm{kJ\,mol^{-1}}$ at 80 mol% PbO (Table 6-7). It should be noted that the implementation of EPSR shell used was limited to 600 points per dataset, and with a step-size of $0.05\,\mathrm{\AA^{-1}}$, the data were modelled out to $Q_{max} = 30\,\mathrm{\AA^{-1}}$. Therefore, the full range of x-ray diffraction data were used, whilst the neutron diffraction data were effectively truncated (down from $Q_{max} = 40\,\mathrm{\AA^{-1}}$). It is evident from Fig. 6-2 and 6-15 that the effects of this truncation become small as the PbO content increases and the high-Q scattering decreases. It should also be noted that the x-ray diffraction data used in the derivation of the EPSR models were not subjected to smoothing using the top-hat convolution method, as in §6.2.2.1, Fig. 6-10, but rather the Compton scattering fraction was reduced as an approximate means of background removal.

The EPSR R-factors (eqn. 4-34) and system energies, U_{EP}, averaged over $> 10^3$ configurations are given in Table 6-7. R-factors of 2×10^{-3} are typical [19], and indicate that the models well reproduce the measured diffraction patterns, see Fig. 6-15. Note that systematic uncertainty in the measurements cannot be completely eliminated, and therefore $R = 0$ can never be reached, without transferring the uncertainty into unphysical features within the models. Recalling that, even in the ideal case, where at least $M(M+1)/2$ differently weighted total scattering datasets have been measured, a model capable of reproducing all of them is never unique and must be compared, or constrained, against other structural information whenever possible. In the present

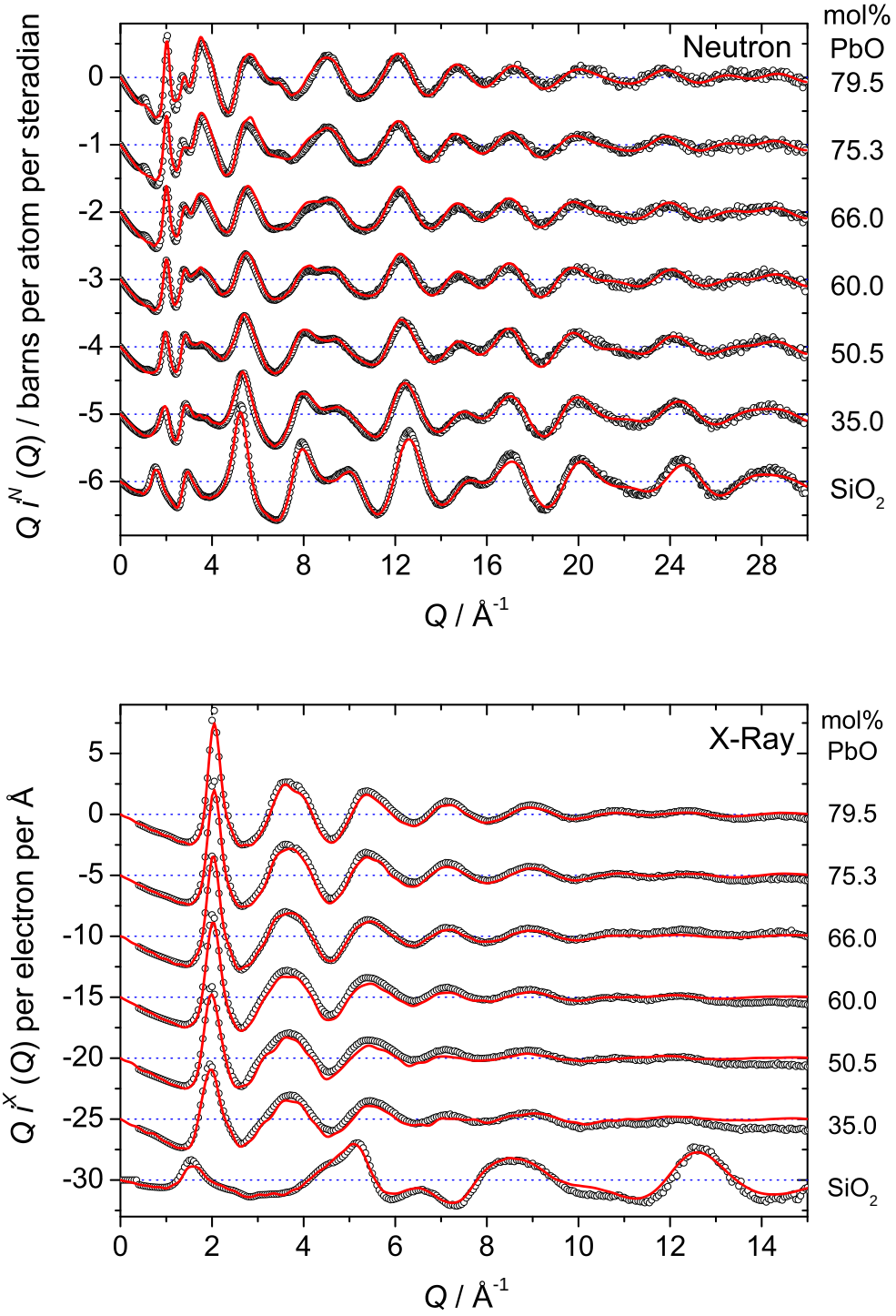

Figure 6-15 EPSR fits (solid red lines) to measured neutron and x-ray interference functions (open circles) from lead silicate glasses. PbO content decreases from top to bottom of each panel, and the model and experimental functions for vitreous silica (lowest) are shown for comparison (see Appendix B). Vertical offsets have been used for clarity.

study, $M = 3$ and $M(M+1)/2 = 6$, whilst only two differently weighted datasets have been used to generate the empirical potentials and derive atomistic models. Therefore, although averaging over many model configurations mitigates against the uniqueness problem to some extent, it is especially important to compare the models to additional information derived by other means. In this regard the available ^{29}Si MAS NMR data provide a key test of the models. Fig. 6-16 compares the Q^n-species distributions extracted from the ^{29}Si MAS NMR spectra of Feller *et al.* [3] to those of the EPSR derived models. Importantly, both the NMR and diffraction experiments were performed

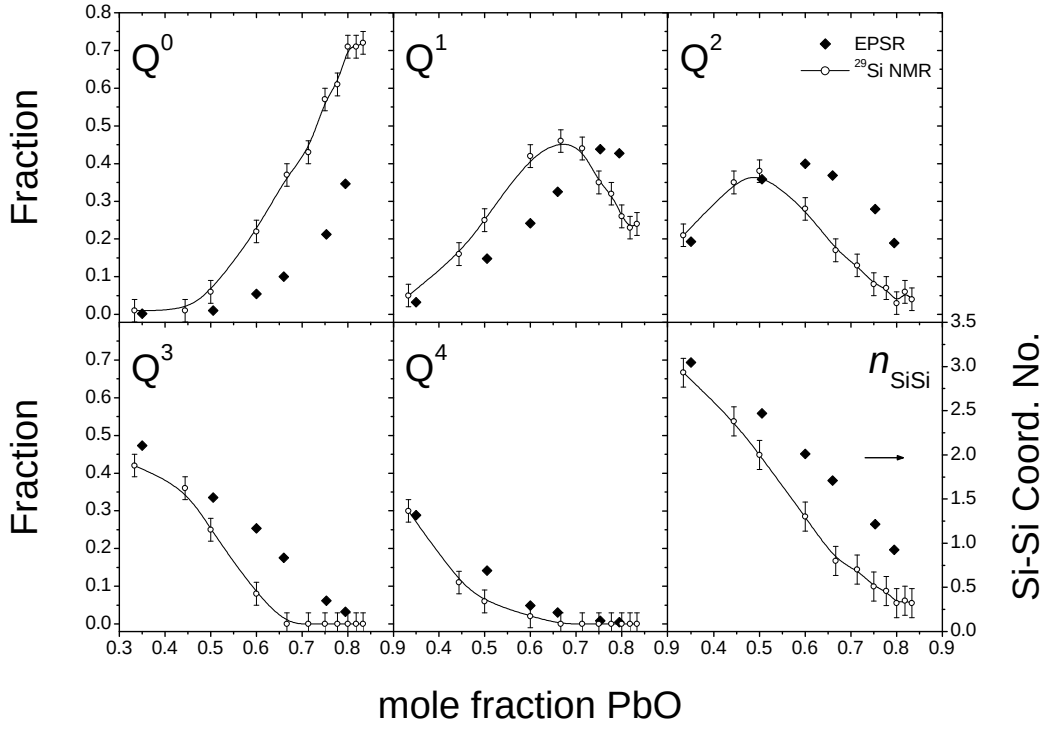

Figure 6-16 Distributions and average Si-Si coordination numbers in lead silicate glasses, from EPSR derived models (filled diamonds) and ^{29}Si MAS NMR [3] (open circles and spline fits).

on roller quenched glasses. The Q^n-species distributions were estimated from the models by calculating the Si-Si coordination number distributions with maximum distance cutoffs determined from the first minimum in $g_{SiSi}(r)$, Fig. 6-17. These were 3.62 Å in most cases, but reduced to 3.48 Å in the case of the 35 mol% PbO silicate glass. Average Si-Si coordination numbers were calculated from the reported Q^n-species distributions by summation over the fractional abundances, Q^n, using equation 2-1, and it is clear in Fig. 6-16 that these values are smaller than those of the corresponding EPSR models, particularly at high and intermediate mole fractions PbO (x). The reason for

the discrepancy becomes clear on inspection of the pair weighting factors, Fig. 4-1. The Si-Si term is small for all glass compositions for both x-ray and neutron radiations, but rapidly becomes negligible with increasing PbO content. As such, the Si-Si term is not directly constrained by the diffraction data and evolves, during modelling, primarily under the influence of the reference potentials. Notably, at 35 mol% PbO, where the Si-Si term has its highest relative weighting for the glass compositions studied, the model and NMR n_{SiSi} are in close agreement, and importantly, so are the full Q^n-species distributions (Fig. 6-16). As the PbO content increases, so the contribution of Si-Si pairs to the scattering data dwindles and the models become progressively overpolymerised as compared to the degree of polymerisation inferred from ^{29}Si MAS NMR measurements. Note that Kohara *et al.* [9] derived an RMC model of a lead silicate glass with 65 mol% PbO which is *under-polymerised* compared to ^{29}Si MAS NMR data [3, 8, 20] on glasses of the same composition. Interatomic potentials play no part in the RMC method, and hence it would appear that the over-polymerisation of the EPSR models occurs as a result of Si clustering under the influence of the interatomic potentials. This situation requires addressing, in both RMC and EPSR cases.

A further shortcoming of the high Pb glass EPSR models is that the low Q pre-peak at $\sim$1.0 Å^{-1} in the neutron diffraction patterns is not reproduced, Fig. 6-15. This is attributed to the capping of the magnitude of the empirical potentials, and is addressed in §6.3.3.

The following sections first discuss (§6.3.2) the trends of key structural parameters with glass composition, bearing in mind the quantitative discrepancies discussed above. §6.3.3 deals with the modelling of the high lead, 80 mol% PbO, silicate glass, including the introduction of various mechanisms to probe the uniqueness of the models, to incorporate the information on Si-Si coordination number distribution from ^{29}Si NMR, and to enable reproduction of the scattering pre-peak. The 35 mol% PbO silicate glass structure model is considered in more detail in §6.3.4, in light of the quantitative consistency with ^{29}Si NMR derived Q^n-species distribution (Fig. 6-16).

6.3.2 Empirical model structural trends with glass composition

Despite the imperfections in the models described above, many qualitative features of lead silicate glass structures and their relationship with chemical composition are

nonetheless captured, and the salient points are discussed in the present section. Furthermore, these models serve as starting points for comparison to the improved models discussed in §6.3.3 and §6.3.4.

6.3.2.1 Pair correlation functions

Fig. 6-17 shows the $g_{jk}(r)$ for all six unique atomic pairs and all six lead silicate glass models. As expected, the nearest neighbour Si-O peak varies little across the compositional series, arising from Si-O bond distances within [SiO_4] tetrahedra throughout. On the other hand, the Pb-O peak does change subtly, becoming sharper with increasing PbO content, consistent with the evidence from direct peak fitting, Fig. 6-7. The same is true for the Pb-Pb and Pb-Si NN peaks, whilst the longer range oscillations in $g_{PbPb}(r)$ and $g_{PbSi}(r)$ become more well defined with increasing PbO content in the glass. Notably $g_{PbO}(r)$ does not fall to zero after its first maximum, as $g_{SiO}(r)$ does, such that the Pb-O bond length distribution has an excess of longer bonds, and no well defined cut-off. Again, this is consistent with the evidence from peak fitting to $T^N(r)$ and $T^X(r)$ in §6.2.1.2 and §6.2.2.2. The function $g_{OO}(r)$ shows two peaks at low r, one at ~2.65 Å corresponding to [SiO_4] intratetrahedral correlations, and another at ~3.18 Å corresponding to O-O distances within lead-oxygen polyhedra. This implies an O-Pb-O bond angle of ~91° between two short (2.23 Å) Pb-O bonds. The $g_{SiSi}(r)$ are poorly constrained by the diffraction data, particularly for the high lead glasses, and their structure arises predominantly from interactions under the reference potentials and indirect constraint by other pair terms.

6.3.2.2 Coordination number distributions

The left hand column of Fig. 6-18 shows average CNs for selected atom pairs, within distance windows indicated in Fig. 6-17. The Si-O, O-Si, and O-O (0 to 2.88 Å) shown in the top left panel behave as expected for [SiO_4] tetrahedra, whilst n_{SiSi} is typically higher than measured by ^{29}Si MAS NMR [3], as discussed above (§6.3.1), and shown in Fig. 6-16. The Pb-O CNs, calculated within three different distance windows, are all approximately constant as a function of glass composition. This is a remarkable result, and is apparently in contradiction to the decrease in n_{PbO} reported in Table 6-4 and Fig. 6-8 from peak fitting to $T^N(r)$. However, this may well be an artefact of the peak fitting

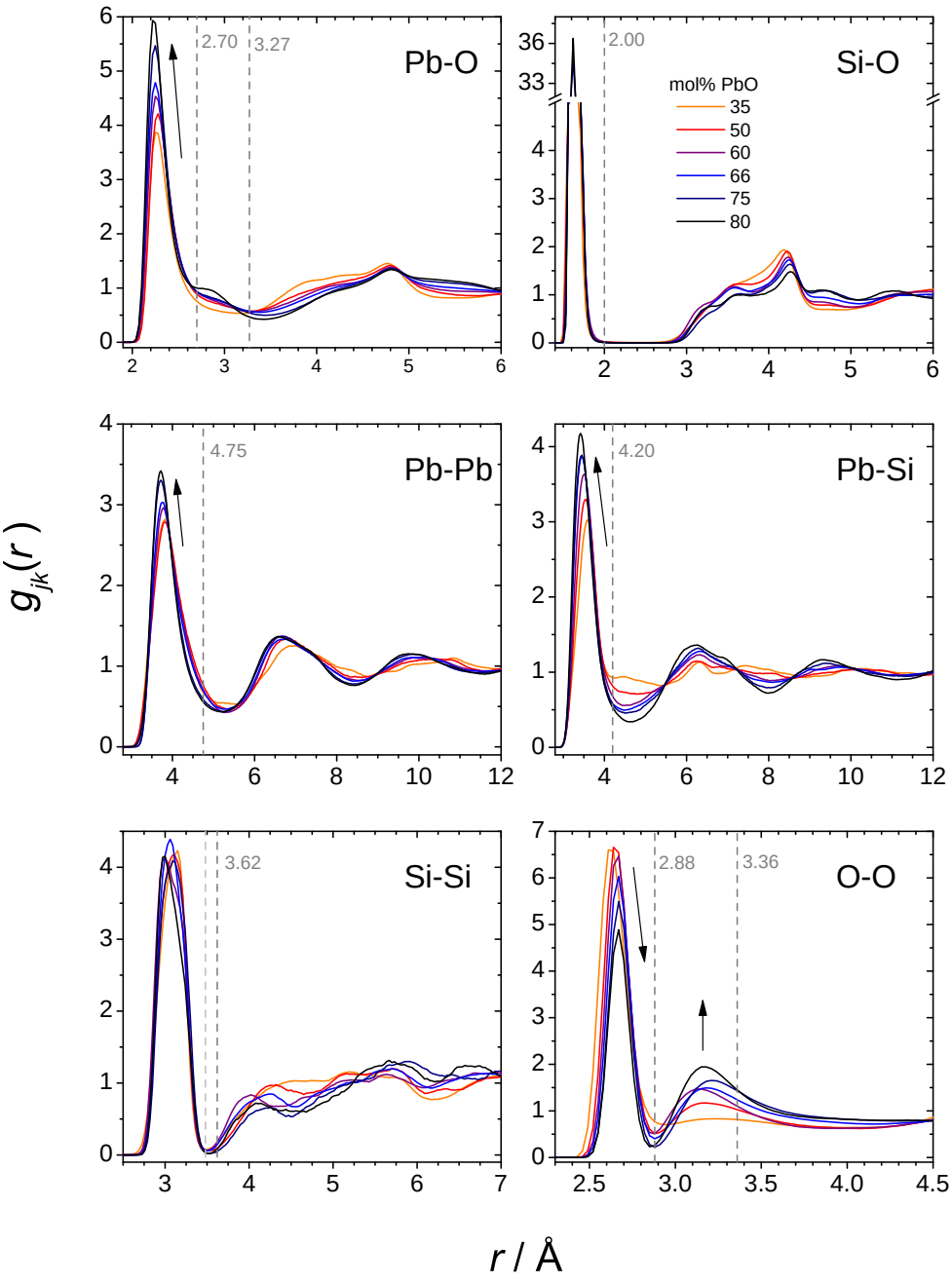

Figure 6-17 Pair correlation functions for lead silicate glass models, derived by EPSR. Arrows indicate the direction of change with increasing PbO content of the glass. Vertical dashed lines indicate upper cut-offs for distance windows used in determination of coordination number and bond angle distributions, with their positions in Ångström given. The lower Si-Si cut-off shown is at 3.48 Å and was used in place of 3.62 Å only for the 35 mol% PbO glass.

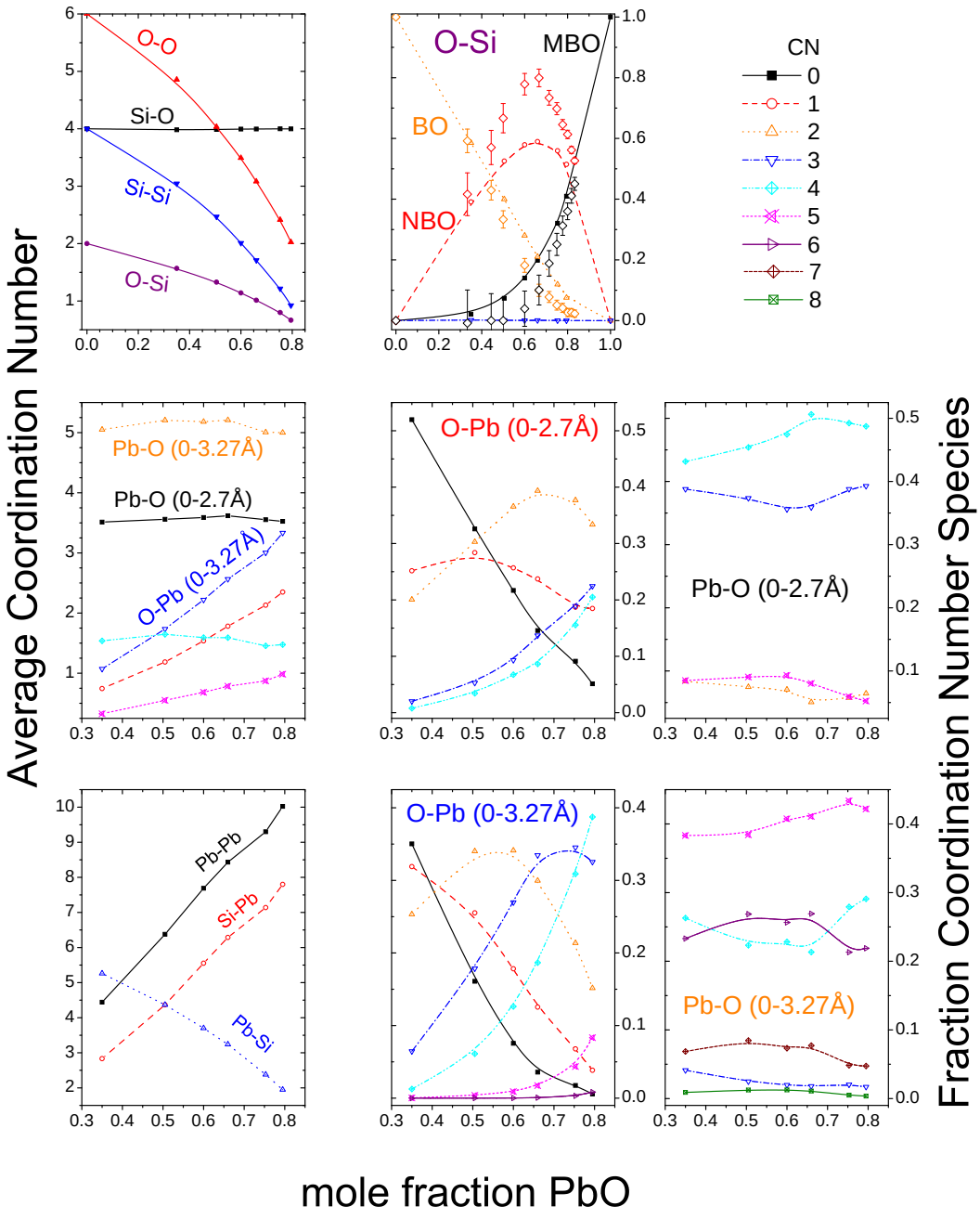

Figure 6-18 Averages (left hand column) and distributions (middle and right hand columns) of coordination numbers for atom pairs within EPSR derived models of six lead silicate glasses. The different Pb-O distance windows used are indicated. Average Pb-O and O-Pb CNs are shown for distance windows of $0 \leq r_{PbO} \leq 2.7$ Å, $0 \leq r_{PbO} \leq 3.27$ Å and $2.7 \leq r_{PbO} \leq 3.27$ Å. For clarity, not all are labelled on the plot (left middle) but Pb-O CNs are approximately constant across the compositional range, whilst O-Pb CNs rise with PbO content, and the $2.7 \leq r_{PbO} \leq 3.27$ Å window contains the smaller contribution to the total (within $0 \leq r_{PbO} \leq 3.27$ Å). Assumed values for mole fractions PbO of $x = 0$ and 1 are shown in some cases. Lines are guides to the eye. The Si-Si CN distribution is shown in Fig. 6-16. The O-Si CN distributions derived from ^{29}Si MAS NMR [3] are shown as open diamonds for comparison.

procedure, which was limited to fitting of Pb-O peaks at shorter interatomic distances than the intratetrahedral O-O separation. Given $n_{PbO} \approx$ a constant, $n_{OPb} = (c_{Pb}/c_O)n_{PbO}$ naturally increases with PbO content, and the values are very similar to those of the crystalline lead silicates calculated in the same manner (Fig. 6-8). The rise of the Pb-Pb and Si-Pb CNs with PbO content is related to the increase in O-Pb CN, as well as to the breakdown of the silicate network and its concurrent replacement by a plumbite based one.

The existence of a plumbite subnetwork within the lead silicate glasses is necessary at PbO contents greater than $x = 2/3$ (mole fraction PbO). In the EPSR models, MBOs, or plumbite oxygen atoms, bonded only to Pb, exist in all of the glasses, as can be seen in the central upper panel of Fig. 6-18. This is a result of speciation reactions of the type 2Si-O-Pb $\longrightarrow$ Pb-O-Pb + Si-O-Si (2NBO $\longrightarrow$ MBO + BO), the occurrence of which is supported by ^{29}Si MAS NMR [3, 20]. However, given the overpolymerisation of the models (excess of BO), the fraction of MBO must also be overestimated with respect to the ^{29}Si MAS NMR interpretation. Quantitative comparison of the models to the evidence from silicon NMR is possible by calculation of the O-Si coordination species distributions (CNDs) from the Q^n-species distributions using equations 2-2, 2-3 and 2-4, as well as the fact that $n_{SiO} = 4$. As is evident from the upper panel of Fig. 6-18, the models do indeed overestimate the fractions f_{MBO} and f_{BO}, and underestimate f_{NBO} in order to maintain the correct average n_{OSi}.

In addition to the approximate invariance of n_{PbO} with glass composition, the Pb-O CNDs (Fig. 6-18) also vary little with PbO content. Most Pb are coordinated by three or four oxygen at short (< 2.7 Å) distances, but typically have zero to three longer bonds, giving total coordination numbers of five, four and six ($r_{PbO} < 3.27$ Å). As such, it is the oxygen environments that change drastically with glass composition, as opposed to the cationic ones. The O-Pb CNDs show that, at low PbO content, oxygen atoms are coordinated by zero (BO), one or two Pb atoms, whilst at high PbO contents, these numbers rise typically to two, three or four Pb.

6.3.2.3 Bond angle distributions

BADs were calculated from the EPSR models using the distance windows defined in Fig. 6-17, and those for selected atom triplets are plotted as histograms in Fig. 6-19. As

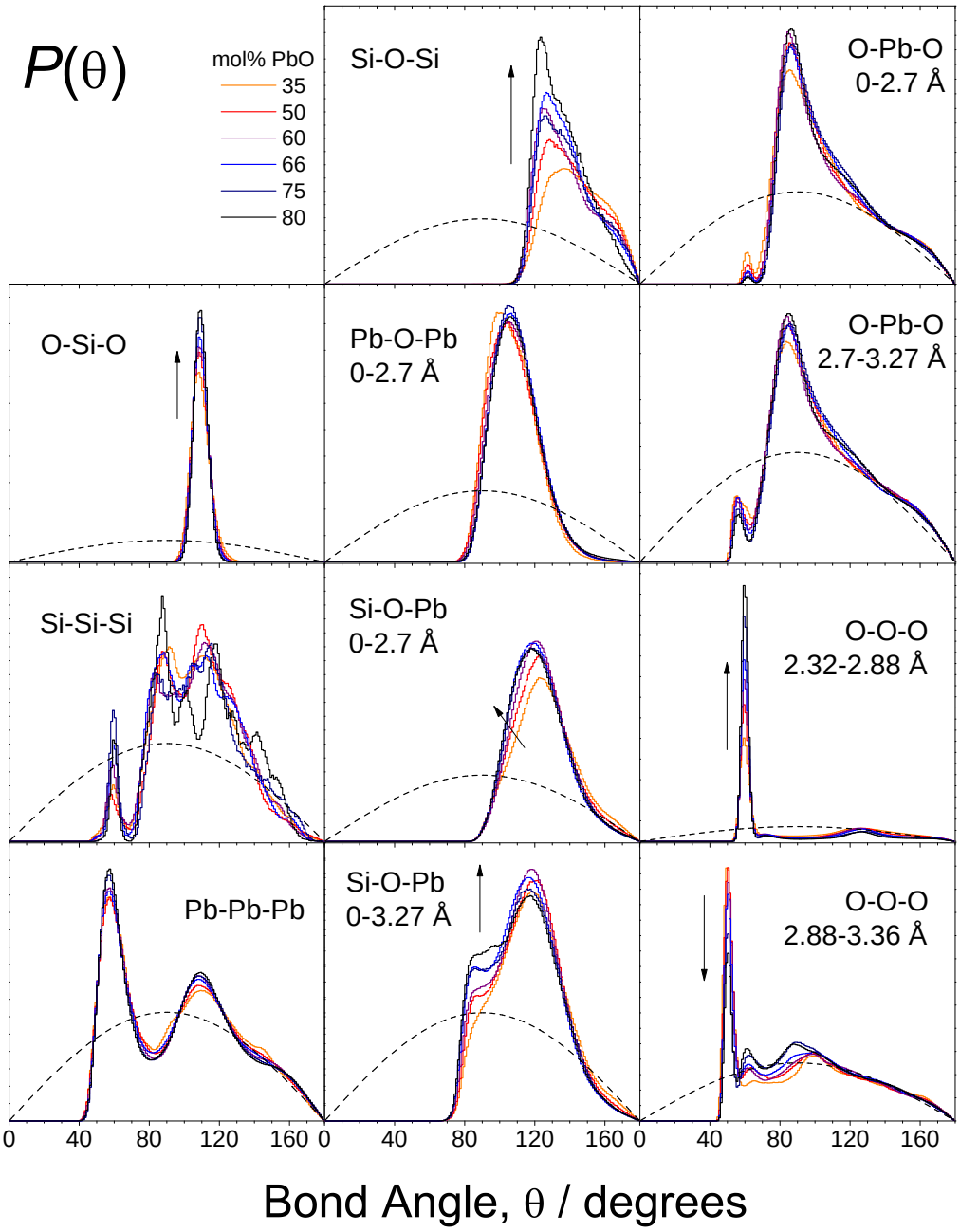

Figure 6-19 Bond angle distributions for atom triplets within EPSR derived models of six lead silicate glasses. The distances indicated are either Pb-O or O-O distance windows used to define atom pairs included in the triplets. All other distance windows are indicated in Fig. 6-17. Arrows indicate the direction of change in the BAD with increasing PbO content of the glass. Dashed lines are proportional to $\sin\theta$ and represent the random BAD limit. Histogram bins of 1° were used.

expected, the mean O-Si-O angles are narrowly distributed about the tetrahedral angle of 109.47°, although there is also an apparent sharpening of the BAD with increasing PbO content, as the silicate network depolymerises and individual tetrahedra become less constrained. Remarkably, the O-Pb-O BADs change little with glass composition, again, as for the CNDs (§6.3.2.2), pointing toward a structural invariance of the Pb environment with glass composition. The O-Pb-O BADs peak at ~86° but have a broad shoulder spanning the obtuse angle region. This BAD morphology is similar to that of crystalline $Pb_{11}Si_3O_{17}$, which contains 22 Pb sites, the majority of which are distorted trigonal and square pyramidal environments (see §3.4.4). A more detailed discussion of the O-Pb-O BAD is given in §6.3.3.

Similarly to the O-Pb-O BAD, the Pb-O-Pb BAD changes relatively little with glass composition. The Pb-O-Pb BADs are broadly distributed about mean values close to the tetrahedral angle, although note that these differ from the peak values (~100° at low PbO content to ~106° at high PbO content) which are at lower θ. A similar distribution is evident in α-PbO, where the O atoms occupy slightly distorted [OPb_4] tetrahedral sites, with four internal bond angles of 105.45°, two of 117.85°, and mean value 109.58°. Therefore, in the glasses, the oxygen environments tend toward a distribution about that of the O site in α-PbO (see also the O-Pb CNDs, §6.3.2.2). Note that at lower PbO contents the peak, and mean, Pb-O-Pb angles are smaller, which implies that, where multiple Pb atoms coordinate a NBO, there is steric repulsion between the coordinating Si (higher valence and shorter bonds to O, compared to Pb) and the Pb. This is supported by the Si-O-Pb BADs having larger peak (~124° at low PbO content to ~118° at high PbO content) and mean (~126° at low PbO content to ~122° at high PbO content) values than the Pb-O-Pb BADs. The decrease in peak and mean Si-O-Pb bond angles with increasing PbO content (see Fig. 6-19) is a consequence of the increasing number of Pb atoms coordinating NBOs. This has consequences for the average Si-O bond length, because a decrease in Si-O-Si, and presumably Si-O-Pb, angle results in elongation of the Si-O bond (see §3.4.2) which is exactly what is directly observed in the glasses by diffraction (Fig. 6-7), and indeed in the lead silicate crystals.

Interpretation of the O-O-O BADs, Fig. 6-19, is complicated by the fact that the silicate and plumbite intrapolyhedral O-O bond length distributions (Fig. 6-17) are not fully resolved in $g_{OO}(r)$. Nonetheless, the O-O-O BAD calculated for O-O distances up

to 2.88 Å contains a sharp peak at 60°, as expected from the equilateral triangular faces of [SiO_4] tetrahedra. Considering longer O-O distances (2.88 Å to 3.36 Å), the O-O-O BAD contains a peak at ~50°, which may correspond to a similar three body correlation to that of an oxygen triplet within a square based [PbO_4] pyramid, where an angle of 45° occurs between a pair on opposite corners of the basal plane, and a pair defining one edge of the same plane. Note that peaks in this O-O-O BAD at ~60° and ~90° emerge at higher PbO contents, which are internal angles for trigonal and square based pyramids respectively. Again, it should be mentioned that interpretation of the O-O-O BADs is complicated, and that they contain both intra- and interpolyhedral contributions.

Finally, the Si-Si-Si and Si-O-Si BADs are not expected to be representative of the real glasses, given that the models contain excess BOs. The various peaks in the Si-Si-Si BADs may well correspond to internal angles of different silicate rings, for example that at 60° may correspond to three-membered rings (containing three [SiO_4] tetrahedra), whilst subsequent peaks appear close to 90, 108 and 120°, corresponding to four, five and six membered rings. Unfortunately, no algorithm suitable for extraction of the ring size distributions was available at the time of writing.

6.3.3 High lead silicate glass structure models

6.3.3.1 Introduction

The present section aims to address some of the shortcomings of the preliminary EPSR derived models, discussed above (§6.3.1). Namely these were:

1. the quantitative differences in Q^n speciations between the high Pb silicate glass EPSR derived models and those derived from ^{29}Si MAS NMR spectra obtained from similarly rapidly quenched glasses [3].
2. the lack of a pre-peak at ~1.0 $Å^{-1}$ in the EPSR model diffraction patterns, which is clearly observed in the neutron diffraction patterns of the high Pb silicate glasses.

The highest Pb content glass (nominally 80 mol% PbO) was chosen for improved modelling, as it is the most dominated by the lead-oxygen subnetwork, and is therefore the most novel composition. Initially, the following changes were made to the modelling process with respect to those stated in §6.3.1:

1. the maximum allowed amplitude of the empirical potential was increased to ~30% of $U_{MC}(T = 300\ \mathrm{K})$, which was sufficient to allow the ~1.0 $\mathrm{Å}^{-1}$ pre-peak to be reproduced by the model distributions.
2. the radii at which the pair potentials were truncated were increased by a factor 4/3 to $r_l = 12$ Å and $r_u = 16$ Å.

The second point was found necessary after the increase in empirical potential amplitude. With the original, smaller, $r_u = 12$ Å, anomalous features in the real space $T^R(r)$, and in particular in $g_{PbPb}(r)$, appeared as a result of the truncation, resulting in spurious oscillations of period ~0.5 $\mathrm{Å}^{-1}$ in the model diffraction patterns. This is a consequence of the sharpness of the FSDP (see Table 6-5), the corresponding long correlation length, and the high weighting of the Pb-Pb term (particularly for x-ray scattering). Note also that the x-ray diffraction data used here were subject to smoothing by the top-hat convolution method, as in §6.2.2.1, and the Compton scattering fraction was not reduced as in §6.3.1.

6.3.3.2 A set of models to address the uniqueness problem

Four different models were derived, each labelled for convenience as the:

1. ionic model,
2. Q^0 model,
3. lone-pair model,
4. Q^0 + lone-pair model.

Their nomenclature should become clear from the following. The ionic model was constructed in the same way as the models of §6.3.1, but with larger empirical potential amplitude and potential truncation radii. The Q^0 model was identical in all respects, other than the inclusion of an additional minimum distance term, applied to Si-Si pairs, with $r^{min}_{SiSi} = 3.5$ Å. This was introduced to force depolymerisation of the silicate subnetwork, and hence to bring the model Q^n speciation into closer agreement with that derived from ^{29}Si MAS NMR.

In order to visualise the positions of stereochemically active lone-pairs within the glass structural model, Pb were introduced as dipoles (pseudomolecular entities), as a crude means of representing a stereochemically active LP of electrons on all Pb sites.

Table 6-8 Details of EPSR models for $80\,PbO \cdot 20\,SiO_2$ glass. RMS deviations of the BADs are given in parentheses.

Model	U_{EP} kJ mol^{-1}	R-factor $\times 10^{-3}$	⟨O-Ŝi-O⟩ °	⟨Pb-Ô-Pb⟩ °
Ionic	-540.5	1.88	109.4(4.2)	110.8(13.9)
Q^0	-541.9	1.84	109.4(4.0)	110.1(13.3)
LP	-592.2	1.95	109.4(4.4)	110.4(14.4)
Q^0 + LP	-572.6	1.82	109.8(5.1)	109.7(14.2)

This also acted as a means of probing the uniqueness of the models, as well as discriminating against structures containing significant proportions of Pb on symmetric, more highly coordinated sites (see §6.3.4 for low PbO content glass models). The Q^0 + lone-pair model simply combined the two aforementioned modifications.

Additional parameters required in the LP containing models were as follows. The Pb-LP separation was set at 1.0 Å, as calculated for α-PbO by lone-pair localisation methods [21, 22], whilst the charges $q_{Pb} = 1.5e$ and $q_{LP} = 0.5e$ were chosen, resulting in a large dipole moment magnitude of 0.75 eÅ. The Pb-LP separation was effectively fixed by assigning a large coefficient of the intramolecular potential energy (1×10^8 a.m.u.$^{-1/2}$), whilst setting the Pb and LP masses to be equal to maximise the reduced mass. No Lennard-Jones potentials were assigned to the LP, rather minimum distances of approach were set at $r^{min}_{LPSi} = 2.6$ Å and $r^{min}_{LPPb} = 2.7$ Å (intermolecular).

6.3.3.3 Model scattering patterns

The system energies and R-factors, averaged over $> 10^3$ configurations, for the four models of $80\,PbO \cdot 20\,SiO_2$ glass are given in Table 6-8, and it is clear that introduction of the lone-pairs (polarisation of the Pb^{2+}) lowers the total energies. The measured x-ray and neutron interference functions are compared to those of the Ionic and LP models in Fig. 6-20. The weighted partial pair interference functions are also displayed, clearly demonstrating the negligible contribution, to the x-ray signal, of terms not containing Pb and the extremely small contribution from the Si-Si terms to both x-ray and neutron diffraction patterns. The main difference between the Ionic and LP models is visible in the O-O pair term, particularly for $Q < 16$ Å^{-1}. This is manifest in the $g_{OO}(r)$, Fig. 6-21, as a deviation between the two model distributions at separations beyond the first (intratetrahedral [SiO_4]) peak, and is interpreted in terms of a modification of the local

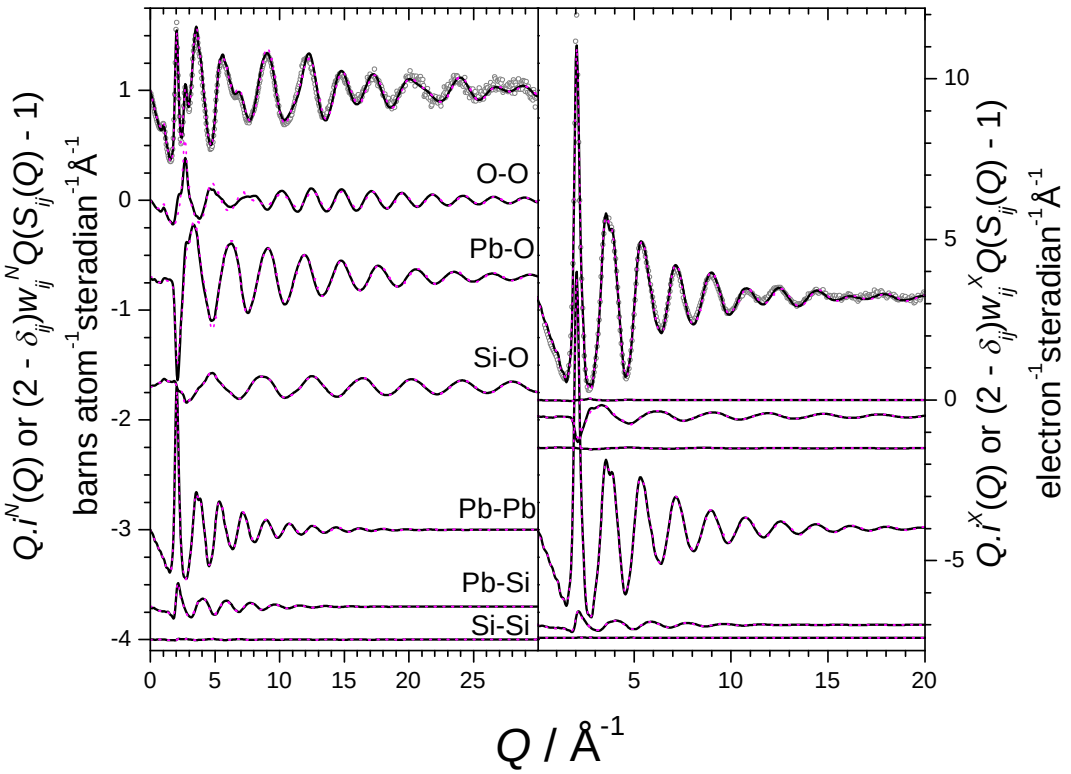

Figure 6-20 Interference functions measured (open circles) by neutron (left) and x-ray (right) diffraction for the $80\,PbO \cdot 20\,SiO_2$ glass, compared with model functions, ionic model: thick (black) line, lone-pair model: thin dotted (magenta) line. The appropriately weighted partial pair interference functions are shown vertically offset for clarity, in the same order in both panels. The functions for the Q^0 and Q^0 + LP models have been omitted.

structure about the Pb atoms, due to LP interactions.

6.3.3.4 Pair correlation functions

The pair correlation functions for the four models are shown in Fig. 6-21. The most striking difference between models is in $g_{SiSi}(r)$, arising from the Si-Si distance constraint applied in the Q^0 models, and clearly illustrates that the Si-Si term is unconstrained by the diffraction data and can be manipulated essentially at will. The large decrease in Si-Si NN CN in the Q^0 models naturally results in larger Pb-Si NN CNs, and therefore the first peak in $g_{PbSi}(r)$ increases in area. $g_{OO}(r)$ displays two peaks at low r, the first (at ~2.65 Å) corresponding to intratetrahedral distances of the $[SiO_4]$ units, the second (at ~3.0 to 3.1 Å) to intrapolyhedral distances of the $[PbO_m]$ polyhedra. It is clear that this latter peak has considerable uncertainty associated with it, being modified between models, with concomitant (small) changes in the intensity of $g_{PbO}(r)$

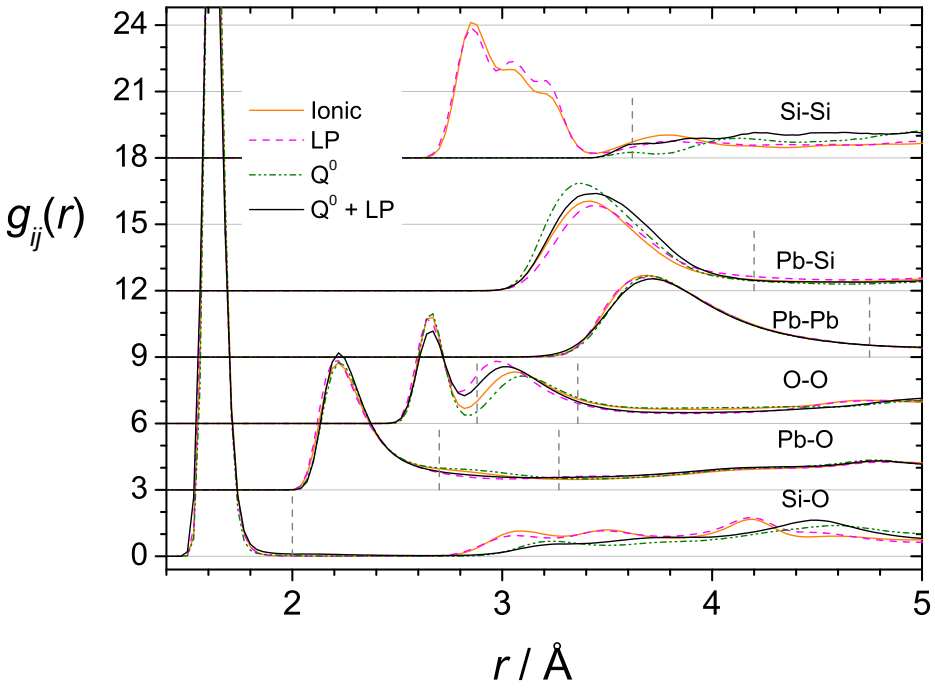

Figure 6-21 Model partial pair correlation functions for the $80\,PbO \cdot 20\,SiO_2$ glass. Vertical offsets have been used for clarity. Vertical dashed lines indicate upper cut-off radii used for determination of CNDs and BADs.

in the ~2.8 Å region.

The function $g_{LPLP}(r)$ is plotted for comparison to $g_{PbPb}(r)$ in Fig. 6-22. Most striking is the LP-LP distance of approach of ~2.85 Å, which is much shorter than the r_{PbPb} ~3.72 Å. The LP-LP distance estimated in α-PbO is much the same, at ~2.88 Å [21, 22]. In α-PbO this short LP-LP distance arises between LPs which occupy inter-layer spaces, see Fig. 3-3. In crystalline $Pb_{11}Si_3O_{17}$, Fig. 3-3 reveals several types of channels along the $[01\bar{1}]$ direction which must also contain LP electron density. Therefore, Fig. 6-22 indicates that similar structures exist within the glass network, see §6.3.3.5.

6.3.3.5 Model snapshot configurations

Slices through single configurations of the LP-containing $80\,PbO \cdot 20\,SiO_2$ glass models are shown in Fig. 6-23, and these illustrate some key characteristics of the plumbite based network. It can be seen that the Pb occupy sites of relatively low coordination number (see §6.3.3.6), with highly asymmetric ligand distributions (see §6.3.3.7) and that these $[PbO_m]$ polyhedra display a distribution of different distortions compared to

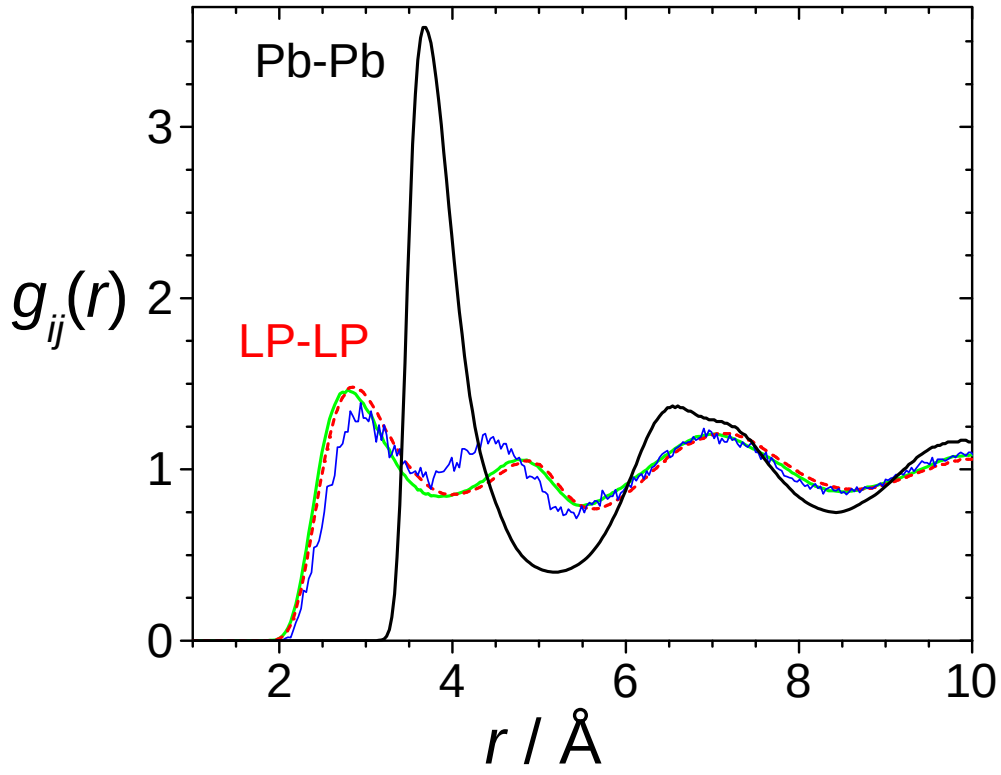

Figure 6-22 LP-LP partial pair correlation functions for the $80\,PbO \cdot 20\,SiO_2$ glass, from the LP model (red dashed) and Q^0 + LP model (green). The more noisy (solid blue) line is derived from the LP-LP distribution of a single Monte Carlo configuration, prior to perturbation by, and refinement of, the empirical potential. The Pb-Pb pair correlation function (LP model) is shown for comparison.

ideal square or trigonal pyramids. Moreover, inspection of Fig. 6-23 reveals that the $[PbO_m]$ polyhedra often share edges with each other, and with $[SiO_4]$ tetrahedra, and that voids exist within the plumbite network, which tend to be occupied by electron lone-pairs. Such voids are the analogue of the layers and channels observed within α-PbO [23] and $Pb_{11}Si_3O_{17}$ [14] respectively, Fig. 3-3.

6.3.3.6 Coordination number distributions

Various CNDs are plotted as histograms in Fig. 6-24 for all four glass models, and compared to those calculated from ^{29}Si MAS NMR measurements [3] on the glass, and from the $Pb_{11}Si_3O_{17}$ [14] crystal structure. Both in the crystal, and in the glass, the $[PbO_m]$ units tend to have $m = 4$ or 3 short bonds (≤ 2.7 Å) as well as 1, 0 or 2 longer ($2.70 < r_{PbO} \leq 3.27$ Å) bonds, giving most common total CNs of $m = 5$, 4 or 6. The O-Pb CNDs are broader, reflecting a variety of $[OPb_pSi_q]$ environments, and oxygen

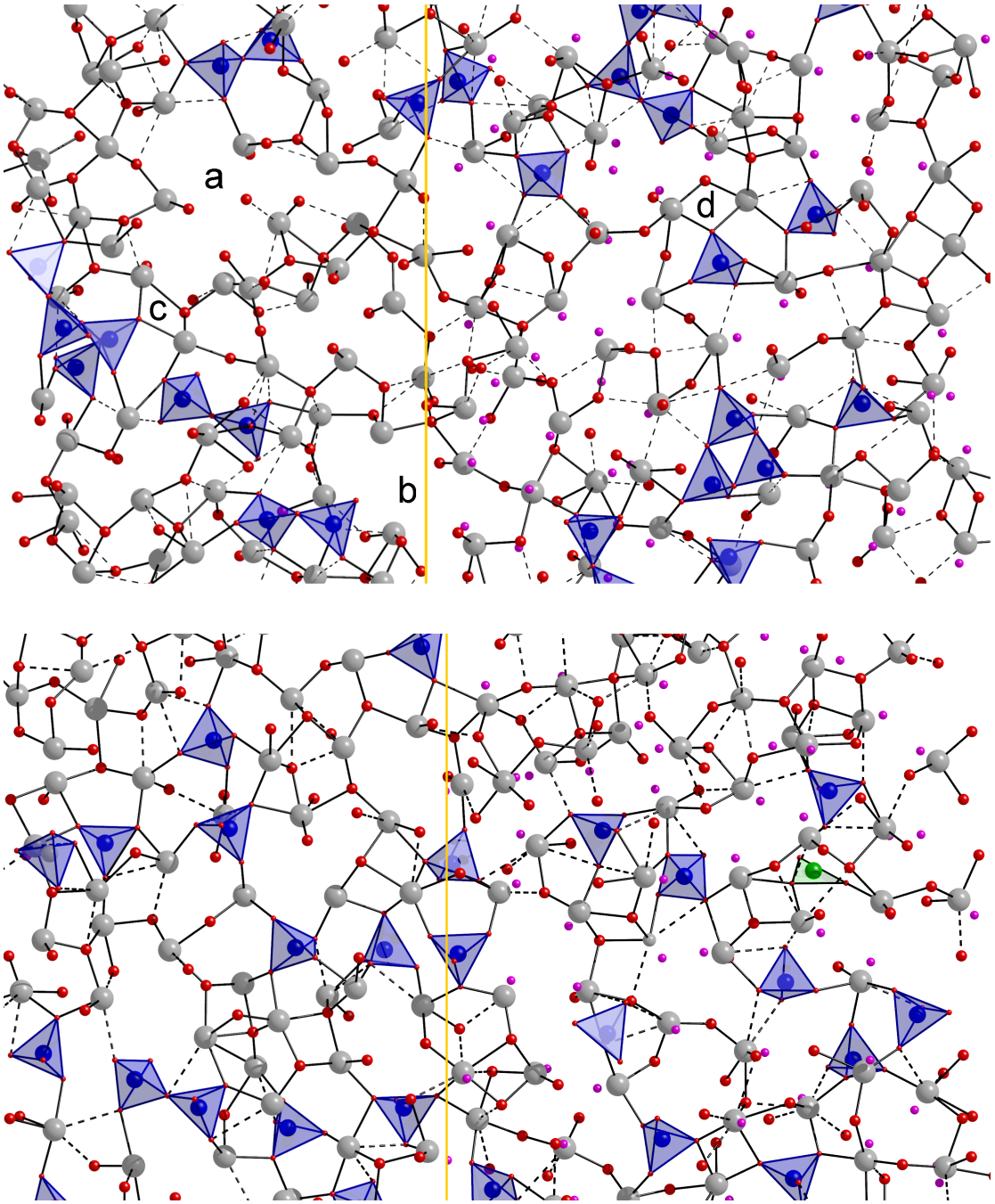

Figure 6-23 Slices, ~5 Å thick, through single configurations of EPSR models of 80 $PbO \cdot 20\ SiO_2$ glass. The areas shown are ~44 × 27 Å and correspond to the LP (upper) and Q^0 + LP (lower) models. Si atoms are shown within shaded (blue) tetrahedra, Pb atoms as large (grey) spheres, bonded to O atoms (smaller spheres, red). Pb-O bonds shorter than 2.7 Å are shown as solid lines, whilst those between 2.7 and 3.27 Å are dashed. LPs are shown as small pink spheres on the right hand side of the vertical divide, and omitted from the left hand side for comparison, and to make the voids that they occupy, such as those at a and b, more obvious. Edge sharing [PbO_m] units are in evidence, e.g. c and d. The cationic coordination spheres have been completed, whereas the anionic ones have not. The green triangle is a [SiO_3] defect.

tend to have a maximum of four Pb in their first coordination sphere. This is true also in the lead silicate crystals, Fig. 3-1, whilst in the PbO polymorphs, all O have four Pb neighbours.

The O-Si CNDs of the depolymerised Q^0 and Q^0 + LP models are, by construction, in better agreement with the values from ^{29}Si MAS NMR than are the Ionic and LP models. Notably the most highly constrained model (Q^0 + LP) contains a significant fraction (9.5(6)%) of [SiO_3] defects (see Si-O CNDs, Fig. 6-24), which may in part be due to the crude nature of the Si-Si distance constraint, which, although resulting in better agreement with ^{29}Si MAS NMR (O-Si and Si-Si CNDs), does not permit enough Q^1 units to give full quantitative agreement. Hence there is a need for more sophisticated methods of constraint which drive the models towards desired average coordination numbers and CNDs.

An interesting observation can be made regarding the Pb-Si CNDs (Fig. 6-24), in that the vast majority of Pb have at least one Si within 4.20 Å. Indeed, only 13% of the Pb atoms do not have such a near Si atom in the Ionic and LP models, whilst in the Q^0 and Q^0 + LP models, where the Si atoms are more homogeneously distributed, in closer accord with ^{29}Si MAS NMR, this drops to only 7%. These silicate anions are clearly crucial for providing sufficient structural frustration to prevent crystallisation of the supercooled melt.

6.3.3.7 Bond angle distributions

Key BADs, for O-X-O and X-O-X triplets, are displayed in Fig. 6-25. For all four models the O-Si-O BAD is narrowly distributed about the tetrahedral angle (see Table 6-8) with RMS deviation close to that estimated for vitreous silica [18], indicating well defined [SiO_4] tetrahedra. In the Q^0 model, the tetrahedra are not confined in chains or small rings, resulting in a smaller RMS deviation (Table 6-8) of 4.0°, whilst in the Q^0 + LP model, the large number of constraints leads to formation of a fraction of 3-fold Si sites, leading to a larger O-Si-O BAD RMS. The O-Pb-O BAD is comparatively broad and asymmetric, peaking close to 80°, but with a broad shoulder spanning the obtuse angle region. This is remarkably similar to the distribution in the crystal $Pb_{11}Si_3O_{17}$ [14], and is therefore characteristic of highly asymmetric [PbO_m] polyhedra typical of Pb with sp^3 or sp^3d hybridisation and stereochemically active electron lone-pairs occu-

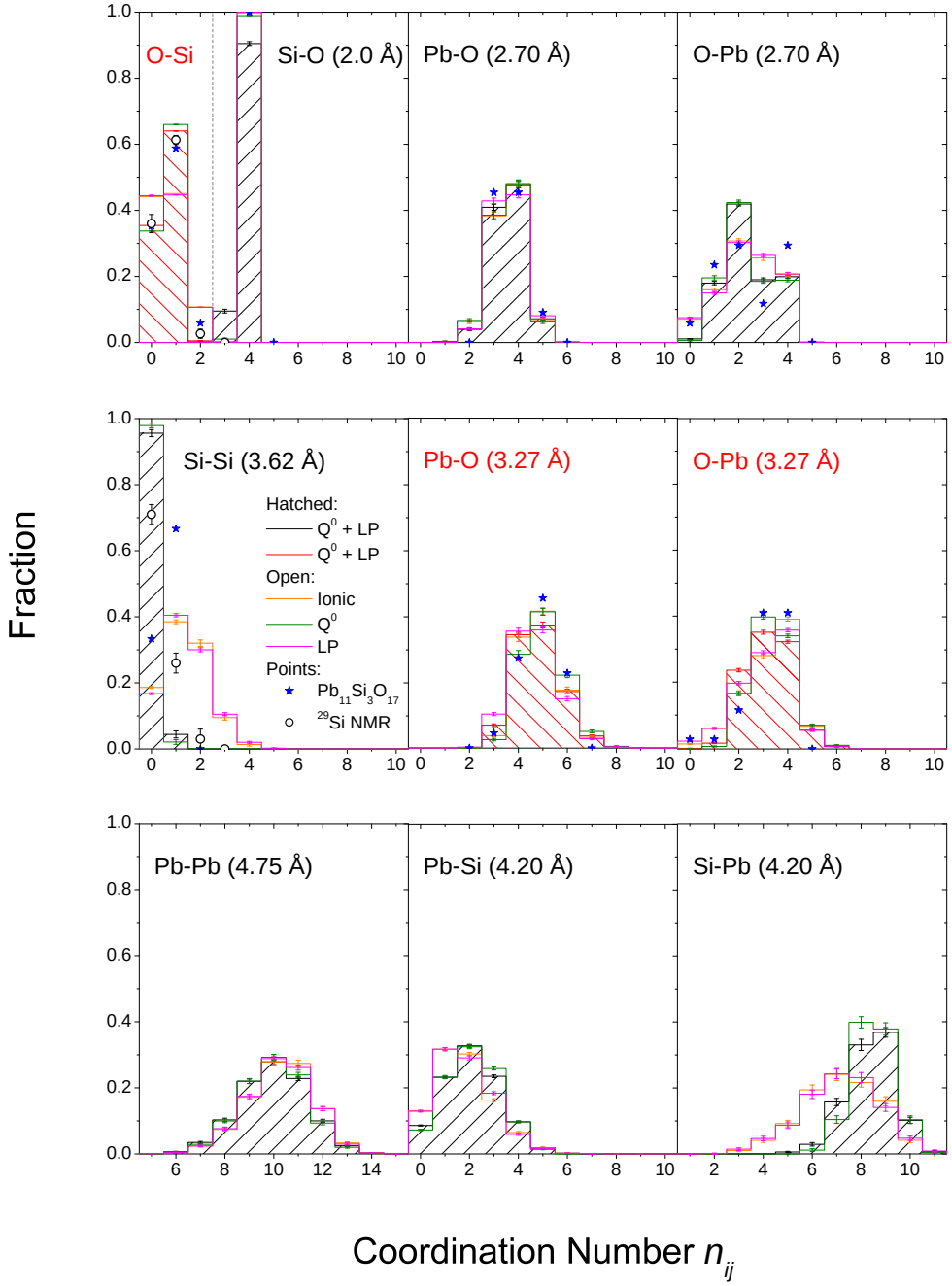

Figure 6-24 Selected coordination number distributions for EPSR models of $80\,PbO \cdot 20\,SiO_2$ glass, compared to those of crystalline $Pb_{11}Si_3O_{17}$ [14], and values calculated from ^{29}Si MAS NMR measurements [3] on the glass. The upper cut-off radii used are indicated, and can be compared to the pair correlation functions in Fig. 6-21.

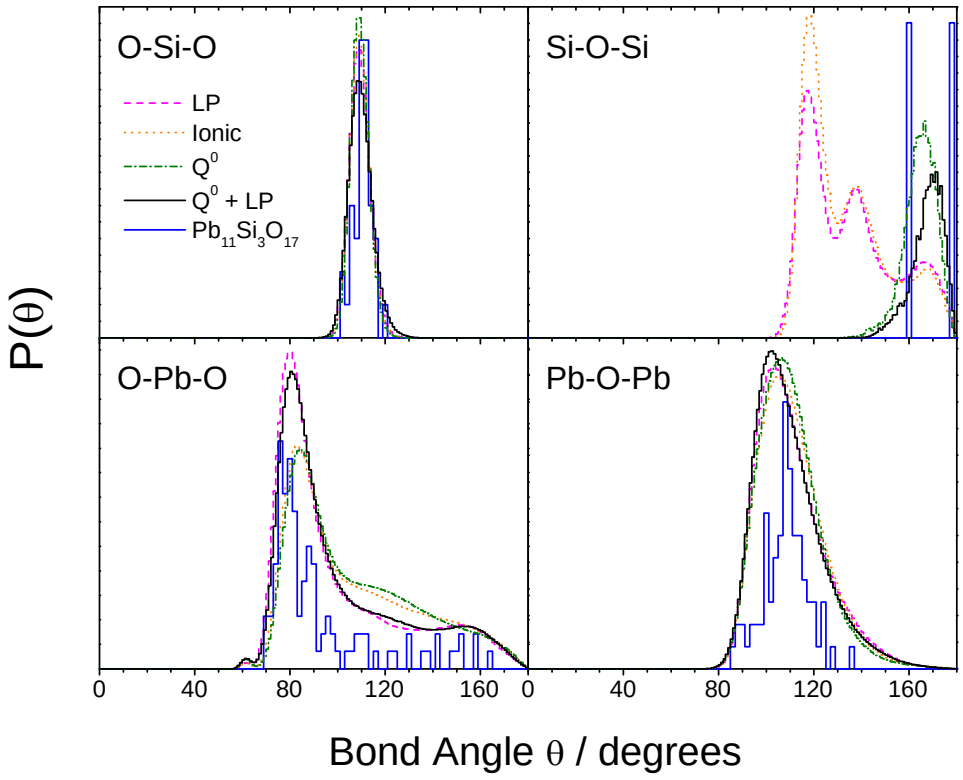

Figure 6-25 Selected bond angle distributions for EPSR models of $80\,PbO \cdot 20\,SiO_2$ glass, compared to those of crystalline $Pb_{11}Si_3O_{17}$ [14]. Only short ($\leq$ 2.7 Å) Pb-O bonds have been included, and Si-O bonds $\leq$ 2.0 Å.

pying one orbital with greater p-character. For comparison, the highly uniform [PbO_4] pyramids found in α-PbO [23] contain four O-Pb-O angles of 74.5° and two of 117.8°, whilst the more distorted [PbO_4] pyramids of β-PbO [24] have corresponding angles of 76.8° (two), 80.0° (two), 90.3° (one) and 146.6° (one). That is, all three crystalline compounds contain a preponderance of angles close to 80°, but with some larger angles, as is necessary for [PbO_m] pyramidal geometries with coordination number $m > 3$. The changes in $g_{OO}(r)$ between models (Fig. 6-21), can be related to the O-Pb-O BADs (Fig. 6-25). The introduction of the LP entities acts to push the oxygen atoms bonded to the Pb atom closer together than in the ionic and Q^0 models, leading to a larger proportion of smaller O-Pb-O bond angles, in accord with VSEPR [25, 26] theory, and to a more well defined [PbO_m] local geometry.

There are striking differences between the O-Pb-O BADs in Fig. 6-25 and that extracted by Kohara *et al.* [9] using RMC and for a lead silicate glass containing 65 mol% PbO. The RMC derived O-Pb-O BAD is broader, extending from 50 to 180°, with a

poorly defined peak close to 60°. Despite differences in glass composition between the two studies, this is suggestive that RMC and EPSR are capable of deriving qualitatively different models that are both consistent with the same diffraction data sets; although note that the real-space resolution of the neutron diffraction data of the present study is higher. A point in favour of the EPSR approach is the qualitative similarity between the O-Pb-O BADs of the model glass and the crystal $Pb_{11}Si_3O_{17}$ [14]. The model Pb-O-Pb BADs are also similar to this crystal (Fig. 6-25). The mean Pb-O-Pb angles (Table 6-8) are all close to 110°, similar to the 106.8° in $Pb_{11}Si_3O_{17}$, whilst the RMS deviations (Table 6-8) are slightly larger than the 9.3° of the crystal. Therefore there is a tendency for the oxygen atom environment to be similar to the $[OPb_4]$ distorted tetrahedral geometry which is present in α-PbO [23] (mean angle 109.6° with RMS deviation 5.8°).

The Si-O-Si BAD of the $Pb_{11}Si_3O_{17}$ [14] crystal resembles only those of the depolymerised, Q^0 and Q^0 + LP, models. The crystal contains Q^0, $[SiO_4]^{4-}$, monomers and Q^1, $[Si_2O_7]^{6-}$, dimers only, and it is the large Si-O-Si bond angles of the dimers that comprise the BAD shown in Fig. 6-25. The large proportion of smaller bond angles in the Ionic and LP models of the glass is a consequence of the presence of more highly polymerised silicate units.

6.3.3.8 Intermediate range order

The first sharp diffraction peak is a consequence of ordering on length scales beyond nearest neighbour correlations. The distinct x-ray and neutron scattering functions of $80\,PbO \cdot 20\,SiO_2$ glass both show this clear, sharp peak at 2.04(1) $Å^{-1}$, as well as a pre-peak at 1.06(1) $Å^{-1}$, which is much more clearly evident in $i^N(Q)$. Tables 6-3 and 6-5 list the positions and widths of the two peaks extracted by fitting of Lorentzian lineshapes [27] (Fig. 6-4) to their leading edges, along with their associated periodicities and correlation lengths. It is clear from Fig. 6-20 that the FSDP arises predominantly from Pb-Pb separations, and that the periodicity of 3.08(2) Å can be related to that of the x-ray $T^X(r)$, which is dominated by the Pb-Pb partial correlation function. The extent of the real-space oscillations, shown by the large correlation length of 19.6(6) Å, is most clearly evident in Fig. 6-26 which shows $D^X(r)$ out to 30 Å. Table 6-3 also lists the parameters of the FSDP of vitreous silica, which has a larger periodicity (4.17(3) Å) and a shorter correlation length (10.3(2) Å) associated with it. Therefore the plumbite

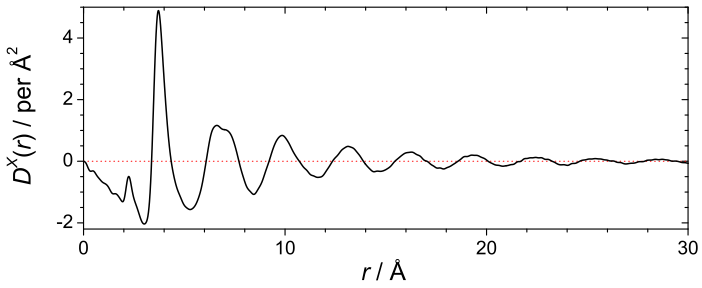

Figure 6-26 Measured x-ray differential correlation function for $80\,PbO \cdot 20\,SiO_2$ glass, illustrating the extent of the real space oscillations, with period 3.08(2) Å, arising from the Pb-Pb term.

glass network is characterised by greater medium range order compared to the silicate network (of pure SiO_2 glass). This appears to be a consequence of the compact nature of the plumbite network, which is characterised by high oxygen-cation coordination numbers, significant edge-sharing of $[PbO_m]$ units and the presence of sterically active electron lone-pairs which organise to create voids in the glass network, see Fig. 6-23. These voids are typically separated by single chains or layers of the plumbite network, with similar character (LP organisation) to regions found within the related crystalline materials.

A pre-peak similar to that observed here has previously been observed by neutron diffraction from high lead (≥ 50 mol% PbO) silicate glasses [6–9, 28], lying at approximately 1.2 Å^{-1}, as well as from high lead aluminate [29] and gallate [30, 31] glasses. The partial structure factors extracted by modelling (Fig. 6-20) indicate that the Si-O and O-O terms are the main contributors to the 1.06(1) Å^{-1} feature, and hence it arises from the broad distribution of nearest-neighbour distances between dispersed silicate anions, presumably those which are separated by chains or layers of the plumbite network. The pre-peak has a longer periodicity than for the lower lead silicate glasses that have been studied previously [6–9, 28], which is consistent with the more dilute silicate anions having, on average, a larger separation. This average silicate anion-anion separation can be calculated from glass density, ρ_0, the atomic fraction of silicon, c_{Si}, and the Q^n distribution, giving

$$r_Q = \left(\frac{2Q^1 + Q^0}{c_{Si}\rho_0} \right)^{1/3}, \tag{6-1}$$

which yields r_Q(100% Q^0) = 5.8 Å, r_Q(100% Q^1) = 7.3 Å and r_Q(NMR) = 6.3 Å using the ^{29}Si MAS NMR derived Q^n speciation (neglecting the 3% Q^2). Although this

Table 6-9 Details of EPSR models for $35\,PbO \cdot 65\,SiO_2$ glass. RMS deviations of the BADs are given in parentheses.

Model	U_{EP} kJ mol^{-1}	R-factor $\times 10^{-3}$	⟨O-Ŝi-O⟩ °	⟨Pb-Ô-Pb⟩ °
Ionic	-730.2	1.43	109.3(6.0)	106.5(13.4)
LP	-792.6	1.60	109.4(5.8)	108.5(13.2)

approach neglects the size and shape of the anions, the fact that r_Q(NMR) is greater than the periodicity of 5.96(6) Å (Table 6-3) implies that the silicate anions are inhomogeneously distributed within the glass. The fact that r_Q(100% Q^0) is less than the periodicity (5.96(6) Å) is indirect evidence for residual polymerisation of the silicate subnetwork, and the existence of Q^1, or more highly polymerised, units. Indeed, this statement is supported by the small shift in the position of the diffraction peak to higher Q (~1.10 Å^{-1}) in the Q^0 model which implies a periodicity of only ~5.7 Å.

6.3.4 Low lead silicate glass structure models

6.3.4.1 Introduction

In a similar vein to the previous section, §6.3.3, which focussed on the modelling of the high Pb content silicate glass, the present section focusses on the low Pb, 35 mol% PbO glass. As before, models with (LP) and without (Ionic) a fixed polarisation on the Pb ions were employed, but no constraints on the Si-Si pairs were necessary based on the quantitative agreement between model and ^{29}Si MAS NMR [3] derived Q^n speciations. Note that this quantitative agreement may arise from the higher relative weighting of the Si-Si scattering term at lower Pb content. However, the Si-Si term is still small (Fig. 4-1) and there may be another explanation. In particular, unlike at 80 mol% PbO, at 35 mol% PbO the Q^n speciation from ^{29}Si MAS NMR can be modelled by a statistical, or random, distribution [3]. Therefore the EPSR models of $35\,PbO \cdot 65\,SiO_2$ glass (and indeed an RMC model for a glass of the same composition [9]) may still be underconstrained by the diffraction data, but agree with the ^{29}Si MAS NMR Q^n speciation simply by virtue of being the statistically most likely.

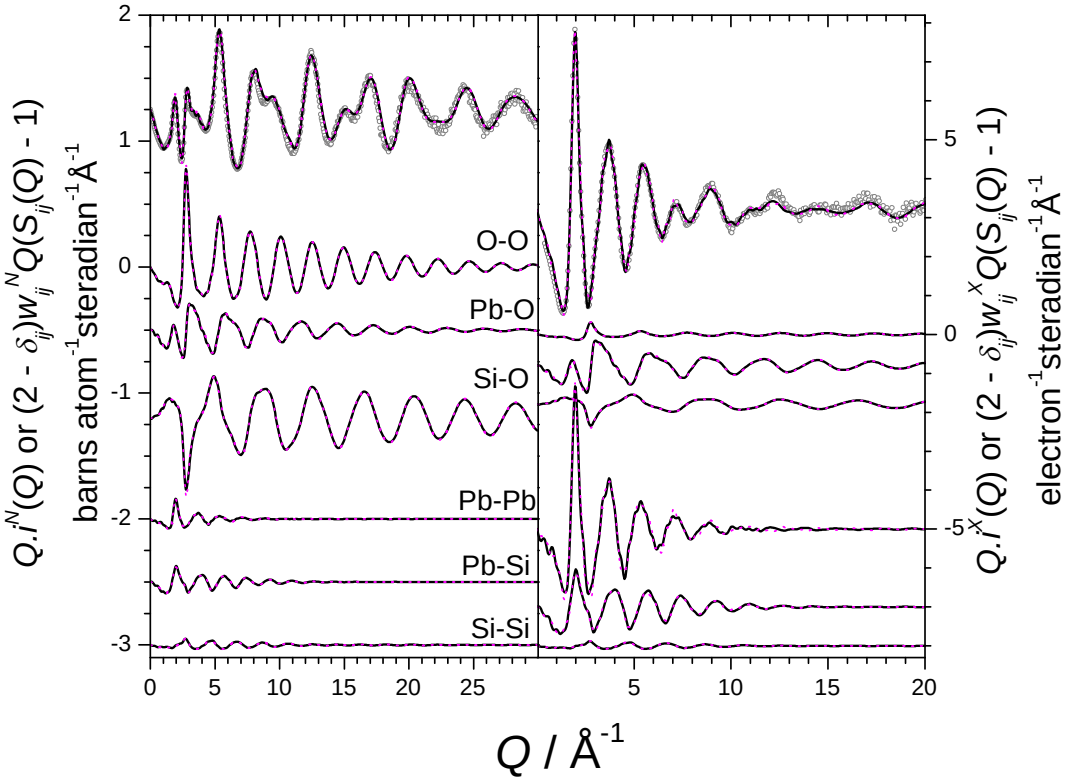

Figure 6-27 Interference functions measured (open circles) by neutron (left) and x-ray (right) diffraction for the $35\,PbO \cdot 65\,SiO_2$ glass, compared with model functions, ionic model: thick (black) line, lone-pair model: thin dotted (magenta) line. The appropriately weighted partial pair interference functions are shown vertically offset for clarity, in the same order in both panels.

6.3.4.2 Model scattering patterns

The system energies and *R*-factors, averaged over $> 10^3$ configurations, for the two models of $35\,PbO \cdot 65\,SiO_2$ glass are given in Table 6-9, and, as for the models of $80\,PbO \cdot 20\,SiO_2$ glass (§6.3.3), it is clear that introduction of the lone-pairs (polarisation of the Pb^{2+}) lowers the total energy. The measured x-ray and neutron interference functions are compared to those of the Ionic and LP models in Fig. 6-27. The weighted partial pair interference functions are also displayed.

6.3.4.3 Pair correlation functions

The pair correlation functions for the two models are shown in Fig. 6-28 and are remarkably similar. This implies that even at low Pb content, the diffraction data are consistent with the presence of sterically active LPs on all of the Pb sites. The function $g_{LPLP}(r)$ is compared to $g_{PbPb}(r)$ in Fig. 6-29. Although there is a nearest neighbour LP-

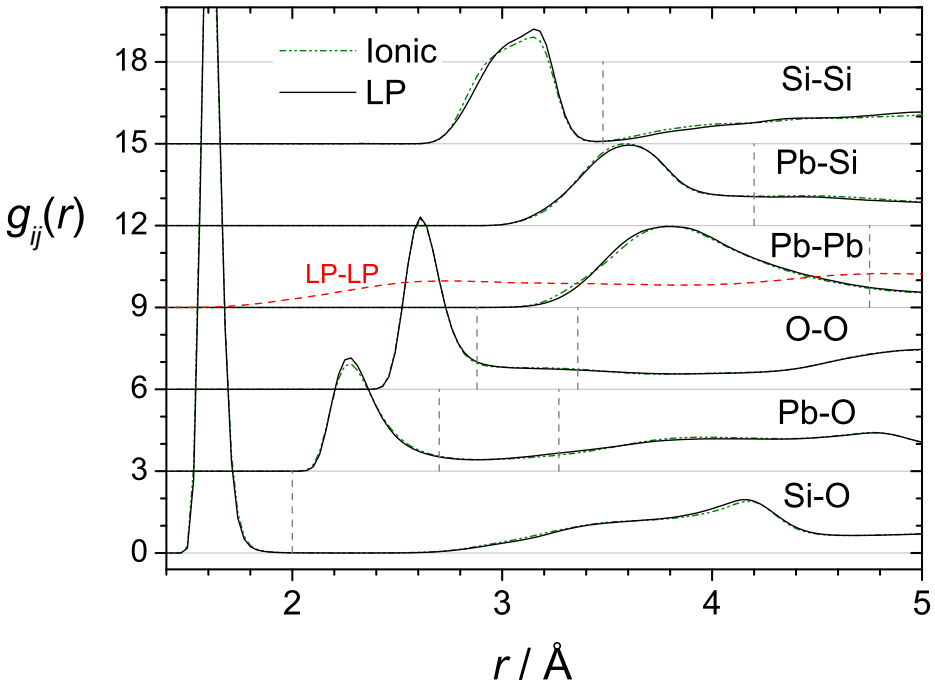

Figure 6-28 Model partial pair correlation functions for the $35\,PbO \cdot 65\,SiO_2$ glass. Vertical offsets have been used for clarity. The LP-LP and Pb-Pb functions are shown on an enlarged scale in Fig. 6-29. Vertical dashed lines indicate upper cut-off radii used for determination of CNDs and BADs.

LP peak at ~2.75 Å, it is much less pronounced than that in the $80\,PbO \cdot 20\,SiO_2$ glass (Fig. 6-22). Meanwhile, the peak at ~4.86 Å is more pronounced for the lower Pb content glass. These two features imply that there is less tendency, in the $35\,PbO \cdot 65\,SiO_2$ glass, for LPs to cluster and form voids, as in the $80\,PbO \cdot 20\,SiO_2$ glass, and this can be seen, to some extent, in the model snapshot configuration in Fig. 6-30.

6.3.4.4 Model snapshot configuration

A slice through a single configuration of the LP model is shown in Fig. 6-30. In this case the glass network is built up predominantly from silicate (mainly Q^3), rather than plumbite, structures, and the Pb atoms are interspersed within this. However, the lead atoms are clearly not playing the role of modifiers, having low coordination numbers, short, strong bonds and therefore partaking in network formation. Furthermore, there is clustering of the Pb atoms in the models, which is apparent in the low Q region of $S_{PbPb}(Q)$, and can be compared to the measured $i^X(Q)$, Fig. 6-31, although the measured SAXS is not ideally reproduced by the models due to the small model box size

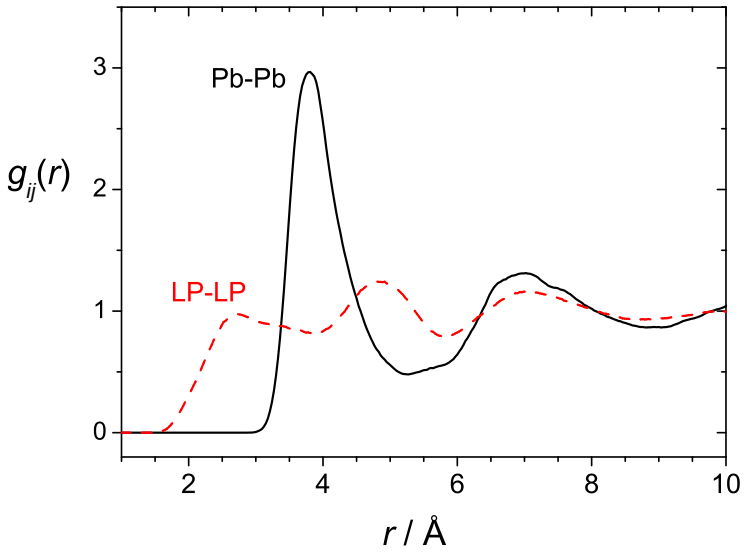

Figure 6-29 LP-LP partial pair correlation function for the $35\,PbO \cdot 65\,SiO_2$ glass. The Pb-Pb pair correlation function is shown for comparison.

(40 Å). Kohara *et al.* [9] attribute the inhomogeneity to regions of "network" and "non-network" Pb, which they define as more and less extended Pb rich regions respectively. Golubkov *et al.* [32] state that the inhomogeneity is "undoubtedly connected with the structural role of lead which acts here as a modifier". From the CNDs discussed in the following section, it is clear that this is not the case for the $35\,PbO \cdot 65\,SiO_2$ glass.

6.3.4.5 Coordination number distributions

Fig. 6-32 shows CNDs derived from the model ensembles of $35\,PbO \cdot 65\,SiO_2$ glass. A key feature is revealed by the Pb-O CNDs, which are broadly similar to those of the $80\,PbO \cdot 20\,SiO_2$ glass, §6.3.3.6. In other words, *all* of the lead atoms tend to have 3 or 4 short bonds and 1, 2 or 0 longer bonds, such that they are acting as network forming cations. There are no Pb atoms acting as modifying cations, for example on symmetric sites, with 6 to 8 bonds (equivalent lengths 2.52 Å to 2.63 Å from BV [33]). This observation is consistent with the large degree of similarity between the Ionic and LP models.

The local Pb environments in the two glasses, containing 80 and 35 mol% PbO, are not identical however. The average n_{PbO} for $r_{PbO} \leq 2.7$ Å is marginally *smaller* for the low lead glass (3.34 in the LP model) compared to the high lead glass (3.57 in the LP model). Including longer bonds ($r_{PbO} \leq 3.27$ Å), the corresponding n_{PbO} are 4.66 and

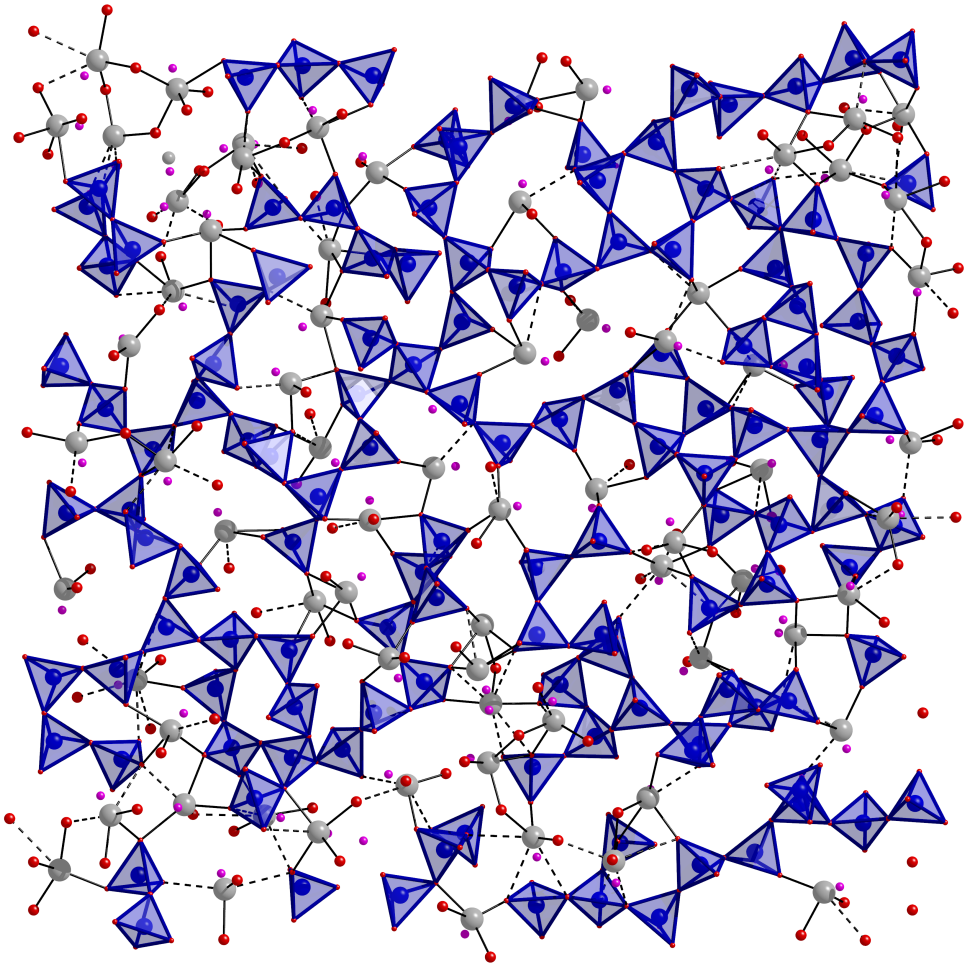

Figure 6-30 Slice, ~5 Å thick, through a single configuration of an EPSR model of $35\,PbO \cdot 65\,SiO_2$ glass. The area shown is ~40 × 40 Å and corresponds to the LP model. Si atoms are shown within shaded (blue) tetrahedra, Pb atoms as large (grey) spheres, bonded to O atoms (smaller spheres, red). Pb-O bonds shorter than 2.7 Å are shown as solid lines, whilst those between 2.7 and 3.27 Å are dashed. LPs are shown as small pink spheres. The cationic coordination spheres have been completed, whereas the anionic ones have not.

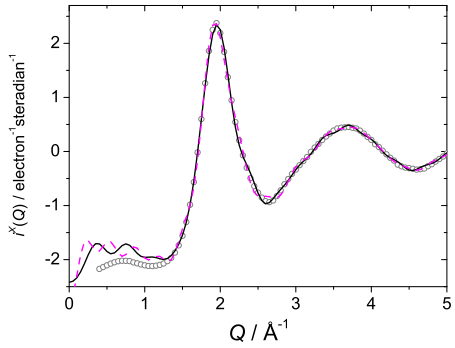

Figure 6-31 Model distinct x-ray scattering patterns for $35\,PbO \cdot 65\,SiO_2$ glass, as compared to the measured data (open grey circles). Ionic model: solid black line, lone-pair model: dotted (magenta) line. The low Q region is shown in order to emphasise the SAXS region below ~1 $Å^{-1}$.

4.65, which means that there are fewer long Pb-O bonds in the high lead glass. This latter point has a large uncertainty associated with it, owing to the overlap of O-O and Pb-O partial pair correlation functions in the 2.7 to 3.27 Å region (see Fig. 6-21 and 6-28). The former point however is more certain, being derived from the distribution of short Pb-O bonds, which are well resolved in the total correlation functions, and the CNDs show an increase in the number of sites with 4 short Pb-O bonds as PbO content increases, at the expense of those with only 3 short Pb-O bonds. It should be noted that this is contrary to the trend apparent from peak fitting to the functions $T^N(r)$, Fig. 6-8 and Table 6-4. The discrepancy arises due to the fact that the peak fits cover slightly different regions of r, and have differently defined cut-offs.

As discussed previously, the models of $35\,PbO \cdot 65\,SiO_2$ glass are in good agreement with evidence from ^{29}Si MAS NMR measurements [3], as can be seen from the Si-Si, O-Si and Si-O CNDs in Fig. 6-32. From the Pb-Pb CND, it is apparent that all lead atoms have at least one lead neighbour, typically 4 or 5.

6.3.4.6 Bond angle distributions

Some interesting points can be made regarding the BADs displayed in Fig. 6-33. First of all, it is evident that the O-Si-O BAD is broader in the 35 mol% PbO glass (RMS of ~6°), as compared to the 80 mol% PbO glass (RMS of ~4°, see also Tables 6-9 and 6-8). This can be considered a consequence of the broader Q^n speciation, since both SiO_2 [18] and $80\,PbO \cdot 20\,SiO_2$ glasses, with narrower Q^n speciations, have smaller RMS

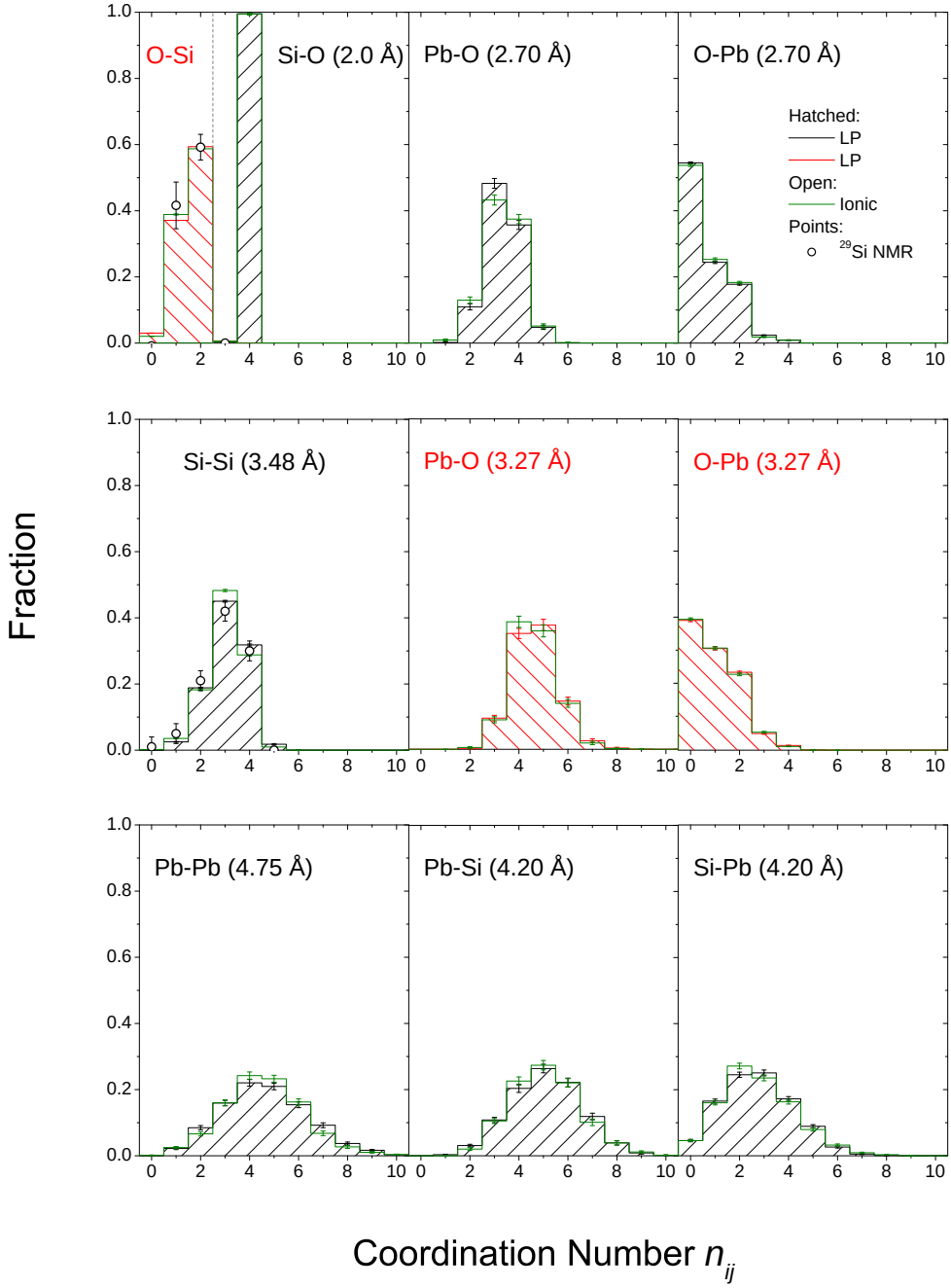

Figure 6-32 Selected coordination number distributions for EPSR models of 35 $PbO \cdot 65\ SiO_2$ glass, compared to the values calculated from ^{29}Si MAS NMR measurements [3]. The upper cut-off radii used are indicated, and can be compared to the pair correlation functions in Fig. 6-28.

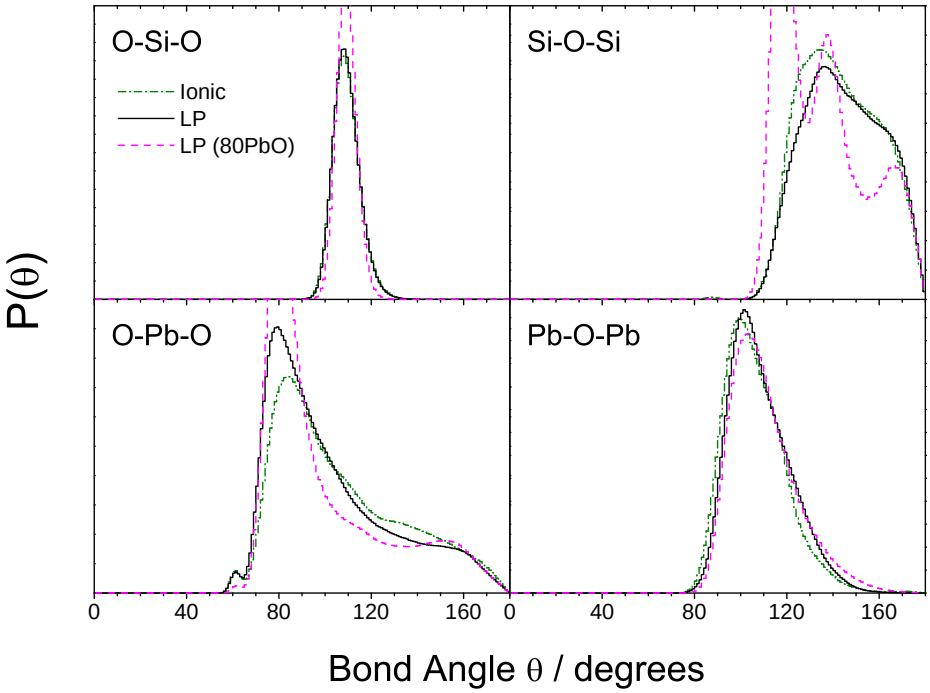

Figure 6-33 Selected bond angle distributions for EPSR models of $35\,PbO \cdot 65\,SiO_2$ glass. The equivalent distributions for the LP model of $80\,PbO \cdot 20\,SiO_2$ glass are shown for comparison (see also Fig. 6-25). Only short (≤ 2.7 Å) Pb-O bonds have been included, and Si-O bonds ≤ 2.0 Å.

deviations of the O-Si-O BAD.

The O-Pb-O BAD has a similar morphology to that of the 80 mol% PbO silicate glass, but has a less pronounced peak at ~80°, and therefore a broader distribution of local geometries. The Pb-O-Pb BAD is shifted subtly to lower angles compared to that of the high lead glass (see Tables 6-9 and 6-8), which indicates that Pb-O-Pb angles within [OPb_pSi], $p > 1$, units tend to be smaller than those within [OPb_p], $p > 1$. In other words, there is greater steric repulsion between Si-Pb pairs than between Pb-Pb pairs, in accord with observations made of the preliminary model BADs, §6.3.2.3.

The Si-O-Si BAD is broad, and intriguingly, introduction of the LPs induces a shift toward larger angles. This is likely a result of attractive Si-LP interactions, for which there is some evidence in $g_{SiLP}(r)$, although it is not clear whether such an effect occurs outside of the model, in the real glass.

Fayon *et al.* [34] proposed a correlation between oxygen p character and Pb-207 NMR isotropic chemical shift, $\delta_{iso}(^{207}Pb)$, showing that the latter decreases with increasing average Pb-O-X bond angle, ψ, and with decreasing number of Si neighbours.

Specifically [34]

$$\delta_{iso}(^{207}\mathrm{Pb}) = A - B\,(\cos\psi/(\cos\psi - 1) + Cn_{PbSi})\,, \tag{6-2}$$

where A, B and $C = 0.2$ are constants. The EPSR models reveal that there are several contributions to the increase in $\delta_{iso}(^{207}\mathrm{Pb})$ with PbO content. Firstly, the average angle $\langle$Pb-Ô-Pb$\rangle$ < $\langle$Pb-Ô-Si$\rangle$, and therefore as PbO replaces SiO_2 in the glass, the average $\langle$Pb-Ô-X$\rangle$ decreases. Furthermore $\langle$Pb-Ô-Si$\rangle$ itself decreases with increasing PbO content, further compounding the effect. On the other hand, the rise in $\langle$Pb-Ô-Pb$\rangle$ with PbO content has the opposite effect and decreases $\delta_{iso}(^{207}\mathrm{Pb})$). Finally, the average Pb-Si coordination number naturally decreases with increasing PbO content, also contributing to an increase in $\delta_{iso}(^{207}\mathrm{Pb})$. In fact, estimating ψ from the models reveals that the angular contributions to the *change* in $\delta_{iso}(^{207}\mathrm{Pb})$ with PbO content, from equation 6-2 are an order of magnitude less than those arising from the term $\propto n_{PbSi}$, due to Si → Pb substitutions. This is due to the counteractive changes in $\langle$Pb-Ô-Pb$\rangle$ and $\langle$Pb-Ô-Si$\rangle$ which have very similar magnitudes, and almost cancel out.

6.4 Discussion and conclusions

6.4.1 Local and intermediate range structure of lead silicate glasses

6.4.1.1 Silicon environments

Silicon atoms occupy tetrahedral [SiO_4] sites within the lead silicate glasses containing 35 to 80 mol% PbO. Over this compositional range there are subtle changes in the Si-O bond length distribution which can be related to changes in the second coordination sphere about the silicon atoms. Firstly, the average bond length, r_{SiO}, increases with PbO content, up to about 67 mol% PbO, at which point it plateaus (Fig. 6-7). This behaviour arises due to cation-cation interactions. The dominant contribution to the observed trend is the increase in O_{nb}-Pb coordination number (or p in [$OSiPb_p$]). The packing of more Pb atoms about an NBO additionally leads to smaller Si-O-Pb bond angles (Fig. 6-19), and this compounds the effect, further lengthening the average Si-O bond. The Si-O-Si bond angle distribution will also contribute to changes in the Si-O bond length distribution, and it is this mechanism to which the plateauing of r_{SiO} at large PbO contents is ascribed. At high PbO contents, the dimeric, $[Si_2O_7]^{6-}$, Q^1, and

monomeric, $[SiO_4]^{4-}$, Q^0, units dominate the silicate Q^n species distribution, and the Q^1 dimers tend to have large Si-O-Si bond angles, as opposed to the smaller angles found within silicate rings in more highly polymerised glasses. There is therefore less atomic overlap between Si pairs, and a concomitant reduction in the Si-O_b bond length [35, 36]. Contributions to the Si-O bond elongation likely also come from a minority of Pb bonding to BOs, as observed in crystalline materials (§3.4).

The width, $\langle u^2_{SiO}\rangle^{1/2}$, of the Si-O bond length distribution (Fig. 6-7) passes through a maximum at ~67 mol% PbO, which relates qualitatively to the Q^n species distribution, whose standard deviation itself passes through a maximum at ~50 mol% PbO. The difference in location of these two maxima points to an additional mechanism of broadening of the Si-O bond length distribution, which is likely the distribution of different O-Pb coordination numbers, and the local structural disorder about the Pb atoms. In other words, the reduction in $\langle u^2_{SiO}\rangle^{1/2}$ with PbO content rising above ~67 mol% is attributed to a narrowing of the oxygen site distribution, due to both the Q^n species and Pb site distributions also narrowing.

6.4.1.2 Lead environments

There is very little change in local lead environment with lead silicate glass composition over the range 35 to 80 mol% PbO. Neutron and x-ray diffraction patterns have been shown to be consistent with models in which all lead atoms are polarised, representing stereochemically active lone electron pairs on all Pb sites, at both 80 and 35 mol% PbO. Such sites have highly asymmetric distributions of surrounding ligands, and low coordination numbers, with typically three or four short Pb-O bonds (≤ 2.70 Å) but with up to an additional two longer ($2.70 \leq r_{PbO} \leq 3.27$ Å) bonds. As found in crystalline lead silicates, there is no clear divide between first and second oxygen coordination shells about lead (as there is for silicon). In other words, $g_{PbO}(r)$ does not return to zero after its first maximum, and average Pb-O coordination numbers always depend on the choice of radial cut-off.

There are however subtle changes in lead environment with glass composition. In particular, modelling suggests that the average number of short Pb-O bonds increases (by ~0.2) while traversing the range 35 to 80 mol% PbO, with a concomitant decrease of the same magnitude in the number of long Pb-O bonds. This difference is similar

to that between Pb sites in $PbSiO_3$ and in $Pb_{11}Si_3O_{17}$ (Fig. 3-2). Furthermore, such a change is likely responsible for the compositional evolution of ^{207}Pb NMR spectra [20] of lead silicate glasses. The isotropic chemical shift, δ_{iso}, has been shown to increase with PbO content in lead silicate crystals and glasses [20, 34, 37], and has been related to a decrease in r_{PbO} in the crystals. The diffraction measurements of the present study confirm that the (short) Pb-O bonds do indeed reduce in length (Fig. 6-7) as PbO is added to the glass. The static ^{207}Pb NMR spectra [20] become more highly asymmetric with increasing PbO content, consistent with a more axially symmetric chemical shift tensor. This is consistent with the trend of increasing number of short Pb-O bonds (increasing towards four) and implies that Pb sites in high lead glasses are more similar to the axially symmetric square based pyramids within α-PbO, than are Pb sites in low lead glasses. Fayon *et al.* [34] proposed an improved correlation between oxygen p character and $\delta_{iso}(^{207}\text{Pb})$, showing that the latter decreases with increasing average Pb-O-X bond angle and with decreasing number of Si neighbours. Empirical potential structure refinements reveal that angular contributions to the increase in $\delta_{iso}(^{207}\text{Pb})$ with PbO content almost cancel out due to counteractive changes in ⟨Pb-Ô-Si⟩ and ⟨Pb-Ô-Pb⟩, such that the contribution due directly to Si → Pb substitutions is an order of magnitude larger.

6.4.1.3 Oxygen environments

Unlike the cationic environments, the anionic environments change drastically with lead silicate glass composition. This can be viewed as a continuous transition from the $[OSi_2]$ bridging oxygen environments, with less p character, in SiO_2 glass, toward the sp^3 hybridised $[OPb_4]$ environments common to the PbO polymorphs and lead silicate crystal structures. Equilibrium constants for reactions of the type 2(Pb-O-Si) ⇌ Pb-O-Pb + Si-O-Si increase with PbO content.

6.4.1.4 Lone-pair distribution and intermediate range order

The emergence of voids within high lead silicate glasses, owing to the organisation of electron lone-pairs, constitutes a key insight, made possible by the use of empirical structural modelling using polarised Pb ions. Such voids in high lead (80 mol% PbO) silicate glass are analogues of the open channels in $Pb_{11}Si_3O_{17}$ and the layered structures

of α- and β-PbO, and are characteristic of the plumbite glass network. At lower PbO contents there is less tendency for LPs to cluster within voids, and rather the Pb^{2+} LP electron density occupies voids within the *silicate* network, which are present owing to the restricted Si-O-Si bond angle distribution and resultant topological constraints. The sharpening of the first sharp diffraction peak with increasing PbO content is considered to be a consequence of the ordering of LPs within voids, and resultant *local* layer-like structures.

Edge sharing of contiguous [PbO_m] polyhedra is another hallmark of plumbite glass networks and is likely related to the lack of glass formation for compositions containing $\gtrsim$ 83 mol% PbO [3] (see §6.4.2). However, it is worth noting that the edge sharing [Pb_2O_4] pairs of trigonal pyramids proposed by Takaishi *et al.* [8] as the basic motif of the plumbite network over the full compositional range is potentially misleading. The unit was proposed on the basis of the nearest neighbour Pb-Pb separation in $T^X(r)$ being independent of glass composition. However, within the structural models, similar Pb-Pb distances are observed between both edge and corner sharing [PbO_m] polyhedra.

Mizuno *et al.* [38] placed the threshold for a percolating plumbite network at between 35 and 50 mol% PbO, based on the dissolution behaviour of the glasses. It is interesting to note that in the 35 mol% PbO silicate glass model, based on the Pb-Pb coordination number distribution (Fig. 6.3.4.5), there are very few (~11%) Pb atoms with only one (~2%) or two (~8%) neighbours, the average $n_{PbPb} = 4.65$, indicative of a close to fully percolating network. The small angle x-ray scattering intensity, discussed at length by Golubkov *et al.* [32], rises sharply below 35 mol% PbO, implying inhomogeneous distributions of Pb atoms. Thus the dramatic drop in diffusion coefficient, interpreted as a percolation threshold, appears to have an observable consequence in the small angle x-ray scattering.

6.4.2 Glass forming limit in the lead silicate system

The traditional glass forming limit in binary alkali and alkaline earth silicate systems occurs at two thirds modifier oxide content, at which point all oxygen atoms would exist as non-bridging species, and all silicate anions as Q^0 monomers, assuming there are no oxygen atoms which bond only to glass modifying cations. Since lead silicate glasses form beyond this limit, what is it that limits glass formation at around 83 mol%

PbO [3], and similarly, why does a pure PbO glass not form? Firstly, it should be noted that the silicate subnetwork retains some degree of polymerisation right up to 83 mol% PbO, and therefore the number of oxygens bonded only to Pb is not minimised (as in the 100% Q^0 case). This can be envisaged as an equilibrium between Pb-O-Si links and a mix of Pb-O-Pb and Si-O-Si links. The presence of Pb-O-Pb entities is related to the presence of edge-sharing [PbO_m] polyhedra, increasing the fraction of which will ultimately destabilise glass formation, with the fully edge-shared PbO crystals being the limiting case. The broad distribution of local Pb environments also plays a role, similar to the distribution of Si-O-Si bond and torsion angles in SiO_2 glass, providing flexibility to allow for disordered network formation. Thus it seems that sufficient corner-sharing and local Pb environment disorder, combined with silicate anions with a (relatively) broad Q species distribution, are required to hinder crystallisation kinetics and allow glass formation. Notably, $MgO{-}SiO_2$ glasses can be formed right up to the conventional glass forming limit of 66.7 mol% MgO [39, 40], using containerless levitation techniques, and, at 66.7 mol% MgO, are more highly polymerised [41, 42] than the stoichiometric mineral enstatite, which is purely Q^0. Another example is the $Li_2O{-}SiO_2$ system, for which glass formation has been observed almost up to the orthosilicate (66.7 mol% M_2O) composition, at which point a degree of silicate anion polymerisation remains [43]. Recently, however, it has been demonstrated that a purely Q^0 glass can be obtained [44], for aerodynamically levitated $72\,(Ca_{0.5}Mg_{0.5}O)\cdot 28SiO_2$. In this case the structural and topological frustration required to prevent crystallisation comes not from a distribution of Q^n species, but from the dissimilarity of the Ca^{2+} and Mg^{2+} cations. On this basis alone one would not expect a purely Q^0 lead silicate glass to form, but it is interesting to consider the possibility of using aerodynamic levitation to increase the accessible glass-forming range. Foreseeable problems with this include the volatilisation of lead from the molten droplet, and the necessity for careful control of the redox conditions to prevent formation of metallic or tetravalent lead.

References

[1] A. J. Havel, S. A. Feller, M. Affatigato, M. Karns and M. Karns, *Glass Technol. Eur. J. Glass Sci. Technol. A* **50** (4), (2009), 227–229.

[2] *SciGlass Professional 7.3* (ITC Inc., 2008).

[3] S. Feller, G. Lodden, A. Riley, T. Edwards, J. Croskrey, A. Schue, D. Liss, D. Stentz, S. Blair, M. Kelley, G. Smith, S. Singleton, M. Affatigato, D. Holland, M. E. Smith, E. I. Kamitsos, C. P. E. Varsamis and E. Ioannou, *J. Non-Cryst. Solids* **356** (6-8), (2010), 304–313.

[4] A. C. Hannon, *Nucl. Instrum. Meth. A* **551** (1), (2005), 88–107.

[5] E. Lorch, *J. Phys. C Solid State* **2**, (1969), 229.

[6] K. Yamada, A. Matsumoto, N. Niimura, T. Fukunaga, N. Hayashi and N. Watanabe, *J. Phys. Soc. Jpn.* **55** (3), (1986), 831–837.

[7] K. Suzuya, D. L. Price, M. L. Saboungi and H. Ohno, *Nucl. Instrum. Meth. B* **133** (1-4), (1997), 57–61.

[8] T. Takaishi, M. Takahashi, J. Jin, T. Uchino, T. Yoko and M. Takahashi, *J. Am. Ceram. Soc.* **88** (6), (2005), 1591–1596.

[9] S. Kohara, H. Ohno, M. Takata, T. Usuki, H. Morita, K. Suzuya, J. Akola and L. Pusztai, *Phys. Rev. B* **82**, (2010), 134209 1–7.

[10] S. M. Antao, I. Hassan, J. Wang, P. L. Lee and B. H. Toby, *Can. Mineral.* **46**, (2008), 1501–1509.

[11] S. Krivovichev and P. Burns, *Zapiski RMO* **133** (5), (2004), 70–76.

[12] W. Petter, A. B. Harnik and U. Keppler, *Z. Kristallogr. Kristallgeom. Kristallphys. Kristallchem.* **133**, (1971), 445–458.

[13] L. S. D. Glasser, R. A. Howie and R. M. Smart, *Acta Crystallogr. B* **37** (Feb), (1981), 303–306.

[14] K. Kato, *Acta Crystallogr. B* **38**, (1982), 57–62.

[15] M. L. Boucher and D. R. Peacor, *Z. Kristallogr. Kristallgeom. Kristallphys. Kristallchem.* **126**, (1968), 98–111.

[16] K. Kato, *Acta Crystallogr. B* **36**, (1980), 2539–2545.

[17] R. Bouchard, D. Hupfeld, T. Lippmann, J. Neuefeind, H. B. Neumann, H. F. Poulsen, U. Rutt, T. Schmidt, J. R. Schneider, J. Sussenbach and M. von Zimmermann, *J. Synchrotron Radiat.* **5**, (1998), 90–101.

[18] H. F. Poulsen, J. Neuefeind, H. B. Neumann, J. R. Schneider and M. D. Zeidler, *J. Non-Cryst. Solids* **188** (1-2), (1995), 63–74.

[19] A. K. Soper, *Phys. Rev. B* **72** (10), (2005), 104204.

[20] F. Fayon, C. Bessada, D. Massiot, I. Farnan and J. P. Coutures, *J. Non-Cryst. Solids* **232**, (1998), 403–408.

[21] D. Lebellac, J. M. Kiat and P. Garnier, *J. Solid State Chem.* **114** (2), (1995), 459–468.

[22] C. Pirovano, M. S. Islam, R. N. Vannier, G. Nowogrocki and G. Mairesse, *Solid State Ionics* **140** (1-2), (2001), 115–123.

[23] R. G. Dickinson and J. B. Friauf, *J. Am. Chem. Soc.* **46**, (1924), 2457–2463.

[24] R. J. Hill, *Acta Crystallogr. C* **41** (Sep), (1985), 1281–1284.

[25] R. Gillespie and R. Nyholm, *Q. Rev. Chem. Soc.* **11** (4), (1957), 339–380.

[26] R. J. Gillespie and I. Hargittai, *The VSEPR Model of Molecular Geometry* (Prentice Hall International, London, 1991).

[27] A. C. Wright, *Phys. Chem. Glasses Eur. J. Glass Sci. Technol. B* **49** (3), (2008), 103–117.

[28] K. Suzuya, S. Kohara and H. Ohno, *Jpn. J. Appl. Phys. 1* **38**, (1999), 144–147.

[29] E. R. Barney, A. C. Hannon, D. Holland, D. Winslow, B. Rijal, M. Affatigato and S. A. Feller, *J. Non-Cryst. Solids* **353** (18-21), (2007), 1741–1747.

[30] A. C. Hannon, J. M. Parker and B. Vessal, *J. Non-Cryst. Solids* **196**, (1996), 187–192.

[31] A. C. Hannon, J. M. Parker and B. Vessal, *J. Non-Cryst. Solids* **232**, (1998), 51–58.

[32] V. V. Golubkov, V. N. Bogdanov, A. Y. Pakhnin, V. A. Solovyev, E. V. Zhivaeva, V. O. Kabanov, O. V. Yanush, S. V. Nemilov, A. Kisliuk, M. Soltwisch and D. Quitmann, *J. Chem. Phys.* **110** (10), (1999), 4897–4906.

[33] N. E. Brese and M. Okeeffe, *Acta Crystallogr. B* **47**, (1991), 192–197.

[34] F. Fayon, I. Farnan, C. Bessada, J. Coutures, D. Massiot and J. P. Coutures, *J. Am. Chem. Soc.* **119** (29), (1997), 6837–6843.

[35] M. B. Boisen, G. V. Gibbs, R. T. Downs and P. Darco, *Am. Mineral.* **75** (7-8), (1990), 748–754.

[36] G. V. Gibbs, F. C. Hill and M. B. Boisen, *Phys. Chem. Miner.* **24** (3), (1997), 167–178.

[37] L. Leventhal and A. J. Bray, *Phys. Chem. Glasses* **6** (4), (1965), 113–125.

[38] M. Mizuno, M. Takahashi, T. Takaishi and T. Yoko, *J. Am. Ceram. Soc.* **88** (10), (2005), 2908–2912.

[39] S. Kohara, K. Suzuya, K. Takeuchi, C. K. Loong, M. Grimsditch, J. K. R. Weber, J. A. Tangeman and T. S. Key, *Science* **303** (5664), (2004), 1649–1652.

[40] S. Kohara, J. Akola, H. Morita, K. Suzuya, J. K. R. Weber, M. C. Wilding and C. J. Benmore, *Proc. Nat. Acad. Sci. U.S.A.* **108** (36), (2011), 14780–14785.

[41] S. Sen, H. Maekawa and G. N. Papatheodorou, *J. Phys. Chem. B* **113** (46), (2009), 15243–15248.

[42] S. Sen and J. Tangeman, *Am. Mineral.* **93** (5-6), (2008), 946–949.

[43] C. Larson, J. Doerr, M. Affatigato, S. Feller, D. Holland and M. E. Smith, *J. Phys. Condens. Mat.* **18**, (2006), 11323–11331.

[44] N. K. Nasikas, T. G. Edwards, S. Sen and G. N. Papatheodorou, *J. Phys. Chem. B* **116** (9), (2012), 2696–2702.

Chapter 7

Lead Germanate Glasses

7.1 Sample preparation and characterisation

7.1.1 Glass preparation

A first series of 15 glasses in the $x\mathrm{PbO} \cdot (100 - x)\mathrm{GeO_2}$ system, and with $5 \leq x \leq 65$ mol% PbO, were prepared by mixing quartz GeO_2 (Alfa Aesar, 99.98%) and Pb_3O_4 (Aldrich, 99%) in sufficient quantities to yield 20 g of glass. The mixed valence compound lead (II, IV) oxide (Pb_3O_4) was used, rather than divalent lead (II) oxide (PbO), in order to provide additional oxygen to suppress the reduction of any part of the melt to metallic Pb. Instead the reduction of the tetravalent Pb to the divalent form, and evolution of oxygen gas occurs at 500 °C [1]. The two powders were well mixed and placed into large 90 Pt · 10 Rh crucibles inside an electric furnace at room temperature, under an air atmosphere. The furnace temperature was increased at a rate of 600 °C h^{-1} typically until 1000 °C, and then held for 25 minutes. The liquids thus obtained were quenched by pouring them onto a steel plate and quickly pressing their upper surface with a brass plate to provide rapid quenching, of the order 10^3 °C s^{-1}, and to yield a thin (∼1 mm) glass disk.

The following exceptions to the above apply. Glasses containing $55 \leq x \leq 65$ mol% PbO were held at 900 °C, whilst the 15 mol% PbO germanate glass was held at 1100 °C and the 5 and 10 mol% PbO glasses at 1200 °C. Despite the higher melt temperature, the latter two melt compositions were too viscous to allow pouring and were therefore quenched by placing the base of the crucible into cold tap water.

Mass loss measurements were made in order to check that all additional oxygen associated with Pb^{IV} had evolved, and for the possibility of volatilisation. In most cases additional mass loss, in excess of that expected due to evolution of oxygen gas, was recorded, and the glass compositions estimated assuming volatilisation only of PbO,

and not of GeO_2, are recorded in Table 7-1. However, in several cases this was not possible owing to the violent fracture of the glass plates obtained, which occurs due to cooling rate differences between the glass surface and its interior, and associated high stresses. This often led to the loss of small glass fragments, rendering calculation of the correct PbO content from the mass loss by weighing not practicable. In these cases (15, 18, 24, 27 mol% PbO) the expected corrected PbO content was calculated by linear interpolation using the successful measurements. The highest Pb content compositions,

Table 7-1 Measured mass and number densities, molar volumes, glass transition temperatures and compositions for lead germanate glasses. Uncertainties in parentheses.

Glass Composition in mol% PbO			ρ_m	ρ_0	V_M	T_g
Nominal	Mass Loss[†]	EDX	g cm^{-3}	nm^{-3}	cm^3 mol^{-1}	± 5 °C
Plate quenched glasses						
0	-	-	3.650(37)	63.05(65)	28.65(32)	-
5	4.74(5)	6.16(10)	3.981(40)	64.23(89)	27.68(42)	467
10	9.72(5)	11.02(13)	4.309(43)	64.86(87)	26.95(39)	455
15	14.73(5)[‡]	16.03(16)	4.669(47)	65.72(85)	26.14(37)	454
18	17.68(5)[‡]	18.81(19)	4.876(49)	66.03(85)	25.75(36)	456
21	20.42(5)	18.70(71)	5.154(52)	67.37(85)	24.99(35)	459
24	23.57(5)[‡]	22.11(53)	5.293(53)	66.48(83)	25.04(34)	455
27	26.51(5)[‡]	26.71(33)	5.548(55)	67.16(83)	24.52(33)	452
30	29.42(5)	29.50(80)	5.688(57)	66.45(81)	24.52(33)	445
35	34.54(5)	34.55(38)	5.965(60)	65.51(78)	24.40(32)	427
40	39.69(5)	38.34(34)	6.193(62)	64.02(75)	24.49(32)	410
45	44.13(5)	43.73(50)	6.493(65)	63.76(74)	24.17(31)	387
50	48.88(5)	47.69(20)	6.701(67)	62.34(71)	24.26(30)	377
55[*]	54.75(5)	52.68(51)	6.980(70)	60.81(68)	24.29(30)	-
60[*]	59.81(5)	57.00(69)	7.351(74)	60.57(67)	23.88(29)	-
65[*]	64.78(5)	62.29(53)	7.634(76)	59.60(65)	23.77(29)	-
Twin-roller quenched glasses						
55	-	56.13(37)	6.885(69)	59.82(67)	24.67(30)	-
60	-	60.83(84)	7.205(72)	59.25(66)	24.40(30)	-
65	-	65.62(98)	7.420(74)	57.80(63)	24.49(30)	-
70	-	71.00(95)	7.662(77)	56.56(61)	24.49(29)	-
75	-	75.09(79)	7.967(80)	55.78(60)	24.29(29)	-

[†] Assuming volatilisation of the PbO component. [‡] Interpolated.
[*] Evidence of crystallisation.

with $55 \leq x \leq 65$ mol% PbO, all contained visible crystalline fractions after quenching, this being extensive in the 65 mol% PbO case and very minor in the 55 mol% PbO case. In the former, laboratory x-ray diffraction confirmed the presence of $Pb_5Ge_3O_{11}$ [2, 3]

and Pb_3GeO_7 [4].

In an attempt to obtain high Pb glasses, free from crystalline inclusions, a second series of glasses was produced using smaller batch sizes and more rapid, twin-roller, quenching. Batches of quartz GeO_2 (Alfa Aesar, 99.98%) and Pb_3O_4 (Sigma-Aldrich, 99%) were mixed in sufficient quantities to yield 10 g of germanate glass, containing $55 \leq x \leq 75$ mol% PbO, in 5 mol% PbO intervals. These were held in 20 cm^3 platinum crucibles and placed inside an electric furnace held at a constant temperature of 900 °C for 20 minutes. The resultant melts were quenched by pouring into a 30 μm gap between two steel cylinders counter-rotating at 590 rpm, resulting in a cooling rate of order 10^5 °C s^{-1} [5]. Whilst the 55 and 60 mol% PbO samples appeared free from inclusions, the higher Pb content samples contained some crystalline inclusions, and these included metallic Pb in the 75 mol% PbO glass. In order to avoid damage of the Pt crucibles by alloying with metallic Pb, batches with > 75 mol% PbO were not melted. Two batches of each glass composition were produced, and those containing the least inclusions chosen for further study, with inclusions removed.

7.1.2 Density measurement

Mass and number densities and molar volumes of PbO−GeO_2 glasses are recorded in Table 7-1 and plotted for comparison with literature data in Fig. 7-1. There are some notable differences in the compositional trends as compared with the equivalent data for PbO−SiO_2 glasses (see also Fig. 6-1). Whilst the mass density always increases with PbO content due to the dominance of the mass of the PbO component, an inflection is apparent at ~27 mol% PbO, and this is apparent as a maximum in the atomic number densities of the glasses at the same composition. Meanwhile, the behaviour of the molar volume is similar to that of the lead silicates, at first decreasing as PbO is added, and then remaining approximately constant from ~27 mol% PbO onwards.

7.1.3 Energy dispersive x-ray spectroscopy

EDX measurements of the glass compositions based on the Pb L and Ge K lines of the spectra are presented in Table 7-1. For the plate quenched glasses containing $\gtrsim$ 20 mol% PbO, these are qualitatively in accord with the mass loss measurements and the

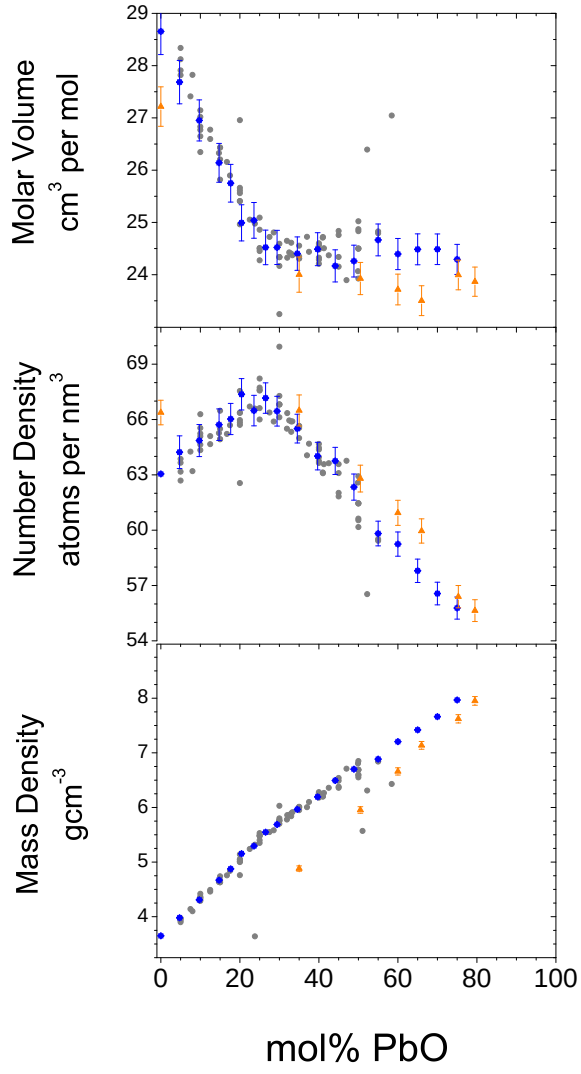

Figure 7-1 Measured mass and number densities and molar volumes for lead germanate glasses (blue diamonds), compared to data from the SciGlass database [6] (grey circles), references therein. The data for lead silicate glasses (orange triangles), Table 6-1, Fig. 6-1, are also shown for comparison.

assumption of preferential volatilisation of PbO from the melt. On the other hand, EDX measurements indicate that the glasses containing $\lesssim$ 20 mol% PbO are lead rich with respect to nominal compositions. This implies that GeO_2 is preferentially volatilised from the melt in this composition region, and at the higher melt temperatures used for the 5, 10 and 15 mol% PbO samples. However, calculating the glass composition based on loss of GeO_2 gives, 10.07(05) mol% PbO, for example, in the case of the nominally 10 mol% PbO composition. Note that although the mass loss from the roller quenched batches was not measured, these were expected to be smaller based on the smaller melt

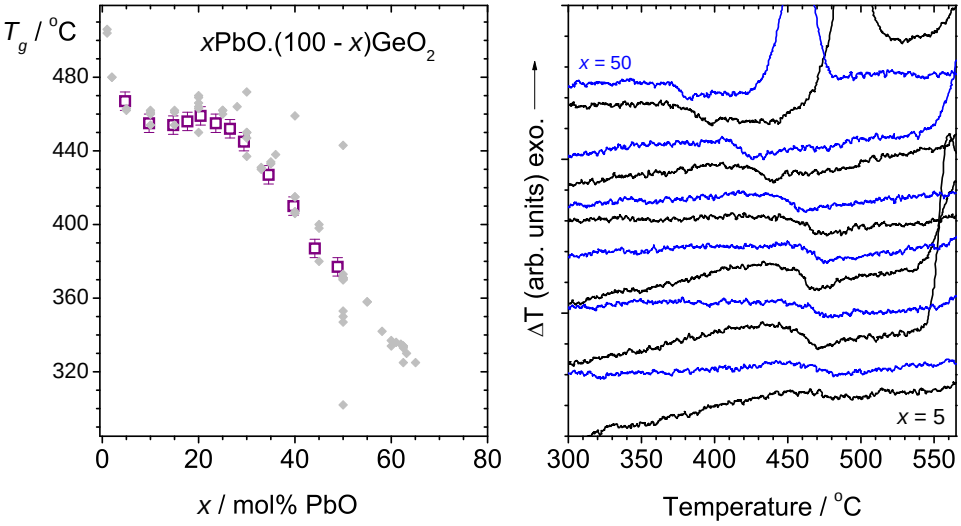

Figure 7-2 Lead germanate glass transition temperatures as a function of glass composition (left panel), as measured by DTA at $dT/dt = 10\,°C\,min^{-1}$. Literature data compiled on the SciGlass database [6] (grey diamonds) are shown for comparison, references therein. The right panel shows the DTA traces, in the locale of the glass transition temperatures, for each glass, offset vertically for clarity. Exothermic crystallisation events, at temperatures above the glass transition, are visible within the range of the plot for some glasses.

surface area to volume ratios, which is supported by the EDX measurements.

7.1.4 Thermal analysis

Glass transition temperatures measured by DTA are displayed in Table 7-1 and Fig. 7-2. As noted by Shelby [7] there is a sharp decrease in glass transition temperature upon initial addition of PbO, from that of pure GeO_2 glass at 526(27) °C*. Following this, the transition temperatures plateau between 10 and ~27 mol% PbO, and it was this feature, along with the detection of a second glass transition, by DSC, at ~540 °C that led Shelby [7] to conclude that his glasses were phase separated. Note however that the DTA traces shown in the right hand panel of Fig. 7-2 do not show any hint of a second glass transition close to 540 °C, although the 15 and 21 mol% PbO germanate glasses do begin to show an exothermic release of energy as a result of crystallisation very close to this temperature. Note also that Shelby's glasses were derived from 30 g batches and were subject to relatively slow cooling rates during vitrification. The decline of the glass transition temperature with subsequent addition of PbO, beyond ~27 mol% PbO,

*Mean, with standard deviation in parentheses, of entries in the SciGlass database [6].

is similar to that observed in lead silicate glasses [8], albeit that the latter are offset to higher temperatures.

7.1.5 Summary

Traditionally, as for the alkali and alkaline earth (Fig. 5-1) germanate glasses, a maximum in mass density, as a function of glass composition, is taken as *the* defining characteristic of the germanate anomaly, but in the case of lead germanate glasses, this is not appropriate because the glass forming and modifying (or intermediate) oxides do not have similar masses. However, the atomic number density does show a clear maximum at ~27 mol% PbO, which is only apparent as an inflection in the mass density. This indicates that structural modifications of the glass are giving rise to a germanate anomaly in the PbO–GeO_2 system. What is more, an inflection is evident in the measured glass transition temperatures, again at ~27 mol% PbO, which, similar to the mass density trend, may not appear as a clear maximum because of the role of PbO, addition of which decreases T_g, this effect being dominant at compositions with >27 mol% PbO.

Plate quenched glasses containing $\leq$ 50 mol% PbO were all obtained free from crystalline inclusions, and hence are suitable for detailed structural analysis. Using rapid twin-roller quenching on high Pb germanate liquids, glasses mostly free from inclusions were obtained up to 75 mol% PbO, and these materials, with any inclusions removed were also chosen as suitable for further study. Evidence for volatilisation of PbO from the melts was obtained by measuring the mass lost during melting, and by EDX analysis, although the latter method indicated that at $\lesssim$ 20 mol% PbO, germania may also be lost during melting. The overall uncertainty on glass composition was estimated to be ±0.5 mol% PbO.

7.2 Total scattering measurements

7.2.1 Neutron diffraction

7.2.1.1 Distinct scattering and correlation functions

The distinct scattering functions, $i^N(Q)$, measured by neutron diffraction from lead germanate glasses are shown in Fig. 7-3. These were measured on the GEM [9] diffrac-

tometer at the ISIS spallation source. The plate quenched glasses, containing $5 \leq x \leq 50$ mol% PbO, were broken into small (mm sized) pieces inside a percussion mortar, and placed within thin-walled, 8.3 mm diameter, vanadium cans. On account of the lesser amount of material available, the roller quenched glasses, containing $55 \leq x \leq 75$ mol% PbO, were placed inside 5 mm diameter vanadium cans. These latter glasses, in the smaller containers, were exposed to the neutron beam for a factor of 1.76 longer than the plate quenched glasses in the larger V cans. This is not a large enough difference to mitigate the factor of $(8.3/5)^2 = 2.76$ arising from the different container diameters, especially considering the relatively low packing fraction of roller quenched glass flakes. Therefore it is clear in Fig. 7-4, which shows the interference functions, $Qi^N(Q)$, that the data for the high Pb, roller quenched glasses, suffer from a slightly poorer signal to noise ratio. Note that the regions of $i^N(Q)$ (Fig. 7-3) below 0.45 Å^{-1} were extrapolated by fitting of a function of form $A + BQ^2$ to the low Q scattering data between $0.45 \leq Q \leq 0.7$ Å^{-1}. The low Q regions of $i^N(Q)$ from the germanate glasses are qualitatively similar to those of the silicates, particularly for the high Pb ($\gtrsim$ 50 mol% PbO) glasses, showing a first sharp diffraction peak at ~2.0 Å^{-1} and a pre-peak developing at ~1.2 Å^{-1} at 45 mol% PbO. Notably this pre-peak feature is not resolved until 60 mol% PbO in the diffraction patterns from lead silicate glasses. Details of the low Q diffraction peaks, extracted by fitting of Lorentzian lineshapes to their leading edges (as illustrated for a lead silicate glass in Fig. 6-4), are summarised in Table 7-2, and the periodicities, $2\pi/Q$, and correlation lengths, $2\pi/\Delta Q$, plotted in Fig. 7-5 and 7-6 where they are compared to the equivalent values derived from x-ray diffraction (§7.2.2) and from lead silicate glasses. Given that the origin of these diffraction peaks is more readily apparent from consideration of both neutron and x-ray diffraction data, disscussion of their significance will be postponed until §7.2.2 in which the x-ray diffraction data are introduced. It can however be noted from Fig. 7-5 and 7-6 that the behaviour of the two diffraction peaks is similar to their counterparts in the lead silicate neutron diffraction patterns, with the most marked difference being in their smaller widths, associated with larger correlation lengths, and therefore a more well developed intermediate range order.

Fourier transformation of the interference functions, $Qi^N(Q)$, Fig. 7-4, with a large $Q_{max} = 40$ Å^{-1}, and Lorch [10] modification, resulted in the total correlation functions

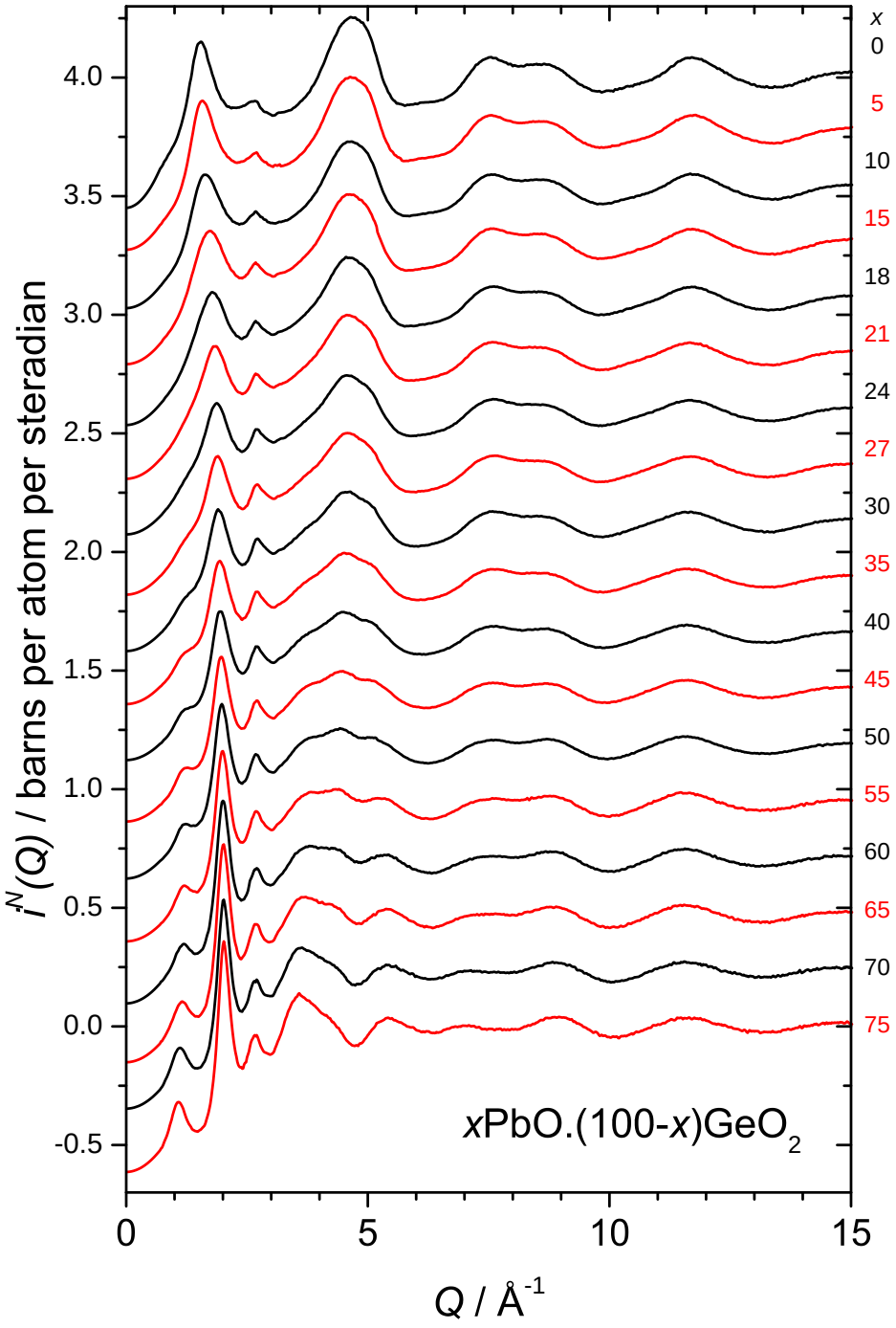

Figure 7-3 Neutron distinct scattering functions for lead germanate glasses, as compared to that measured for vitreous germania, shown to emphasise the low Q region. The molar compositions are indicated on the plot and vertical offsets have been used for clarity.

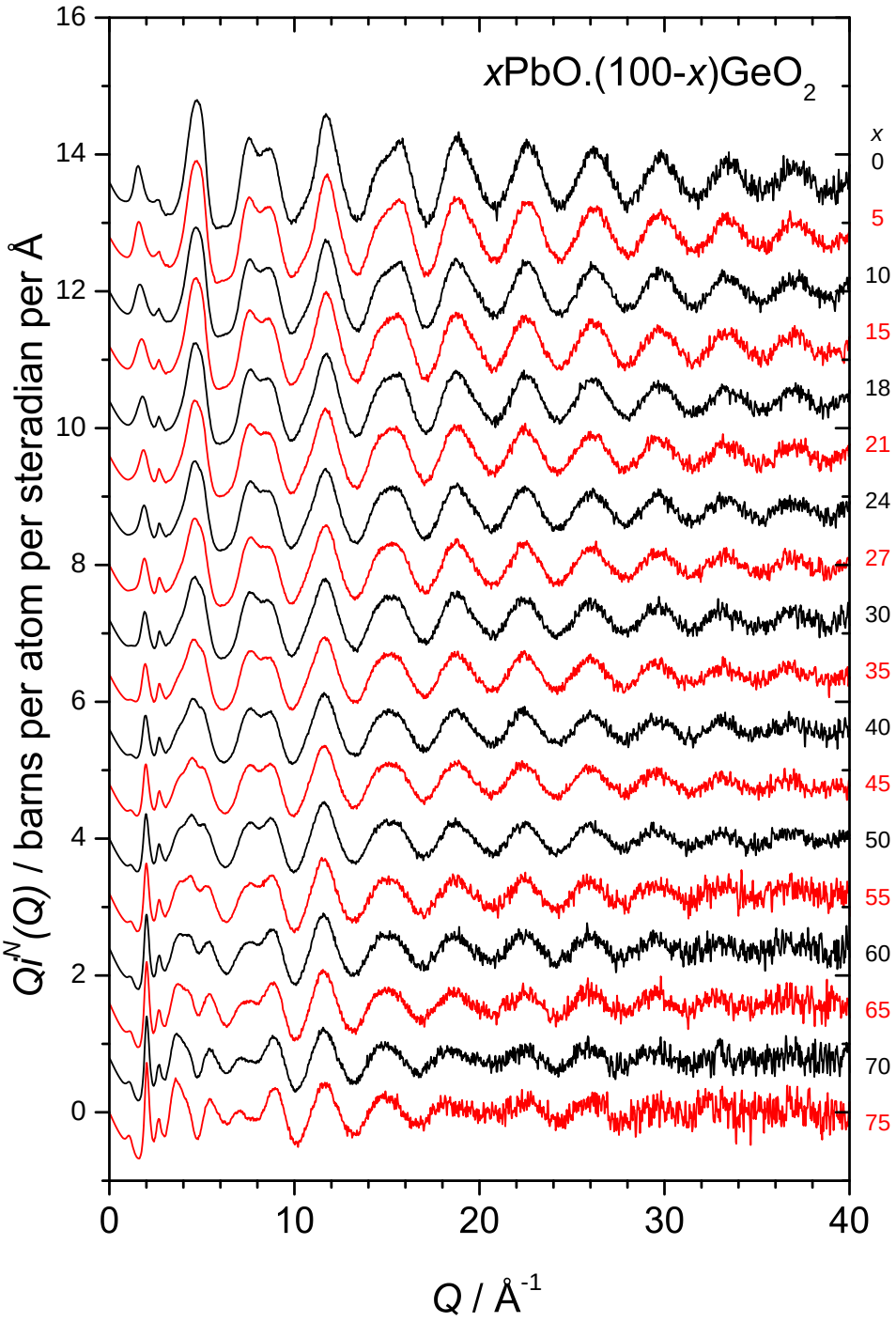

Figure 7-4 Neutron scattering interference functions for lead germanate glasses, as compared to that measured for vitreous germania, shown to emphasise the high Q region. The molar compositions are indicated on the plot and vertical offsets have been used for clarity.

Table 7-2 Details of peaks at low neutron scattering vector magnitude in diffraction patterns from lead germanate glasses.

mol% PbO	Peak position Q (Å^{-1})	Peak width ΔQ (Å^{-1})	Associated periodicity $2\pi/Q$ (Å)	Correlation length $2\pi/\Delta Q$ (Å)	Number of periods $Q/\Delta Q$
			Pre-peak		
44.1	1.25(1)	0.78(2)	5.01(4)	8.0(2)	1.60(05)
48.9	1.24(1)	0.76(2)	5.05(4)	8.2(2)	1.63(06)
55.0	1.22(1)	0.71(1)	5.14(4)	8.9(2)	1.73(05)
60.0	1.20(1)	0.75(2)	5.22(4)	8.3(2)	1.60(05)
65.0	1.17(1)	0.68(1)	5.38(5)	9.2(2)	1.72(05)
70.0	1.12(1)	0.59(1)	5.63(5)	10.6(3)	1.88(06)
75.0	1.09(1)	0.52(1)	5.78(5)	12.0(3)	2.08(08)
			FSDP		
0.0	1.54(1)	0.69(1)	4.08(3)	9.1(2)	2.23(06)
4.7	1.58(1)	0.78(2)	3.97(3)	8.1(2)	2.03(05)
9.7	1.64(1)	0.92(1)	3.83(2)	6.8(1)	1.78(04)
14.7	1.73(1)	1.13(1)	3.63(2)	5.6(1)	1.54(03)
17.7	1.79(1)	1.03(3)	3.51(2)	6.1(2)	1.73(05)
20.4	1.84(1)	0.78(1)	3.41(2)	8.1(1)	2.36(06)
23.6	1.87(1)	0.70(1)	3.35(2)	9.0(2)	2.67(07)
26.5	1.89(1)	0.62(1)	3.32(2)	10.2(2)	3.07(09)
29.4	1.91(1)	0.57(1)	3.29(2)	11.1(3)	3.38(10)
34.5	1.93(1)	0.54(1)	3.25(2)	11.7(3)	3.60(11)
39.7	1.95(1)	0.49(1)	3.22(2)	12.8(4)	3.96(13)
44.1	1.97(1)	0.43(1)	3.19(2)	14.7(5)	4.59(18)
48.9	1.98(1)	0.40(1)	3.18(2)	15.8(6)	4.96(20)
55.0	1.99(1)	0.39(1)	3.15(2)	16.1(6)	5.11(21)
60.0	2.00(1)	0.37(1)	3.14(2)	17.1(7)	5.46(24)
65.0	2.01(1)	0.34(1)	3.13(2)	18.3(8)	5.86(27)
70.0	2.01(1)	0.33(1)	3.12(2)	19.2(8)	6.14(30)
75.0	2.02(1)	0.32(1)	3.11(2)	19.9(9)	6.39(32)

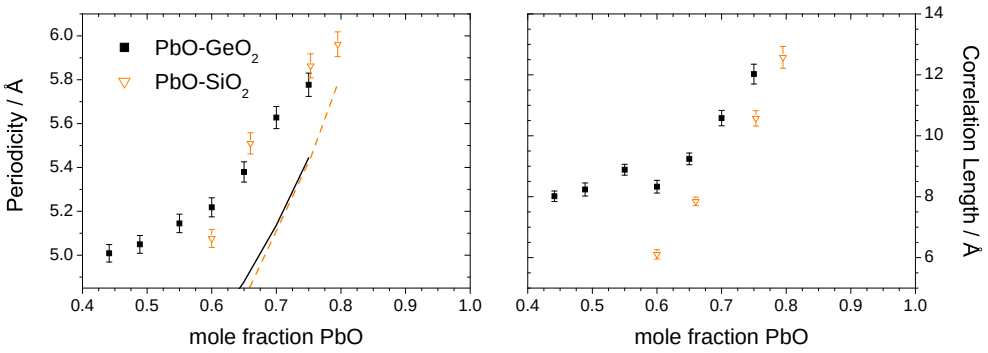

Figure 7-5 Periodicities, $2\pi/Q$, and correlation lengths, $2\pi/\Delta Q$, associated with the low Q pre-peak in neutron diffraction patterns from lead germanate glasses. Analogous data for lead silicate glasses are shown for comparison. The lines represent the average tetravalent cation-cation distances, $r_{XX} = (\rho_0 c_X)^{-1/3}$, assuming a homogeneous dispersion of monomeric $[XO_4]^{4-}$ anions, and are derived from the measured glass densities and compositions.

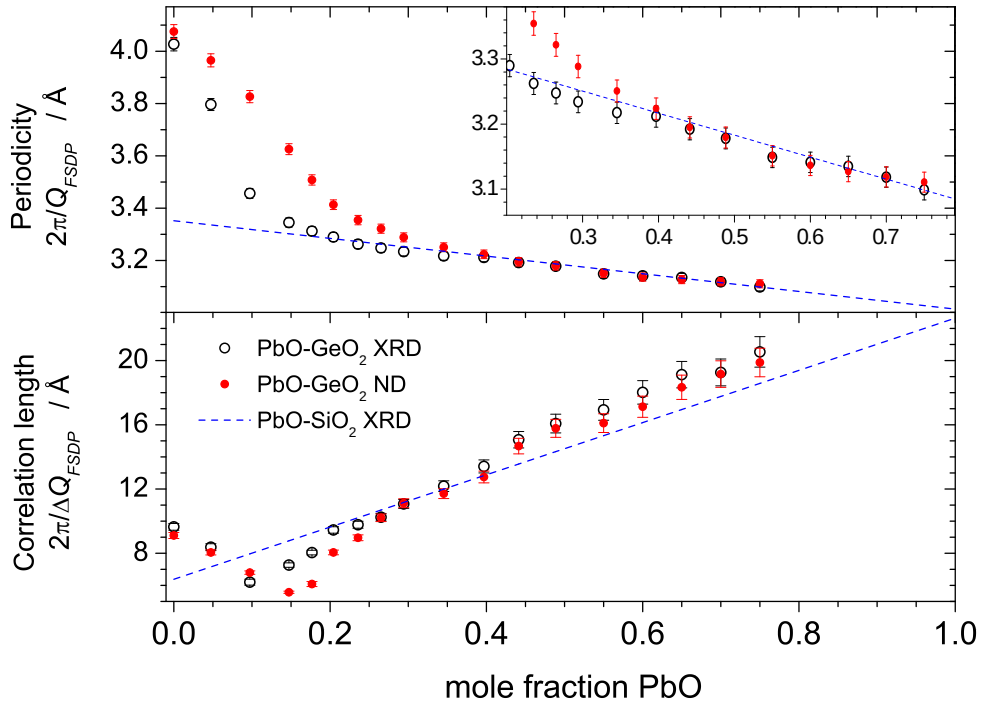

Figure 7-6 Periodicities, $2\pi/Q$, and correlation lengths, $2\pi/\Delta Q$, associated with the first sharp diffraction peak in neutron and x-ray scattering from lead germanate glasses. For comparison, the lines represent linear fits to the x-ray diffraction derived quantities for lead silicate glasses (see Fig. 6-11) over the range 35 to 80 mol% PbO.

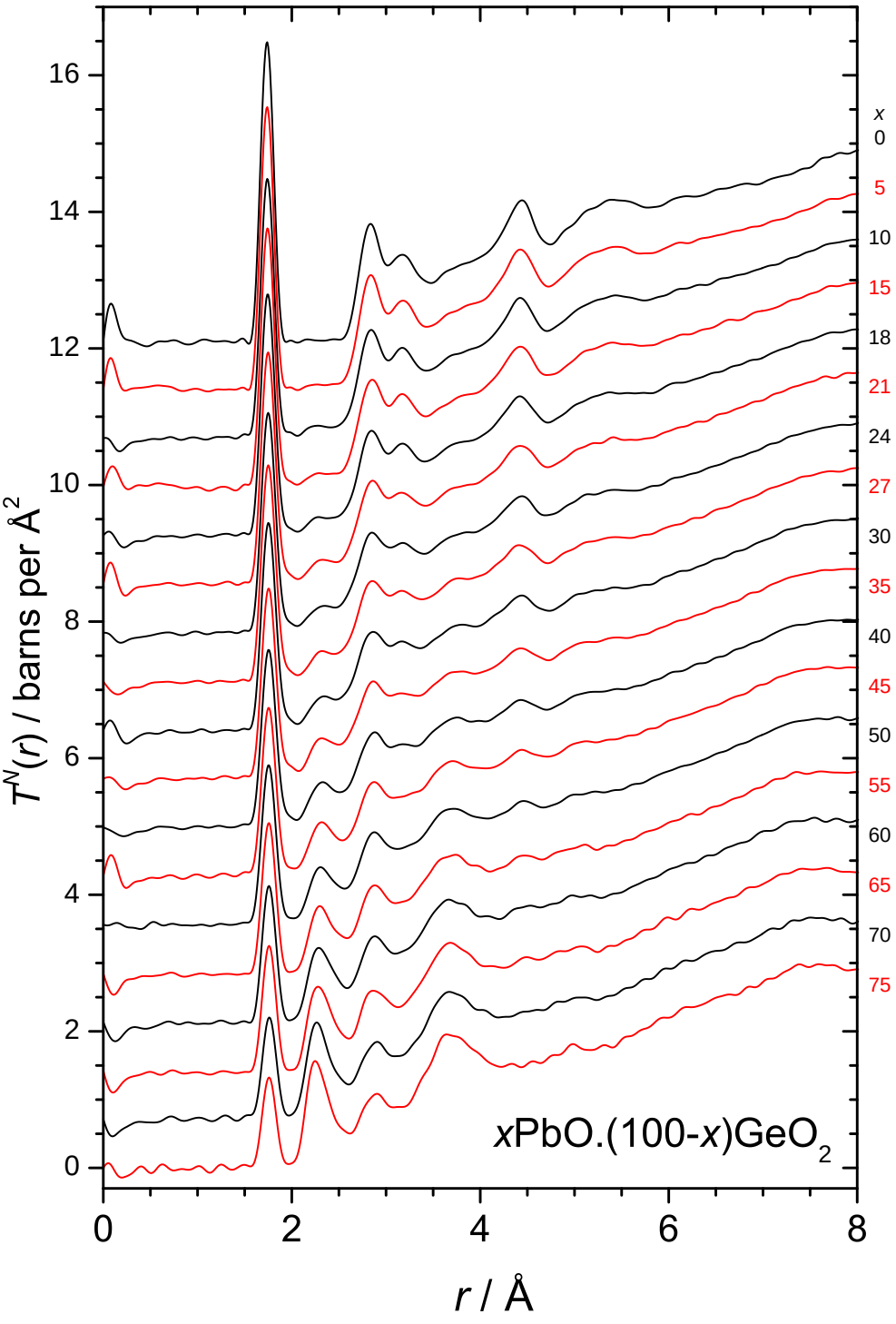

Figure 7-7 Neutron total correlation functions for lead germanate glasses, as compared to that measured for vitreous germania. A Lorch [10] modification function and Q_{max} = 40 Å^{-1} were used. The molar compositions are indicated on the plot and vertical offsets have been used for clarity.

displayed in Fig. 7-7. In order to ensure the correct low r behaviour of $T^N(r)$ (oscillation about zero, with no slope), an effective renormalisation was applied to $i^N(Q)$ prior to transformation. Renormalisation factors were obtained by dividing $T^0(r)/r$ by the modulus of the low r slope of the differential correlation function, $D^N(r)$, obtained prior to renormalisation, which itself was obtained by fitting $D^N(r)$ at low r, including part (low Pb glasses, $\lesssim$ 50 mol% PbO) or all (high Pb glasses, $\gtrsim$ 50 mol% PbO) of the Ge-O peak at ~1.75 Å. These factors account for uncertainties in the measured glass densities and compositions, as well as discrepancies in the normalisation of the diffraction data, but typically deviated from unity by no more than 7%.

A key observation is that a peak in $T^N(r)$ (Fig. 7-7) at ~2.3 Å is present for *all* of the lead germanate glasses, even at 5 mol% PbO. These peaks can be assigned to the Pb-O pair term, and such short Pb-O bonds are typical of Pb^{2+} sites with low coordination number and non-bonding electron lone pairs with p-character that are stereochemically active. This implies that at least some of the lead, in all glasses, are playing network forming roles (low oxygen coordination numbers) rather than acting as typical network modifying cations with higher coordination numbers to oxygen.

7.2.1.2 Ge-O bond length distributions

Closer inspection of the Ge-O bond length distributions at ~1.75 Å reveals that they exhibit asymmetry, particularly in the range $15 \lesssim x \lesssim 50$ mol% PbO, with a small broadening to the high r side. This is characteristic of the presence of Ge coordinated to greater than four oxygen ligands. Comparisons of three Ge-O bond length distributions with those of isomolar caesium [11] and calcium (Chapter 5) germanate glasses containing approximately 79, 76 and 70 mol% GeO_2 are made in Fig. 7-8. This reveals that the asymmetry is less marked in the case of the lead germanate glasses. Table 7-3 summarises the average Ge-O and O-Ge coordination numbers calculated by integration of $rT^N(r)\mathrm{d}r$ from 1.52 Å up to the first minimum (beyond the peak maximum) which occurs at about 2.05 Å, approximately independent of glass composition, and n_{GeO} is plotted as a function of glass composition in Fig. 7-9. As indicated by the small asymmetry of the Ge-O bond length distributions (Fig. 7-8), the Ge-O coordination numbers are smaller in the PbO germanate system, *cf.* the CaO and Cs_2O germanates. Furthermore, n_{GeO} is larger in the $PbGe_4O_9$ [12, 13] and $PbGe_3O_7$ [14] crystal structures than

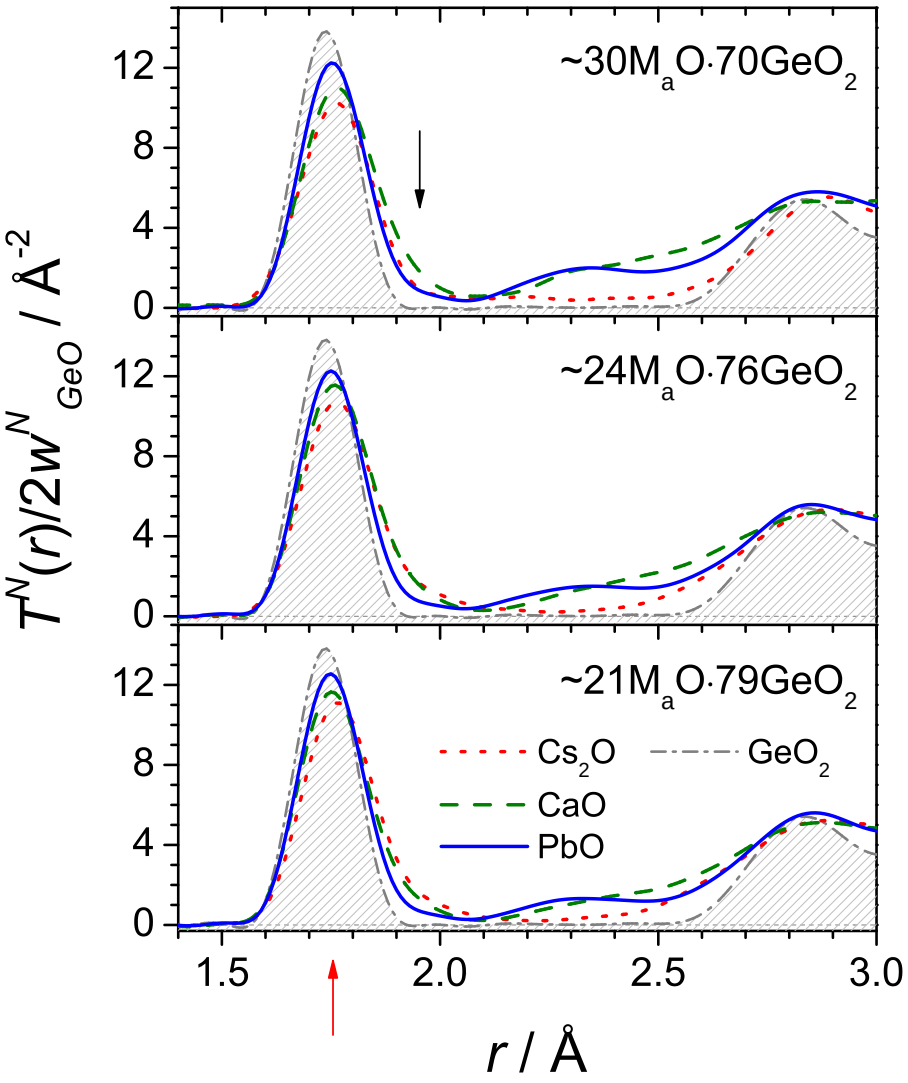

Figure 7-8 Comparison of the Ge-O bond length distributions in binary germanate glasses containing either caesium [11], calcium or lead, and in vitreous GeO_2 (shaded). The neutron total correlation functions, divided by the Ge-O pair weighting factors are shown, and the molar glass compositions are indicated on the plot. The red arrow indicates the main Ge-O peak at ~1.75 Å, whilst the black arrow points to the high r shoulder of the distribution. A Lorch [10] modification function and Q_{max} = 40 Å^{-1} were used.

Table 7-3 Parameters derived from the Ge-O bond length distribution for lead germanate glasses. The fraction of [GeO_5] ([GeO_6]) units, assuming no [GeO_6] ([GeO_5]) is $N_5 = n_{GeO} - 4$ ($N_6 = (n_{GeO} - 4)/2$). The fraction of NBOs is $f_{NBO} = 2 - n_{OGe}$, and the final column lists the number of NBOs per lead ion. Uncertainties in parentheses.

mol% PbO	r_{GeO} (Å)	n_{GeO}	N_5	N_6	n_{OGe}	f_{NBO}	NBO/Pb^{2+}
0	1.7389(6)	3.98(1)	-0.02(1)	-0.01(1)	1.99(1)	0.012(2)	-
4.7(5)	1.7402(32)	3.99(2)	-0.01(2)	0.00(1)	1.95(1)	0.053(3)	2.17(26)
9.7(5)	1.7446(15)	3.95(2)	-0.05(2)	-0.03(1)	1.87(1)	0.127(2)	2.48(13)
14.7(5)	1.7485(20)	4.14(2)	0.14(2)	0.07(1)	1.91(1)	0.094(2)	1.18(5)
17.7(5)	1.7524(49)	4.06(2)	0.06(2)	0.03(1)	1.83(1)	0.167(4)	1.72(6)
20.4(5)	1.7583(48)	4.11(2)	0.11(2)	0.06(1)	1.82(1)	0.178(4)	1.56(5)
23.6(5)	1.7606(67)	4.06(2)	0.06(2)	0.03(1)	1.76(1)	0.243(5)	1.82(5)
26.5(5)	1.7625(85)	4.14(3)	0.14(3)	0.07(1)	1.75(1)	0.246(7)	1.61(5)
29.4(5)	1.7645(86)	4.11(3)	0.11(3)	0.06(1)	1.70(1)	0.299(7)	1.73(5)
34.5(5)	1.7679(117)	4.07(3)	0.07(3)	0.03(2)	1.61(1)	0.390(8)	1.87(5)
39.7(5)	1.7656(58)	4.06(3)	0.06(3)	0.03(1)	1.53(1)	0.473(4)	1.91(3)
44.1(5)	1.7627(67)	3.98(3)	-0.02(3)	-0.01(2)	1.43(1)	0.572(4)	2.02(2)
48.9(5)	1.7598(144)	3.99(4)	-0.01(4)	0.00(2)	1.35(1)	0.650(9)	2.01(3)
55.0(5)	1.7583(22)	3.91(4)	-0.09(4)	-0.04(2)	1.21(1)	0.785(2)	2.07(2)
60.0(5)	1.7609(34)	3.91(4)	-0.09(4)	-0.05(2)	1.12(1)	0.883(2)	2.06(1)
65.0(5)	1.7605(13)	3.91(5)	-0.09(5)	-0.04(2)	1.01(1)	0.986(2)	2.05(1)
70.0(5)	1.7611(95)	3.91(6)	-0.09(6)	-0.05(3)	0.90(1)	1.099(4)	2.04(1)
75.0(5)	1.7615(108)	3.99(7)	-0.01(7)	-0.01(4)	0.80(1)	1.202(4)	2.00(1)

in the glasses of similar composition. This is a qualitatively similar result to that found for the calcium germanate series (Fig. 5-9). In other words, whilst the n_{GeO} of the lead tetra- and trigermanate crystals (containing [GeO_4] and [GeO_6], and [GeO_4] and [GeO_5] respectively) follow the model predictions of Hannon *et al.* [15], the lead germanate glasses contain excess NBOs. Despite significant scatter of the $n_{GeO}(x)$ points, a broad maximum is apparent, with a peak value of $n_{GeO}(0.265(5)) = 4.14(3)$, beyond which, at higher PbO contents, the coordination numbers decline toward the tetrahedral value of 4 at ~50 mol% PbO. This result implies a maximum of 14(3)% of Ge atoms in 5-fold coordination or 7(1)% in 6-fold coordination. These are small fractions compared to the Ca and Cs modified germanate glasses, indicating that Pb is playing a different structural role (see §7.2.1.3).

Fig. 7-10 compares the average Ge-O bond lengths, derived from the first moments of the Ge-O bond length distributions, of lead, calcium and caesium germanate glasses. In the PbO–GeO_2 series, r_{GeO} increases upon addition of PbO, and passes through a maximum at 35 mol% PbO, similar to the behaviour in CaO–GeO_2 glasses. The r_{GeO}

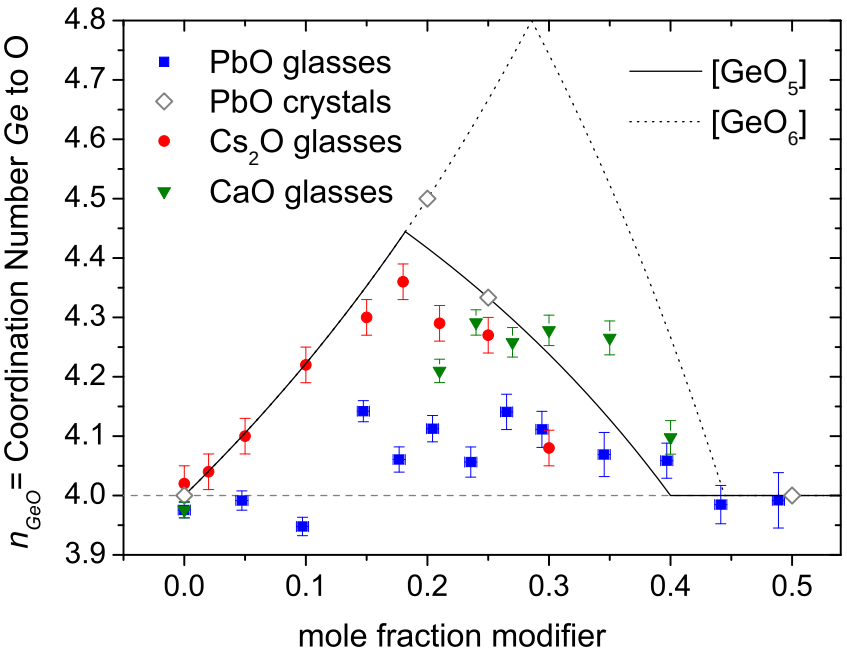

Figure 7-9 Ge-O coordination numbers in lead germanate glasses, extracted by means of integration of $rT^N(r)\mathrm{d}r$ (filled squares) as a function of glass composition. Values for ambient pressure crystalline lead germanates [12–14, 16, 17] (open diamonds), as well as vitreous calcium (Chapter 5, filled triangles) and caesium [11] (filled circles) germanates are shown for comparison. The lines represent the models of Hannon *et al.* [15] for five (solid) and six (dashed) coordinated germanium, see equations 2-6 and 2-7.

in the lead germanate glasses are also systematically smaller than in the CaO–GeO_2 glasses, consistent with the smaller n_{GeO}. The position of the peak r_{GeO} at 35 mol% MO, higher than the peak in n_{GeO}, indicates that there is another mechanism of bond elongation, in addition to the conversion of [GeO_4] to [GeO_5] or [GeO_6]. Indeed, this is supported by the fact that the average Ge-O bond length in PbO–GeO_2 glasses does not return to its value in pure GeO_2 glass (1.7382(6) Å, see appendix B) for $\gtrsim$ 50 mol% PbO, but appears to plateau at an intermediate value of $\approx$ 1.761 Å.

As for the Si-O bond length and Si-O-Si bond angle [25, 26], so r_{GeO} has been correlated with the reciprocal cosine of the Ge-O-Ge bond angle [27]. The Ge-O bond length is therefore also a function of the degree of *s* (or *p*) electron character of the oxygen, with greater *s* character correlating with shorter Ge-O bonds. Therefore, as in the lead silicates (§3.4.2, §6.4.1.1), an increase in oxygen *p* character is expected with increasing PbO content owing to the increase of O_{nb}-Pb coordination (Pb about a NBO) number and the reduction in Ge-O-Pb bond angle. In other words, the NBOs tend toward sp^3 hybridised [OPb_3Ge] type environments, whilst the contribution from

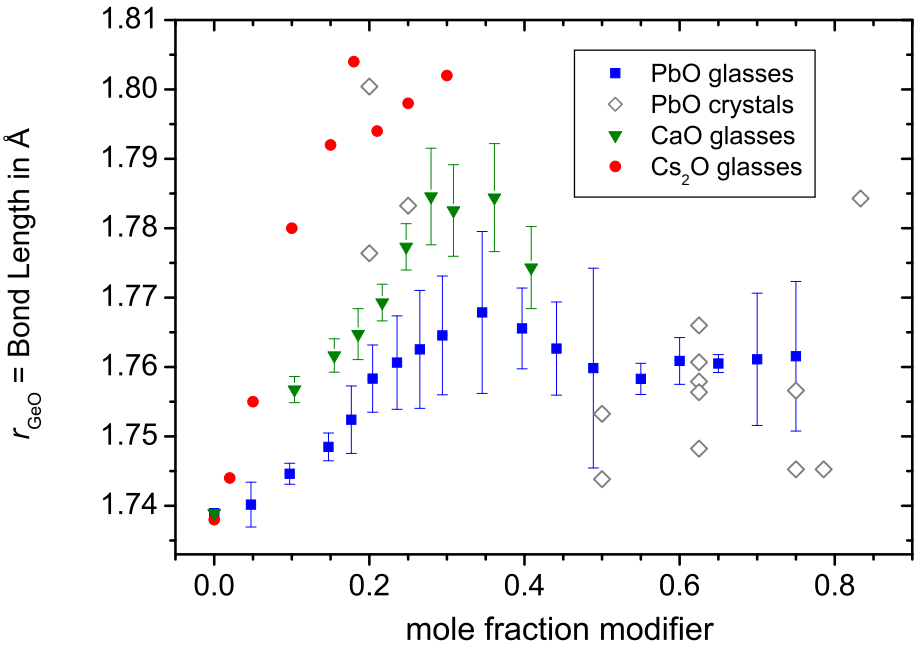

Figure 7-10 Average Ge-O bond lengths in lead germanate glasses, extracted by means of integration of $rT^N(r)\mathrm{d}r$ (filled squares) as a function of glass composition. Values for ambient pressure crystalline lead germanates [2, 4, 12–14, 16–24] (open diamonds), as well as vitreous calcium (Chapter 5, filled triangles) and caesium [11] (filled circles) germanates are shown for comparison.

Ge-O-Ge (Ge-O_b) bonds decreases with the germanate network depolymerisation and the number of BOs.

7.2.1.3 Correlation function peak fits

The neutron $T^N(r)$ were fitted differently in the high PbO (> 50 mol%) and low PbO (≤ 50 mol%) regions. Low PbO compositions were fitted typically with two Ge-O peaks, as necessary to reproduce the asymmetric bond length distributions, along with the leading edges of the Pb-O peaks. Intrapolyhedral O-O correlations could not be accurately simulated based on the presence of multiple Ge centred polyhedral environments, with unknown geometries. Fig. 7-11 shows an example fit to the $T^N(r)$ for $27\,PbO \cdot 73\,GeO_2$ glass. Here an O-O peak based on all Ge in ideal [GeO_4] tetrahedral sites has been simulated, with the width equal to that measured for vitreous germania (see Appendix B). Owing to the total Ge-O coordination of 4.14(3), one would in fact expect a larger contribution to the correlation function from intrapolyhedral O-O pairs, and one which would be asymmetrically broadened to both the high r and low r sides

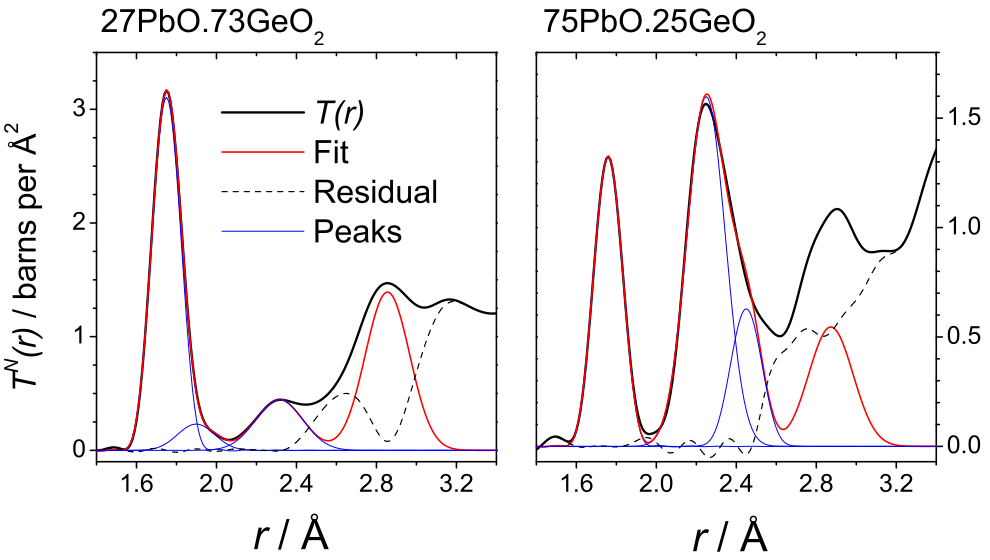

Figure 7-11 Example peak fits to neutron total correlation functions from 27 and 75 mol% PbO lead germanate glasses. A Lorch [10] modification function and $Q_{max} = 40$ Å^{-1} were used during Fourier transformation. Pb-O peaks have been fitted at ~2.25 Å. Two Ge-O peaks have been used to reproduce the asymmetric Ge-O bond length distribution in 27 $PbO \cdot 73\ GeO_2$. Intratetrahedral O-O correlations have been calculated (at ~2.86 Å) in both cases based on all Ge in ideal [GeO_4] tetrahedral sites. This is a valid model in 75 $PbO \cdot 25\ GeO_2$ glass, allowing the fitting of a second Pb-O correlation at ~2.45 Å, but is a less good approximation in 27 $PbO \cdot 73\ GeO_2$ glass, where the intrapolyhedral O-O correlation would likely be broadened asymmetrically to both sides due to the presence of [GeO_5] and/or [GeO_6].

of the O-O peak shown. This fact prevented the useful fitting of Pb-O and/or O-O peaks to the ~2.6 Å region.

For the high PbO composition glasses, a symmetric Ge-O peak in $T^N(r)$, coupled with lower n_{GeO}, close to four, was taken as evidence for all Ge in tetrahedral environments, and therefore the intrapolyhedral O-O peak could be more accurately simulated. Fig. 7-11 shows an example fit for 75 $PbO \cdot 25\ GeO_2$ glass in which the knowledge of the O-O contribution allows an additional Pb-O correlation to be fitted at 2.450(3) Å. Although additional intensity in the ~2.6 Å region remains unassigned, it also is likely due to Pb-O scattering pairs (see §7.2.2 on x-ray diffraction).

The results from peak fitting are represented graphically in Fig. 7-12, 7-13 and 7-14. The parameters r_{GeO} and n_{GeO} calculated from two fitted Ge-O peaks agree well with those obtained by integration of $rT^N(r)\mathrm{d}r$. Note that the marginally depressed values (below 4) of n_{GeO} in the high PbO region are consistent with a small excess of PbO

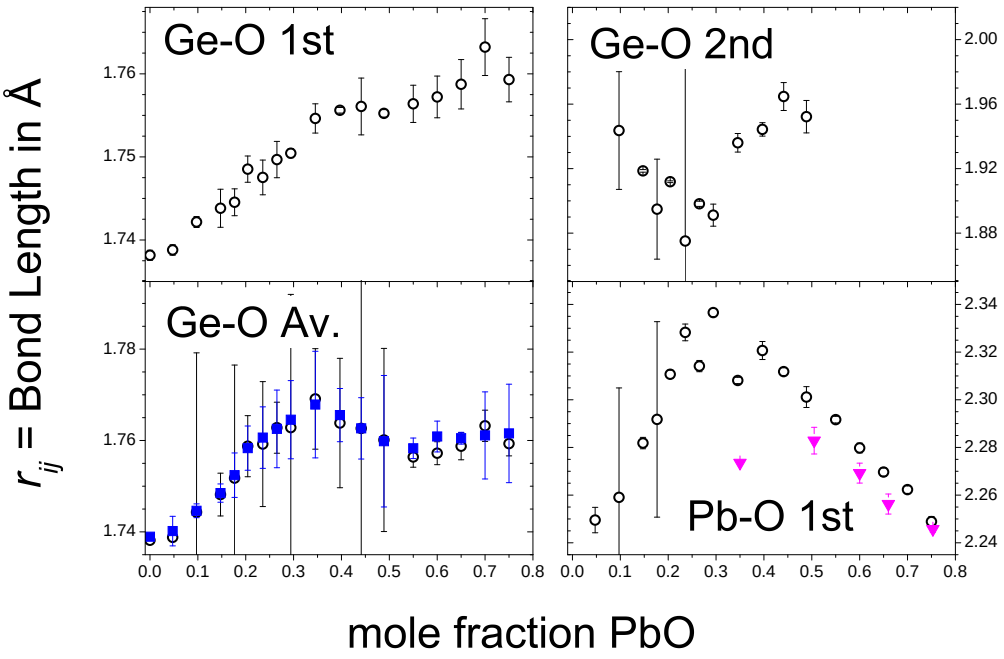

Figure 7-12 Average bond lengths, r_{ij}, from peak fits to neutron total correlation functions from lead germanate glasses. Error bars represent the statistical uncertainties of the fits. Points obtained by integration of $rT^N(r)\mathrm{d}r$ are shown as blue squares. Equivalent values for lead silicate glasses are shown as magenta triangles.

compared to nominal compositions, as indicated by EDX measurements (Table 7-1).

The most accurately determined parameters derived from peak fitting are the r_{ij}, Fig. 7-12, and these show that the position of the main Pb-O peak passes through a maximum at approximately the same glass composition as does the average r_{GeO}. The two parameters are correlated as a result of bonds from lead to BO which are underbonded by germanium as a result of the presence of 5- or 6-fold Ge centred polyhedra. This may indicate the presence of some Pb with relatively high coordination numbers (*cf.* PbO−SiO_2 glasses, Chapter 6), and therefore playing a more network modifying, than network forming, role.

The coordination numbers, Fig. 7-13 and RMS bond length deviations, Fig. 7-14, are less well determined than the bond lengths themselves because they are more prone to uncertainties arising from baseline oscillations (reciprocal space noise), overlap with other contributions to $T^N(r)$, and normalisation (and glass composition and density) in the case of the n_{ij}. Nonetheless, the Pb-O coordination numbers do indeed tend to follow the trend of the r_{PbO}, passing through a maximum, despite considerable scatter,

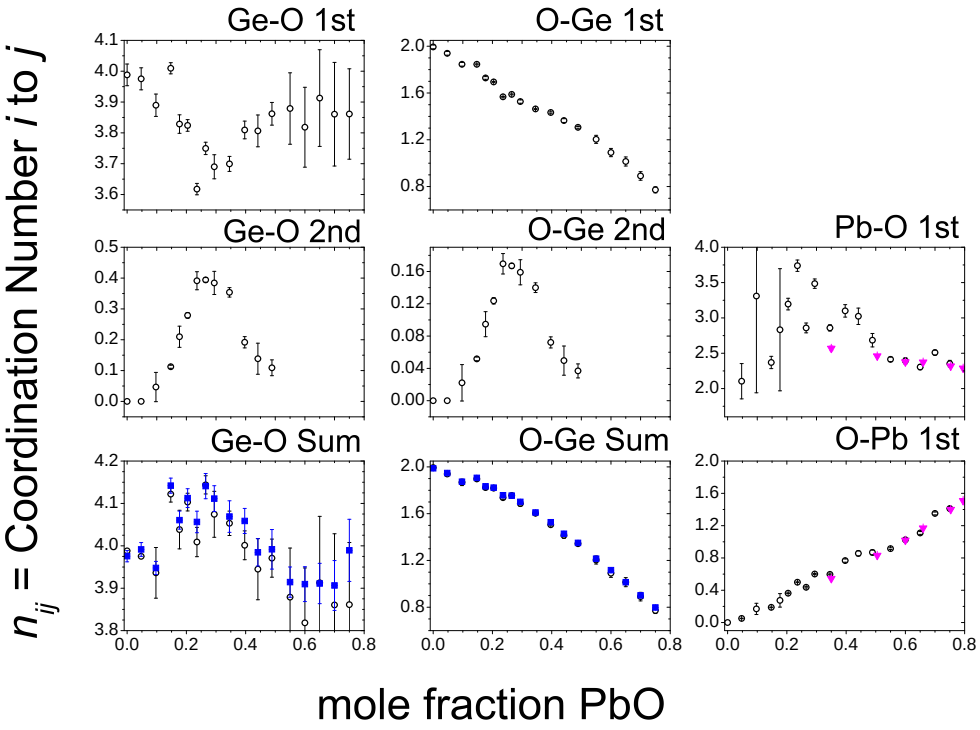

Figure 7-13 Average coordination numbers, n_{ij}, from peak fits to neutron total correlation functions from lead germanate glasses. Error bars represent the statistical uncertainties of the fits. Points obtained by integration of $rT^N(r)\mathrm{d}r$ are shown as blue squares. Equivalent values for lead silicate glasses are shown as magenta triangles.

which correlates with the scatter in the measured peak widths, $\langle u^2_{PbO}\rangle^{1/2}$.

Comparison is made in Fig. 7-12, 7-13 and 7-14 to the analogous Pb-O peak fit parameters from lead silicate glasses (see also §6.2.1.2). It is clear, particularly at ~35 mol% PbO, that both r_{PbO} and n_{PbO} are larger in the germanate glass, than in the silicate. At higher PbO contents the n_{PbO} converge, whilst the r_{PbO} remain marginally (~1 pm) longer in the germanates, which can be attributed to the higher electronegativity of Ge compared to Si [28].

Therefore, there is evidence that Pb, on average, is acting more like a network modifier and less like a network former at compositions where [GeO_5] and/or [GeO_6] are present. Such an effect is indeed apparent in crystalline lead germanates (see §3.6), where, for example Pb may be isomorphous with Ba or Sr (α-$PbGe_4O_9$ [12]), playing a purely network modifying role, or may occupy distorted 7-fold sites (γ-$PbGe_4O_9$ [13] and $PbGe_3O_7$ [14]), playing an intermediate role. However, it is important to remember that the n_{GeO} and the r_{GeO} measured for the crystals are significantly larger than for the

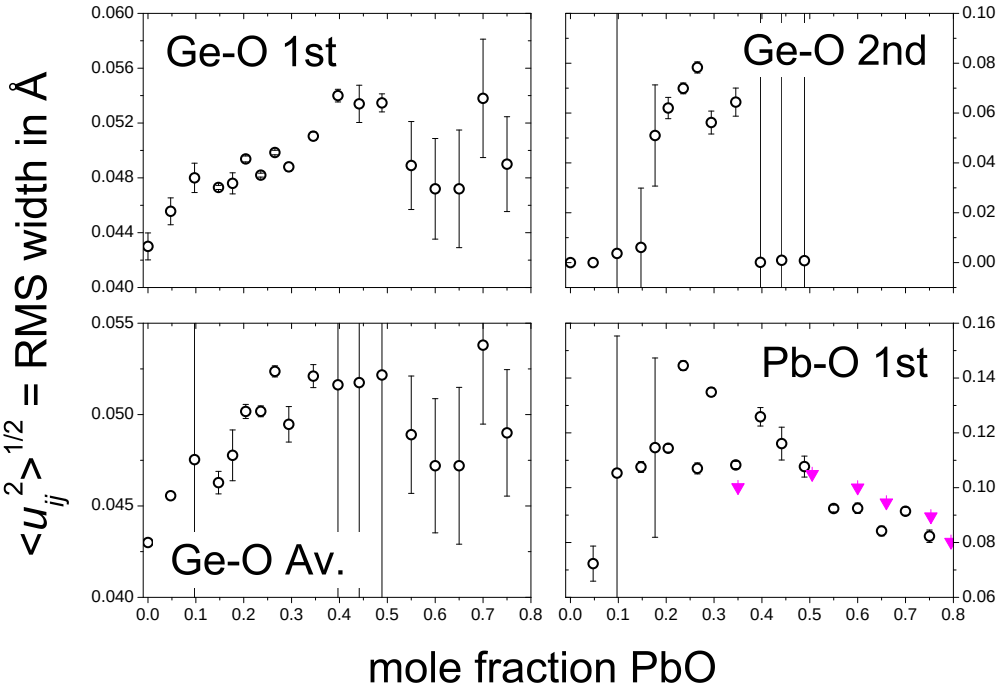

Figure 7-14 RMS bond length deviations, $\langle u_{ij}^2 \rangle^{1/2}$, from peak fits to neutron total correlation functions from lead germanate glasses. Error bars represent the statistical uncertainties of the fits, with very large values indicating divergence of the fits (toward $\langle u_{GeO}^2 \rangle^{1/2} = 0$ Å) to very small high r shoulders on the Ge-O bond length distributions for some points. Equivalent values for lead silicate glasses are shown as magenta triangles.

glasses (Fig. 7-9 and 7-10), and that the differences in Pb environment for high and low PbO content germanate glasses are therefore more subtle. Futhermore, the total neutron scattering measurements do not distinguish between all Pb on intermediate (γ-$PbGe_4O_9$ [13] and $PbGe_3O_7$ [14]) type sites, or a mixture of network forming, modifying and/or intermediate type sites. What is clear is that there are always a large number of short bonds, definitively ruling out all Pb acting as glass network modifier.

7.2.2 X-ray diffraction

High energy x-ray diffraction measurements were made on powdered glasses at the wiggler beamline BW5 [29, 30] on the synchrotron radiation source DORIS III, HASYLAB at DESY. X-ray energies of 85.336 keV and 84.768 keV were used for low (≤ 50 mol%) and high (> 50 mol%) PbO glasses respectively, yielding values of $Q_{max} = 23.78$ Å^{-1} and $Q_{max} = 23.62$ Å^{-1}.

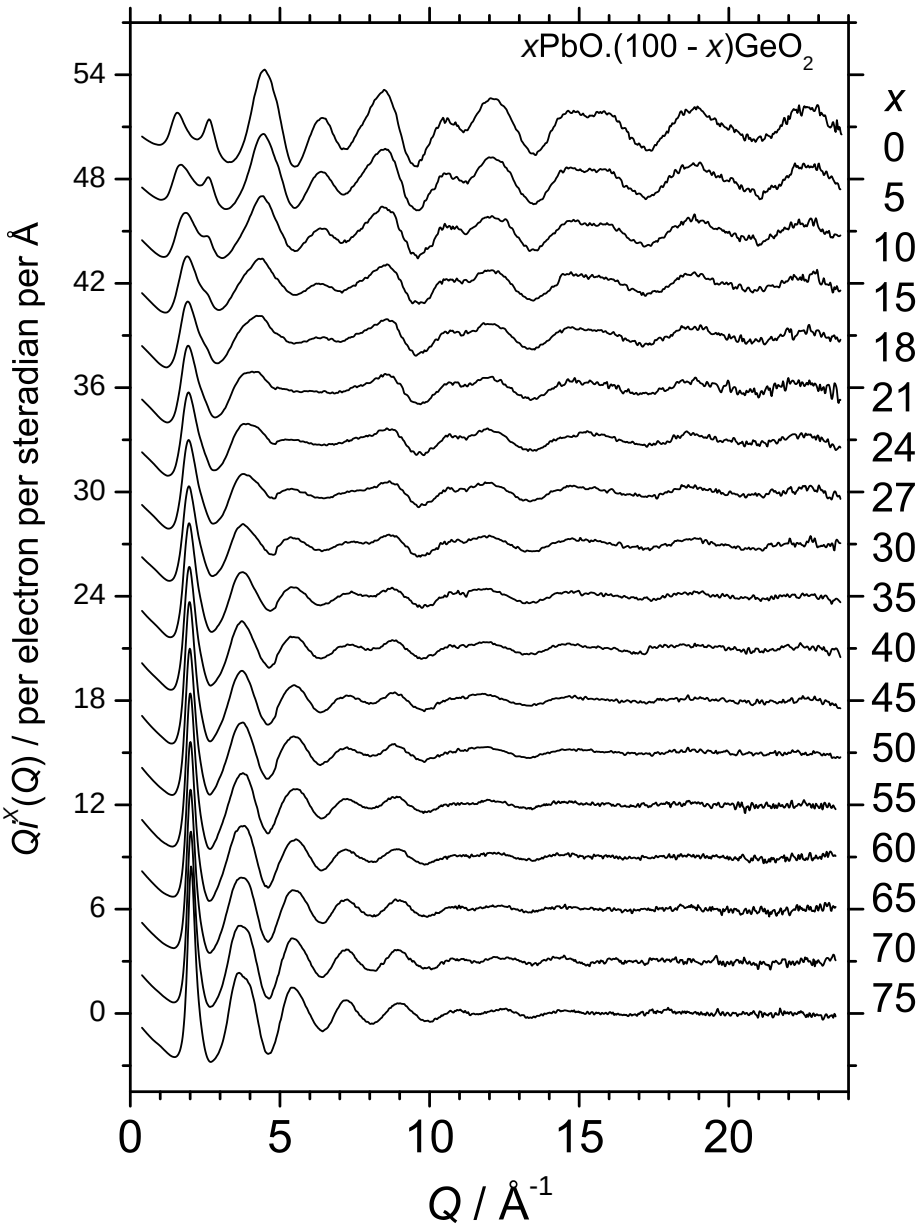

Figure 7-15 X-ray scattering interference functions for lead germanate glasses, as compared to that measured for vitreous germania, shown to emphasise the high Q region. The molar compositions are indicated on the plot and vertical offsets have been used for clarity.

Interference functions for lead germanate glasses, and for vitreous germania are shown in Fig. 7-15. A most striking feature is the FSDP at ~2.0 $Å^{-1}$, which is most dominant and narrow at the highest PbO composition and shows great similarity to that observed for lead silicate glasses (§6.2.2.1). Lorentzian fits to the leading edges of the FSDPs of each diffraction pattern allow the extraction of its position and width, which are reciprocally related to the periodicities and correlation lengths plotted in Fig. 7-6. The pair weighting factors should be borne in mind when traversing the compositional

series, and Fig. 4-1 shows that the dominant terms are Ge-O and Ge-Ge at low PbO content, and Pb-Pb followed by Pb-O and Pb-Ge at high PbO content, whilst an intermediate region also exists where the Pb-Ge term is dominant. The FSDP at ~2.0 Å^{-1} can therefore be attributed to Pb-Pb scattering pairs, and it can be seen that its associated periodicity follows the same linear trend with glass composition as for the lead silicate glasses (see also Fig. 6-11), at least for compositions with $\gtrsim$ 21 mol% PbO. Divergence of the points (Fig. 7-6) from the linear trend below 21 mol% PbO can be seen as a consequence of terms other than Pb-Pb becoming dominant, which is supported by the fact that the ND derived points diverge at the higher value of ~40 mol% PbO. A similar argument can be applied to the correlation lengths, in the lower part of Fig. 7-6, but in addition, it is apparent that the points for the lead germanate glasses do not follow the same trend as the lead silicate glasses, in fact they are systematically longer by ~1.9 Å (at $\gtrsim$ 45 mol% PbO). This is qualitatively similar to the behaviour of the pre-peaks observed in the neutron diffraction patterns, Fig. 7-5, where again the periodicities follow the same trend as do the $PbO-SiO_2$ glasses, whilst the correlation lengths are systematically longer in the case of $PbO-GeO_2$ glasses. All of these observations point toward a significant degree of intermediate range ordering present in the plumbite rich glasses, and one which is able to develop further in the presence of germanate anions, than in the presence of the more strongly bound silicate anions.

The x-ray distinct scattering, at low Q, is illustrated in Fig. 7-16. Between 5 and ~40 mol% PbO there is a rise in SAXS intensity which gradually shifts to higher Q with increasing PbO content. This is not evident in $i^X(Q)$ for GeO_2 or for the lead germanate glasses with > 40 mol% PbO. SAXS from lead germanate glasses has been studied by Bogdanov *et al.* [31] who found a similar limit ($\gtrsim$ 40 mol% PbO) beyond which there was little contribution from concentration fluctuations. The authors [31] also showed that the SAXS intensity (extrapolated to $Q = 0$) peaks at lower (10 mol%) PbO content in the germanate glasses, than in the silicates (25 mol% PbO [32]). Fig. 7-16b further shows that at 35 mol% PbO the form of the SAXS curve is broader for the germanate glass, than for the silicate, spreading into the 1.0 to 1.5 Å^{-1} region.

The total correlation functions, obtained by Fourier transform of the interference functions in Fig. 7-15 are displayed in Fig. 7-17. At high PbO content, the Pb-Pb term is dominant and the $T^X(r)$ are highly similar to those of high lead silicate glasses

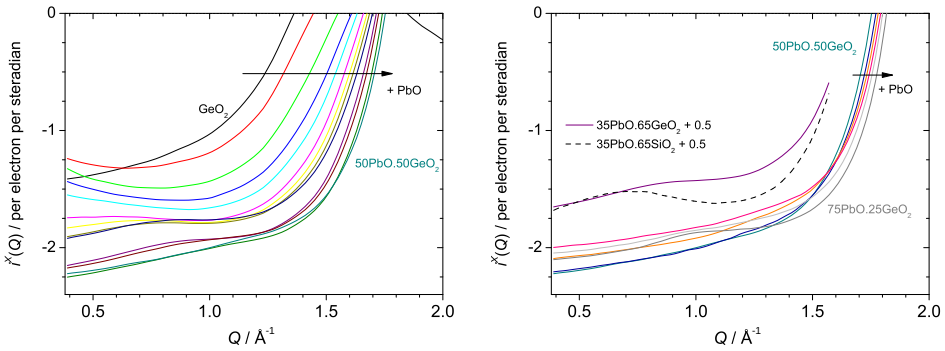

(a) **(b)**

Figure 7-16 X-ray distinct scattering functions at low Q for lead germanate glasses, as compared to that measured for vitreous germania. a) 0 to 50 mol% PbO, b) 50 to 75 mol% PbO. All molar compositions in Fig. 7-15 are represented, and can be identified, for example, using the increase in the Q value at which $i^X(Q)$ is first equal to zero with increasing PbO content, indicated by the arrows. In part b) a comparison is also made between $x\text{PbO} \cdot (100 - x)\text{JO}_2$ glasses with x = 35 mol% PbO and J = Ge or Si, offset for clarity.

(Fig. 6-13). At low PbO content it is interesting to note that a peak at ~3.75 Å appears immediately upon addition of PbO to germania, between the Ge-Ge peak at ~3.17 Å and the second Ge-O at ~4.45 Å. This is coincident with the position of the first Pb-Pb peak at high PbO content, but in the low PbO region must be ascribed to the Pb-Ge term based on the pair weighting factors (see Fig. 4-1). This implies a most probable Ge-O-Pb bond angle of ~135°, larger than the Pb-O-Pb angle of ~109°.

The peaks fitted to the $T^N(r)$ measured by neutron diffraction (Fig. 7-11) have been weighted and broadened appropriately for comparison to $T^X(r)$ in Fig. 7-18, for the 27 and 75 mol% PbO lead germanate glasses. In the former case, the residual at ~2.6 Å is attributed to longer Pb-O bonds. In the case of the 75 mol% PbO germanate glass, the Pb-Pb peak has been estimated from that fitted to the leading edge of $T^X(r)$ for an $80\,\text{PbO} \cdot 20\,\text{SiO}_2$ glass (see §6.2.2.2). Given the small difference in PbO contents of the glasses, and the fact that small Pb-O and Pb-Si contributions were neglected in the fitting procedure, the Pb-Pb peak is likely an overestimate of the contribution to $T^X(r)$ for $75\,\text{PbO} \cdot 25\,\text{GeO}_2$ glass. Therefore the asymmetric contribution to the residual function between 3.0 and ~3.6 Å (Fig. 7-18) is likely underestimated in magnitude, and can be attributed predominantly to the Ge-Pb term, with some contribution from Pb-O (Ge-Ge, Ge-O and O-O being negligible).

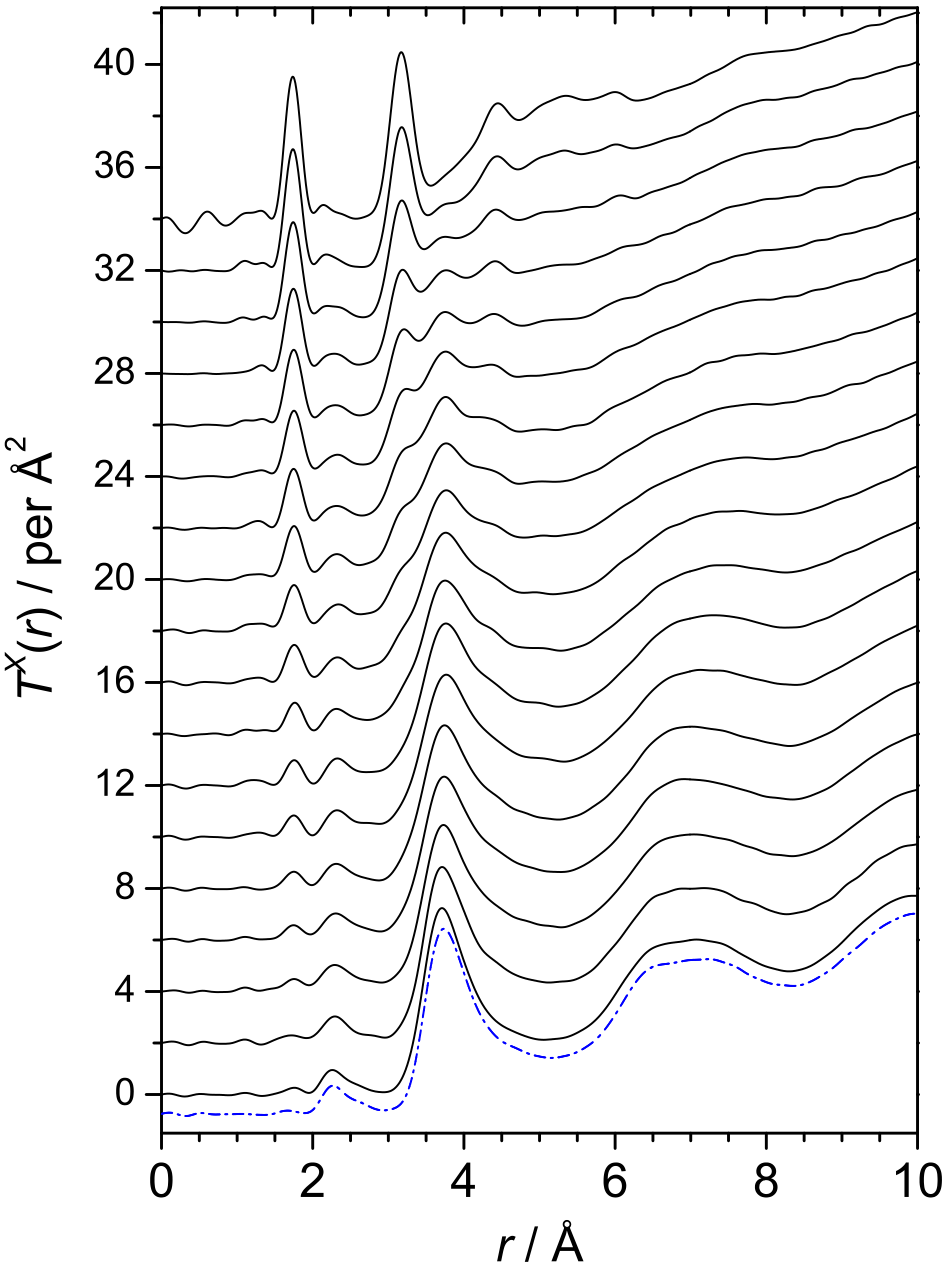

Figure 7-17 X-ray total correlation functions for lead germanate glasses, as compared to those measured for vitreous germania (top) and $75\,PbO \cdot 25\,SiO_2$ glass (bottom, broken curve). A Lorch [10] modification function and $Q_{max} = 23.78\,Å^{-1}$ (≤ 50 mol% PbO) and $Q_{max} = 23.62\,Å^{-1}$ (> 50 mol% PbO) were used. The molar compositions are as indicated in Fig. 7-15 and vertical offsets have been used for clarity.

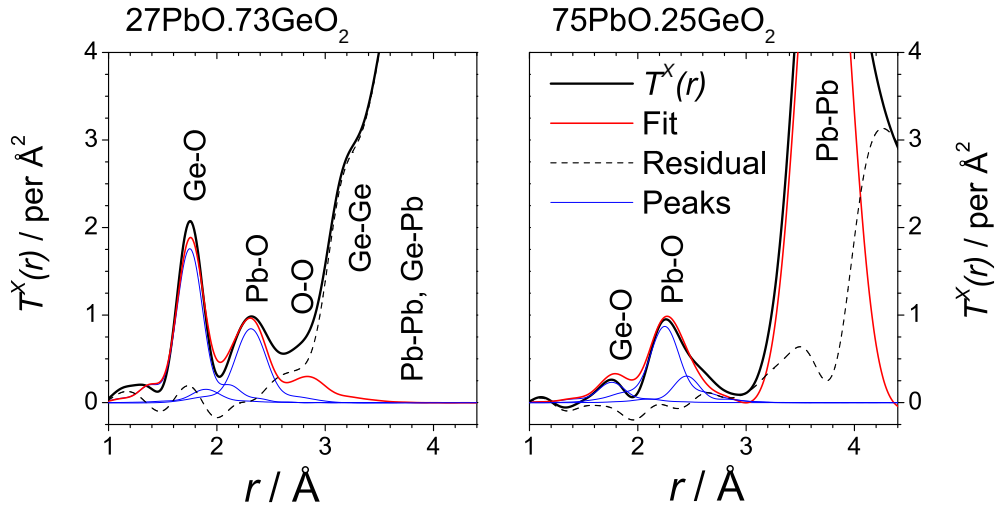

Figure 7-18 Comparison of neutron peak fits to x-ray total correlation functions from 27 and 75 mol% PbO lead germanate glasses. A Lorch [10] modification function and $Q_{max} = 23.78\,\text{Å}^{-1}$ and $Q_{max} = 23.62\,\text{Å}^{-1}$ were used during Fourier transformation respectively. See Fig. 7-11 for the neutron weighted functions.

7.3 Empirical potential structure refinement

7.3.1 Introduction

The $27\,\text{PbO} \cdot 73\,\text{GeO}_2$ glass has the highest average Ge-O coordination number, $n_{GeO} = 4.14(3)$, and was therefore chosen for EPSR in order to determine possible distributions of $[\text{GeO}_n]$ and $[\text{PbO}_m]$ polyhedra, and in particular if more highly coordinated Pb sites are associated with the $[\text{GeO}_n]$ with $n > 4$.

A 4000 atom model was built containing 2537 O, 1075 Ge and 388 Pb atoms, and constrained to the measured number density of $\rho_0 = 67.16\ \text{nm}^{-3}$ inside a cubic box of edge length $L = 39.05\,\text{Å}$, with periodic boundary conditions. As was found necessary during EPSR using scattering data from lead silicate glasses (see §6.3.3), the potential truncation radii were set at $r_l = 12\,\text{Å}$ and $r_u = 16\,\text{Å}$. Reference potential parameters for oxygen, as well as ϵ_{Pb} and q_{Pb} were the same as those used for lead silicate compositions, Table 6-7, whilst $\sigma_{Pb} = 2.29$ Å and those for Ge were set at $\epsilon_{Ge} = 2.49\ \text{kJ mol}^{-1}$, $\sigma_{Ge} = 1.10$ Å and $q_{Ge} = 2.0\ e$. Minimum distances of approach were set at $r^{min}_{PbPb} = 3.15$ Å and $r^{min}_{PbGe} = 2.90$ Å.

Monte Carlo simulations were performed, under the reference potentials, beginning

initially with a random distribution of atoms at $T = 1300$ K. The temperature was lowered stepwise, first to 700 K and finally to 300 K, with sufficient iterations allowed at each step for equilibration. The empirical potential was then allowed to accumulate in order to obtain best agreement between model and measured neutron and x-ray diffraction patterns (out to $Q_{max} = 30\,\text{Å}^{-1}$), with a requested maximum amplitude of 236 kJ mol^{-1} (~30% of the total energy of the Monte Carlo configuration at $T = 300$ K).

7.3.2 Model scattering patterns

Model structural parameters were averaged over 1100 configurations, with average energy -788.2 kJ mol^{-1} and R-factor of 0.46×10^{-3}. The model interference functions are compared to those measured by neutron and x-ray diffraction in Fig. 7-19, where it is made clear from the partial interference functions (offset below) which terms are dominant. In the neutron case it is the Ge-O term which is strongest, followed by the O-O term, whilst in the x-ray case the Ge-Pb term is strongest and the O-O term is weakest, giving excellent contrast between the two radiation types.

7.3.3 Pair correlation functions

Fig. 7-20 shows the pair correlation functions extracted from the model atomic configurations. A key feature is revealed by comparison of $g_{PbO}(r)$ with that derived by EPSR for $35\,\text{PbO} \cdot 65\,\text{SiO}_2$ glass. In particular, it can be seen that there are excess Pb-O bonds in the ~2.5 to 3.0 Å region in the lead germanate glass, revealing that Pb^{2+}, in this case, is playing a subtly more glass modifying role, than in the silicate.

Another important feature is evident in $g_{PbGe}(r)$, where it is evident that the nearest neighbour peak is structured. The main Pb-Ge peak is at similar position to that of $g_{PbPb}(r)$, but there is also a shoulder to lower r which, upon inspection of model atomic configurations, can be associated with the sharing of edges, and even faces, between [GeO_n] ($n = 4, 5$) and [PbO_m] polyhedra.

7.3.4 Model snapshot configuration

A slice through a single configuration of the model is shown in Fig. 7-21. In this case the glass network is built up predominantly from germanate tetrahedra (green), but

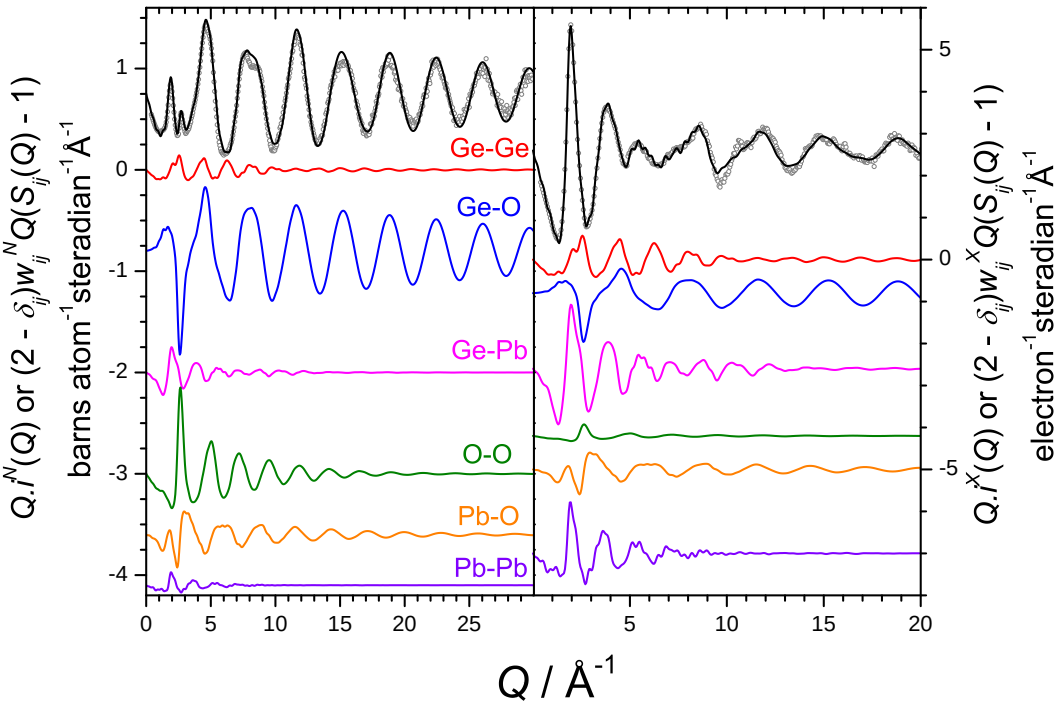

Figure 7-19 Interference functions measured (open circles) by neutron (left) and x-ray (right) diffraction for the $27\,PbO \cdot 73\,GeO_2$ glass, compared with model functions. The appropriately weighted partial pair interference functions are shown vertically offset for clarity, in the same order in both panels.

shown in blue are the 8.7% [GeO_5] (see §7.3.5) which also participate, and are found in a distribution of sites between the trigonal bipyramidal and square pyramidal configurations. Pb atoms tend to have highly asymmetric distributions of oxygen ligands, as found in lead silicate glasses (§6.3), which typically implies the presence of sterically active electron lone-pairs.

Also present are some unexpected configurations, including corner sharing pairs of [GeO_5] polyhedra, and [GeO_5] polyhedra with non-bridging oxygen ligands. The single [GeO_6] octahedron shown is in an edge sharing configuration with a [GeO_5], and although not shown, these form a three-membered ring with a [GeO_4] tetrahedron.

7.3.5 Coordination number distributions

The average Ge-O coordination number of the model is 4.104 (RMS deviation of 0.332) and Fig. 7-22 shows the CND is comprised of 90.4(3)% 4-fold, 8.7(4)% 5-fold and 0.8(1)% 6-fold sites. The average value is slightly lower than the n_{GeO} = 4.14(3) measured, and in fact a model with higher n_{GeO}, in better agreement with experiment was

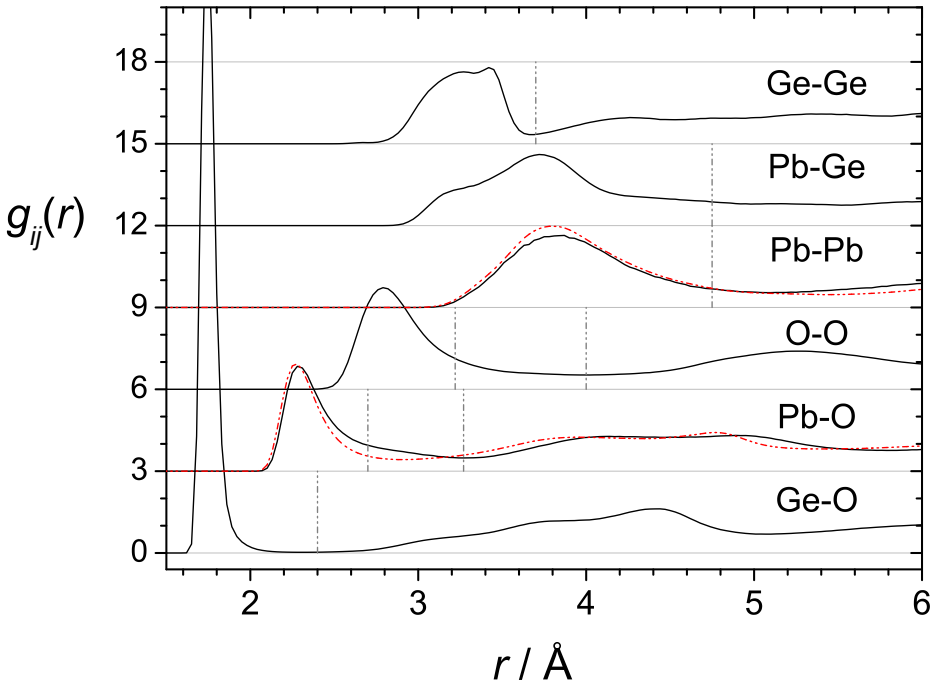

Figure 7-20 Model partial pair correlation functions for the $27\,PbO \cdot 73\,GeO_2$ glass. Vertical offsets have been used for clarity. Vertical dashed lines indicate upper cut-off radii used for determination of CNDs and BADs. Red broken curves represent model functions for $35\,PbO \cdot 65\,SiO_2$ glass (Fig. 6-28).

derived, albeit with smaller potential truncation radii. The key difference however was that the cap on the empirical potential magnitude was increased in several steps, rather than in a single step, as for the present model under discussion. This is indicative of the presence of local minima in the potential energy surface, and is supported by the observation of relatively large oscillations in total energy (± 5 kJ mol^{-1}) during empirical potential structure refinement.

The Pb-O CNDs, in both distance windows shown in Fig. 7-22, can both be seen to be shifted to higher coordination number, as compared to the $35\,PbO \cdot 65\,SiO_2$ silicate glass. Average values for $r_{PbO} \leq 2.70$ Å are 3.74(90) and 3.33(81) for the germanate and silicate respectively, and 5.51(1.02) and 4.61(94) for $r_{PbO} \leq 3.27$ Å (standard deviations of the distributions in parentheses). This is again supporting the observation that the Ge-O and Pb-O average coordination numbers are positively correlated. There is no indication of a bimodal CND, separating network forming and modifying Pb, for example.

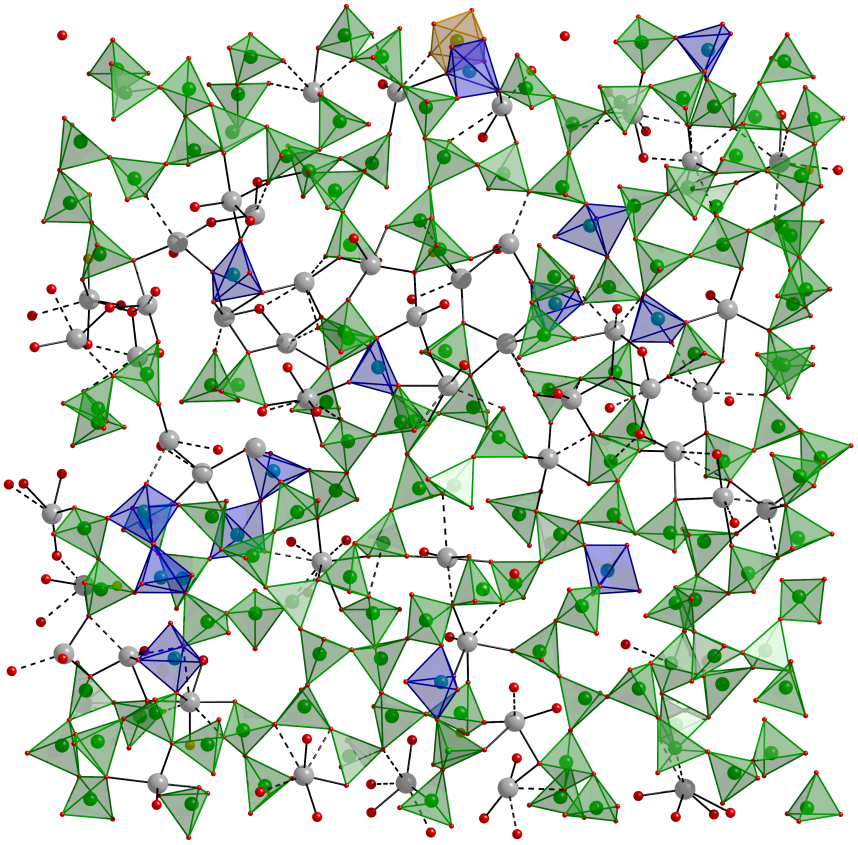

Figure 7-21 Slice, ~5 Å thick, through a single configuration of an EPSR model of 27 $PbO \cdot 73\ GeO_2$ glass. The area shown is ~40 × 40 Å. Ge atoms are shown within shaded green [GeO_4], blue [GeO_5] or orange [GeO_6] polyhedra, Pb atoms as large (grey) spheres, bonded to O atoms (smaller spheres, red). Pb-O bonds shorter than 2.7 Å are shown as solid lines, whilst those between 2.7 and 3.27 Å are dashed. The cationic coordination spheres have been completed, whereas the anionic ones have not.

7.3.6 Bond angle distributions

Selected BADs for 27 $PbO \cdot 73\ GeO_2$ glass are shown in Fig. 7-23. The O-Ge-O BAD clearly indicates the presence of non-tetrahedral [GeO_n] polyhedra, there being a ~90° shoulder on the main tetrahedral peak, as well as a broadening to the high angle side (*cf.* O-Si-O BAD) and a peak at ~170°.

The O-Pb-O BAD is broadly similar to that in 35 $PbO \cdot 65\ SiO_2$ glass, although with a slightly less well defined peak. An additional feature at ~65° can be attributed to the edge sharing of [GeO_n] and [PbO_m] polyhedra. The O-O distance (edge length) within [GeO_n] polyhedra is ~2.8 Å, which is shorter than the typical O-O distance found for [PbO_m] polyhedra within lead silicate glasses of ~3.0 to 3.1 Å (§6.3.3.4). Therefore

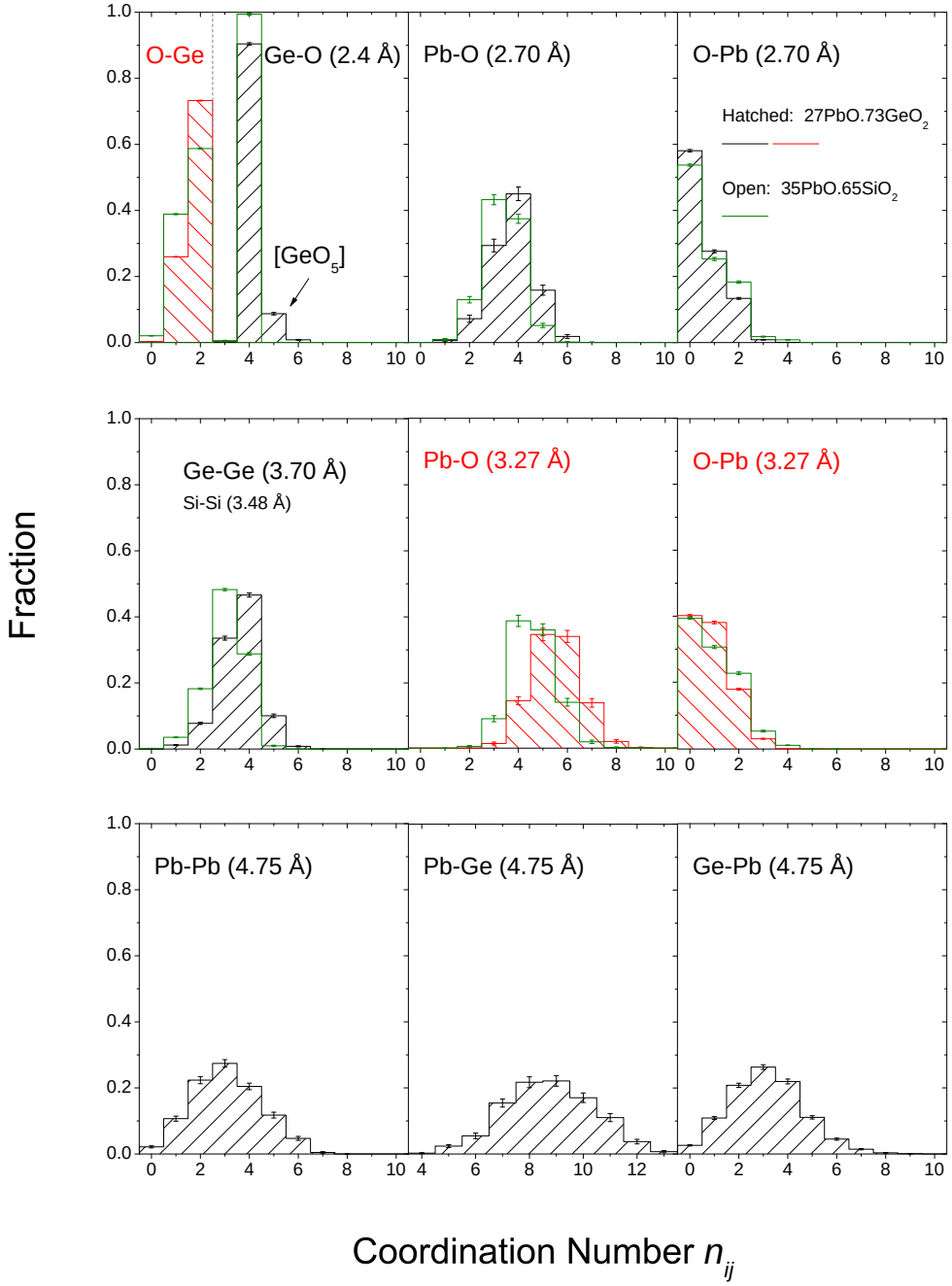

Figure 7-22 Selected coordination number distributions for EPSR models of 27 $PbO \cdot 73\,GeO_2$, compared to some CNDs from 35 $PbO \cdot 65\,SiO_2$ glass (Fig. 6-32). The upper cut-off radii used are indicated, and can be compared to the pair correlation functions in Fig. 7-20.

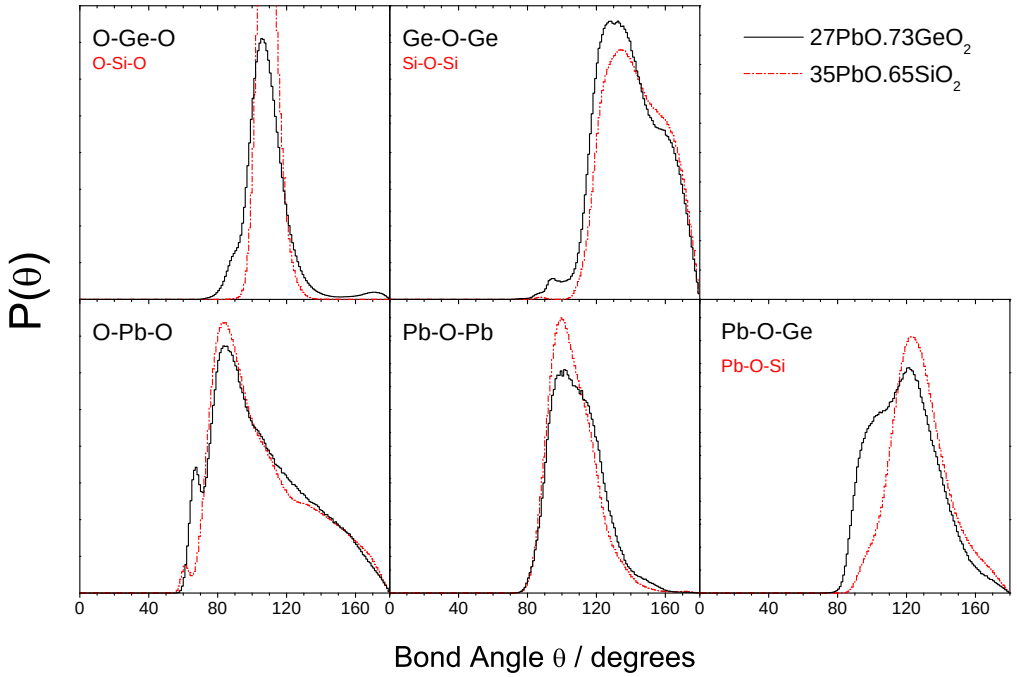

Figure 7-23 Selected bond angle distributions for EPSR models of $27\,PbO \cdot 73\,GeO_2$ glass. The equivalent distributions for $35\,PbO \cdot 65\,SiO_2$ glass are shown for comparison (see also Fig. 6-33). Only short (≤ 2.7 Å) Pb-O bonds have been included.

in order to share edges with [GeO_n], the O-Pb-O angles must reduce below their peak value (~84°).

Ge-O-Ge bond angles in glassy GeO_2 tend to be smaller than Si-O-Si angles in glassy SiO_2, and a similar difference is apparent in Fig. 7-23 for the lead germanate and silicate glasses. A small feature at ~95° in the Ge-O-Ge BAD is attributed to the edge-sharing of 5- and 6-fold Ge polyhedra with other Ge centred polyhedra.

The Pb-O-Pb BAD for the lead germanate is shifted to higher angle compared to that for the lead silicate glass. The predominant oxygen configurations contributing to the Pb-O-Pb BADs are likely [$OPb_2(Ge,Si)_q$], $q = 1, 2$ (see CNDs, Fig. 7-22), with similar abundances in both glasses. Therefore the difference may simply arise from the longer Ge-O bonds compared to Si-O, and hence smaller steric and Coulombic repulsion between Pb-Ge pairs compared to Pb-Si. This argument is complicated however by the fact that the Ge-Pb pair correlation function shows structure as a result of both edge-sharing (and face-sharing) and corner-sharing polyhedra. Therefore although the corner-sharing Pb-Ge distance is larger than the Pb-Si distance in lead silicate glasses, the Pb-Ge distance in edge- and face-sharing configurations is shorter.

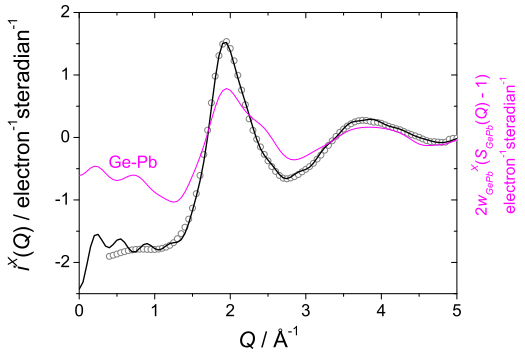

Figure 7-24 Model distinct x-ray scattering pattern for $27\,PbO \cdot 73\,GeO_2$ glass, as compared to the measured data (open grey circles). The low Q region is shown in order to emphasise the SAXS region below ~1.5 Å^{-1}. Also shown is the Ge-Pb partial pair term, which is dominant at this composition.

The Ge-O-Pb BAD, Fig. 7-23, shows a large excess of smaller bond angles as compared to the Si-O-Pb BAD of $35\,PbO \cdot 65\,SiO_2$ glass. This is a result of a larger number of Pb-O bonds forming to bridging oxygen atoms, which itself is a consequence of the presence of 5- and 6-fold Ge, which give rise to BOs under-bonded by Ge alone. This difference in bonding schemes between (low) lead germanate and silicate glasses is likely related to the presence of edge- and face-sharing between [GeO_n] and [PbO_m] polyhedra, however, the more closely commensurate O-O edge lengths of [GeO_n] and [PbO_m] polyhedra, as compared to [SiO_4] and [PbO_m] polyhedra, is also clearly an important factor.

7.3.7 Small angle x-ray scattering

Fig. 7-24 shows the SAXS both measured, and calculated from the model atomic configurations. As in the case of $35\,PbO \cdot 65\,SiO_2$ glass (Fig. 6-31), the SAXS region is not ideally reproduced for the $27\,PbO \cdot 73\,GeO_2$ glass due to the box size limit of ~40 Å. Nonetheless, the model clearly contains an inhomogeneous distribution of cations, indicating mechanisms of clustering, such as sharing of NBOs by pairs of Pb atoms.

7.4 Discussion

7.4.1 Disagreement with a previous neutron scattering study

A key feature of lead germanate glasses, as evidenced by the present study, is that the rise of the Ge-O coordination number, above the tetrahedral value of four, is strongly suppressed in the presence of Pb, as compared to alkali germanate glasses, and indeed to calcium germanate glasses, which were the subject of Chapter 5. Nonetheless a shallow maximum in n_{GeO} of 4.14(3) at 26.5(5) mol% PbO was measured by high resolution neutron diffraction, and the most comprehensive and accurate set of Ge-O coordination numbers obtained over the full glass forming range (0 to 75 mol% PbO).

The present results are not however consistent with a previous high resolution neutron diffraction study by Umesaki *et al.* [33]. The authors [33] reported n_{GeO} as high as 4.77(5) at 40 mol% PbO, as well as much higher Pb-O coordination numbers, with n_{PbO} = 6.23(13) for the same glass. For this reason neutron scattering measurements were made on the *same* 4.5 mm diameter, annealed, $40\,PbO \cdot 60\,GeO_2$ glass rod as was used by Umesaki *et al.* [33]. The measurements were made using the GEM [9] diffractometer at the ISIS spallation source, and the data collected were corrected and normalised in an identical manner as for the glasses used in the present study, although without the necessity of subtracting background scattering from a vanadium container. The distinct scattering and total correlation function obtained are compared in Fig. 7-25 to those of the isomolar glass of the present study.

It is clear that the differences between the two scattering patterns are small. Average Ge-O coordination numbers are 4.06(3) (this study) and 4.17(1) (glass of Umesaki *et al.* [33]) by integration of $rT^N(r)\mathrm{d}r$ (Table 7-4), with equivalent parameters from fitting two Ge-O and one Pb-O peak to $T^N(r)$ being 4.00(3) (this study) and 4.08(18) (glass of Umesaki *et al.* [33]). Meanwhile Pb-O coordination numbers of 3.10(9) and 3.26(15) were obtained from the fitted peaks respectively. As can be seen from the comparison made in Table 7-4, the coordination numbers found by remeasurement of the glass of Umesaki *et al.* [33] are much lower than reported in the paper [33]. On the other hand, bond lengths r_{ij} and their standard deviations, $\langle u_{ij}^2 \rangle^{1/2}$, are essentially the same. This points to an error in normalisation, or similar, in the published work [33], whilst supporting the results found in the present study.

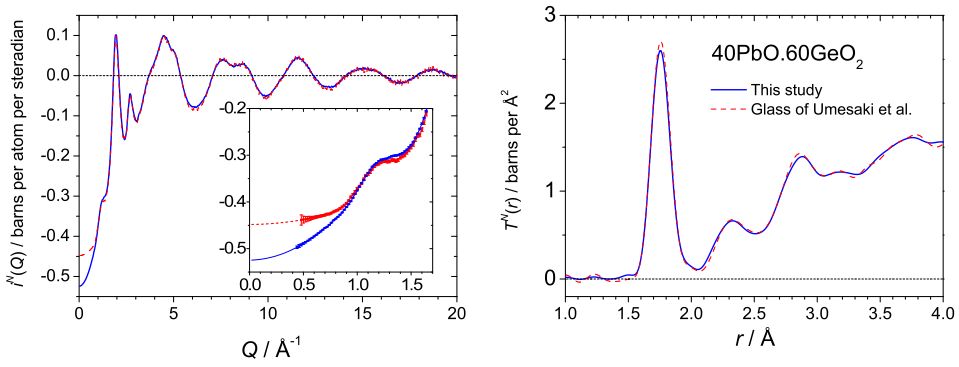

Figure 7-25 Neutron distinct scattering (left) and total correlation (right) functions for $40\,PbO \cdot 60\,GeO_2$ glasses, comparing the measurement of the glass from the present study with an analogous measurement on the glass rod of Umesaki *et al.* [33]. A Q_{max} of 40 Å^{-1} was used for Fourier transformation in both cases. Inset shows the low Q region of $i^N(Q)$, where data points are shown with error bars and extrapolations as lines.

The coordination numbers measured for the glass of Umesaki *et al.* [33] do appear to be slightly larger than for the glass measured in the present study. Such a result can arise if the thermal histories of the two glasses are different. Indeed in the present study, the glass was rapidly plate quenched, whilst the glass rod ([33]) was annealed after quenching, allowing for relaxation processes to occur, and resulting in a lower fictive temperature. What is interesting is that this result supports the supposition made, based on the n_{GeO} of calcium germanate glasses (Chapter 5), that n_{GeO} should increase with decreasing fictive temperature. This was based on the smaller n_{GeO} of the glasses than of the equilibrium crystal phases, and the same observation can be made for materials in the PbO–GeO_2 system, see Fig. 7-9.

There is a noticeable difference in the low Q neutron scattering limits of the two $40\,PbO \cdot 60\,GeO_2$ glasses, Fig. 7-25 (inset). Note that although the $i^N(Q)$ functions were extrapolated below 0.45 Å^{-1} by fitting of a quadratic to the 0.45 to 0.70 Å^{-1} region, the differences in low Q scattering appear as high as ~1.0 Å^{-1}. What the results suggest are that the annealed glass ([33]) has a higher degree of chemical inhomogeneity, which is supported by the study of Morinaga and Nakashima [34] who showed that the region of metastable immiscibility extends at least as high as 40 mol% PbO, and that at this composition, a small volume fraction of particles of a second amorphous phase will grow under isothermal conditions (440 °C).

Table 7-4 Details of Ge-O and Pb-O correlations in $40\,PbO \cdot 60\,GeO_2$ glasses.

Parameter	This study	Glass of Umesaki *et al.* [33]	Reported by Umesaki *et al.* [33]
$n_{GeO}{}^{\dagger}$	4.06(3)	4.17(1)	-
$n_{GeO}{}^{\ddagger}$	4.00(3)	4.08(3)	4.77(5)
r_{GeO} (1)‡ (Å)	1.7556(3)	1.7584(3)	1.7572
r_{GeO} (2)‡ (Å)	1.944(4)	1.967(5)	1.877(15)
$r_{GeO}{}^{\dagger}$ (Å)	1.766(6)	1.767(4)	1.772*
$\langle u^2_{GeO}\rangle^{1/2}$ (1)‡ (Å)	0.0540(4)	0.0555(4)	0.054
$n_{PbO}{}^{\ddagger}$	3.10(9)	3.26(12)	6.23(13)
$r_{PbO}{}^{\ddagger}$ (Å)	2.321(4)	2.336(5)	2.336(6)
$\langle u^2_{PbO}\rangle^{1/2\ddagger}$ (Å)	0.126(3)	0.128(4)	0.121(4)

† By integration over $rT^N(r)\mathrm{d}r$. ‡ From peak fitting to $T^N(r)$.
* Area weighted average from two fitted peaks.

7.5 Conclusions

At 26.5(5) mol% PbO, a low maximum in average Ge-O coordination number, of n_{GeO} = 4.14(3), occurs in the glasses of the system $PbO{-}GeO_2$. Evidence for this comes from high resolution measurement of the neutron total correlation functions, whereby coordination numbers were extracted directly by integration over the region attributed solely to Ge-O bond distances, as well as by fitting to Ge-O and Pb-O correlations, which overlap each other to a minor extent. Furthermore, the Ge-O bond length distributions were clearly observed to show asymmetrical broadening to the high r side, indicative of the presence of 5- or 6-fold Ge, in addition to the majority of 4-fold, tetrahedral, sites. For glasses containing > 50 mol% PbO, the Ge-O bond length distributions are symmetric and the vast majority of Ge occupy tetrahedral sites.

The rise in n_{GeO} in $PbO{-}GeO_2$ glasses is less pronounced than that measured for alkali, Tl or Ca germanate glasses. PbO in the lead germanate glasses therefore plays a truly intermediate role, between that of modifying oxides (A_2O etc.) and glass forming oxides. For example, no increase in n_{GeO} above four is observed [35] in the binary glass former, $B_2O_3{-}GeO_2$, system. This in itself is indirect evidence for the formation of short, strong, Pb-O bonds, even at low PbO contents, and these necessarily form to non-bridging oxygen atoms. Direct evidence for short Pb-O bonds was observed in neutron and x-ray correlation functions for all glasses in the range 5 to 75 mol% PbO.

The n_{PbO} change subtly with glass composition (although the change is more pro-

nounced across the series than for $PbO-SiO_2$ glasses (Chapter 6)), showing positive correlation with n_{GeO}, such that when the latter is greater than four, so the former is greater than at the high PbO limit, at which the Pb in the silicate and germanate glasses appear to behave in the same way. The reason that the two parameters should be linked is due to the presence of bridging oxygen which are under-bonded if either or both of the coordinating germanium atoms have greater than four oxygen ligands.

There is evidence to suggest that the average n_{PbO} does *not* arise from a mixture of glass former (low CN) and glass modifying (high CN) Pb sites. Rather the great flexibility and variability of the Pb^{2+} oxygen coordination shell allows for sites that are themselves 'intermediate' in character. This is evident in the lead silicate and germanate crystal chemistry, and in particular the γ-$PbGe_4O_9$ polymorph [13] contains highly asymmetric [PbO_7] polyhedra, in coexistence with [GeO_5] units, which are 'intermediate' between the glass forming sites with lower coordination numbers, and glass modifying sites, such as the [PbO_{10}] polyhedra in α-$PbGe_4O_9$ [12].

An atomistic model consistent with the diffraction data measured for a 26.5(5) mol% PbO germanate glass was derived by empirical potential structure refinement. This model supports the above conclusion that Pb^{2+} may occupy sites with 'intermediate' character. The non-tetrahedral germanium sites within the model were predominantly 5-fold, not 6-fold coordinated. However, it is most likely that diffraction data, which are used to derive such models, are insensitive to differences between structures (with the same average n_{GeO}) containing 5- or 6-fold Ge, especially at such low abundances.

The presence of edge-, and even face-sharing, between [GeO_n] and [PbO_m] polyhedra was evident in the model 26.5(5) mol% PbO germanate glass. This was associated with features in the Ge-Pb partial correlation function, and in the Ge-O-Pb bond angle distribution, and thereby compared to a silicate glass of similar composition, in which edge-sharing is much less apparent. This can be attributed to the larger edge lengths of [GeO_n] compared to [SiO_4] polyhedra, as well as to the greater degree of bonding of Pb to bridging oxygen in the germanate glass.

The fact that crystalline lead germanates with $n_{GeO} > 4$ also have larger n_{GeO} than the isomolar glasses implies that n_{GeO} is a function of the liquid temperature and therefore of the glass fictive temperature. This is analogous to the observations made within the $CaO-GeO_2$ system (Chapter 5). Evidence in support of this hypothesis comes from the

comparison of neutron scattering from $40\,PbO \cdot 60\,GeO_2$ glasses with different thermal histories and fictive temperatures. The glass with the lower fictive temperature was found to have higher n_{GeO}, as would be expected from the higher values in the crystalline state.

The measured maximum in n_{GeO} is consistent with trends observed in many physical properties of lead germanate glasses. These include maxima in resistivity [36], and the Young's and shear moduli [37] at ~30 mol% PbO. The composition range over which the glass transition temperatures plateau (Fig. 7-2, [7, 36]) coincides with the region over which n_{GeO} is increasing with PbO content. Therefore, the interpretation of this plateau in terms of phase separation by Shelby [7] may be incorrect, although a definitive statement cannot be made based on differences in glass preparations. The alternative explanation is that there is a delicate balance between the effects of increasing n_{GeO}, which increases the number of bond constraints, and therefore the T_g, and the increase in the number of weaker Pb-O bonds, which causes a decrease in T_g and becomes dominant as n_{GeO} decreases and PbO content increases above ~27 mol% PbO.

Other bulk glass properties, such as mass density, refractive index and third order electric susceptibility [38] do not show extrema as functions of glass composition due to the dominance of the properties (mass, polarisability etc.) of the Pb^{2+} ion. However, the atomic number densities do pass through a maximum at ~27 mol% PbO (Fig. 7-1), although, as discussed previously (§5.3.3), it is difficult to directly relate n_{GeO} to the mass or number density.

The average Ge-O bond length naturally rises with the increase in n_{GeO}. However, at PbO contents higher than that at which n_{GeO} is maximised, r_{GeO} does not return to its value in GeO_2 glass but instead reduces and then plateaus at a higher value (Fig. 7-10). In alkali germanate glasses, r_{GeO} is only observed to rise to a plateau with addition of alkali oxide [39], and this has been posed by Henderson [39] as inconsistent with observed maxima in n_{GeO}, and the fact that bonds from Ge to non-bridging oxygen tend to be shorter than those to bridging oxygen. In fact it should be stated that the behaviour of r_{GeO} with binary glass composition can only be explained by consideration of a number of variables. In addition to changes in n_{GeO} and the polymerisation state of the germanate network, these include Ge-O-Ge and Ge-O-M bond angles and the coordination numbers, O-M, of both BO and NBO to metal ions (M).

References

[1] *Revised Nuffield Advanced Science Book of Data* (Longman, 1985).

[2] Y. Iwata, N. Koyano and I. Shibuya, *J. Phys. Soc. Jpn.* **35** (4), (1973), 1269–1269.

[3] Y. Iwata, H. Koizumi, N. Koyano, I. Shibuya and N. Niizeki, *J. Phys. Soc. Jpn.* **35** (1), (1973), 314–314.

[4] S. A. Ivanov, N. V. Rannev, A. A. Bush, A. I. Leichenko and Y. N. Venevtsev, *Kristallografiya+* **24** (2), (1979), 252–256.

[5] A. J. Havel, S. A. Feller, M. Affatigato, M. Karns and M. Karns, *Glass Technol. Eur. J. Glass Sci. Technol. A* **50** (4), (2009), 227–229.

[6] *SciGlass Professional 7.3* (ITC Inc., 2008).

[7] J. E. Shelby, *J. Am. Ceram. Soc.* **66** (6), (1983), 414–416.

[8] S. Feller, G. Lodden, A. Riley, T. Edwards, J. Croskrey, A. Schue, D. Liss, D. Stentz, S. Blair, M. Kelley, G. Smith, S. Singleton, M. Affatigato, D. Holland, M. E. Smith, E. I. Kamitsos, C. P. E. Varsamis and E. Ioannou, *J. Non-Cryst. Solids* **356** (6-8), (2010), 304–313.

[9] A. C. Hannon, *Nucl. Instrum. Meth. A* **551** (1), (2005), 88–107.

[10] E. Lorch, *J. Phys. C Solid State* **2**, (1969), 229.

[11] A. C. Hannon, D. Di Martino, L. F. Santos and R. M. Almeida, *J. Phys. Chem. B* **111** (13), (2007), 3342–3354.

[12] A. Y. Shashkov, V. A. Efremov, I. Matsichek, N. V. Rannev, Y. N. Venevtsev and V. K. Trunov, *Zh. Neorg. Khim+* **26** (3), (1981), 583–587.

[13] A. Y. Shashkov, N. V. Rannev and Y. N. Venevtsev, *Zh. Neorg. Khim+* **26** (11), (1981), 2926–2928.

[14] H. H. Otto, *Z. Kristallogr.* **149** (3-4), (1979), 197–205.

[15] A. C. Hannon, D. Di Martino, L. F. Santos and R. M. Almeida, *J. Non-Cryst. Solids* **353** (18-21), (2007), 1688–1694.

[16] Y. Z. Nozik, B. A. Maksimov, L. E. Fykin, V. Y. Dudarev, L. S. Garashina and V. T. Gabrielyan, *J. Struct Chem+* **19** (4), (1978), 628–630.

[17] Y. Xu, L. Y. Cheng, G. P. Zhou and Y. L. Wang, *Acta Crystallogr. E* **62**, (2006), I135–I137.

[18] Y. Iwata, *J. Phys. Soc. Jpn.* **43** (3), (1977), 961–967.

[19] M. I. Kay, R. E. Newnham and R. W. Wolfe, *Ferroelectrics* **9** (1-2), (1975), 1–6.

[20] R. E. Newnham, R. W. Wolfe and C. N. W. Darlington, *J. Solid State Chem.* **6** (3), (1973), 378–383.

[21] T. Baikie, S. S. Pramana, C. Ferraris, Y. Z. Huang, E. Kendrick, K. S. Knight, Z. Ahmad and T. J. White, *Acta Crystallogr. B* **66**, (2010), 1–16.

[22] H. H. Otto, *Z. Kristallogr.* **149** (3-4), (1979), 227–240.

[23] K. Kato, K. Hirota, Y. Kanke, A. Sato, K. Ohsumi, T. Takase, M. Uchida, O. Jarchow, K. Friese and G. Adiwidjaja, *Z. Kristallogr.* **210** (3), (1995), 188–194.

[24] K. Kato, *Acta Crystallogr. B* **35** (Apr), (1979), 795–797.

[25] M. B. Boisen, G. V. Gibbs, R. T. Downs and P. Darco, *Am. Mineral.* **75** (7-8), (1990), 748–754.

[26] G. V. Gibbs, F. C. Hill and M. B. Boisen, *Phys. Chem. Miner.* **24** (3), (1997), 167–178.

[27] R. J. Hill, S. J. Louisnathan and G. V. Gibbs, *Aust. J. Chem.* **30** (8), (1977), 1673–1684.

[28] G. V. Gibbs, M. B. Boisen, F. C. Hill, O. Tamada and R. T. Downs, *Phys. Chem. Miner.* **25** (8), (1998), 574–584.

[29] R. Bouchard, D. Hupfeld, T. Lippmann, J. Neuefeind, H. B. Neumann, H. F. Poulsen, U. Rutt, T. Schmidt, J. R. Schneider, J. Sussenbach and M. von Zimmermann, *J. Synchrotron Radiat.* **5**, (1998), 90–101.

[30] H. F. Poulsen, J. Neuefeind, H. B. Neumann, J. R. Schneider and M. D. Zeidler, *J. Non-Cryst. Solids* **188** (1-2), (1995), 63–74.

[31] V. N. Bogdanov, A. V. Anan'ev, V. V. Golubkov, A. V. Golovnev, L. V. Maksimov, A. Y. Pakhnin, V. A. Solovyev, S. N. Smerdin, O. V. Yanush and B. Champagnon, *J. Phys. Conf. Ser.* **93**, (2007), 012033.

[32] V. V. Golubkov, V. N. Bogdanov, A. Y. Pakhnin, V. A. Solovyev, E. V. Zhivaeva, V. O. Kabanov, O. V. Yanush, S. V. Nemilov, A. Kisliuk, M. Soltwisch and D. Quitmann, *J. Chem. Phys.* **110** (10), (1999), 4897–4906.

[33] N. Umesaki, T. M. Brunier, A. C. Wright, A. C. Hannon and R. N. Sinclair, *Physica B* **213**, (1995), 490–492.

[34] K. Morinaga and K. Nakashima, *J. Non-Cryst. Solids* **103** (1), (1988), 108–116.

[35] S. K. Lee, H. N. Kim, B. H. Lee, H. I. Kim and E. J. Kim, *J. Phys. Chem. B* **114** (1), (2010), 412–420.

[36] J. A. Topping, I. T. Harrower and M. K. Murthy, *J. Am. Ceram. Soc.* **57** (5), (1974), 209–212.

[37] J. A. Topping, *J. Am. Ceram. Soc.* **57** (10), (1974), 455–455.

[38] H. Yamamoto, K. Kamiya, J. Matsuoka and H. Nasu, *J. Ceram. Soc. Jpn.* **101** (9), (1993), 974–979.

[39] G. S. Henderson, *J. Non-Cryst. Solids* **353** (18-21), (2007), 1695–1704.

Chapter 8

Conclusions and Predictions

The present thesis has highlighted numerous subtleties in the composition-structure relationships of binary oxide glasses. This has been made possible by the study of related systems, and the combined use of very high real-space resolution neutron and x-ray total scattering, and in several cases empirical structural modelling techniques, as well as reference to complementary structural probes such as solid-state nuclear magnetic resonance. In particular, the role of lone-pair cation Pb^{2+} in oxide glasses has been studied in detail, in the binary silicate and germanate systems, including studies of glasses with the highest lead content to date, yielding unique insight into the formation of a plumbite glass network stabilised by monomeric and dimeric silicate and germanate anions. In all glasses studied, lead behaves predominantly as a network forming cation, with a stereochemically active electron lone-pair, although subtle changes with glass composition could be determined. The plumbite network is characterised by a high degree of intermediate range order, arising from local layer-like regions similar to those found in the crystalline PbO polymorphs. This is a consequence of the tendency for the cationic electron lone-pairs to organise to form voids, analogous to the interlayer spaces in the PbO polymorphs, and the channels found within several binary lead oxide crystals.

The presence of a germanate anomaly in the lead germanate glass system has been confirmed, and, for the first time, revealed in the calcium germanate glass system. In both cases the behaviour is markedly different from the more well characterised alkali germanate glasses. In particular, mass and number density maxima typically occur at higher modifier oxide content (~27 mol%), correlating with Ge-O coordination number maxima, whilst non-bridging oxygen atoms are present in all glasses, and are higher in abundance in the lead germanate glasses owing to the network forming behaviour of Pb^{2+}. Nonetheless, slight differences in the Pb^{2+} environment are evident in low lead germanate glasses, as compared to their silicate analogues. Indeed a positive correlation between Ca-O or Pb-O coordination and Ge-O coordination is apparent. The Ge-O

and Pb-O coordination numbers measured for lead germanate glasses differ from those reported in the only published neutron diffraction study [1], but are considered more reliable.

The following sections draw some more general conclusions, and make some predictions and suggestions for further measurements, upon which future studies could be based.

8.1 Lead in binary oxide glasses

Pb^{2+} plays an incredibly flexible role in oxide materials. It may have a low coordination number, and act as a network forming cation, as in the plumbite based glasses, including $80\,PbO \cdot 20\,SiO_2$, studied herein, and in high lead aluminate, gallate and borate glasses, or it may have a high coordination number and behave as a network modifying cation, such as in the low PbO borate, and lead phosphate glasses. However, the flexibility in behaviour is truly represented by a continuum, and goes far beyond the 'binary', former/modifier, picture. This is supported by: empirical models of $27\,PbO \cdot 73\,GeO_2$ glass which show that sites of 'intermediate' character reproduce the measured diffraction patterns; by very subtle variations in lead environment with glass composition in the lead silicate series; and is borne out in the lead oxide crystal chemistry.

It is instructive to make comparison to some other related binary oxide glass systems. For example, thallium germanate glasses [2] show a large increase in Ge-O coordination number with Tl_2O content, and correspondingly, Tl^+ behaves as a network modifying cation at low concentrations, but transforms progressively toward a glass forming role, with Tl occupying $[TlO_3]$ sites with sterically active lone-pairs. The transformation completes at a hypothesised limit of 50 mol% Tl_2O.

Lead in $PbO–B_2O_3$ glasses also appears to change role with glass composition [3, 4], and again this is related to a change in coordination of the network forming cation. Indeed, it is remarkable that even at 80 mol% PbO, more than 10% of the boron are present as $[BO_4]^-$. Note that the ratio Pb:X (X a glass forming cation) is 2:1 for $80\,PbO \cdot 20\,B_2O_3$, equivalent to $67\,PbO \cdot 33\,XO_2$. It would certainly be of interest to attempt to form lead borate glasses beyond 88.9 mol% PbO, Pb:X = 4:1, as for the $80\,PbO \cdot 20\,SiO_2$ glass studied herein, by rapid quenching or levitation techniques. This

would facilitate study of the plumbite network yet closer to the pure PbO limit, which may be stabilised by the presence of a mixture of 3-fold and 4-fold boron, as well as by the very strong B-O bonds.

Tin germanate glasses have been studied by neutron diffraction [5], but the large degree of overlap between Ge-O and Sn-O correlations prevented accurate Ge-O coordination numbers from being extracted. Given the comparative behaviour of Sn^{2+} and Pb^{2+} in borate glasses [6] (lower B-O coordination numbers in tin borates), it is quite conceivable that any change in Ge-O coordination number is completely suppressed in $SnO-GeO_2$ glasses, in light of the very small rise in $PbO-GeO_2$ glasses measured herein. Testing of such a prediction is difficult, but would best be achieved by ^{17}O NMR or Ge isotope substitution in neutron diffraction.

The above comparisons paint a bigger picture which is consistent with the observations made of lead silicate and germanate glasses in this thesis. In particular, changes in coordination number of lone-pair cations, and hence in the stereochemical activity of their electron lone-pairs, are correlated with coordination number changes of the glass forming cations in the binary system. Comparison of results obtained for calcium germanate glasses to the literature on calcium silicate glasses would suggest that the correlation is more general, and holds not only for lone pair cations but also for more typical modifiers, such as Ca.

8.2 Germanate glasses

The observed correlation between Ca-O or Pb-O and Ge-O coordination numbers can be simply rationalised in terms of Pauling electrostatic bond strength sums, and has clear implications for other germanate glass-forming systems. For example, Sr and Ba are typically found with larger coordination numbers to oxygen than is Ca. Therefore one would expect the Ge-O coordination number to be larger in binary (Sr,Ba)O-GeO_2 glasses, and for there to be correspondingly less non-bridging oxygen.

Furthermore, consideration of atomic packing fractions and number densities supports a germanate network cage-filling model, in which Ca^{2+} is smaller than the average cage size. Number density maxima therefore occur as a result of saturation of available cages, at which point non-bridging oxygen atoms must be introduced. This is how-

ever intricately linked with the presence of [GeO_n], $n > 4$, since the added oxygen must be accommodated somehow into the germanate framework. Contributions from cage and ring size redistributions are also important. The cations Sr^{2+} and Ba^{2+} are similar in size, or larger than, the average network cage, and this would likely have implications for their local environments, in particular a narrower bond length distribution ($\langle u^2_{AeO}\rangle^{1/2}$), than that measured for Ca^{2+}, is predicted. Na^+ has a very similar ionic radius to Ca^{2+}, but since there are twice as many Na^+ as Ca^{2+} per unit charge, the network cage volume is filled up more rapidly with increasing modifier content in the sodium case, and charge avoidance between [GeO_5] has a chance to come into play. As discussed below, the charge avoidance assumption should not be considered strictly between pairs of [GeO_n], $n > 4$, but rather between larger scale entities.

Heavy alkali germanate glasses containing K^+, Rb^+ or Cs^+ are notably different from the Na^+ and Ca^{2+} germanate glasses, because their number density maxima do not correlate with the known Ge-O coordination number maxima at ~18.2 mol% A_2O. Fig. 8-1 illustrates why this is the case. The heavy alkali cations are much larger in

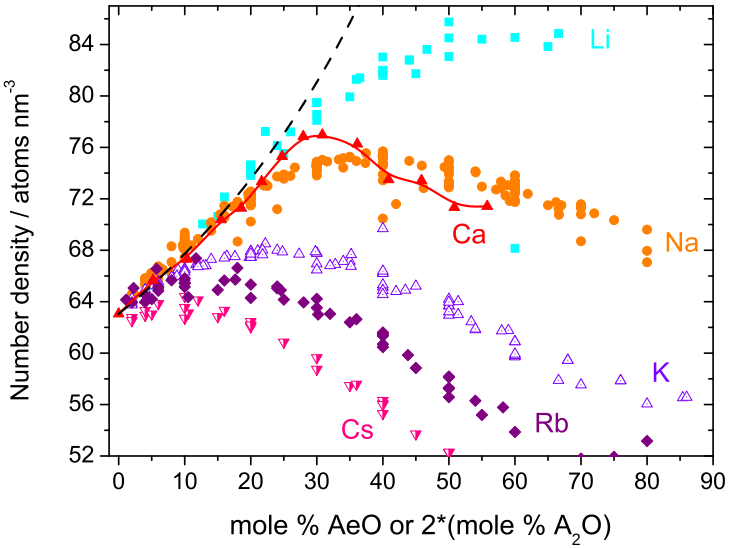

Figure 8-1 Alkali and Ca germanate number densities as a function of glass composition, see Fig. 5-14 for comparison to Sr and Ba germanates. The alkali germanate mass densities used are collated in the SciGlass database [7], references therein. The dashed line represents that of constant volume per mole $J2\,AO_{1/2}\cdot GeO_2$ or $J\,AeO\cdot GeO_2$.

volume than are the alkaline earth cations, and so force a redistribution of germanate

network cage sizes, and lower the number densities so that they fall below the curve of constant volume per mole $J2\,AO_{1/2}\cdot GeO_2$, at or below ~5 mol% A_2O. Notably the Li_2O–GeO_2 glasses follow the constant molar volume prediction over the widest range, and the number density continues to rise to very large values. It is interesting to speculate that this may facilitate a continued rise in n_{GeO}, beyond the saturation point at ~18.2 mol% A_2O for an alternating network of [GeO_4] and [GeO_5], although this is far from clear cut. Notably this would require a reinterpretation of existing Raman spectra [8, 9].

There exists a distinct need for calculations of the frequencies of local vibrational modes in germanates, particularly those associated with [GeO_5] and [GeO_6] polyhedra, due to ambiguities in the assignments of Raman and IR absorption bands [10, 11], which lead to apparent inconsistencies between vibrational spectroscopic results, and those obtained by neutron diffraction.

The position of the Ge-O coordination number maximum at higher modifier oxide content (~27 mol%) in the lead and calcium germanate glasses, compared to alkali germanates, is attributed to the stabilisation of pairs of [GeO_n], $n > 4$, which share at least one corner, and/or [GeO_6], as opposed to only [GeO_5] as is thought to be the case in alkali germanate glasses. Triclusters, [OGe_3], cannot be definitively excluded by the measurements, but are not present in an empirically derived model of $27\,PbO\cdot 73\,GeO_2$ glass. Note that corner-sharing pairs of [GeO_n], $n > 4$, violates the charge avoidance assumption made in models [12] for n_{GeO} as a function of glass composition, and the analogous assumption made in models for borate systems. However, in borates [13] it is well known that superstructural ring units containing corner-sharing pairs of $[BO_4]^-$ exist, and furthermore, the charge avoidance assumption is apparently violated in alkaline earth, as well as lead, borate glasses. Note however, that charge avoidance between anionic species on *larger length scales* may well be important. Both empirical and predictive modelling of germanate glasses are therefore required to ascertain the likely configurations of germanate units present. Notably, classical MD models of Na_2O–GeO_2 glasses contain edge-sharing [GeO_n], $n > 4$ [14], as well as either small [15] or large [14] numbers of [OGe_3] triclusters. The latter are not apparent in ^{17}O 3QMAS NMR spectra [16, 17], but there is a clear need for both *ab initio* modelling and further ^{17}O NMR and diffraction measurements on other alkali, and on alkaline earth germanate

glasses, in order to illuminate the bigger picture.

The average Ge-O coordination numbers in Ca and Pb germanate crystals (<50 mol% MO) are greater than those of corresponding glasses. This is used to infer that n_{GeO} decreases with increasing liquid temperature T and glass fictive temperature T_f. This supposition is borne out in measurements of n_{GeO} in $40\,PbO \cdot 60\,GeO_2$ glasses with very different T_f, and the phenomenon may well be related to growth of compositional inhomogeneities. The implications of such relationships are that reactions such as $[GeO_5] \rightleftharpoons [GeO_4]$ + NBO are instrumental in processes of viscous flow. Furthermore, both the presence of significant edge-sharing [18, 19], *and* a strong dependence of local structure on liquid temperature [20] have been associated with high liquid fragility [21], that is, highly non-Arrhenius temperature dependence of the liquid viscosity. The Ca and Pb germanate melts are therefore expected to fall under the fragile liquid classification on both counts.

Diffraction measurements on liquid and supercooled liquid $MO-GeO_2$ germanates are required to confirm, or otherwise, the predicted decrease in n_{GeO} with temperature. In addition, measurements on glasses of the same composition, with widely different, and well known, fictive temperatures are necessary.

References

[1] N. Umesaki, T. M. Brunier, A. C. Wright, A. C. Hannon and R. N. Sinclair, *Physica B* **213**, (1995), 490–492.

[2] E. R. Barney, A. C. Hannon, N. Laorodphan and D. Holland, *J. Phys. Chem. C* **115** (30), (2011), 14997–15007.

[3] H. Ushida, Y. Iwadate, T. Hattori, S. Nishiyama, K. Fukushima, Y. Ikeda, M. Yamaguchi, M. Misawa, T. Fukunaga, T. Nakazawa and S. Jitsukawa, *J. Alloy. Compd.* **377** (1-2), (2004), 167–173.

[4] T. Takaishi, J. S. Jin, T. Uchino and T. Yoko, *J. Am. Ceram. Soc.* **83** (10), (2000), 2543–2548.

[5] D. Holland, M. E. Smith, I. J. F. Poplett, J. A. Johnson, M. F. Thomas and J. Bland, *J. Non-Cryst. Solids* **293**, (2001), 175–181.

[6] A. C. Hannon, E. R. Barney and D. Holland, *Phys. Chem. Glasses Eur. J. Glass Sci. Technol. B* **50** (5), (2009), 271–283.

[7] *SciGlass Professional 7.3* (ITC Inc., 2008).

[8] L. G. Soltay and G. S. Henderson, *Can. Mineral.* **43**, (2005), 1643–1651.

[9] L. G. Soltay and G. S. Henderson, *Phys. Chem. Glasses* **46** (4), (2005), 381–384.

[10] E. I. Kamitsos, Y. D. Yiannopoulos, M. A. Karakassides, G. D. Chryssikos and H. Jain, *J. Phys. Chem-US* **100** (28), (1996), 11755–11765.

[11] G. S. Henderson, L. G. Soltay and H. M. Wang, *J. Non-Cryst. Solids* **356** (44-49), (2010), 2480–2485.

[12] A. C. Hannon, D. Di Martino, L. F. Santos and R. M. Almeida, *J. Phys. Chem. B* **111** (13), (2007), 3342–3354.

[13] A. C. Wright, *Phys. Chem. Glasses Eur. J. Glass Sci. Technol. B* **51** (1), (2010), 1–39.

[14] T. Nanba, J. Kieffer and Y. Miura, *J. Non-Cryst. Solids* **277** (2-3), (2000), 188–206.

[15] A. Karthikeyan and R. M. Almeida, *J. Non-Cryst. Solids* **281** (1-3), (2001), 152–161.

[16] S. K. Lee and B. H. Lee, *J. Phys. Chem. B* **110** (33), (2006), 16408–16412.

[17] L. S. Du and J. F. Stebbins, *J. Phys. Chem. B* **110** (25), (2006), 12427–12437.

[18] C. J. Benmore, J. K. R. Weber, M. C. Wilding, J. Du and J. B. Parise, *Phys. Rev. B* **82** (22), (2010), 224202.

[19] L. B. Skinner, C. J. Benmore, J. K. R. Weber, S. Tumber, L. Lazareva, J. Neuefeind, L. Santodonato, J. Du and J. B. Parise, *J. Phys. Chem. B* **116** (45), (2012), 13439–13447.

[20] G. N. Greaves and S. Sen, *Adv. Phys.* **56** (1), (2007), 1–166.

[21] R. Bohmer and C. A. Angell, in: *Disorder Effects on Relaxational Processes*, edited by R. Richert and A. Blumen (Springer-Verlag, Berlin, 1994), pp. 11–54.

Appendix A

Melt Quenching of PbO

In order to investigate a claim in the literature of a 96 mol% PbO lead silicate glass [1], the preparation was replicated. β-PbO (20.86 g of Sigma-Aldrich Lead (II) oxide, Massicot) was placed into a 25 ml squat-form porcelain crucible. However, the powder was not ground using a pestle and mortar, since this was found to induce the $\beta \rightarrow \alpha$-PbO phase transformation. The crucible was placed into a furnace, and the reported [1] temperature profile reproduced (held at 500 °C for 30 minutes, ramped at 800 °C h^{-1} for 30 minutes, to reach 900 °C, held for 10 minutes), followed by splat quenching. The resultant material was predominantly a homogeneous, deep orange/brown, translucent glass, but regions containing streaks of yellow, presumably crystalline, material also existed, as well as a cloudiness on parts of the upper surface, indicating that a low density layer may have existed, floating on top of the melt. As reported by Dayanand *et al.* [1] the crucible showed clear signs of attack by the melt. The homogeneous material was confirmed to be x-ray amorphous using a laboratory diffractometer (Brucker D5005). However, EDX measurements revealed a glass composition of $72.8(1.0)PbO \cdot 16.6(5)SiO_2 \cdot 10.6(5)Al_2O_3$, indicating a large contamination from the crucible, which had approximate composition $84\,SiO_2 \cdot 16\,Al_2O_3$, as well as small amounts of Ca, Mg, Na, P and K. Glass density was measured at 7.25(5) g cm^{-3}, much lower than that reported by Dayanand *et al.* [1].

An attempt was also made to obtain a high PbO glass by melting in a vitreous silica crucible. The crucible containing PbO powder was placed into a furnace at 900 °C and held for 10 minutes, before rapid cooling via twin-roller quenching. The material obtained appeared to be a homogeneous yellow glass. The composition measured by EDX was $65.6(8)PbO \cdot 34.4(8)SiO_2$, again demonstrating the highly corrosive nature of liquid PbO. The measured glass composition is consistent with the measured density of 7.22(5) g cm^{-3} and glass transition temperature of 346(3) °C.

References

[1] C. Dayanand, G. Bhikshamaiah and M. Salagram, *Mater. Lett.* **23** (4-6), (1995), 309–315.

Appendix B

Vitreous Silica and Germania

B.1 Introduction

The glass-forming end members of the three binary oxide glass systems studied in this thesis are either vitreous silica, SiO_2, or vitreous germania, GeO_2. Both of these materials have been studied extensively owing to their fundamental importance as archetypal network glasses, see for example Wright [1] (silica), Salmon *et al.* [2] (germania), and §2.3. This appendix contains results from neutron and x-ray scattering measurements on glassy SiO_2 and GeO_2 which were performed alongside those on the binary oxide glasses, and where they act as standard samples for verifying the efficacy of the measurements and data analysis procedures.

B.2 Sample details

Commercial vitreous silica powder (Alfa Aesar, 99.8%) was used for x-ray scattering measurements, and this was held inside a 1.5 mm diameter silica capillary. For neutron diffraction an 8.0 mm diameter silica glass rod was used, this did not require a vanadium foil container. Diffraction measurements were performed in an identical manner to those on the lead silicate glasses, Chapter 6. The same sample of vitreous germania was used for both x-ray and neutron experiments, where it was treated identically to the lead germanate glasses, Chapter 7. Glass densities are shown in Table B-1, and are close to the average values calculated over many (226 for SiO_2, 57 for GeO_2) measurements reported in the literature, as collated in the SciGlass database [3].

Table B-1 Mass, number densities and molar volumes for pure silica and germania glasses.

	ρ_m, g cm^{-3}	ρ_0, nm^{-3}	V_M, cm^3 mol^{-1}
SiO_2	2.208(22)	66.38(67)	27.22(38)
GeO_2	3.650(37)	63.05(65)	28.65(32)

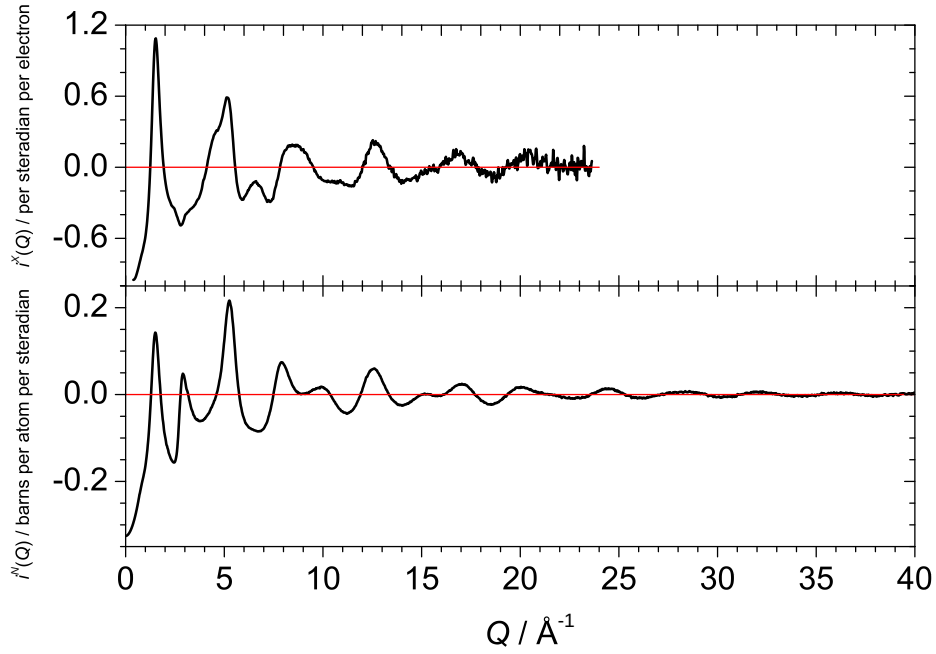

Figure B-1 Distinct neutron (lower) and x-ray (upper) scattering functions for silica glass.

B.3 Total scattering

B.3.1 Silica

The functions $i^X(Q)$ and $i^N(Q)$ measured for vitreous silica are shown in Fig. B-1. Their Fourier transforms, $T^X(r)$ and $T^N(r)$, are shown in Fig. B-2. Note that the top-hat convolution method [4, 5] was not applied to $i^X(Q)$ to remove any background which varied slowly with Q, however, the Compton fraction was increased by 2.5%, which compensated for a small background which was present. The significant amount of noise present at high-Q in $i^X(Q)$ is a result of measuring the silica sample under identical conditions to the lead silicates, and ideally a larger sample diameter would be used, if one was interested in the silica sample beyond its use as a standard and diagnostic aid. The Si-O and O-O peaks shown in Fig. B-2 were derived by fitting to the neutron

Table B-2 Parameters from peak fitting to $T^N(r)$ and $T^X(r)$ measured for vitreous silica and germania, see main text for details of the peak fitting procedure. Statistical errors from the fitting are given in parentheses. The final column indicates whether the values are obtained from fitting $T^N(r)$ or $T^X(r)$, see text for details.

Pair $j-k$	r_{jk} (Å)	$\langle u_{jk}^2 \rangle^{1/2}$ (Å)	n_{jk}	Origin
		Silica		
Si-O	1.6093(3)	0.0419(5)	3.96(2)	N
O-Si			1.98(1)	N
O-O	2.6257(8)	0.0786(9)	5.79(4)	N
Si-Si†	3.085(2)	0.118(3)	4.80(9)	X
		Germania		
Ge-O	1.7382(6)	0.0430(10)	3.99(4)	N
O-Ge			1.99(2)	N
O-O	2.828(7)	0.100(6)	5.99(34)	N
Ge-Ge†	3.166(2)	0.109(2)	4.22(6)	X

† Neglecting contributions from second X-O (X = Si,Ge) and second O-O shells.

$T^N(r)$, whilst the Si-Si peak was derived by fitting to the x-ray $T^X(r)$, holding the peak parameters for the Si-O and O-O peaks (derived from the neutron data) fixed. Peak parameters are given in Table B-2. It is clear from this analysis that both x-ray and neutron diffraction yield quantitatively accurate coordination numbers. The Si-Si coordination is overestimated (expected value of 4) due to overlap in this region with second Si-O and O-O shells [6, 7] which were not accounted for in the fitting procedure. The Si-O and O-O coordination numbers are damped below their expected values of 4 and 6 as a result of the Q-space resolution of the measurements. This was taken into account when predicting the areas of the intratetrahedral O-O correlations for the lead silicate glasses in Chapter 6, where the same factor of 5.79/6 (96.5%) was used to suppress the areas below their expected values.

The peak positions listed in Table B-2 can be used to infer a most probable angle for O-Si-O triplets of 109.33(6)° and for Si-O-Si triplets of 146.9(3)°. The former is close to the ideal tetrahedral angle of $2\arctan\sqrt{2} \simeq 109.47°$, supporting the notion of the [SiO_4] tetrahedron as the basic building block of the network, whilst the latter is in accord with previous studies [1, 6, 7], albeit a crude approximation due to the poor implicit assumption of a symmetric bond angle distribution, see Wright [1] and

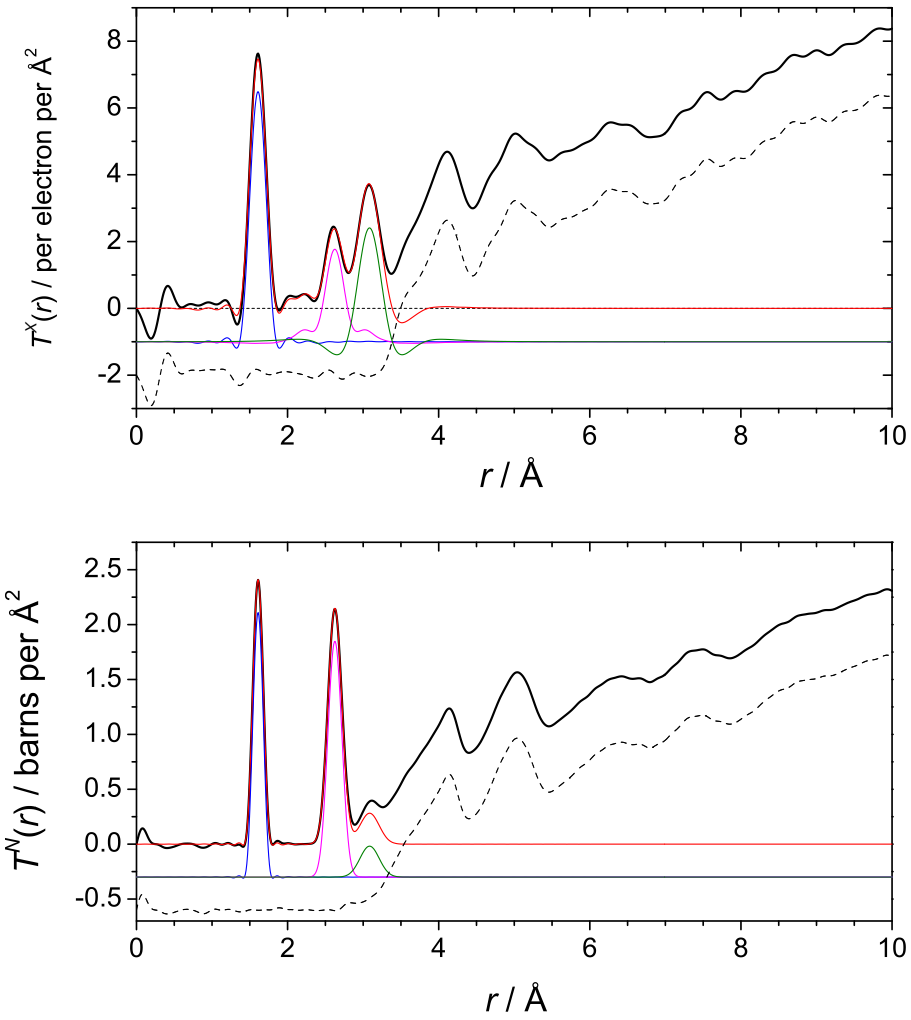

Figure B-2 Neutron (lower) and x-ray (upper) total correlation functions for silica glass, with $Q_{max} = 40\,\text{Å}^{-1}$ and $Q_{max} = 23.63\,\text{Å}^{-1}$ respectively. Sums of fitted peaks are overlaid, with individual Si-O, O-O and Si-Si peaks offset below and residuals (dashed) further offset below.

references therein.

B.3.2 Germania

The functions $i^X(Q)$ and $i^N(Q)$ measured for vitreous germania are shown in Fig. B-3. Their Fourier transforms, $T^X(r)$ and $T^N(r)$, are shown in Fig. B-2. Note that the top-hat convolution method [4, 5] was not applied to $i^X(Q)$ to remove any background which varied slowly with Q. A renormalisation of $i^N(Q)$ by a factor of 1.05 was found necessary in order to yield a $T^N(r)$ function with zero gradient in the low $0 \leq r \lesssim 2.4\,\text{Å}$ region (ignoring the Ge-O peak). Peaks were fitted to the total correlation functions in an analogous way to the silica case. The Ge-O and O-O peaks shown in Fig. B-4

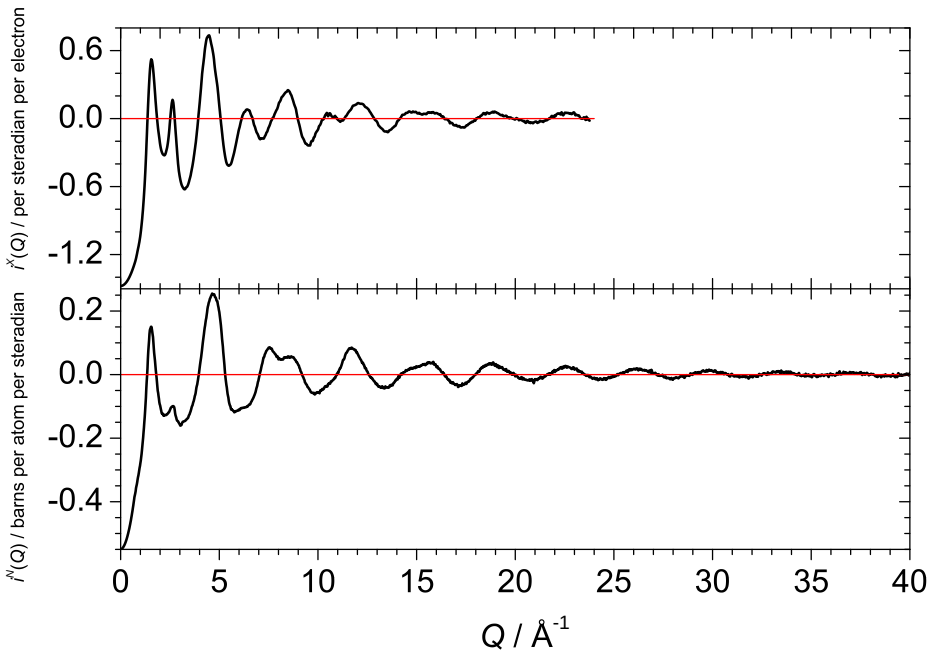

Figure B-3 Distinct neutron (lower) and x-ray (upper) scattering functions for germania glass.

were derived by fitting to the neutron $T^N(r)$, whilst the Ge-Ge peak was derived by fitting to the x-ray $T^X(r)$, holding the peak parameters for the Ge-O and O-O peaks (derived from the neutron data) fixed. Peak parameters are given in Table B-2. Again it is clear that both x-ray and neutron diffraction yield quantitatively accurate coordination numbers, although notably the O-O correlation in $T^X(r)$ is completely obscured by the negative wing of the nearest neighbour Ge-Ge correlation. The Ge-Ge coordination is overestimated (expected value of 4) due to overlap in this region with second Ge-O and O-O shells which were not accounted for in the fitting procedure, although the overestimation is less severe than in the silica case due to the larger relative x-ray scattering weighting factor of Ge-Ge in GeO_2 compared to Si-Si in SiO_2 (see Fig. 4-1). The O-O coordination number is not damped below its expected value of 6 as is the case for silica. This is attributed to a key structural difference between the two materials which becomes apparent from consideration of the three nearest neighbour peak positions and the most probable bond angles that can be inferred from these. From the values listed in Table B-2 one obtains a most probable O-Ge-O angle of 108.9(4)° and approximately 131.2(2)° for Ge-O-Ge triplets, in accord with previous measurements, see Salmon *et al.* [2], and references therein. The Ge-O-Ge angles in germania therefore

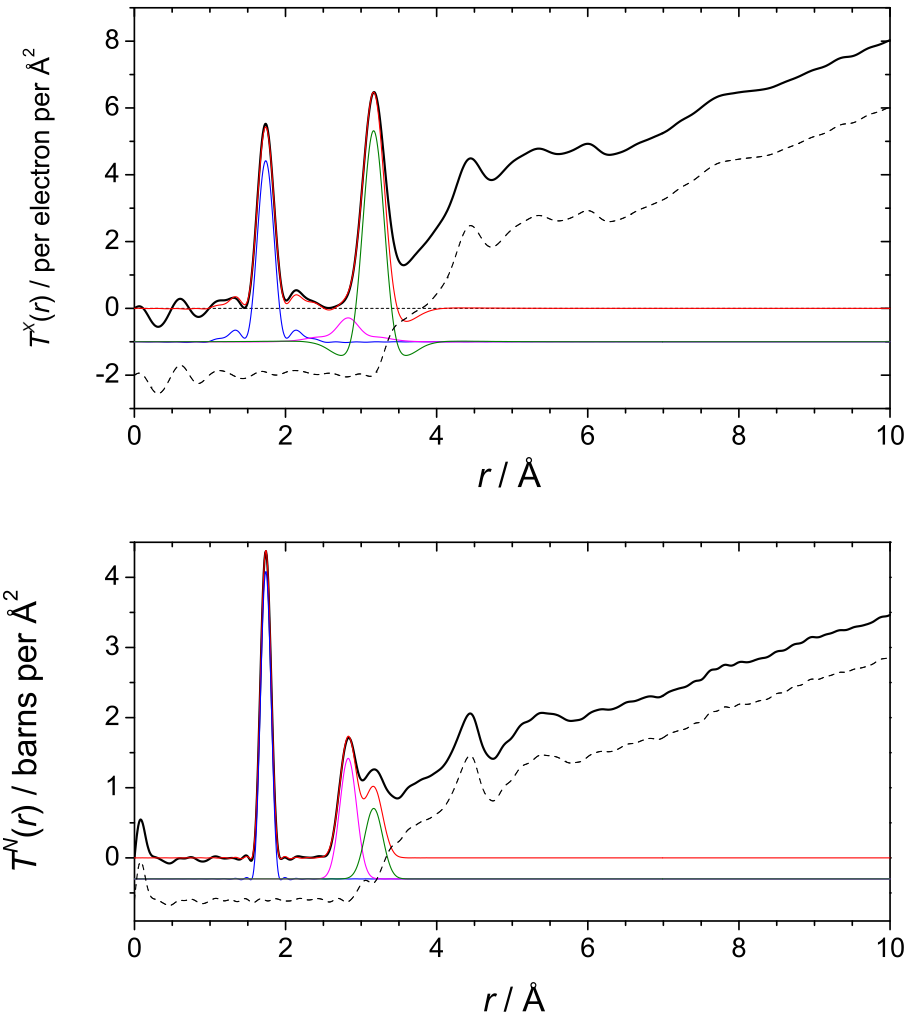

Figure B-4 Neutron (lower) and x-ray (upper) total correlation functions for germania glass, with $Q_{max} = 40$ Å^{-1} and $Q_{max} = 23.77$ Å^{-1} respectively. Sums of fitted peaks are overlaid, with individual Ge-O, O-O and Ge-Ge peaks offset below and residuals (dashed) further offset below.

tend to be smaller than the Si-O-Si angles in silica, and this results in a greater overlap of the nearest neighbour O-O and Ge-Ge correlations in the total correlation functions, as well as some overlap with second neighbour O-O and Ge-O distances, which is apparent from the full set of partial pair correlation functions measured by Salmon *et al.* [2] using neutron diffraction with Ge isotope substitution.

References

[1] A. C. Wright, *J. Non-Cryst. Solids* **179**, (1994), 84–115.

[2] P. S. Salmon, A. C. Barnes, R. A. Martin and G. J. Cuello, *J. Phys. Condens. Mat.* **19** (41), (2007), 415110.

[3] *SciGlass Professional 7.3* (ITC Inc., 2008).

[4] A. K. Soper and E. R. Barney, *J. Appl. Cryst.* **44**, (2011), 714–726.

[5] A. K. Soper, *Mol. Phys.* **107** (16), (2009), 1667–1684.

[6] R. Mozzi and B. Warren, *J. Appl. Cryst.* **2** (4), (1969), 164–172.

[7] H. F. Poulsen, J. Neuefeind, H. B. Neumann, J. R. Schneider and M. D. Zeidler, *J. Non-Cryst. Solids* **188** (1-2), (1995), 63–74.